ISBN 978-82-326-6090-2 (printed ver.)
ISBN 978-82-326-6497-9 (electronic ver.)
ISSN 1503-8181 (printed ver.)
ISSN 2703-8084 (electronic ver.)

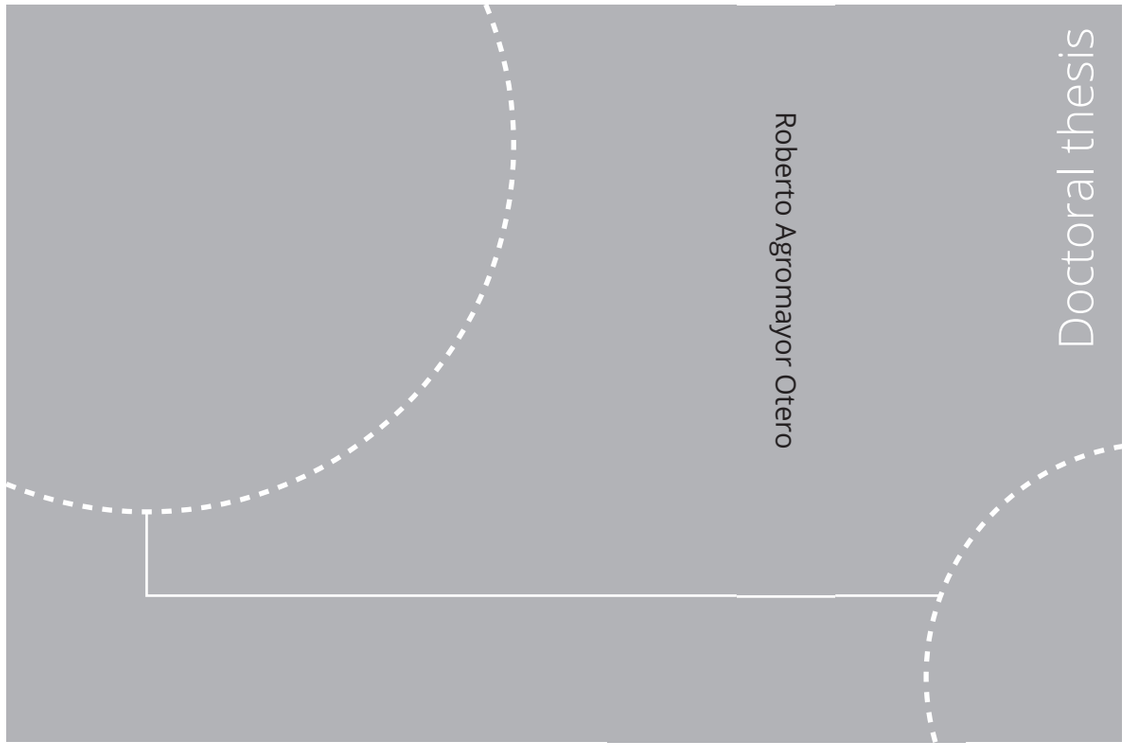

Doctoral theses at NTNU, 2021:180

Roberto Agromayor Otero

Advancements in Automated Methods for Fluid-Dynamic Turbomachinery Design

Doctoral theses at NTNU, 2021:180

NTNU
Norwegian University of Science and Technology

NTNU
Norwegian University of Science and Technology
Thesis for the degree of Philosophiae Doctor
Faculty of Engineering
Department of Energy and Process Engineering

NTNU
Norwegian University of Science and Technology

Roberto Agromayor Otero

Advancements in Automated Methods for Fluid-Dynamic Turbomachinery Design

Thesis for the degree of Philosophiae Doctor

Trondheim, May 2020

Norwegian University of Science and Technology
Faculty of Engineering
Department of Energy and Process Engineering

NTNU
Norwegian University of Science and Technology

Thesis for the degree of Philosophiae Doctor

Faculty of Engineering
Department of Energy and Process Engineering

ISBN 978-82-326-6090-2 (printed ver.)
ISBN 978-82-326-6497-9 (electronic ver.)
ISSN 1503-8181 (printed ver.)
ISSN 2703-8084 (electronic ver.)

Doctoral theses at NTNU, 2021:180

Printed by Skipnes Kommunikasjon AS

Preface

This thesis is submitted in partial fulfillment of the requirements for the degree of Doctor of Philosophy (Ph.D.) at the Norwegian University of Science and Technology (NTNU). The research described herein was carried out from August 2017 to December 2020 at the Department of Energy and Process Engineering of the Faculty of Engineering, with Associate Professor Lars Olof Nord as main supervisor and Professor Bernhard Müller and Professor Petter Nekså as co-supervisors. Two external research stays were undertaken during the course of this Ph.D. project, one from August 2018 to December 2018 at the Faculty of Aerospace Engineering of the Technical University of Delft, hosted by Assistant Professor Matteo Pini and Professor Piero Colonna, and the other from June 2019 to December 2019 at the Division of Aerospace Engineering and Fluid Mechanics of Queen Mary University of London, hosted by Reader Jens-Dominik Müller. The present Ph.D. project was founded by the Norwegian Research Council and industrial partners Equinor, Hydro, Alcoa, GE Power Norway and FrioNordica.

Abstract

Automated design methods are emerging as a powerful tool for the fluid-dynamic design of turbomachinery components. Such automated methods integrate mathematical models of different level of sophistication with numerical optimization techniques to explore large design spaces in a systematic way. This, in turn, allows the designer to achieve higher performance gains and shorten the development time with respect to traditional design workflows based on trial-and-error. In this context, the present thesis proposes a collection of models and methods for the preliminary and aerodynamic design optimization of turbomachinery that addresses some of the limitations of the design methods currently in use.

With regards to the preliminary design phase, this work proposes a design optimization method for axial turbines with any number of stages. The method is based on a new mean-line model that accepts arbitrary equations of state to evaluate the thermodynamic properties of the fluid and empirical loss models to estimate the entropy generation. In addition, the kinetic energy recovered at the exit of the last stage is predicted using a new one-dimensional annular diffuser model based on the balance equations for mass, momentum, and energy. In contrast with existing methods, the preliminary design problem was formulated as a constrained optimization problem and solved using a gradient-based algorithm. This choice of optimization method allows the designer to: (1) integrate the turbine, diffuser, and loss models in a simple way by means of equality-constraints and (2) find the optimal solution of multi-stage design problems with tens of design variables at a low computational cost. The preliminary design method was applied to a case study and a sensitivity analysis revealed that there exists a locus of maximum efficiency in the specific speed and diameter plane (i.e, the Baljé diagram) that can be predicted with a simple analytical expression.

Concerning the aerodynamic design phase, the present work proposes a unified geometry parametrization method based on computer-aided design (CAD) for axial, radial and mixed-flow turbomachinery blades. The method uses conventional engineering parameters (e.g., chord, metal angles, thickness distribution) and it exploits the mathematical properties of non-uniform rational basis spline (NURBS) curves and surfaces to produce blades with continuous curvature and rate of change of curvature. In addition, the method provides the sensitivity of the blade coordinates with respect to the design variables by means of the complex-step method, allowing the integration of the parametrization into automated, gradient-based shape optimization workflows. The proposed parametrization also allows one to replicate the geometry of an existing blade given by scattered point coordinates by solving a two-step optimization problem. The capabilities of this

reverse engineering strategy were demonstrated by replicating the geometry of eight turbomachinery blades in two and three dimensions with an accuracy comparable to the tolerances of current manufacturing technologies.

Furthermore, this thesis proposes an aerodynamic design method for turbomachinery blades operating under non-ideal thermodynamic conditions. The proposed method supports the simultaneous optimization of multiple blade rows in two dimensions and it relies on a new gradient-based shape optimization framework that integrates the proposed CAD-based parametrization with a Reynolds-Averaged Navier-Stokes (RANS) solver and its discrete adjoint counterpart. The aerodynamic design method developed in this work offers three main advantages with respect to other design systems: (1) the real-gas flow solver enables the optimization of unconventional turbomachinery (e.g., organic Rankine cycle turbines, supercritical carbon dioxide compressors) in which the fluid properties deviate from ideal gas behavior, (2) the discrete adjoint solver allows the designer to evaluate the cost function gradients at a computational cost that is essentially independent of the number of design variables, which, in turn, enables the exploration of large design spaces that would be untractable with gradient-free methods, and (3) compared with mesh-based parametrization methods, the CAD-based parametrization allows the designer to impose high-level geometric constraints, such as constant axial chord length, minimum trailing edge thickness, or smooth curvature distribution in a straightforward way.

In order to demonstrate the capabilities of the automated design tools developed during this project, the proposed preliminary and aerodynamic design methods are applied to design a new single-stage axial turbine operating with isobutane (R600a) that is is going to be built and tested in the EXPAND facility at the Norwegian University of Science and Technology. The preliminary design method was successfully applied to design a turbine geometry and velocity triangles that maximize the total-to-total isentropic efficiency of the turbine and satisfy the technical constraints imposed by the EXPAND facility. In addition, the aerodynamic design method was used to define stator and rotor blade shapes that minimize the entropy generation within the turbine and satisfy the design specifications established during the preliminary design phase. In particular, the gradient-based shape optimization framework was able to reduce the entropy generation by 36%, relative to the baseline geometry, which corresponds to a total-to-total isentropic efficiency increase of about 4 percentage points. Furthermore, the aerodynamic optimization did not only produce a quantitative improvement in performance, but also caused qualitative changes in the flow field. Most notably, the baseline stator cascade featured a trailing edge shock pattern and a shock-induced separation bubble that were eliminated as a result of the optimization.

Acknowledgements

I want to express my deepest gratitude to my supervisor, Lars O. Nord, for his trust and support through each stage of this project. Thank you for giving me the freedom to define my own research path and for fostering my independent thinking skills. I am proud of what I accomplished under your guidance and I hope that we will have more opportunities to work together in the future.

I also want to send my gratitude to Matteo Pini and Piero Colonna for hosting me at the Faculty of Aerospace Engineering of TU Delft and to Jens-Dominik Müller for hosting me at the Division of Aerospace Engineering and Fluid Mechanics of Queen Mary University of London. These two research stays, along with the long discussions about fluid dynamics and shape optimization, have been an essential part of this Ph.D. project.

Studying at NTNU was a very exciting stage of my life. I am grateful to all the professors and researchers who shared their knowledge of science and engineering with me. In particular, I would like to thank Ivar Ertesvåg, Simen Ellingsen, Geir Skaugen and Petter Nekså. In addition, I want to send a very warm thank you to Berhnard Müller and Reidar Kristoffersen for introducing me to the beauty and rigor of computational fluid dynamics. What I learnt from you sparked a flame that I will try to keep burning in the years to come.

I would also like to thank my friend Eduardo Liz. Thank you for all the advice that you gave me and for sharing your love for mathematics with me. Your words of encouragement are still present in my thoughts. *Lo mejor está por llegar.*

Completing this Ph.D. project was a long journey. I feel indebted to everyone who has been part of my life during these years. Let me start with my colleagues and friends at NTNU, TU Delft and Queen Mary. Thank you for providing such a warm and welcoming environment. A especial mention is due to Nitish, Adam and Lucia for making me feel among friends during my time in Delft. I also want to thank my friends David, Valeria, Magdalena and Marina. I will never forget our adventures in Russia. I am also thankful to Andrea, Celine and Adinda for all the good times that we spent in Norway and Spain. I wish you all the best in your ongoing Ph.D. projects. I also would like to show my gratitude to my *Xantar* friends: Marta, Anxo, Raquel, Michi, María, Alexis, Rubén, María, Borja and Inés. You made Trondheim feel like home to me.

As the old song goes, *no matter who you are, no matter where you go in your life, at some point you're going to need somebody to stand by you.* In my case, that somebody are my friends Giorgia and Jairo. Thank you for putting up with me all these years.

Finally, I would like to dedicate all the effort put into this Ph.D. project to my family. Gracias por enseñarme el valor del esfuerzo. Gracias por enseñarme a disfrutar de mis éxitos y sobreponerme a las dificultades. Y, sobre todo, gracias por apoyarme durante todos estos años a pesar de la distancia. Os quiero mucho.

Roberto Agromayor Otero
Oslo, 6$^{\text{th}}$ of May of 2021

Contents

Preface i

Abstract iii

Acknowledgements v

List of Figures xi

List of Tables xiii

Nomenclature xv

1 Introduction 1

1.1 Background and motivation 1
1.2 Objectives and scope 2
1.3 Contributions 3
1.4 Thesis organization 4
1.5 List of publications 5

2 One-Dimensional Flow Model for Annular Diffusers 7

2.1 Introduction 8
2.2 Diffuser model 11
2.2.1 Diffuser geometry 11
2.2.2 Velocity vector conventions 12
2.2.3 Thermodynamic properties 12
2.2.4 Mathematical model 13
2.3 Verification and validation of the model 17
2.4 Sensitivity analysis 19
2.4.1 Skin friction coefficient 20
2.4.2 Inlet hub-to-tip ratio 21
2.4.3 Mean wall cant angle 22
2.4.4 Inlet swirl angle 23

2.4.5 Inlet Mach number 23
2.5 Conclusions 24

3 Preliminary Design Method for Axial Turbines 27
3.1 Introduction 28
3.2 Axial turbine model 30
3.2.1 Axial turbine geometry 30
3.2.2 Velocity vector conventions 32
3.2.3 Design specifications 33
3.2.4 Cascade model 33
3.2.5 Loss model 37
3.2.6 Diffuser model 38
3.3 Validation of the axial turbine model 39
3.4 Optimization problem formulation 40
3.4.1 Objective function 40
3.4.2 Design variables 41
3.4.3 Fixed parameters 42
3.4.4 Constraints 42
3.4.5 Optimization algorithm 42
3.5 Design optimization of a case study 43
3.6 Sensitivity analysis 45
3.6.1 Isentropic power output 45
3.6.2 Tip clearance gap 46
3.6.3 Hub-to-hip-ratio constraint 46
3.6.4 Diffuser area ratio 47
3.6.5 Diffuser skin friction coefficient 47
3.6.6 Total-to-static pressure ratio 48
3.6.7 Number of stages 49
3.6.8 Angular speed and diameter 49
3.7 Conclusions 51

4 Parametrization Method for Turbomachinery Blades 53
4.1 Introduction 54
4.2 Background on NURBS curves and surfaces 57
4.3 Blade parametrization in two dimensions 59
4.4 Blade parametrization in three dimensions 63

4.5 Sensitivity computation and verification 70
4.6 Blade matching methodology 74
4.7 Conclusions 78

5 Aerodynamic Design Method for Turbomachinery Blades 79
5.1 Introduction 80
5.2 Aerodynamic shape optimization framework 83
5.2.1 CAD parametrization 83
5.2.2 Mesh generation and deformation 85
5.2.3 Direct flow solver 85
5.2.4 Adjoint flow solver and gradient evaluation 87
5.2.5 Optimization 89
5.3 Validation of the flow solver 89
5.4 Application to a case study: EXPAND facility 91
5.4.1 Preliminary design 92
5.4.2 Aerodynamic design 93
5.5 Conclusions 99

6 Conclusions and Further Work 101
6.1 Conclusions 101
6.2 Further work 103

References 105

A Derivation of the Equations for the Flow in an Annular Duct A1
A.1 Groundwork A1
A.2 Transport equation for mass A2
A.3 Transport equation for a general quantity A4
A.4 Transport equations for momentum A5
A.5 Transport equations for energy A6
A.5.1 Total energy A6
A.5.2 Mechanical energy A7
A.5.3 Thermal energy A8
A.6 Transport equation for entropy A9

B Kacker–Okapuu Loss Model B1
B.1 Overview of the method B1

B.2 Reynolds number correction factor B1
B.3 Mach number correction factor B2
B.4 Profile loss coefficient B2
B.5 Secondary loss coefficient B3
B.6 Tip clearance loss coefficient B4
B.7 Trailing edge loss coefficient B4

C Derivation of Leading and Trailing Edge Curvature Formulas C1

D Design Data of the EXPAND Turbine D1

E Publications E1

List of Figures

2.1 Geometry of a general annular diffuser 11
2.2 Decomposition of the velocity vector 12
2.3 Control volume used to derive the flow governing equations 14
2.4 Cross section of an annular diffuser with straight walls 16
2.5 Connection of the diffuser model with a turbomachine model . . . 16
2.6 Enthalpy and entropy error analyses for the reference case 18
2.7 Comparison of model output with experimental data 18
2.8 Influence of the skin friction coefficient 22
2.9 Influence of the hub-to-tip ratio 22
2.10 Influence of the mean wall cant angle (area ratio) 23
2.11 Influence of the mean wall cant angle (axial length) 23
2.12 Influence of the inlet swirl angle 24
2.13 Influence of the inlet Mach number 24

3.1 Geometry of a general axial turbine and exhaust diffuser 31
3.2 Velocity triangle notation and conventions 32
3.3 Automated workflow for preliminary turbomachinery design 40
3.4 Influence of the isentropic power output and tip clearance gap . . . 47
3.5 Influence of the isentropic power output and hub-to-tip ratio . . . 47
3.6 Influence of the diffuser area ratio and skin friction coefficient . . . 48
3.7 Influence of the diffuser area ratio and pressure ratio 48
3.8 Influence of the pressure ratio and number of stages 49
3.9 Baljé diagram and optimal blade speed rule 49

4.1 Construction of NURBS curves and surfaces 58
4.2 Construction of the blade geometry in two dimensions 60
4.3 Construction of the flow domain in two dimensions 62
4.4 Geometry and curvature distribution of several blade profiles . . . 64
4.5 Blade, hub, and shroud surfaces in the meridional plane 65
4.6 Construction of the blade shape in the meridional plane 66
4.7 Evolution of a design variable along the spanwise direction. 66

4.8 B-spline defining the tangential coordinates of the camber line . . . 66
4.9 Camber surface control points 66
4.10 Blade surface control points 66
4.11 Construction of the blade flow domain in three dimensions 69
4.12 Geometry of the AACHEN stator blade 71
4.13 Geometry of the NASA R67 rotor blade 71
4.14 Geometry of the XPROP propeller blade 71
4.15 Geometry of the APU rotor blade 72
4.16 Sensitivity of the blade geometry 73
4.17 Sensitivity computation error analysis 74
4.18 Blade matching problem in two dimensions 75
4.19 Re-parametrization error as the design space is refined 77

5.1 Outline of the aerodynamic shape optimization framework 83
5.2 Outline of the CAD-based parametrization method 84
5.3 Mach number and surface pressure for the Kiock cascade 90
5.4 Mach number and surface pressure for the Hodson cascade 90
5.5 Mach number and surface pressure for the Arts cascade 90
5.6 T–s diagram of the expansion and cross section of the turbine . . . 92
5.7 Velocity triangles at the inlet and outlet of the rotor cascade . . . 93
5.8 Computational grid for the stator and rotor flow domains 95
5.9 Mesh independence study in terms isentropic efficiency 96
5.10 Direct and adjoint solver convergence history 96
5.11 Verification of the adjoint-based sensitivities 96
5.12 Optimization convergence history 96
5.13 Baseline relative Mach number contours 97
5.14 Optimal relative Mach number contours 97
5.15 Surface pressure distribution over the stator and rotor blades . . . 98
5.16 Boundary layer profile for the stator and rotor blades 98
5.17 Rotor boundary layer downstream the suction side shock 98
5.18 Entropy distribution at the plane 2 mm downstream the blades . . 98

B.1 Profile loss of reaction blades B5
B.2 Profile loss of impulse blades B5
B.3 Hub-to-mean Mach number ratio B5
B.4 Trailing edge energy loss coefficient B5

List of Tables

2.1 Survey of diffuser modeling for preliminary turbine design 9
2.2 Survey of one-dimensional diffuser models 10
2.3 Definition of the reference case 20
2.4 Definition of the validation case 21
2.5 Comparison of the model output with experimental data 21

3.1 Survey of axial turbine mean-line models 29
3.2 Validation of the axial turbine model against experimental data . . 39
3.3 Definition of the reference cases 44
3.4 Optimization results for the two reference cases 45
3.5 Specific blade speed rule against optimization results 51

4.1 Survey of constructive blade parametrization methods 55
4.2 List of two-dimensional design variables 59
4.3 List of three-dimensional design variables 65
4.4 Summary of the test cases and matching results 77

5.1 Survey of adjoint-based turbomachinery design methods 81
5.2 Design variables of the parametric CAD model 84
5.3 Boundary conditions of the validation test cases 91
5.4 Design specifications used for the preliminary design 94
5.5 Boundary conditions used for the aerodynamic design 94
5.6 Thermophysical properties of isobutane (R600a) 94

A.1 Normal vectors and surface elements of the control volume A2

D.1 Preliminary and aerodynamic design of EXPAND turbine D1

Nomenclature

Latin symbols

a	Speed of sound	m/s
A	Flow area	m^2
A	Coefficient matrix	several
AR	Area ratio	–
b	Diffuser channel height	m
$\hat{b}_{\text{in}}$	Diffuser inlet channel height	m
c	Blade chord	m
c_{ax}	Blade axial chord	m
c_p	Specific heat capacity at constant pressure	J/kg K
C_{f}	Skin friction coefficient	–
C_p	Pressure recovery coefficient	–
$\mathbf{C}$	NURBS curve coordinates	m
d	Tangent proportion	–
d	Mean diameter	m
d_{s}	Specific diameter	–
D_{h}	Hydraulic diameter	m
e	Internal energy	J/kg
f	NURBS start point curvature function	m
g	NURBS end point curvature function	m
h	Step size	several
h	Static specific enthalpy	J/kg
h_0	Stagnation specific enthalpy	J/kg
Δh_s	Isentropic specific enthalpy change	J/kg
H	Blade height	m

H_{out}	Outlet turbomachinery blade height	m
i	Cascade incidence angle	°
I_{t}	Turbulence intensity	–
J	Cost function	several
k	Heat conductivity	W/m K
L	Arc length	m
m	Meridional coordinate	m
$\dot{m}$	Mass flow rate	kg/s
Ma	Mach number	–
$\mathbf{n}$	Unitary normal vector	–
$N_{i,p}$	B-spline basis polynomial of degree p	–
N_{b}	Number of blades	–
N_Q	Number of prescribed points	–
N_{s}	Number of stages	–
Nu	Nusselt number	–
o	Blade opening	m
p	Static pressure	Pa
p_0	Stagnation pressure	Pa
PR	Pressure ratio	–
Pr	Prandtl number	–
$\mathbf{P}$	NURBS control point coordinates	m
$\dot{q}_{\text{w}}$	Heat flux at the wall	W/m^2
$\mathbf{Q}$	Prescribed point coordinates	m
r	Radial coordinate	m
r	Mean radius	m
r	Radius of curvature	m
r_{h}	Radius at the hub of the blades	m
r_{t}	Radius at the tip of the blades	m

$\hat{r}_{\mathrm{in}}$	Diffuser inlet mean radius	m
R	Gas constant	J/kg K
R_{out}	Outlet turbomachinery radius	m
Re	Reynolds number	–
s	Specific entropy	J/kg K
s	Blade pitch, also known as spacing	m
s_{ax}	Axial spacing between cascades	m
S	Source term vector	several
$\mathbf{S}$	NURBS surface coordinates	m
t^{l}	Blade lower thickness distribution	m
t^{u}	Blade upper thickness distribution	m
t_{cl}	Blade tip clearance gap	m
t_{max}	Blade maximum blade thickness	m
t_{te}	Blade railing edge thickness	m
T	Static temperature	K
T_0	Stagnation temperature	K
T_{w}	Temperature at the wall	K
u	Blade velocity	m/s
u	NURBS parametric coordinate	–
U	Solution vector	several
U	NURBS knot vector	–
U_h	Overall heat transfer coefficient	W/m K
v	Absolute flow velocity	m/s
v	NURBS parametric coordinate	–
v_0	Isentropic velocity, also known as spouting velocity	m/s
V	NURBS knot vector	–
w	Relative flow velocity	m/s
w	NURBS control point weights	–

$\dot{W}$	Actual power output	W
$\dot{W}_s$	Isentropic power output	W
x	Axial coordinate	m
$\hat{x}_{\text{in}}$	Diffuser inlet axial coordinate	m
X_s	Boundary mesh coordinates	m
X_v	Interior mesh coordinates	m
y	Tangential coordinate	m
y^+	Non-dimensional wall distance	–
Y	Pressure loss coefficient, $Y = \frac{p_{0\,\text{rel,in}} - p_{0\,\text{rel,out}}}{p_{0\,\text{rel,out}} - p_{\text{out}}}$	–
z	Radial coordinate	m
Z	Compressibility factor, $Z = p/\rho RT$	–

Greek symbols

α	Set of design variables	–
α	Absolute flow angle	°
β	Relative flow angle	°
γ	Heat capacity ratio	–
δ	Cascade deviation angle	°
δ	Diffuser divergence semi-angle	°
δ_{fl}	Blade flaring angle	°
η_{ts}	Total-to-static isentropic efficiency	–
η_{tt}	Total-to-total isentropic efficiency	–
θ	Circumferential angle	°
θ	Metal blade angle	°
$\Delta\theta$	Camber angle	°
κ	Curvature	m^{-1}
λ	Hub-to-tip radii ratio	–
Λ	Degree of reaction, $\Lambda = \frac{h_2 - h_3}{h_1 - h_3}$	–

μ	Molecular dynamic viscosity	Pa s
μ_t	Turbulence dynamic viscosity	Pa s
ξ	Stagger angle, also known as setting angle	°
ρ	Static density	kg/m^3
$\dot{\sigma}$	Entropy generation per unit volume	W/m^3 K
τ_w	Shear stress at the wall	Pa
$\boldsymbol{\tau}$	Unitary tangent vector	–
ϕ	Kinetic energy loss coefficient ($\phi^2 + \Delta\phi^2 = 1$)	–
ϕ	Mean wall cant angle	°
ϕ_1	Inner wall cant angle	°
ϕ_2	Outer wall cant angle	°
ω	Acentric factor	–
Ω	Angular speed	rpm
Ω_s	Specific speed	–

Abbreviations

AD	Algorithmic Differentiation
BFGS	Broyden–Fletcher–Goldfarb–Shanno optimization algorithm
BL	Boundary Layer
CAD	Computed-Aided Design
CEV	Constant Eddy Viscosity
CFD	Computational Fluid Dynamics
CFL	Courant-Friedrichs-Lewy number
CS	Complex Step
EOS	Equation of State
FD	Finite Differences
FVM	Finite Volume Method
GMRES	Generalized Minimal Residual method

MUSCL	Monotonic Upstream-centered Scheme for Conservation Laws
NURBS	Non Uniform Rational Basis Spline
ODE	Ordinary Differential Equation
RANS	Reynolds-Averaged Navier-Stokes equations
SQP	Sequential Quadratic Programming
SU2	Stanford University Unstructured multiphysics suite

Subscripts and superscripts

0	Stagnation state
1	Inlet flow station
2	Outlet flow station or flow station between stator and rotor
3	Outlet flow station
in	Inlet or leading edge
out	Outlet or trailing edge
b	Blade
c	Camber
crit	Critical point
l	Blade lower side
m	Meridional direction
r	Radial direction
rel	Rotating frame of reference
s	Isentropic state
u	Blade upper side
x	Axial direction
θ	Tangential direction

Chapter 1

Introduction

1.1 Background and motivation

Before the advent of digital computers, the design of turbomachinery was dominated by experimental campaigns and simple design rules based on physical intuition and the experience gained from previous designs. Prototypes were built and tested, and the experience acquired was used to guide the design process until a satisfactory performance was obtained. Over time, however, advances in computational power and numerical analysis allowed a significant fraction of the experimental efforts to be replaced by computer simulations. As a result, the fluid-dynamic design of turbomachinery currently relies on a range of mathematical models of different level of sophistication, and it is often conceptualized into the preliminary and aerodynamic design phases (Pini et al. 2017).

During the preliminary design phase, the objective of the designer is to select a machine architecture and an approximate geometry that satisfies the design specifications obtained from a system-level analysis. In this phase, the performance of the machine is estimated using a mean-line model, whereby the flow is assumed to be uniform along the blade span and the balance equations for mass and rothalpy are solved at the inlet and outlet of each cascade (Dixon et al. 2013). By contrast, the objective of the aerodynamic design phase is to define detailed blade shapes that produce a flow field satisfying the aerodynamic targets established during the preliminary design phase (e.g., flow angles, degree of reaction). To this aim, the geometry is defined in a computer-aided design (CAD) environment and the equations governing the flow are solved by means of computational fluid dynamics (CFD) to determine the machine performance (Denton et al. 1998).

Despite significant advances in turbomachinery flow modeling, the trial-and-error nature of the design process has largely endured and many designs are still carried out by manually sampling the design space until a configuration with an acceptable performance is found (Denton 2010). These manual design workflows may be feasible for design problems involving only a handful of design variables, but they rapidly become time-consuming and error-prone as the complexity of the problem increases. In addition, the design variables are often interrelated in complicated ways and it is easy to miss potential interactions that could lead to superior designs. As an alternative, automated design workflows that integrate flow models with numerical optimization techniques are emerging as a powerful

tool that enables the systematic exploration of large design spaces. This, in turn, allows the designer to achieve higher performance gains, shorten the development time of new products, and make the design process reproducible (Van den Braembussche 2008). Moreover, automated design workflows offer a great potential for unconventional applications, in which a large body of previous design experience does not yet exist. Prominent among these, are turbomachines operating in the Non-Ideal Compressible Fluid Dynamics (NICFD) regime (Kluwick 2017; Vitale et al. 2017), including the turbines and compressors used in organic Rankine cycle (ORC) and supercritical carbon dioxide (sCO_2) power systems (Colonna et al. 2008; Romei et al. 2020).

Thanks to these advantages, automated design methods based on numerical optimization are expected to play a significant role in the fluid-dynamic design of turbomachinery components (Verstraete 2019). At the time of this writing, the majority of automated design systems rely on gradient-free optimization methods. Presumably, this is because of their robustness, ease of integration with black-box models, and ability to handle non-smooth or discontinuous optimization problems (Audet et al. 2017). However, gradient-free methods require a large number of function evaluations to converge to the optimum solution, especially when the problem involves many design variables. This, in turn, results in high execution times that hinder the application of these methods to complex industrial design problems. Consequently, the fluid-dynamic design of turbomachinery may benefit significantly from the development of differentiated design chains and the adoption of efficient gradient-based optimization methods (Pini et al. 2017).

Moreover, one limitation of many of the design methods currently in use is that they assume that the fluid behaves as an ideal gas. However, this is not appropriate in some unconventional applications, such as ORC or sCO_2 power systems, where the fluid is often being expanded or compressed in the thermodynamic region close to the critical point or to the vapor saturation line (Colonna et al. 2008). In such applications, it is recognized that the fluid-dynamic design of turbomachinery may benefit significantly from the use of systematic optimization methods and accurate equations of state (Vitale et al. 2017; Persico et al. 2019).

Despite recent advances in the field, automated turbomachinery design methods still need to be improved and become more mature before they can be routinely used to solve complex industrial design problems or explore unconventional turbomachinery concepts for which no previous design experience is available.

1.2 Objectives and scope

Considering the limitations of the existing design systems, the goal of this Ph.D. thesis is to develop a set of automated methods for the fluid-dynamic design of turbomachines operating under NICFD conditions. This principal goal was divided into four objectives that could be managed individually:

- Develop an optimization strategy for turbomachinery preliminary design.
- Develop a CAD-based parametrization method for turbomachinery blades.
- Integrate the proposed parametrization method with a high-fidelity flow solver to develop an aerodynamic design method for turbomachinery blades operating under non-ideal thermodynamic conditions.
- Demonstrate the capabilities of the proposed methods by carrying out the complete fluid-dynamic design of a new turbomachine.

As the scope of the present thesis is the development of *fluid-dynamic* design methods, the influence of other disciplines, such as stress analysis, conjugate heat transfer, or aero-elasticity, was not considered. In addition, the automated design methods proposed in this thesis rely on *physical models* and *gradient-based* optimization algorithms, and the use of gradient-free algorithms and meta-modeling techniques was not investigated. Furthermore, the methods developed herein are formulated from a *deterministic* point of view and the uncertainty in the model predictions was not quantified or accounted for. Finally, this thesis does not contain any experimental work, but the proposed models were validated against experimental data when possible.

1.3 Contributions

The main contributions of this thesis can be summarized as:

- Development of a one-dimensional model for annular diffusers.
- Development of a mean-line model for axial turbines.
- Development of an optimization strategy for the preliminary design of turbomachinery that integrates the axial turbine and diffuser models.
- Development of a unified CAD-based parametrization for axial, radial, and mixed-flow turbomachinery blades that also provides the sensitivity of the geometry with respect to the design variables.
- Development of a reverse engineering method that enables the parametrization of an existing blade geometry defined by a set of scattered coordinates.
- Development of an aerodynamic shape optimization framework that combines the proposed CAD-based parametrization with a real-gas, multi-row turbomachinery flow solver and its discrete adjoint counterpart.
- Application of the proposed preliminary and aerodynamic design methods to accomplish the complete fluid-dynamic design of a new single-stage axial turbine using isobutane (R600a) as working fluid.

The novel aspects of each contribution are discussed in the context of the relevant scientific literature in the body of the thesis. With regards to authorship, the proposed annular diffuser model, axial turbine mean-line model, and preliminary design optimization strategy were developed solely by the author, whereas the CAD-based parametrization and shape optimization framework were developed in collaboration with Ph.D. candidate Nitish Anand at TU Delft.

To date, most of the computational turbomachinery research has been carried out using in-house or proprietary codes, thus hindering the widespread adoption of new methods and the replication of published results. As an alternative, the open-source paradigm offers several advantages from the scientific standpoint, including: transparency, reproducibility, and ease of development (e.g., fixing errors, extending the code with new features). For this reason, the author decided to follow the example set by Denton (2017) and release the computer implementations of the contributions documented in this thesis under open-source licenses and make them available in public repositories:

- *AxialOpt v1.0* (2019). DOI: https://doi.org/10.5281/zenodo.2635586
- *Parablade v1.0* (2020). DOI: https://doi.org/10.5281/zenodo.3894778

By doing so, the author hopes that these codes may be useful to other researchers and industry practitioners and, perhaps, serve as a basis for the development of new turbomachinery design methods.

1.4 Thesis organization

This document is structured as a collection of articles and it comprises this introduction, four chapters based on scientific publications, and one final chapter that summarizes the conclusions drawn from this work and suggests directions for further research. A brief summary of the four main chapters is provided here.

Chapter 2 describes the formulation of a one-dimensional annular diffuser model intended for the preliminary design of NICFD turbomachinery. The model is validated against experimental data and the accuracy of the numerical solution is verified against analytical results. In addition, a sensitivity analysis is performed to investigate the influence of several input parameters on the performance of the diffuser and draw design guidelines.

Chapter 3 documents the development of a mean-line model for axial turbines operating in the NICFD regime. The accuracy of the model is validated against experimental data from two different test cases. In addition, the preliminary turbomachinery design problem is formulated as a constrained optimization problem that integrates the proposed mean-line and annular diffuser models by means of equality-constraints. The design optimization method is applied to a case study and a sensitivity analysis is carried out to investigate the influence of several design variables on the optimal turbine design.

Chapter 4 presents a CAD-based parametrization method for two-dimensional blade profiles and three-dimensional axial, radial, and mixed-flow turbomachinery blades. The method is based on conventional engineering parameters (e.g., chord, metal angles, thickness distribution) and it exploits the mathematical properties of NURBS curves and surfaces to produce blades with continuous curvature and rate of change of curvature. Moreover, the proposed method is capable of re-parametrizing an existing blade geometry given by a set of scattered point coordinates by solving a two-step optimization problem. The capabilities of the method are demonstrated by replicating eight turbomachinery blades with an accuracy comparable to the tolerances of current manufacturing technologies.

Chapter 5 proposes a gradient-based shape optimization framework for the aerodynamic design of turbomachinery blades operating under NICFD conditions. The framework supports the simultaneous optimization of multiple blade rows in two dimensions and it integrates the proposed CAD-based parametrization with a real-gas turbomachinery flow solver and its discrete adjoint counterpart. The flow solver is validated against experimental data from three different linear cascades and the accuracy of the adjoint-based gradient evaluation is verified against a finite difference approximation. In addition, the capabilities of the proposed preliminary and aerodynamic design methods are demonstrated by carrying out the design optimization of a single-stage axial turbine operating with isobutane (R600a).

1.5 List of publications

The research carried out during this Ph.D. project resulted in four journal publications that are compiled in this thesis and are subject to evaluation. Moreover, during the course of the present project, the author was involved in three additional journal publications and five conference papers. These works are not part of this thesis and are not subject to evaluation.

Publications included in the thesis

R. Agromayor, B. Müller, and L. O. Nord (2019a). "One-Dimensional Annular Diffuser Model for Preliminary Turbomachinery Design". *International Journal of Turbomachinery, Propulsion and Power* 4.3, pp. 1–31. DOI: https://doi.org/10.3390/ijtpp4030031 (Chapter 2)

R. Agromayor and L. O. Nord (2019b). "Preliminary Design and Optimization of Axial Turbines Accounting for Diffuser Performance". *International Journal of Turbomachinery, Propulsion and Power* 4.3, pp. 1–32. DOI: https://doi.org/10.3390/ijtpp4030032 (Chapter 3)

R. Agromayor, N. Anand, J.-D. Müller, M. Pini, and L. O. Nord (2021a). "A Unified Geometry Parametrization Method for Turbomachinery Blades". *Computer-Aided Design* 133, pp. 1–16. DOI: https://doi.org/10.1016/j.cad.2020.102987 (Chapter 4)

R. Agromayor, N. Anand, M. Pini, and L. O. Nord (2021b). "Multi-row Adjoint-based Optimization of NICFD Turbomachinery Using a CAD-based Parametrization". *To be submitted to: Journal of Engineering for Gas Turbines and Power* (Chapter 5)

Other journal articles

H. Nami, I. S. Ertesvåg, R. Agromayor, L. Riboldi, and L. O. Nord (2018). "Gas Turbine Exhaust Gas Heat Recovery by Organic Rankine Cycles (ORC) for Offshore Combined Heat and Power Applications – Energy and Exergy Analysis". *Energy* 165, pp. 1060–1071. DOI: https://doi.org/10.1016/j.energy.2018.10.034

J. Rúa, R. Agromayor, M. Hillestad, and L. O. Nord (2020). "Optimal Dynamic Operation of Natural Gas Combined Cycles Accounting for Stresses in Thick-Walled Components". *Applied Thermal Engineering* 170, pp. 1–13. DOI: https://doi.org/10.1016/j.applthermaleng.2019.114858

B. Hagen, R. Agromayor, and P. Nekså (2021). "Equation-Oriented Methods for Design Optimization and Performance Analysis of Radial Inflow Turbines". *Submitted to: Energy*

Conference proceedings

R. Agromayor and L. O. Nord (2017a). "Fluid Selection and Thermodynamic Optimization of Organic Rankine Cycles for Waste Heat Recovery Applications". *Energy Procedia* 129, pp. 527–534. DOI: https://doi.org/10.1016/j.egypro.2017.09.180

R. Agromayor, J. Rúa, and R. Kristoffersen (2017b). "Simulation of Starting and Stopping Vortices of an Airfoil". *Proceedings of the 58th Conference on Simulation and Modelling*, pp. 66–75

I. Encabo-Cáceres, R. Agromayor, and L. O. Nord (2017). "Thermodynamic Optimization of an Organic Rankine Cycle for Power Generation From a Low Temperature Geothermal Heat Source". *Proceedings of the 58th Conference on Simulation and Modelling*, pp. 251–262

R. Pili, N. Siamisiis, R. Agromayor, L. O. Nord, C. Wieland, and H. Spliethoff (2019). "Efficiency Correlations for Off-Design Performance Prediction of ORC Axial-Flow Turbines". *Proceedings of the 5th International Seminar on ORC Power Systems*, pp. 1–8

Á. Á. Pardiñas, M. Pilarczyk, R. Agromayor, and L. O. Nord (2019). "Design of an Experimental ORC Expander Setup Using Natural Working Fluids". *Proceedings of the 5th International Seminar on ORC Power Systems*, pp. 1–8

Chapter 2

One-Dimensional Flow Model for Annular Diffusers

Part of the contents of this chapter appear in:

> R. Agromayor, B. Müller, and L. O. Nord (2019a). "One-Dimensional Annular Diffuser Model for Preliminary Turbomachinery Design". *International Journal of Turbomachinery, Propulsion and Power* 4.3, pp. 1–31. DOI: https://doi.org/10.3390/ijtpp4030031

Abstract

This chapter presents a one-dimensional annular diffuser model indented for the preliminary design of turbomachinery. The model formulation is more general than that of previous works, allowing one to use arbitrary equations of state and to include the effects of area change, heat transfer, and friction. The mathematical model poses an implicit system of ordinary differential equations that can be solved when the Mach number in the meridional direction is different than one. The model was verified against a reference case to assess that: (1) the stagnation enthalpy is conserved and (2) the entropy computation is consistent, finding that the error of the numerical solution was always lower than the prescribed integration tolerance. In addition, the model was validated against experimental data, finding that deviation between the predicted and measured pressure recovery coefficients was less than 2% when the best-fit skin friction coefficient is used. Finally, the influence of several design variables on the performance of the diffuser was investigated, concluding that: (1) the area ratio is not a suitable optimization variable because the pressure recovery coefficient increases asymptotically as this variable tends to infinity, (2) the diffuser should be designed with a positive mean wall cant angle to recover the tangential component of kinetic energy, (3) the performance of the diffuser declines when the hub-to-tip ratio of the last turbomachinery stage increases because the diffuser channel height is reduced.

2.1 Introduction

A diffuser is a device used to reduce the velocity and increase the static pressure of a fluid flow. The performance of the diffuser is usually characterized in terms of the pressure recover coefficient, which is defined as

$$C_p = \frac{p_{\text{out}} - p_{\text{in}}}{p_{0,\text{in}} - p_{\text{in}}}, \quad \text{or as} \quad C_{p,\text{inc}} = \frac{p_{\text{out}} - p_{\text{in}}}{\frac{1}{2}\rho v_{\text{in}}^2} \tag{2.1}$$

for the limiting case of incompressible flow (White 2011, pp. 404–408). In the context of turbomachinery, *annular diffusers* are frequently used to recover the kinetic energy at the discharge of compressors and turbines and increase their total-to-static isentropic efficiency (Lohmann et al. 1979). However, the design of an effective diffuser is a challenging task due to the presence of adverse pressure gradients. Indeed, if the adverse pressure gradient is strong enough, the boundary layer close to the wall will separate and lead to flow reversal, reducing the pressure recovery (Lohmann et al. 1979).

The diffuser has a strong influence on the design and performance of turbomachines. For instance, Macchi et al. (1981) showed that the optimal design (i.e., maximum efficiency) of axial turbines can vary significantly depending on the amount of kinetic energy that can be recovered at the exit of the last stage. Similarly, Bahamonde et al. (2017) recognized that, in the absence of a diffuser, the discharge kinetic energy can be one of the main mechanisms of efficiency loss. Despite its strong influence, the diffuser is often overlooked during the preliminary design phase. As surveyed in Table 2.1, many works ignore the diffuser, while others account for it in a simplistic way by considering that an arbitrary fraction of the outlet kinetic energy is recovered. In addition, some works assume that only the meridional component of the kinetic energy is recovered when, in fact, most annular diffusers also recover the swirling kinetic energy as the diffuser radius increases (Lohmann et al. 1979). Furthermore, none of the works surveyed in Table 2.1 considered the influence of the diffuser design on the kinetic energy recovery and, to the knowledge of the author, a preliminary design method that combines the turbomachinery and diffuser models is still lacking.

Although the diffuser performance can be predicted and optimized using high-fidelity flow simulations and shape optimization, this approach would be computationally expensive and unpractical during the preliminary design phase. Instead, one-dimensional flow models that account for the main features of the flow, such as the effects of geometry (e.g., flow area, mean radius), heat transfer, and friction are better suited for the level of detail required in the preliminary design phase. There are several one-dimensional models for the flow within annular diffusers available in the open literature, including the ones proposed by Stanitz (1952), Johnston et al. (1966), Elgammal et al. (1981), and Dubitsky et al. (2008), see Table 2.2. These models were developed for vaneless diffusers downstream com-

Table 2.1: Survey of diffuser modeling in context of turbine preliminary design.

Reference	Turbine type	Diffuser modeling
Macchi et al. (1981)	Axial flow	Fixed recovery[a]
Lozza et al. (1982)	Axial flow	Fixed recovery[a]
Da Lio et al. (2014)	Axial flow	Fixed recovery[b]
Astolfi et al. (2015)	Axial flow	Fixed recovery[b]
Da Lio et al. (2016)	Axial flow	Fixed recovery[b]
Al Jubori et al. (2016)	Axial flow	Not considered
Talluri et al. (2017)	Axial flow	Not considered
Tournier et al. (2010)	Axial flow	Not considered
Meroni et al. (2016a)	Axial flow	Not considered
Meroni et al. (2016b)	Axial flow	Not considered
Meroni et al. (2018a)	Axial flow	Fixed recovery[b]
Perdichizzi et al. (1987)	Radial inflow	Fixed recovery[a]
Uusitalo et al. (2015)	Radial inflow	Not considered
Rahbar et al. (2015)	Radial inflow	Not considered
Da Lio et al. (2017)	Radial inflow	Not considered
Pini et al. (2013)	Radial outflow	Fixed recovery[a]
Casati et al. (2014)	Radial outflow Axial flow	Fixed recovery[a]
Bahamonde et al. (2017)	Radial inflow Radial outflow	Not considered

[a] Fixed recovery of the total kinetic energy.
[b] Fixed recovery of the meridional kinetic energy.

pressors and pumps (i.e., diffusers without guiding vanes), but they can be used for annular ducts in general because the flow is governed by the same equations.

Ideally, the diffuser model should accept any equation of state and account for the effects of area change, heat transfer, and friction. However, none of the models available in the literature meets all these requirements. For instance, the model proposed by Stanitz (1952) accounts for the effects of area change, heat transfer, and friction, but it assumes that the fluid behaves as a perfect gas. Similarly, the models proposed by Johnston et al. (1966) and Elgammal et al. (1981) also account for the effects of area change and friction, but they assume that the flow is adiabatic and incompressible. Lastly, the model proposed by Dubitsky et al. (2008) is the most advanced. It is formulated as a two–zone model that accounts for real gas effects, area change, and friction, but it neglects heat transfer. Moreover, one limitation of the model proposed by Dubitsky et al. (2008) is that it is necessary to specify several ad-hoc parameters that might not be known in the early design phase such as the *turbulence mixing loss coefficient* or the *secondary flow area fraction*.

Table 2.2: Survey of one-dimensional diffuser models.

Reference	Friction	Heat transfer	Fluid properties
Stanitz (1952)	Yes	Yes	Ideal gas
Johnston et al. (1966)	Yes	No	Incompressible
Elgammal et al. (1981)	Yes	No	Incompressible
Dubitsky et al. (2008)	Yes	No	Non-ideal gas
Present work	Yes	Yes	Non-ideal gas

In view of the limitations of the existing models, this work presents a one-dimensional annular diffuser model intended for the preliminary design of turbomachinery. The equations governing the flow are similar to those presented in previous works, refer to Table 2.2, but are formulated in a general way to account for heat transfer, friction, and arbitrary geometry and equations of state. The solution algorithm and discussion of the mathematical properties in terms of the meridional Mach number of the flow are original. In addition, the detailed derivation of the equations, which is omitted in other works, and the physical interpretation of the different terms are presented. Furthermore, the model was *verified* against a reference case to assess that the numerical solution is correct and *validated* against experimental data from a test case documented in the open literature. Finally, a sensitivity analysis with respect to (1) the skin friction coefficient, (2) inlet hub-to-tip ratio, (3) mean wall cant angle, (4) inlet swirl angle, and (5) inlet Mach number was performed to gain insight into the impact of these variables on diffuser performance and design.

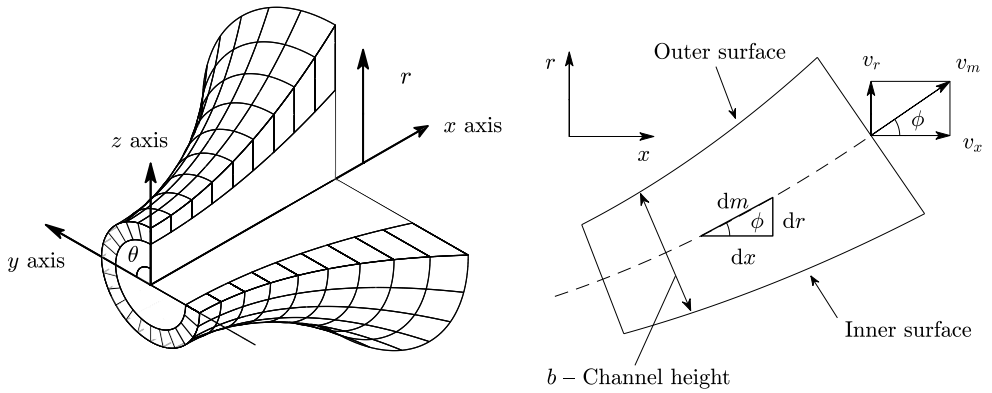

(a) Three-dimensional view. **(b)** Axial–radial view.

Figure 2.1: Geometry of a general annular diffuser.

2.2 Diffuser model

This section describes the diffuser model proposed in this work. First, the geometry of annular diffusers and the conventions for the velocity vector are described. After that, the treatment for the equations of state is presented. Finally, the mathematical model for the flow and the solution algorithm are explained.

2.2.1 Diffuser geometry

A sectioned view of a general annular diffuser geometry is shown in Figure 2.1a. The fluid flows within the annular duct defined by the inner and outer surfaces and the static pressure increases as the kinetic energy of the fluid is reduced. More specifically, the tangential component of velocity decreases as the mean radius of the channel increases and, for subsonic flow, the meridional component of velocity decreases when the flow area increases (Lohmann et al. 1979).

In general, the meridional direction m will not be exactly aligned with the axial x or the radial r directions. This is illustrated in Figure 2.1b, where an axial–radial view of the diffuser is presented. The mean line of the diffuser can be parametrized as $r = r(m)$ and $x = x(m)$ such that the meridional, radial, and axial directions are related by the angle ϕ given by

$$\tan\phi = \frac{\mathrm{d}r}{\mathrm{d}x} = \left(\frac{\mathrm{d}r}{\mathrm{d}m}\right) \cdot \left(\frac{\mathrm{d}x}{\mathrm{d}m}\right)^{-1}. \tag{2.2}$$

In addition, the flow area of the annular duct is given by

$$A = 2\pi r\, b, \tag{2.3}$$

where r is the mean radius of the annular channel and b is height of the channel, measured normal to the meridional direction. The channel height can be pre-

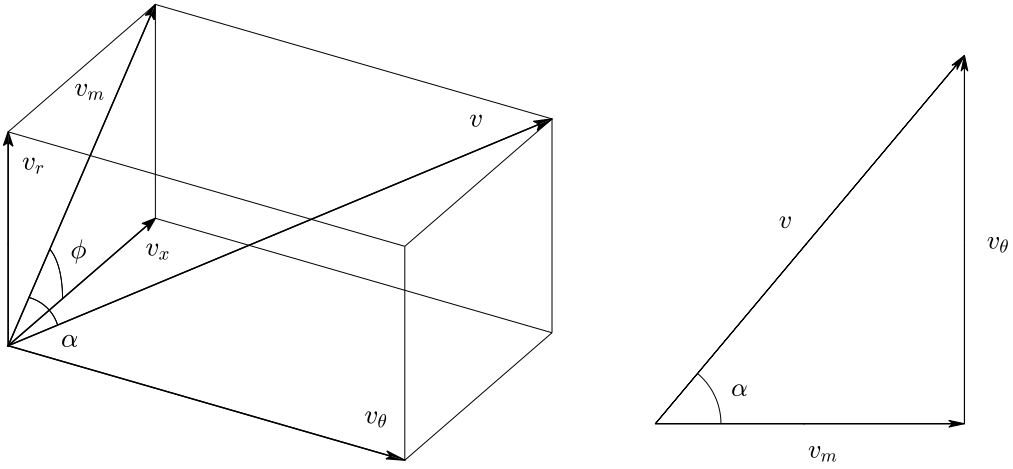

Figure 2.2: Decomposition of the velocity vector.

scribed as an arbitrary function of the meridional direction $b(m)$. Furthermore, the area ratio is defined as the ratio of the outlet to the inlet areas

$$AR = \frac{A_{\text{out}}}{A_{\text{in}}}. \tag{2.4}$$

The geometry relations Eqs. (2.2) to (2.4) are valid for any annular channel. The particular geometry of straight-walled annular diffusers is described in detail under the heading *geometry sub-model*.

2.2.2 Velocity vector conventions

The velocity is denoted by the symbol v, and its components are denoted by the subscripts θ–tangential, m–meridional, x–axial, and r–radial. The velocity vector is illustrated in Figure 2.2 and the different components are given by

$$v_m = v\cos(\alpha), \tag{2.5}$$
$$v_\theta = v\sin(\alpha), \tag{2.6}$$
$$v_x = v_m\cos(\phi) = v\cos(\phi)\cos(\alpha), \text{ and} \tag{2.7}$$
$$v_r = v_m\sin(\phi) = v\sin(\phi)\cos(\alpha), \tag{2.8}$$

where the flow angle α is measured from the meridional to the tangential direction.

2.2.3 Thermodynamic properties

The diffuser model was formulated in a general way such that the properties of the working fluid can be computed with any thermodynamic library that support pressure–density function calls such as Lemmon et al. (2013) or Bell et al. (2014).

2.2.4 Mathematical model

The diffuser model is based on the transport equations for mass, meridional and tangential momentum, and energy in an annular channel. It assumes that the flow is steady, axisymmetric, and varies only the meridional direction. In addition, the model accounts for effects of area change, heat transfer, and friction and the fluid properties can be described by any thermophysical model. Under these conditions the governing equations of the flow are given by

$$v_m \frac{\mathrm{d}\rho}{\mathrm{d}m} + \rho \frac{\mathrm{d}v_m}{\mathrm{d}m} = -\frac{\rho v_m}{b\,r} \frac{\mathrm{d}}{\mathrm{d}m}(b\,r), \tag{2.9}$$

$$\rho v_m \frac{\mathrm{d}v_m}{\mathrm{d}m} + \frac{\mathrm{d}p}{\mathrm{d}m} = \frac{\rho v_\theta^2}{r} \sin(\phi) - \frac{2\tau_\mathrm{w}}{b} \cos(\alpha), \tag{2.10}$$

$$\rho v_m \frac{\mathrm{d}v_\theta}{\mathrm{d}m} = -\frac{\rho v_\theta v_m}{r} \sin(\phi) - \frac{2\tau_\mathrm{w}}{b} \sin(\alpha), \text{ and} \tag{2.11}$$

$$\rho v_m \frac{\mathrm{d}p}{\mathrm{d}m} - \rho v_m\, a^2 \frac{\mathrm{d}\rho}{\mathrm{d}m} = \frac{2(\tau_\mathrm{w} v + \dot{q}_\mathrm{w})}{b \left(\frac{\partial e}{\partial p}\right)_\rho}, \tag{2.12}$$

where ρ is the density, p is the static pressure, e is the internal energy, a is the speed of sound, τ_w is the shear stress at the walls, and $\dot{q}_\mathrm{w}$ is the heat flux at the walls. These equations are derived from the mass, momentum, and energy balances applied to the infinitesimal control volume shown in Figure 2.3. The detailed derivation of these equations and a discussion of the physical meaning of the different terms is presented in Appendix A.

Eqs. (2.9) to (2.12) pose a system of Ordinary Differential Equations (ODE) that can be expressed compactly in matrix-form as

$$A \frac{\mathrm{d}U}{\mathrm{d}m} = S, \tag{2.13}$$

where $U = [v_m,\, v_\theta,\, \rho,\, p]$ is the solution vector, A is the coefficient matrix

$$A = \begin{bmatrix} \rho & 0 & v_m & 0 \\ \rho v_m & 0 & 0 & 1 \\ 0 & \rho v_m & 0 & 0 \\ 0 & 0 & -\rho v_m\, a^2 & \rho v_m \end{bmatrix}, \tag{2.14}$$

and S is the source term vector given by

$$S = \begin{bmatrix} -\frac{\rho v_m}{b\,r} \frac{\mathrm{d}}{\mathrm{d}m}(b\,r) \\ \frac{\rho v_\theta^2}{r} \sin(\phi) - \frac{2\tau_\mathrm{w}}{b} \cos(\alpha) \\ -\frac{\rho v_\theta v_m}{r} \sin(\phi) - \frac{2\tau_\mathrm{w}}{b} \sin(\alpha) \\ \frac{2(\tau_\mathrm{w} v + \dot{q}_\mathrm{w})}{b \left(\frac{\partial e}{\partial p}\right)_\rho} \end{bmatrix}. \tag{2.15}$$

It can be readily shown that the determinant of matrix A is given by

$$\det(A) = \rho^3 v_m^2 \, a^2 \left(\frac{v_m^2}{a^2} - 1 \right) = \rho^3 v_m^2 \, a^2 \left(\mathrm{Ma}_m^2 - 1 \right), \tag{2.16}$$

which means that, if the Mach number in the meridional direction is different than unity, the linear system of equations given by Eq. (2.13) can be solved to compute the derivatives of the solution vector. Furthermore, the singular case

$$\mathrm{Ma}_m = 1 \tag{2.17}$$

corresponds to choked flow conditions and it implies that diffuser can only be choked due to the meridional component of velocity (Stanitz 1952).

In order to solve the problem, the vector $\frac{\mathrm{d}U}{\mathrm{d}m}$ is computed from Eq. (2.13) using Gaussian elimination and then provided as input for an explicit ODE solver. In this work, the adaptative solver based on fourth- and fifth-order explicit Runge-Kutta methods proposed by Shampine et al. (1997) was used to perform the numerical integration. The initial conditions for the integration are given by

$$U^0 = [v_m, \, v_\theta, \, \rho, \, p]^0 = [v_m, \, v_\theta, \, \rho, \, p]^{\mathrm{out}}, \tag{2.18}$$

where it is assumed that the flow variables do not change from the exit of the turbine or compressor to the inlet of the diffuser. In order to evaluate the source term vector, it is necessary to prescribe the variation of the channel height $b(m)$ and radius $r(m)$ and to provide models for the shear stress τ_w and heat flux $\dot{q}_\mathrm{w}$ at the walls.

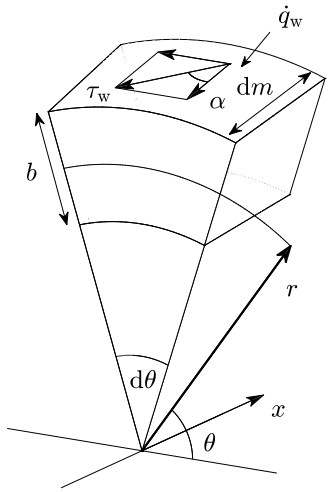

Figure 2.3: Differential control volume used to derive the flow governing equations.

Geometry sub-model

The diffuser model was formulated in a general way so that the geometry can be described by any set of arbitrary functions $r(m)$, $x(m)$, and $b(m)$. However, the proposed model is not conceived to define the detailed shape of the diffuser, but to estimate the exhaust pressure recovery during the preliminary design phase.

In this context, the geometry of the diffuser was defined in a simple way by assuming that the inner and outer surfaces are straight. This type of diffusers are known as conical or straight-walled annular diffusers and their geometry is illustrated in Figure 2.4. For this particular geometry, the angle ϕ is constant and it is given by the arithmetic mean of the inner and outer wall cant angles, $\phi = (\phi_1 + \phi_2)/2$. In addition, the relations for $r(m)$, $x(m)$, and $b(m)$ can be deduced from Figure 2.4 and they are given by

$$r(m) = \hat{r}_{\,\mathrm{in}} + m \, \sin(\phi), \tag{2.19}$$

$$x(m) = \hat{x}_{\,\mathrm{in}} + m \, \cos(\phi), \text{ and} \tag{2.20}$$

$$b(m) = \hat{b}_{\,\mathrm{in}} + 2m \, \tan(\delta), \tag{2.21}$$

where $\delta = (\phi_2 - \phi_1)/2$ is the divergence semi-angle. A depicted in Figure 2.5, the mean radius $\hat{r}_{\,\mathrm{in}}$ and channel height $\hat{b}_{\,\mathrm{in}}$ at the inlet of the diffuser can computed according to

$$\hat{r}_{\,\mathrm{in}} = R_{\mathrm{out}} \text{ and} \tag{2.22}$$

$$\hat{b}_{\,\mathrm{in}} = H_{\,\mathrm{out}} \,/\, \cos(\phi) \tag{2.23}$$

where, R_{out} is the turbomachine outlet mean radius and $H_{\,\mathrm{out}}$ is the turbomachine outlet blade height, establishing the connection between the proposed diffuser model and a generic mean-line turbomachinery model.

Friction sub-model

The friction is modeled as a body force that does not do work. This approach is often used in the context of one-dimensional flow models because they do not take into account the velocity gradient in the direction normal to the wall (Stanitz 1952; Dubitsky et al. 2008). The viscous stress at the wall τ_{w} is computed according to

$$\tau_{\mathrm{w}} = C_{\mathrm{f}} \, \frac{\rho v^2}{2}, \tag{2.24}$$

where C_{f} is the skin friction coefficient. The viscous force is assumed to have the opposite direction as the velocity vector such that the friction components in the meridional and tangential direction are given by $-\tau_{\mathrm{w}} \cos(\alpha)$ and $-\tau_{\mathrm{w}} \sin(\alpha)$, respectively, see Figure 2.3.

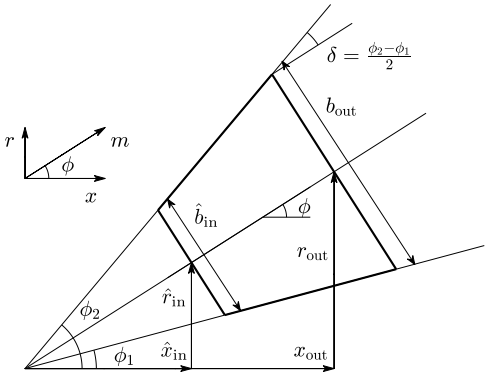

Figure 2.4: Axial–radial cross section of an annular diffuser with straight walls.

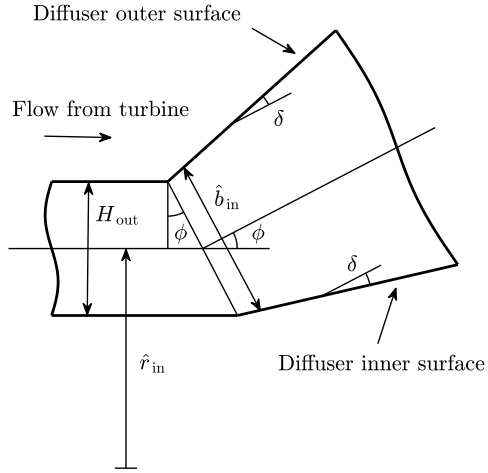

Figure 2.5: Connection of the diffuser model with a generic turbomachine model.

To the knowledge of the author, there are no available correlations to predict the skin friction coefficient in annular channels with swirling flow. Using ordinary skin friction correlations for internal flows is discouraged because they do not consider the influence of swirl on the shear stress at the wall. However, it is possible to estimate a reasonable value for the skin friction coefficient based on experimental data from existing vaneless diffusers. For example Brown (1947) measured the local skin friction coefficient for different vaneless diffusers and obtained values in the range from 0.003 to 0.010. In the absence of better estimates, Johnston et al. (1966) recommend values within the range from 0.005 to 0.010 for the global skin friction coefficient. In a similar way, Dubitsky et al. (2008) suggested 0.010 as a reasonable estimate for the global skin friction coefficient, but noted that values from 0.005 to 0.020 may be required to fit experimental data, depending on the application. The values that were reported in this paragraph are representative of well-designed diffusers without flow separation.

Heat transfer sub-model

The most common approach in the design and analysis of diffusers for turbomachinery applications is to neglect the heat transfer and to assume that the flow is adiabatic $\dot{q}_{\text{w}} = 0$. To the knowledge of the author, Stanitz (1952) is the only reference that accounts for the effect of heat transfer in the energy transport equation. Although heat transfer is usually neglected, the heat transfer modeling is discussed in this section for the sake of completeness.

Stanitz (1952) suggested that the heat flux is proportional to the temperature difference between the fluid and the wall,

$$\dot{q}_{\text{w}} = U_h \, (T_{\text{w}} - T_0), \tag{2.25}$$

where U_h is the heat transfer coefficient, T_0 is the stagnation temperature of the fluid, and $T_\mathrm{w}(m)$ is the wall temperature, which is prescribed as a function of the meridional direction. Eq. (2.25) involves the stagnation rather than the static temperature of the fluid because the fluid is at rest at the wall and it is assumed that the energy recovery factor in the boundary layer is equal to one.

In addition, Stanitz (1952) suggested to use the Reynolds analogy given by

$$\mathrm{Nu} = \frac{1}{2} C_\mathrm{f} \,\mathrm{Re}\,\mathrm{Pr} \quad \text{and} \tag{2.26}$$

$$U_h = \frac{\rho v c_p}{2} C_\mathrm{f} \tag{2.27}$$

to obtain an approximate value for the heat transfer coefficient in terms of the skin friction coefficient, where the usual definitions for the Nusselt number $\mathrm{Nu} = \frac{U D_\mathrm{h}}{k}$, Reynolds number $\mathrm{Re} = \frac{\rho v D_\mathrm{h}}{\mu}$, and Prandtl $\mathrm{Pr} = \frac{c_p \mu}{k}$ are used. The hydraulic diameter of an annular duct is given by the channel height (i.e., $D_\mathrm{h} = b$), but it is immaterial for the computation of the heat transfer coefficient.

Alternatively, the heat transfer coefficient can be estimated using the Chilton–Colburn analogy (Cengel 2002, pp. 358–360) given by

$$\mathrm{Nu} = \frac{1}{2} C_\mathrm{f} \,\mathrm{Re}\,\mathrm{Pr}^{1/3} \quad \text{and} \tag{2.28}$$

$$U_h = \frac{\rho v c_p}{2} C_\mathrm{f} \,\mathrm{Pr}^{-2/3}. \tag{2.29}$$

This analogy extends the Reynolds analogy to fluids with a Prandtl number different than unity. Both these analogies can be used to get a rough estimate of the heat transfer coefficient from a known value of the skin friction coefficient. Using ordinary heat transfer correlations for internal flows is discouraged, because they do not take into account the impact of the swirl into the heat transfer process.

2.3 Verification and validation of the model

The aim of this section is the *verification* (i.e., solving the equations right) and *validation* (i.e., solving the right equations) of the proposed diffuser model. In order to verify the model, the reference case summarized in Table 2.3 was analyzed and the error of the numerical solution in terms of stagnation enthalpy and entropy was assessed. The case study proposed considers a subsonic annular diffuser with air as working fluid. The skin friction coefficient was assumed to be $C_\mathrm{f} = 0.010$, which is deemed to be a realistic value based on the suggestions from Johnston et al. (1966); Dubitsky et al. (2008); Brown (1947), and the heat transfer was neglected.

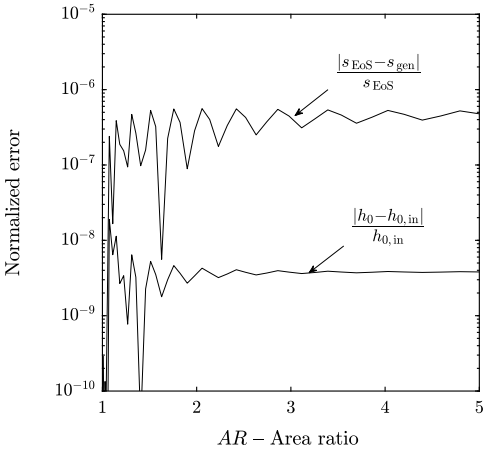

Figure 2.6: Enthalpy and entropy error analyses for the reference case of Table 2.3.

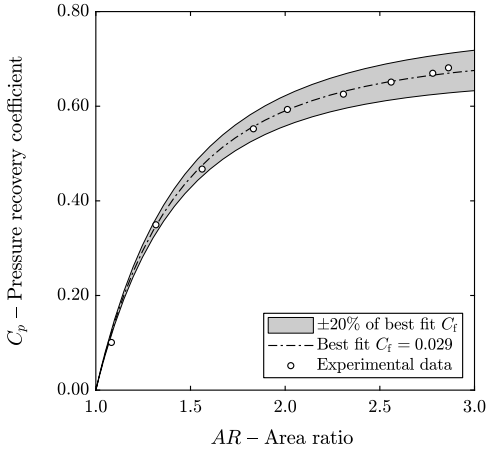

Figure 2.7: Comparison of model output with the data from Kumar et al. (1980).

In the absence of heat transfer, the stagnation enthalpy of the flow remains constant, see Appendix A, and any change in stagnation enthalpy can be attributed to the error in the numerical solution. The stagnation enthalpy error as a function of the area ratio in shown in Figure 2.6 and it was evaluated using

$$h_{0,\,\mathrm{error}} = \frac{|h_0 - h_{0,\,\mathrm{in}}|}{h_{0,\,\mathrm{in}}}, \tag{2.30}$$

where the stagnation enthalpy is computed according to

$$h_0 = h(p, \rho) + \frac{v_m^2}{2} + \frac{v_\theta^2}{2}. \tag{2.31}$$

It can be seen that the stagnation enthalpy is properly conserved and that the relative error is of the order of 10^{-9}, which is smaller than the prescribed relative tolerance of 10^{-6} for the integration of the ODE system.

The entropy error was analyzed in a similar way. The entropy of the flow was computed with pressure–density function calls using the Lemmon et al. (2013) thermodynamic library at each integration step,

$$s_{\,\mathrm{EoS}} = s(p, \rho), \tag{2.32}$$

and also evaluated integrating the transport equation for entropy given by

$$\rho v_m \left(\frac{\mathrm{d}s_{\mathrm{gen}}}{\mathrm{d}m} \right) = \dot{\sigma} = 2 \frac{\tau_{\mathrm{w}} v}{b T}, \tag{2.33}$$

where $\dot{\sigma}$ is the rate of entropy generation per unit volume due to friction. See Appendix A for the details about the derivation of the transport equation for

entropy. The entropy error was thus computed according to

$$s_{\,\mathrm{error}} = \frac{|s_{\,\mathrm{EoS}} - s_{\mathrm{gen}}|}{s_{\,\mathrm{EoS}}} \tag{2.34}$$

and it is shown as a function of the diffuser area ratio in Figure 2.6. It can be observed that the entropy error is of the order of 10^{-7}, which is smaller than the prescribed integration tolerance of 10^{-6}. As both the stagnation enthalpy and entropy errors are smaller than the prescribed tolerance, it can be concluded that the solution algorithm solves the flow equations satisfactorily.

In addition, the diffuser model was validated against the annular diffuser experimental data from Kumar et al. (1980). The conditions that define this case are summarized in Table 2.4 and the experimental and computed pressure recovery coefficients are compared in Table 2.5 and in Figure 2.7. The heat transfer was neglected for the validation ($U_h = 0$) because the experimental data from Kumar et al. (1980) corresponds to an open-loop, low-speed annular diffuser where the difference between fluid temperature and wall temperature is expected to be very small. The skin friction coefficient was fitted to minimize the two-norm of the error between the experimental data and the model output. In addition, the range of variation of the pressure recovery coefficient for skin friction coefficients ranging between $\pm 20\%$ of the best-fit value is shown as a shaded area to illustrate the impact of this parameter on the diffuser performance.

Ignoring the point corresponding to $AR = 1.082$, it can be observed that the relative deviation of the pressure recovery coefficient is always less than 2% when the best-fit skin friction coefficient ($C_{\mathrm{f}} = 0.029$) is used. Likely, the deviation between experiment and model when $AR = 1.082$ is due to the development of the flow at the inlet of the diffuser. This analysis showed that the model can be used to make accurate predictions when skin friction coefficient can be fitted to experimental data.

2.4 Sensitivity analysis

This section contains a sensitivity analysis of the reference case summarized in Table 2.3 to gain insight about the impact of several input parameters on diffuser performance and design. The next sections investigate the influence of: (1) the skin friction coefficient, (2) inlet hub-to-tip ratio, (3) mean wall cant angle, (4) inlet swirl angle, and (5) inlet meridional Mach number on the pressure recovery coefficient as a function of the area ratio of the diffuser. The divergence semi-angle was not included in the analysis because increasing this parameter may lead to boundary layer separation close to the walls and the one-dimensional model used in this work cannot predict this phenomenon[1]. Each case analyzes

[1]Kline et al. (1959) provide stability maps that can be used to predict flow separation for straight-walled and conical diffusers as a function of divergence semi-angle and area ratio. However, the author is not aware of similar maps for annular diffusers in the open literature.

Table 2.3: Definition of the reference case.

Variable	Symbol	Value	Unit
Working fluid	–	Air	–
Inlet static pressure	p_{in}	101.3	kPa
Inlet static temperature	T_{in}	20.0	°C
Inlet meridional Mach number	$\mathrm{Ma}_{\mathrm{m,in}}$	0.30	–
Inlet swirl angle	α_{in}	30.0	°
Turbomachine outlet radius	R_{out}	1.0	m
Outlet hub-to-tip ratio	$(r_{\mathrm{h}}/r_{\mathrm{t}})_{\mathrm{out}}$	0.7	–
Mean wall cant angle	ϕ	30.0	°
Divergence semi-angle	δ	5.0	°
Diffuser area ratio	AR	1.0–5.0	–
Skin friction coefficient	C_{f}	0.010	–
Heat transfer coefficient	U_h	0	$\mathrm{W/m^2\,K}$

the influence of one variable while the other parameters are the same as in the reference case (i.e., one-at-a-time sensitivity analysis) and the ranges of variation were selected to cover the flow conditions encountered in most turbomachinery applications. In addition, the influence of heat transfer on diffuser performance was analyzed for different wall temperatures using the Chilton–Colburn analogy to estimate the heat transfer coefficient. As it could be expected, heat addition accelerates the flow and penalizes the pressure recovery coefficient. However, the details of the heat transfer investigations are not reported because the influence of heat addition was secondary compared to that of the other parameters.

2.4.1 Influence of the skin friction coefficient

As discussed in Section 2.2, the author is not aware of any correlations to predict the skin friction coefficient in annular channels with swirling flow. In this analysis, the friction factor was varied from 0.00 (i.e., frictionless) to 0.03 (i.e., high friction) and the impact on the pressure recovery coefficient as a function of the area ratio is shown in Figure 2.8.

It can be observed that increasing the friction factor decreases the pressure recovery in a *linear* way (i.e., the different curves are equispaced) and that the effect is more notable when the area ratio increases because the length of the channel is larger. In addition, the pressure recovery increases monotonously with the area ratio and has an asymptotic behavior, irrespective of the numerical value of the friction coefficient. This suggests that an optimum value of the area ratio that maximizes the pressure recovery does not exist and that the pressure recovery always increases with the area ratio up to a limiting value. This, perhaps counter-intuitive, result may be explained as the consequence of two conflicting effects.

Table 2.4: Definition of the validation case from Kumar et al. (1980).

Variable	Symbol	Value	Unit
Working fluid	–	Air	–
Inlet static pressure	p_{in}	101.3	kPa
Inlet static temperature	T_{in}	20.0	°C
Inlet meridional Mach number	$\text{Ma}_{\text{m,in}}$	0.07	–
Inlet swirl angle	α_{in}	0.0	°
Inlet mean radius	$\hat{r}_{\text{in}}$	57.8	mm
Inlet channel height	$\hat{b}_{\text{in}}$	39.5	mm
Mean wall cant angle	ϕ	15.0	°
Divergence semi-angle	δ	0.0	°
Diffuser area ratio	AR	1.0–3.0	–
Skin friction coefficient	C_{f}	Fitted	–
Heat transfer coefficient	U_h	0	$\text{W/m}^2\,\text{K}$

Table 2.5: Comparison of the model output with the data from Kumar et al. (1980).

AR	C_p^{exp}	C_p^{model}	Relative error
1.082	0.101	0.122	21.27%
1.317	0.349	0.347	-0.64%
1.561	0.467	0.475	1.73%
1.832	0.552	0.557	0.89%
2.012	0.593	0.592	-0.14%
2.308	0.626	0.631	0.89%
2.560	0.651	0.653	0.23%
2.779	0.670	0.666	-0.58%
2.863	0.681	0.670	-1.67%

On the one hand, when the area ratio increases the diffuser length and wetted surface also increase. However, as the area ratio increases, the velocity and shear stress at the wall are reduced because the shear stress is proportional to the dynamic pressure. If this second effect dominates, friction becomes negligible and the pressure recovery increases asymptotically as the area ratio tends to infinity.

2.4.2 Influence of the inlet hub-to-tip ratio

In order to accommodate the changes in density, the hub-to-tip ratio is usually high at the outlet of compressors and low at the outlet of turbines. In this section the hub-to-tip ratio at the inlet of the diffuser was varied between 0.50 and 0.95 and the results were plotted in Figure 2.9. It can be observed that the diffuser performance is penalized as the hub-to-tip ratio increases and that this effect is

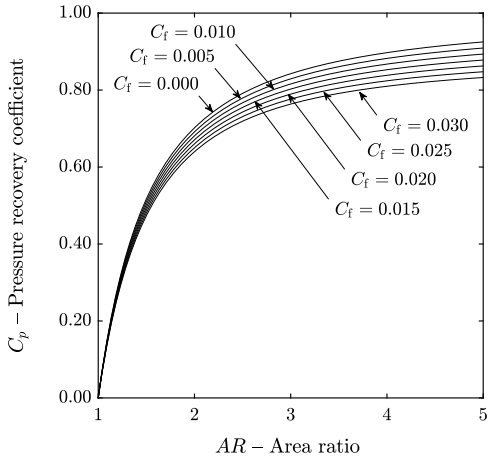

Figure 2.8: Influence of the skin friction coefficient as a function of the area ratio.

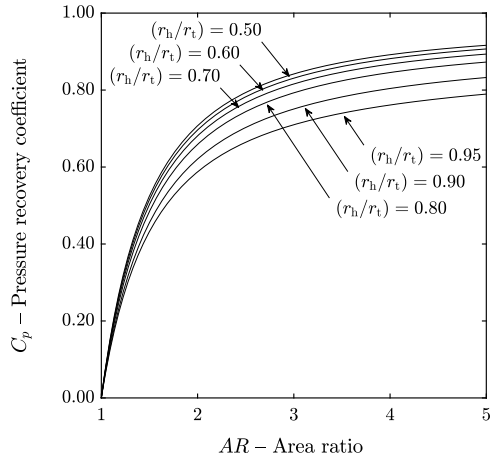

Figure 2.9: Influence of the hub-to-tip ratio as a function of the area ratio.

not linear. Indeed, the pressure recovery coefficient is reduced more rapidly at high hub-to-tip ratios. The reason for this behavior is that, as the hub-to-tip ratio increases, the channel height of the diffuser is reduced according to

$$\hat{b}_{\text{in}} = H_{\text{out}} \,/\, \cos(\phi) = 2\, R_{\text{out}} \left(\frac{1 - (r_{\text{h}}/r_{\text{t}})}{1 + (r_{\text{h}}/r_{\text{t}})} \right)_{\text{out}} \,/\, \cos(\phi) \tag{2.35}$$

and, since the channel height appears in the denominator of the friction terms of the momentum equations, Eqs. (2.10) and (2.11), the diffuser performance declines. Another possible interpretation based on physical intuition is that the channel height is the hydraulic diameter of the annular diffuser and reducing this parameter will increase the friction losses.

2.4.3 Influence of the mean wall cant angle

Figure 2.10 shows the pressure recovery coefficient as a function of the area ratio when the mean cant angle is varied from 0° to 40°. It can be seen that the pressure recovery coefficient is very low when $\phi = 0°$ because the radius of the diffuser remains constant and the tangential component of velocity is not recovered. Moreover, the pressure recovery coefficient increases rapidly when the mean cant angle is small, see the change from 0° to 10°, and slowly for higher cant angles: the change from 30° to 40° is almost insignificant.

The same results are plotted as a function of the normalized axial length, rather than the area ratio, in Figure 2.11. The end of the lines corresponds to the point where $AR = 5$. It can be be observed that, for a fixed diffuser axial length, the pressure recovery coefficient increases as the mean wall cant angle increases because both the area and the mean radius of the channel increase. These results

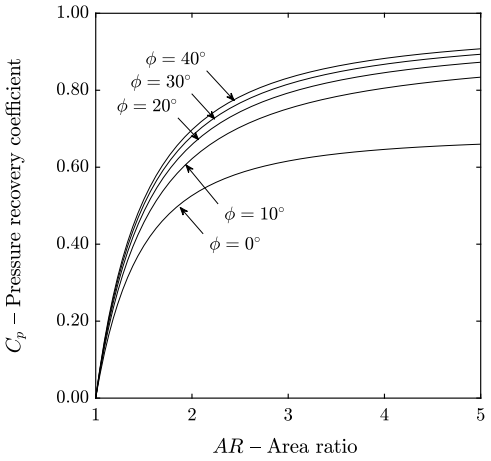

Figure 2.10: Influence of the mean wall cant angle as a function of the area ratio.

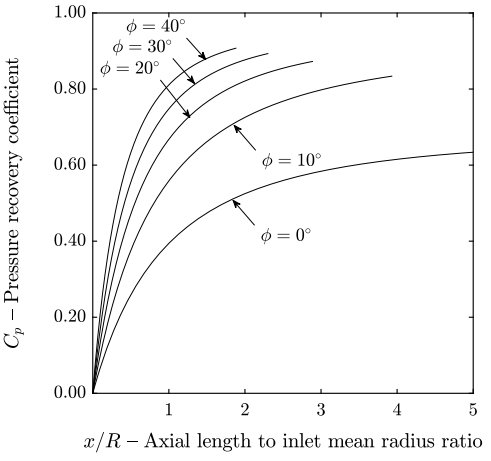

Figure 2.11: Influence of the mean wall cant angle as a function of the axial length.

illustrate that the mean cant angle is not a critical parameter when there are no space limitations, but that adopting a high mean wall cant angle is advantageous when the maximum axial length of the diffuser is constrained.

2.4.4 Influence of the inlet swirl angle

The results from Figure 2.12 show that, for a fixed inlet meridional velocity, increasing the swirl angle decreases the pressure recovery coefficient and that this effect is more marked at higher swirl angles. The reason for this is that the presence of swirl increases the available dynamic pressure at the inlet and, for this reason, the area ratio required to reach the same pressure recovery coefficient as for the case $\alpha = 0°$ is higher. Moreover, the presence of swirl leads to wall shear stress in the circumferential direction that increases the friction losses.

2.4.5 Influence of the inlet Mach number

The influence of the inlet Mach number (i.e., compressibility effects) on the diffuser performance, including the limiting case of incompressible flow, is shown in Figure 2.13. This analysis was performed assuming frictionless flow instead of $C_\mathrm{f} = 0.010$ so that the numerical results can be compared with the analytical formula for inviscid, incompressible flow, which is given by

$$C_{p,\mathrm{inc}} = 1 - \frac{\tan\left(\alpha_\mathrm{in}\right)^2 + \left(\frac{\hat{b}_\mathrm{in}}{b}\right)^2}{1 + \tan\left(\alpha_\mathrm{in}\right)^2} \cdot \left(\frac{\hat{r}_\mathrm{in}}{r}\right)^2 . \tag{2.36}$$

Eq. (2.36) is a well-known result (Lohmann et al. 1979) that can be proved integrating the mass and momentum equations, Eqs. (2.9) to (2.11), for constant

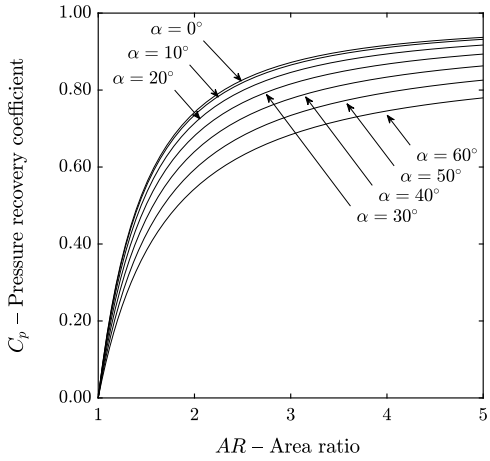

Figure 2.12: Influence of the inlet swirl angle as a function of the area ratio.

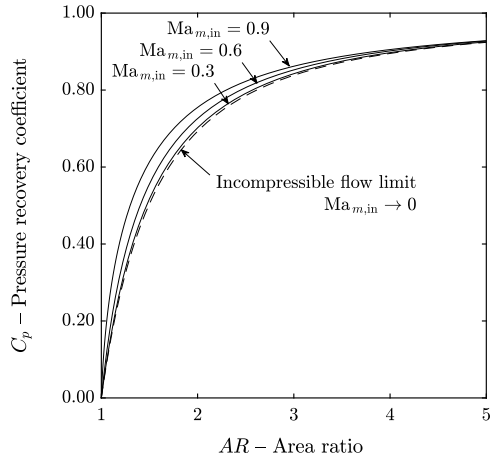

Figure 2.13: Influence of the inlet Mach number as a function of the area ratio.

density and zero wall shear stress. It can be observed that the model predicts a modest increase on the pressure recovery coefficient as the inlet Mach number increases. In addition, the results obtained when the inlet meridional Mach number is 0.30 or lower (i.e., low speed flow) are consistent with the analytical results for incompressible flow. This result can be regarded as part of the model verification.

2.5 Conclusions

A one-dimensional flow model for annular diffusers was proposed and the connection of this model with the preliminary design of turbomachinery was discussed. The model formulation is more general than that of previous works, allowing one to use arbitrary equations of state and to include the effects of area change, heat transfer, and friction. The mathematical model poses a system of ordinary differential equations and it was shown that: (1) the solution does not exist when the meridional Mach number is equal to one and (2) the circumferential Mach number does not compromise the solution. In addition, the detailed derivation of the equations, which is omitted in other works, was presented in Appendix A to provide physical insight about the flow in annular channels.

The model was *verified* against a reference case assessing that: (1) the stagnation enthalpy is conserved and (2) the entropy generation computed using the equations of state and using the second law of thermodynamics are consistent; and it was found that the error of the numerical solution was always smaller than the prescribed integration tolerance. Moreover, the model was *validated* against the experimental data from Kumar et al. (1980), finding that the relative deviation between the predicted and measured pressure recovery coefficients was always less than 2% when the best-fit skin friction coefficient is used.

Furthermore, the influence of the: (1) skin friction coefficient, (2) inlet hub-to-tip ratio, (3) mean wall cant angle, (4) inlet swirl angle, and (5) inlet meridional Mach number on the diffuser performance was investigated and the following conclusions were gathered:

- The pressure recovery coefficient increases asymptotically as the area ratio tends to infinity, regardless of the value of the skin friction coefficient. This suggests that the area ratio is not a suitable optimization variable if the size of the diffuser is not constrained.
- The hub-to-tip ratio of the last turbomachinery stage has a strong impact on the pressure recovery because it is closely related to the channel height of the diffuser. The pressure recovery is penalized as the hub-to-tip ratio increases and the effect is more marked at high hub-to-tip ratios. This implies that, in general, the design of efficient diffusers for compressors (high hub-to-tip ratios and short blades at the last stage) is more challenging than that of turbines (low hub-to-tip ratios and long blades at the last stage).
- The pressure recovery is low when the mean wall cant angle is zero because the radius of the diffuser remains constant and the tangential component of velocity is not recovered. This indicates that the diffuser should be designed with an increasing mean radius in order to recover the kinetic energy of swirling flows effectively.
- Assuming that there is no flow separation, increasing the mean wall cant angle always improves the pressure recovery. In cases when the *area ratio* is fixed, the mean wall cant angle only has a small impact on the pressure recovery, whereas, in cases when the *axial length* is fixed, increasing the wall cant angle can improve the pressure recovery significantly. This implies that the mean wall cant angle is not a critical parameter when there are no space limitations, but that adopting a high mean wall cant angle is advantageous when the maximum axial length of the diffuser is constrained.
- Increasing the swirl angle at the inlet of the diffuser reduces the pressure recovery coefficient because the wall shear stress in the circumferential direction increases. This implies that the diffuser performance will be improved if the velocity triangle of the last turbomachinery stage is designed so that the absolute velocity has a small tangential component.
- The pressure recovery coefficient increases as the inlet meridional Mach number increases. The effect on the inlet Mach number has only a modest impact on the pressure recovery, compared with the other variables. In addition, the results from the compressible and incompressible analyses are almost identical when the inlet meridional Mach number is lower than 0.30.

Chapter 3

Mean-Line Design Method for Axial Turbines

Part of the contents of this chapter appear in:

> R. Agromayor and L. O. Nord (2019b). "Preliminary Design and Optimization of Axial Turbines Accounting for Diffuser Performance". *International Journal of Turbomachinery, Propulsion and Power* 4.3, pp. 1–32. DOI: https://doi.org/10.3390/ijtpp4030032

Abstract

This chapter presents a mean-line model and optimization methodology for the preliminary design of axial turbines. The mean-line model was formulated in a general way so as to use arbitrary equations of state and empirical loss models and it accounts for the influence of the diffuser using the one-dimensional flow model presented in Chapter 2. The mean-model was validated against two test cases from the literature and it was found that the deviation between experimental data and model prediction in terms of mass flow rate and power output was less than 1.2% in both cases and that the deviation of the total-to-static efficiency was within the uncertainty of the empirical loss model. In addition, the preliminary design problem was formulated as a constrained optimization problem and solved using a gradient-based algorithm. The proposed design method was applied to a case study from the literature and a sensitivity analysis was performed to investigate the influence of several variables on turbine performance, concluding that: (1) the minimum hub-to-tip ratio constraint is always active at the outlet of the last stage and the value of this parameter should be selected as a trade-off of aerodynamic performance and mechanical integrity, (2) the total-to-static isentropic efficiency of turbines without diffuser deteriorates rapidly when the pressure ratio is increased, and (3) there exist a locus of maximum efficiency in the specific speed and specific diameter plane (i.e., the Baljé diagram) that can be predicted with a simple analytical expression.

3.1 Introduction

Axial turbines are the most common turbine configuration for electric power generation and propulsion systems, including: open gas turbine Brayton cycles (Saravanamuttoo et al. 2009), closed Brayton cycles using helium (McDonald 2012) or carbon dioxide at supercritical conditions (Romei et al. 2020), and Rankine cycles using steam (Kehlhofer et al. 2009) or organic substances (Colonna et al. 2015) as working fluid. In addition, axial turbines are also used in cryogenic applications such as gas separation processes and natural gas liquefaction (Flynn 2004). Axial turbines probably owe their widespread use to their versatility in terms of power capacity and range of operating conditions. Indeed, the power capacity of axial turbines can vary from a few kilowatts for some small-scale organic Rankine cycle power systems to hundreds of megawatts for large-scale steam and gas turbine units. In addition, the operating temperatures range from below $-200°C$ in some cryogenic applications to temperatures in excess of $1500°C$ for some advanced gas turbines, whereas the operating pressures can vary from a few millibars at the exhaust of some steam turbines to hundreds of bars at the inlet of supercritical steam and carbon dioxide power systems.

The fluid-dynamic design of axial turbines involves mathematical models of different level of complexity ranging from mean-line models for the preliminary design phase up to high-fidelity flow simulations for the aerodynamic design of the blade shapes (Pini et al. 2017). Even if mean-line models are the simplest approach to analyze the flow within turbomachinery, they still are an essential step of the fluid-dynamic design chain because they provide the information required by more advanced flow models (Denton 2017). Mean-line model assume that the flow is uniform along the blade span and evaluate the flow conditions at the inlet and outlet of each cascade using: (1) the balance equations for mass and rothalpy, (2) a set of equations of state to compute thermodynamic and transport properties, and (3) empirical loss correlations to evaluate the entropy generation within the turbine (Dixon et al. 2013). Furthermore, mean-line models can be readily integrated with numerical optimization methods in order to automate the preliminary design phase. This, in turn, enables the systematic exploration of large design spaces, which is especially advantageous to design new turbine concepts for which there is no previous design experience (Pini et al. 2017).

Despite mean-line models are being covered to some extent in turbomachinery textbooks (Saravanamuttoo et al. 2009; Dixon et al. 2013), only some scientific publications present a comprehensive formulation of the preliminary design problem. Table 3.1 surveys some of the mean-line axial turbine models described in the open literature. The main differences in the model formulation include: (1) considering single-stage or multistage turbines, (2) using the restrictive repeating-stage assumption or not, (3) using the ideal gas law or arbitrary equations of state, and (4) whether or not the model accounts for the influence of the diffuser on turbine performance. In addition, one of the recurring limitations of many mean-line

Table 3.1: Survey of axial turbine mean-line models documented in the open literature

Reference	Optim.[a]	Stages[b]	Rep.[c]	Diffuser[d]	Fluid properties[e]	Validation[f]
Balje et al. (1968b)	Direct	1	No	No	Incompressible	EXP
Macchi et al. (1981)	Direct	1	No	Fixed	Ideal gas	No
Lozza et al. (1982)	Direct	1, 2, 3	No	Fixed	Ideal gas	No
Astolfi et al. (2015)	Direct	1 ,2, 3	No	Fixed	Non-ideal gas	No
Tournier et al. (2010)	No	Any	Yes	No	Non-ideal gas	EXP
Da Lio et al. (2014)	No	1	Yes	Fixed	Non-ideal gas	No
Da Lio et al. (2016)	No	1	Yes	Fixed	Non-ideal gas	No
Meroni et al. (2016b)	Direct	1	No	Fixed	Non-ideal gas	EXP/CFD
Meroni et al. (2018a)	Direct	Any	No	Fixed	Non-ideal gas	EXP/CFD
Bahamonde et al. (2017)	Direct	Any	No	No	Non-ideal gas	CFD
Talluri et al. (2017)	Direct	1	Yes	No	Non-ideal gas	No
Denton (2017)	No	Any	No	No	Ideal gas	CFD
Present work	Gradient	Any	No	Yes	Non-ideal gas	EXP

[a] If applicable, type of optimization algorithm used: gradient-based or gradient-free (direct search).
[b] Number of turbine stages that the model can handle.
[c] Whether or not the model relies on the repeating-stage assumption (this reduces the design space significantly).
[d] Whether the model accounts for the influence of the diffuser or not. The models that accounted for the diffuser assumed a *fixed fraction* of kinetic energy recovery and did not consider the flow within the diffuser.
[e] Thermodynamic model used to compute the properties of the fluid.
[f] Whether or not the model has been validated with experimental or CFD data.

models is the lack of validation against experimental data or CFD simulations. Furthermore, to the knowledge of the author, all the works documented in the open literature formulate the mean-line model as a system of nonlinear equations and then explore the design space manually or by means of gradient-free optimization methods, which, in turn, require a large number of function evaluations to converge to the optimal solution.

In response to the shortcomings of the existing methods, this work proposes a mean-line model and optimization approach for the preliminary design of axial turbines. The mean-model was formulated in a general way so as to use arbitrary equations of state and empirical loss models and it accounts for the influence of the diffuser using the one-dimensional flow model presented in Chapter 2. In addition, the preliminary design problem was formulated as a constrained optimization problem and it was solved using a gradient-based method. In contrast with the existing gradient-free approaches, adopting a gradient-based algorithm enabled: (1) the optimization multi-stage design problems with tens of design variables at a low computational cost and (2) the use equality-constraints to integrate the turbine, diffuser, and loss models in a simple way. The proposed design method was applied to a case study documented in the literature and the optimal design was assessed in terms of total-to-static efficiency, angular speed, and mean diameter. In addition, a sensitivity analysis was carried out to study the influence of several input parameters on the optimal turbine design.

3.2 Axial turbine model

This section describes the proposed axial turbine model. First, the geometry of axial turbines and the variables involved in the model are introduced. After that, the conventions used for the velocity triangles are explained. Finally, the design specifications (i.e., boundary conditions) and the mathematical model for the axial turbine are described. This mathematical model is composed of three sub-models that are used as building blocks: (1) the cascade model, (2) the loss model, and (3) the diffuser model. These sub-models are combined in Section 3.4 to formulate the turbine preliminary design as a constrained optimization problem.

3.2.1 Axial turbine geometry

Axial turbines are rotary machines that convert the energy from a fluid flow into work. An axial turbine is composed of one or more stages in series and each stage consists of one cascade of stator blades that accelerate the flow and one cascade of rotor blades that deflect the flow, converting the enthalpy of the fluid into work as a result of the net change of angular momentum.

As illustrated in Figure 3.1a, turbine blades are characterized by a mean camber line halfway between the suction and pressure surfaces. The most forward point of the camber line is the leading edge and the most rearward point is the trailing edge. The blade chord c is the length of the straight line connecting the leading and the trailing edges. The blade thickness is the distance between the pressure and suction surfaces, measured perpendicular to the camber line. The aerodynamic performance of the blade is highly influenced by the maximum thickness $t_{\max}$ and the trailing edge thickness t_{te}. The angle between the axial direction and the tangent to the camber line is the metal angle θ and the difference between inlet and outlet metal angles is the camber angle $\Delta\theta = |\theta_{\text{in}} - \theta_{\text{out}}|$.

An axial–tangential cross section of a turbine stage is shown in Figure 3.1b. The blade pitch or spacing s is the circumferential separation between two contiguous blades and the opening o is defined as the distance between the trailing edge of one blade and the suction surface of the next one, measured perpendicular to the direction of the outlet metal angle. The angle between the axial direction and the chord line is the stagger angle or setting angle ξ and the projection of the chord onto the axial direction is known as the axial chord c_{ax}. The cascade spacing s_{ax} is the axial separation between one blade cascade and the next one.

An axial–radial cross section of a three-stage axial turbine is depicted in Figure 3.1c. The working fluid flows parallel to the shaft within the annular duct defined by the inner and outer diameters. The hub is the surface defined by the inner diameter and the shroud is the surface defined by the outer diameter. The blade height H is defined as the difference between the blade radius at the tip r_{t} and the blade radius at the hub r_{h} and the spacing between the tip of the rotor blades and the shroud is known as tip clearance gap t_{cl}. The mean radius r is

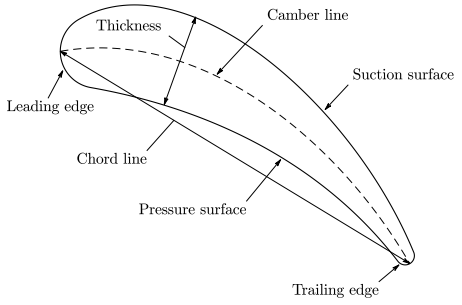

(a) Geometry of a blade section.

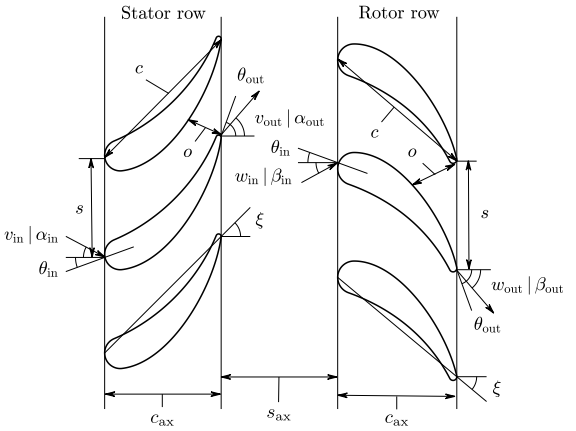

(b) Axial-tangential view of a cascade.

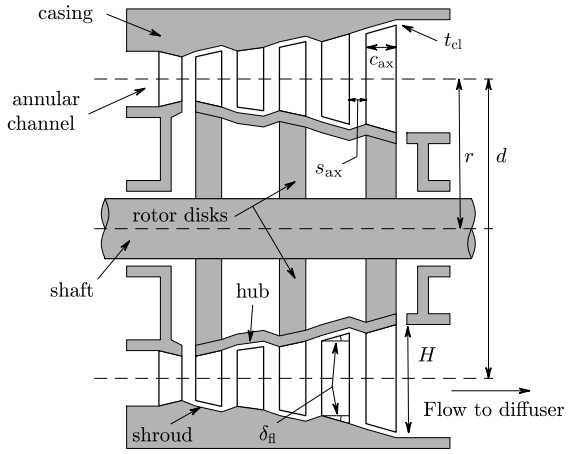

(c) Axial-radial view of an axial turbine.

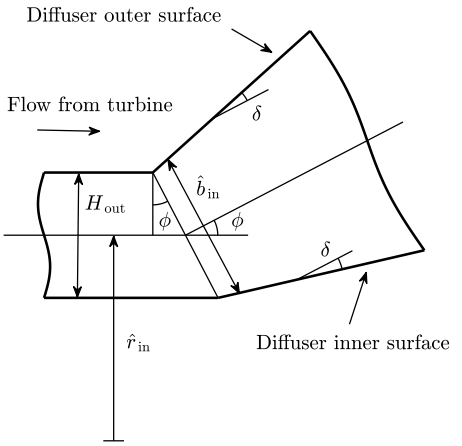

(d) Annular diffuser geometry.

Figure 3.1: Geometry of a general axial turbine and exhaust diffuser.

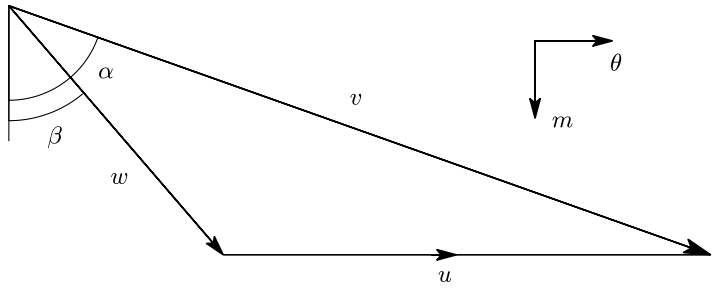

Figure 3.2: Velocity triangle showing the notation and conventions used in this work.

often defined as the arithmetic mean of the hub and tip radii, but other definitions are possible. The blade height can vary along the axial direction, but the flaring angle δ_{fl} should be limited to avoid flow separation close to the annulus walls.

In some cases, the kinetic energy of the flow at the outlet of the last stage can be significant and, for this reason, it is common to use a diffuser to recover the exhaust kinetic energy and increase the turbine power output. The cross sectional view of an annular diffuser is shown in Figure 3.1d. The fluid leaving the last turbine stage enters the annular channel and it reduces its meridional component of velocity as the flow area increases (for subsonic flow) and its tangential component of velocity as the mean radius of the channel increases. The flow area of the diffuser is given by $A = 2\pi\hat{r}\,\hat{b}$, where $\hat{r}$ is the mean radius and $\hat{b}$ is the channel height of the diffuser. The area ratio is defined as the ratio of outlet to inlet areas, $AR = A_{\text{out}}/A_{\text{in}}$. As described in Chapter 2, a diffuser with straight inner and outer walls is known as a conical annular diffuser and its geometry can be parametrized in terms of the mean wall cant angle ϕ and the divergence semi-angle δ.

3.2.2 Velocity vector conventions

In this work, the symbol v is used for the absolute velocity, w for the relative velocity, and u for the blade velocity. The components of velocity in the tangential and meridional directions are denoted with the subscripts θ and m, respectively. For the case of axial turbines the meridional direction coincides with the axial direction. Regarding the sign convention for the velocity components, the positive axial direction is taken along the shaft axis from the inlet of the turbine to the outlet and the positive radial direction is taken as the turbine radius increases. The positive circumferential direction is taken in the direction of the blade speed.

Moreover, the symbol α is used to denote the absolute flow angle, whereas β is used for the relative flow angle. As shown in the velocity triangle of Figure 3.2, all angles are measured from the meridional towards the tangential direction. This is the usual convention in gas turbines and it limits the flow angles to the interval $[-\frac{\pi}{2}, \frac{\pi}{2}]$ (Saravanamuttoo et al. 2009, p. 316). The main advantage of this angle convention is that it allows one to use single-input inverse trigonometric functions.

For the sake of consistency, this work uses the same sign convention for the stator and rotor blades. However, the loss model that is used in this work (Kacker et al. 1982) employs a different sign convention for stator and rotor blades and some of the formulas of the loss model had to be adapted, see Appendix B.

3.2.3 Design specifications

A turbine is a component of a larger system (e.g., a power cycle or a chemical process) that will impose some requirements on its design such as: (1) stagnation state at the inlet of the turbine, (2) static pressure at the outlet of the turbine, and (3) mass flow rate. Alternatively, it is possible to specify the isentropic power output instead of the mass flow rate because both are related according to

$$\dot{W}_s = \dot{m}\ (h_{01} - h_{2s}) = \dot{m}\,\Delta h_s, \tag{3.1}$$

where the subscripts 1 and 2 refer to the states at the inlet and outlet of the turbine, respectively, and the subscript s refers to an isentropic expansion. These design requirements can be regarded as the thermodynamic boundary conditions for the expansion and they are given inputs for the turbine model.

3.2.4 Cascade model

This section describes the equations used to model the flow within each row of blades. All flow variables are evaluated at the inlet and outlet of each cascade at a constant mean radius. The cascade model presented herein is solved sequentially and it contains three blocks: (1) computation of the velocity triangles, (2) determination of the thermodynamic properties using the principle of conservation of rothalpy and equations of state, and (3) calculation of the cascade geometry.

Velocity triangles

The equations used to compute the velocity diagrams for rotor and stator rows are the same, provided that the blade velocity is given by $u = 0$ for the stators and $u = \Omega\, r$ for the rotors, where the angular speed Ω and mean radius r are given as input variables.

The velocity triangles at the inlet of each cascade are computed according to

$$v_\theta = v\ \sin(\alpha), \tag{3.2}$$

$$v_m = v\ \cos(\alpha), \tag{3.3}$$

$$w_\theta = v_\theta - u, \tag{3.4}$$

$$w_m = v_m, \tag{3.5}$$

$$w = \sqrt{w_\theta^2 + w_m^2},\ \text{and} \tag{3.6}$$

$$\beta = \arctan\left(\frac{w_\theta}{w_m}\right), \tag{3.7}$$

where the subscripts that refer to inlet conditions have been dropped for simplicity. For the first stator, the absolute velocity v and flow angle α are given as inputs. For the rest of cascades the absolute velocity and flow angle are obtained from the outlet of the previous cascade. Similarly, the velocity triangles at the outlet of each cascade are computed according to

$$w_\theta = w \sin(\beta), \tag{3.8}$$

$$w_m = w \cos(\beta), \tag{3.9}$$

$$v_\theta = w_\theta + u, \tag{3.10}$$

$$v_m = w_m, \tag{3.11}$$

$$v = \sqrt{v_\theta^2 + v_m^2}, \text{ and} \tag{3.12}$$

$$\alpha = \arctan\left(\frac{v_\theta}{v_m}\right), \tag{3.13}$$

where the subscripts that refer to outlet conditions have been dropped for simplicity. The relative velocity w and flow angle β at the outlet of each cascade are provided as an input for the model.

Thermodynamic properties

The axial turbine model was formulated in a general way so that the thermodynamic properties of the working fluid can be computed with any thermodynamic library that supports pressure–enthalpy and enthalpy–entropy function calls such as Lemmon et al. (2013) or Bell et al. (2014). The stagnation state at the inlet of the first stator (e.g., temperature and pressure) is an input for the model and the corresponding static state is determined according to

$$h_{\text{in}} = h_{0,\text{in}} - \frac{1}{2} v_{\text{in}}^2, \tag{3.14}$$

$$s_{\text{in}} = s\left(p_{0,\text{in}},\, h_{0,\text{in}}\right), \text{ and} \tag{3.15}$$

$$[T,\, p,\, \rho,\, a,\, \mu]_{\text{in}} = [T,\, p,\, \rho,\, a,\, \mu]\left(h_{\text{in}},\, s_{\text{in}}\right). \tag{3.16}$$

The static thermodynamic properties at the inlet of of the remaining cascades are obtained from the outlet of the previous cascade.

In addition, the thermodynamic properties at the outlet of each row of blades is computed exploiting the fact that rothalpy is conserved in the stator and rotor cascades (Dixon et al. 2013, pp. 10–11). For purely axial turbines (i.e., constant mean radius), the conservation of rothalpy is reduced to the conservation of relative stagnation enthalpy, and the static enthalpy at the outlet of each cascade can be computed according to

$$h_{\text{out}} = h_{\text{in}} + \frac{1}{2} w_{\text{in}}^2 - \frac{1}{2} w_{\text{out}}^2. \tag{3.17}$$

Since the entropy at the outlet of each cascade is provided as an input to the model, any other static thermodynamic property can be determined with enthalpy–entropy function calls,

$$[T,\, p,\, \rho,\, a,\, \mu]_{\,\mathrm{out}} = [T,\, p,\, \rho,\, a,\, \mu]\,(h_{\mathrm{out}},\, s_{\mathrm{out}})\,. \tag{3.18}$$

Cascade geometry

The geometry of the annulus is obtained from the principle of conservation of mass and the geometric relations given by

$$A = \frac{\dot{m}}{\rho\, v_m}, \tag{3.19}$$

$$H = \frac{A}{2\pi r}, \tag{3.20}$$

$$r_{\mathrm{h}} = r - H/2, \tag{3.21}$$

$$r_{\mathrm{t}} = r + H/2, \text{ and} \tag{3.22}$$

$$\lambda = \frac{r_{\mathrm{h}}}{r_{\mathrm{t}}}, \tag{3.23}$$

where the mass flow rate $\dot{m}$ is given as an input for the model. Eqs. (3.19) to (3.23) are valid both at the inlet and outlet of the cascade and the subscripts were not included for simplicity. In addition, the mean blade height of the cascade is determined as the inlet and outlet blade height arithmetic mean,

$$H = \frac{1}{2}\,(H_{\mathrm{in}} + H_{\mathrm{out}})\,. \tag{3.24}$$

The blade chord is determined from the blade aspect ratio (input variable) and the mean blade height according to

$$c = \frac{H}{\big(H/c\big)}, \tag{3.25}$$

whereas the blade spacing is determined from the pitch to chord ratio (input variable) and the blade chord,

$$s = c \cdot \big(s/c\big)\,. \tag{3.26}$$

The incidence i and deviation δ angles are assumed to be zero and, therefore, the metal angle at the inlet and outlet of each cascade are given by

$$\theta_{\mathrm{in}} = \beta_{\mathrm{in}} - i = \beta_{\mathrm{in}}, \text{ and} \tag{3.27}$$

$$\theta_{\mathrm{out}} = \beta_{\mathrm{out}} - \delta = \beta_{\mathrm{out}}. \tag{3.28}$$

The blade opening is approximated by the cosine rule (Saravanamuttoo et al. 2009, pp. 343–344), which is given by

$$o \approx s \cdot \cos\left(\theta_{\text{out}}\right). \tag{3.29}$$

The maximum blade thickness is computed according to the formula proposed by Kacker et al. (1982) that correlates the blade maximum thickness to chord ratio with the camber angle as given by

$$\left(t_{\max}/c\right) = \begin{cases} 0.15 & \text{for} \quad \Delta\theta \leq 40^\circ & (3.30) \\ 0.15 + 1.25 \cdot 10^{-3} \cdot (\theta - 40) & \text{for} \quad 40^\circ \leq \Delta\theta \leq 120^\circ & (3.31) \\ 0.25 & \text{for} \quad \Delta\theta \geq 120^\circ, & (3.32) \end{cases}$$

where the blade camber angle is defined as $\Delta\theta = |\theta_{\text{in}} - \theta_{\text{out}}|$.

The stagger angle is computed according to

$$\xi = \frac{1}{2}\left(\theta_{\text{in}} + \theta_{\text{out}}\right), \tag{3.33}$$

which assumes that the blades have a circular-arc camberline (Dixon et al. 2013, p. 72). Alternatively, the stagger angle could be computed from the graphical relation proposed by Kacker et al. (1982) or given as an input for the model.

The axial chord is computed from the chord and stagger angle according to

$$c_{\text{ax}} = c \cdot \cos\left(\xi\right). \tag{3.34}$$

and is used in combination with the change in blade height across the cascade to compute the flaring angle,

$$\tan\left(\delta_{\text{fl}}\right) = \frac{H_{\text{out}} - H_{\text{in}}}{2\, c_{\text{ax}}}. \tag{3.35}$$

The trailing edge thickness is computed using the trailing edge thickness to opening ratio (input variable) and the cascade opening and is given by

$$t_{\text{te}} = o \cdot \left(t_{\text{te}}/o\right). \tag{3.36}$$

In addition, the axial spacing between cascades s_{ax} can be computed as fraction of the axial chord. However, this variable does not affect the performance predicted by the model because the Kacker et al. (1982) loss correlations neglect the influence of this parameter. Saravanamuttoo et al. (2009, pp. 332–333) suggests that axial spacing to axial chord ratios between 0.20 and 0.50 are satisfactory. Finally the tip clearance gap of the rotor blades t_{cl} is given as a fixed input to the model that depends on manufacturing limits.

The geometry relations presented in this section describe the turbine geometry in a level of detail that is adequate for preliminary design purposes. A more detailed description of the turbine geometry that is suitable for the aerodynamic design phase is presented in Chapter 4.

3.2.5 Loss model

During the preliminary design phase, it is common to rely on empirical correlations to estimate the losses within the turbine. These sets of correlations are known as loss models. A loss can be interpreted as any mechanism that leads to entropy generation and reduces the power output of the turbine, such as viscous friction in boundary layers, wake mixing, or shock waves. The work of Denton (1993) presents a detailed description of loss mechanisms in turbomachinery.

Perhaps, the most popular loss model for axial turbines is the one proposed by Ainley et al. (1951b); Ainley et al. (1951a) and its subsequent refinements by Dunham et al. (1970) and Kacker et al. (1982). The Kacker–Okapuu loss model has been further refined to account for off-design performance by Moustapha et al. (1982) and by Benner et al. (1997). One remarkable aspect of the Ainley–Mathieson family of loss methods is that it has been updated with new experimental data several times since the first version of the method was published. This was not the case for other loss prediction methods such as the ones proposed by Balje et al. (1968a), Craig et al. (1971), Traupel (1982), or Aungier (2006a).

In this work, the Kacker et al. (1982) loss model was adopted because of its popularity and maturity. The improvements of this loss model to account for off-design performance were not considered because the proposed methodology is aimed towards the optimization of the turbine performance at its design point. The Kacker–Okapuu loss model is described in detail in Appendix B. The original formulation of the loss model has been adapted to the nomenclature and sign conventions used in this work for the convenience of the reader.

As described by Denton (1993) and by Dahlquist (2008), there are several possible definitions for the loss coefficient. In this work, the stagnation pressure loss coefficient was used because the Kacker–Okapuu loss model was developed based on this definition. This loss coefficient is meaningful for stator or rotor cascades with a constant mean radius and it is defined as the ratio of relative stagnation pressure drop across the cascade to relative dynamic pressure at the outlet of the cascade,

$$Y = \frac{p_{0\mathrm{rel,in}} - p_{0\mathrm{rel,out}}}{p_{0\mathrm{rel,out}} - p_{\mathrm{out}}}. \tag{3.37}$$

When the proposed axial turbine model is evaluated, the loss coefficient computed from its definition, Eq. (3.37), and the loss coefficient computed using the loss model, Appendix B, may not have the same value. In Section 3.4, the turbine design is formulated as an optimization problem that relies on equality constraints to ensure that the value of both loss coefficients are consistent for each cascade. Therefore, the loss coefficient error is given by

$$Y_{\mathrm{error}} = Y_{\mathrm{definition}} - Y_{\mathrm{loss\,model}}. \tag{3.38}$$

3.2.6 Diffuser model

The flow within the exhaust diffuser was modeled with the one-dimensional model presented in Chapter 2. This model is based on the transport equations for mass, meridional and tangential momentum, and energy for steady and axisymmetric flow in an annular duct. The model can use arbitrary equations of state and it accounts for effects of area change, heat transfer, and friction. Under these conditions, the governing equations of the flow are given by

$$v_m \frac{\mathrm{d}\rho}{\mathrm{d}m} + \rho \frac{\mathrm{d}v_m}{\mathrm{d}m} = -\frac{\rho v_m}{\hat{b}\,\hat{r}} \frac{\mathrm{d}}{\mathrm{d}m}(\hat{b}\,\hat{r}), \tag{3.39}$$

$$\rho v_m \frac{\mathrm{d}v_m}{\mathrm{d}m} + \frac{\mathrm{d}p}{\mathrm{d}m} = \frac{\rho v_\theta^2}{\hat{r}} \sin(\phi) - \frac{2\tau_\mathrm{w}}{\hat{b}} \cos(\alpha), \tag{3.40}$$

$$\rho v_m \frac{\mathrm{d}v_\theta}{\mathrm{d}m} = -\frac{\rho v_\theta v_m}{\hat{r}} \sin(\phi) - \frac{2\tau_\mathrm{w}}{\hat{b}} \sin(\alpha), \text{ and} \tag{3.41}$$

$$\rho v_m \frac{\mathrm{d}p}{\mathrm{d}m} - \rho v_m\, a^2 \frac{\mathrm{d}\rho}{\mathrm{d}m} = \frac{2(\tau_\mathrm{w} v + \dot{q}_\mathrm{w})}{\hat{b}\left(\frac{\partial e}{\partial p}\right)_\rho}. \tag{3.42}$$

The viscous term is modeled using a constant skin friction coefficient C_f such that $\tau_\mathrm{w} = C_\mathrm{f} \frac{\rho v^2}{2}$ and heat transfer is neglected, $\dot{q}_\mathrm{w} = 0$. The inner and outer surfaces of the diffuser are assumed to be straight, see Figure 3.1d. For this particular geometry, the diffuser channel height $\hat{b}$ and mean radius $\hat{r}$ are given by

$$\hat{r}(m) = \hat{r}_\mathrm{in} + m \sin(\phi) = r + m \sin(\phi), \text{ and} \tag{3.43}$$

$$\hat{b}(m) = \hat{b}_\mathrm{in} + 2m \tan(\delta) = H_\mathrm{out} / \cos(\phi) + 2m \tan(\delta), \tag{3.44}$$

where the mean cant angle ϕ and divergence semi-angle δ are given as input parameters for the model.

The initial conditions required to integrate the system of ordinary differential equations are prescribed assuming that the thermodynamic state and velocity vector do not change from the turbine outlet to the diffuser inlet. The integration starts from the initial conditions and stops when the prescribed value of outlet to inlet area ratio AR is reached. In this work, the adaptive solver based on fourth- and fifth-order explicit Runge-Kutta methods proposed by Shampine et al. (1997) was used to perform the numerical integration.

In general, the static pressure given as a design specification from a system-level analysis will not match the pressure at the outlet of the diffuser evaluated from the model. In Section 3.4, the turbine design is formulated as an optimization problem that uses an equality constrain to ensure that the static pressure at the outlet of the diffuser and the target pressure are consistent. Therefore, the dimensionless outlet static pressure error is given by

$$p_\mathrm{error} = \frac{p_\mathrm{out}^\mathrm{diff} - p_\mathrm{target}}{p_\mathrm{target}}. \tag{3.45}$$

Table 3.2: Validation of the axial turbine model against experimental data.

Number of stages	Variable[a,b,c]	Kofskey et al. (1972)	Present work	Deviation
1 stage	T_{01}	22.5 °C	Same	n.a.
	p_{01}	1.380 bar	Same	n.a.
	PR	2.298	Same	n.a.
	Ω	15533 rpm	Same	n.a.
	$\dot{m}$	2.695 kg/s	2.729 kg/s	0.91%
	$\dot{W}$	136.17 kW	135.03 kW	-0.42%
	η_{ts}	80.00%	78.85%	1.15 points
2 stages	T_{01}	25.8 °C	Same	n.a.
	p_{01}	1.240 bar	Same	n.a.
	PR	4.640	Same	n.a.
	Ω	15619 rpm	Same	n.a.
	$\dot{m}$	2.407 kg/s	2.434 kg/s	1.12%
	$\dot{W}$	212.06 kW	211.10 kW	-0.46%
	η_{ts}	82.00%	81.40%	0.60 points

[a] Kofskey et al. (1972) reported the turbine performance in terms of *equivalent* variables. These were converted to ordinary variables using ambient conditions at sea level (101.325 kPa and 288.15 K).
[b] The power output is computed from the measured torque and angular speed.
[c] The total-to-static isentropic efficiency is a dependent variable that is computed from the thermodynamic conditions, mass flow rate, and power output.

3.3 Validation of the axial turbine model

The aim of this section is to validate the proposed axial turbine model using the experimental data of the one- and two-stage turbines reported by Kofskey et al. (1972). The flow in both turbines is subsonic and they use air as working fluid. To validate the model, the geometry and operating conditions reported by Kofskey et al. (1972) were replicated and the design-point performance of both test cases was compared with the output of the model, see Table 3.2. The inlet thermodynamic state, angular speed, and total-to-static pressure ratio were matched at the design point and the validation was performed analyzing the deviation in mass flow rate, power output, and total-to-static isentropic efficiency. This approach is consistent with the definition of the design point given by Kofskey et al. (1972).

The data reported in Table 3.2 shows that the agreement between the predicted and measured mass flow rates and power outputs is satisfactory and that the relative deviation is less than 1.2% for both turbines. In addition, the deviation of total-to-static isentropic efficiency between model and experiment is 1.15 percentage points for the one-stage turbine and 0.60 points for the two-stage turbine, which is within the efficiency-prediction uncertainty of the loss model of ± 1.5 percentage points (Kacker et al. 1982). This analysis showed that the axial turbine model can be used to predict the design-point performance of turbines with one or more stages. However, the validation was restricted to subsonic turbines

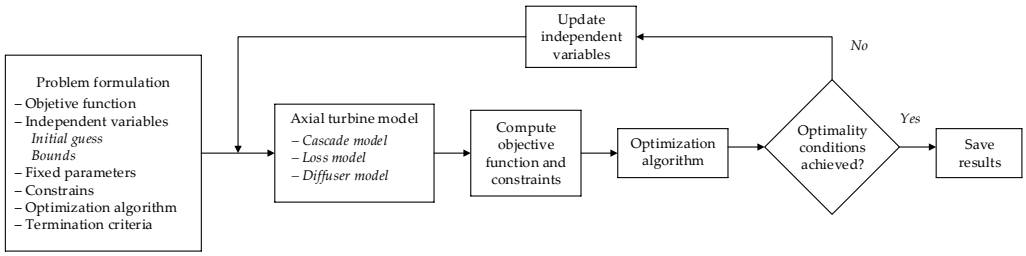

Figure 3.3: Automated workflow for preliminary turbomachinery design.

using air and it is likely that the efficiency predictions will not be as accurate for cascades operating at supersonic conditions or when the fluid behavior deviates from ideal gas, such as in Rankine cycles using organic fluids with high molecular complexity or in supercritical carbon dioxide power systems.

3.4 Optimization problem formulation

The sub-models presented in Section 3.2 can be integrated to formulate the preliminary turbine design as a nonlinear, constrained optimization problem. In order to formulate this problem it is necessary to specify: (1) the objective function to be optimized, (2) the design variables and fixed parameters, and (3) the inequality and equality constraints that limit the design space.

Once the problem is formulated, the workflow illustrated in Figure 3.3 is used to carry out the preliminary design systematically. First, the fixed parameters and an initial guess for the design variables are provided and the mean-line axial turbine model is evaluated. After that, the optimization algorithm uses values and gradients of the objective function and constraints to determine the values of the design variables for the next iteration. This process is repeated until the solution meets the termination criteria and the optimal turbine design is found.

3.4.1 Objective function

The objective function is an performance indicator of interest that is minimized or maximized. The total-to-static and total-to-total isentropic efficiencies are often used as objective function for the preliminary design of turbomachinery (Dixon et al. 2013, pp. 23–24). These performance indicators are defined as

$$\eta_{\mathrm{ts}} = \frac{h_{01} - h_{02}}{h_{01} - h_{2s}} \quad \text{and} \quad \eta_{\mathrm{tt}} = \frac{h_{01} - h_{02}}{h_{01} - h_{2s} + v_2^2/2}, \tag{3.46}$$

where the subscripts 1 and 2 refer to the states at the inlet and outlet of the turbine, respectively, and the subscript s refers to an isentropic expansion.

3.4.2 Design variables

The choice of design variables, also known as independent variables, is not unique and different sets of variables can be used to formulate the same problem. Ideally, the set of design variables should allow one to compute the dependent variables in a sequential way and avoid inner iterations in the evaluation of the model. In addition, it is preferable to use a properly scaled set of independent variables (i.e., design variables with a similar order of magnitude) because this can increase the convergence rate of some algorithms and reduce the round-off error when the problem gradients are evaluated using a finite difference approximation (Nocedal et al. 2006, pp. 26–27).

Table 3.3 contains the set of design variables adopted in this work as well as the lower and upper bounds that were used to formulate the optimization problem for the case study discussed in Section 3.5. This formulation uses 6 design variables per cascade (i.e., 12 design variables per stage) plus three additional global design variables. This set of independent variables is well-scaled and it enables the evaluation of the turbine model in a sequential way with no inner iterations[1] from the inlet of the first stator to the exit of the diffuser. The lower and upper bounds of the design variables were selected to span a large design space that respects the range of applicability of the Kacker et al. (1982) loss system.

The specific speed and specific diameter were selected as independent variables, rather than the angular speed and mean diameter, because they have an order of magnitude of unity and it is easier to provide a reasonable initial guess since they are independent of the scale of the problem (Balje et al. 1968a). The angular speed and mean diameter can be readily obtained from their specific counterparts

$$\Omega_\mathrm{s} = \Omega \, \frac{\left(\dot{m}/\rho_{2s}\right)^{1/2}}{\left(h_{01} - h_{2s}\right)^{3/4}} \quad \text{and} \quad d_s = d \, \frac{\left(h_{01} - h_{2s}\right)^{1/4}}{\left(\dot{m}/\rho_{2s}\right)^{1/2}}. \tag{3.47}$$

In addition, the flow velocities were normalized using the isentropic velocity, which is also known as the spouting velocity

$$v_0 = \sqrt{2 \, \left(h_{01} - h_{2s}\right)}. \tag{3.48}$$

The entropy at the exit of each cascade was normalized using the inlet entropy and bounded by a reference entropy value s_ref computed according to

$$s_\mathrm{ref} = s(p_2, h_\mathrm{ref}) \text{ and} \tag{3.49}$$

$$h_\mathrm{ref} = h_{01} - \eta_\mathrm{ref} \cdot \left(h_{01} - h_{2s}\right). \tag{3.50}$$

The remaining design variables did not need to be scaled.

[1] Except for the inner iterations that may occur when interrogating the thermodynamic library.

3.4.3 Fixed parameters

In order to evaluate the model and compute the dependent variables, it is necessary to provide several fixed parameters that do not change during the optimization. Table 3.3 contains the fixed parameters that are used as input for the axial turbine model as well as the numerical values used for the case study. The isentropic power output, given by Eq. (3.1), and thermodynamic boundary conditions are kept constant because they are given by the system design requirements, see Section 3.2.3. Notably, all independent variables are dimensionless and the isentropic power output is the parameter that scales-up the problem. In addition, the flow angle at the inlet of the first stator is fixed because it is assumed that there is no swirl at the inlet of the turbine. Furthermore, the tip clearance gap is constant and it is given by manufacturing limits. Finally, the diffuser model inputs are given as fixed parameters because the total-to-static isentropic efficiency is a monotonic function of these variables, see Chapter 2.

3.4.4 Constraints

In addition to the bounds for the degrees of freedom, the axial turbine model relies on nonlinear equality and inequality constraints to guarantee that the model is consistent and that the design is feasible. These constraints and the numerical values used for the case study are summarized in Table 3.3. The pressure ratio in each cascade was constrained to avoid compression within the turbine, which is equivalent to constrain the degree of reaction between zero and one, and the flaring angle was limited to avoid designs that result in flow separation close to the annulus walls (Ainley et al. 1951b). In addition, the constrains for the inlet relative flow angles were imposed to avoid blades with too low deflection (Kacker et al. 1982) and the meridional component of the Mach number at the inlet of the diffuser was constrained to ensure that the diffuser model, Eqs. (3.39) to (3.42), is not singular, see Chapter 2. Furthermore, the hub-to-tip ratio was constrained because this parameter is a dependent variable that the designer might want to control as it has a great influence on: (1) the optimal angular speed and diameter and (2) the centrifugal and gas bending stresses (Saravanamuttoo et al. 2009). Finally, as discussed in Section 3.2.5 and Section 2.2, equality constrains were imposed on the loss coefficient error and the outlet static pressure error to ensure that the model is consistent. Depending on each application, it is possible to implement additional constraints or to ignore some of them.

3.4.5 Optimization algorithm

Optimization algorithms can be classified as gradient-free or gradient-based depending on the use of derivative information. Gradient-based methods are particularly suited to solve differentiable problems involving a large number of design variables and they use the gradients of the objective function and constraints to

determine the next iterate (Nocedal et al. 2006). Gradient-free methods, on the other hand, only use the values of the objective function and constraints and, for this reason, they can be used when the gradients of the problem are not available or when the problem is not smooth or even discontinuous (Audet et al. 2017). However, gradient-free methods require a large number of model evaluations to converge, especially when the number of design variables is large, and they are not well-suited to solve problems with equality constraints.

In this work, a gradient-based optimization algorithm was adopted because the proposed mean-line axial turbine model is smooth[2] and it involves several tens of design variables for multistage configurations. In particular, a Sequential Quadratic Programming (SQP) algorithm (Nocedal et al. 2006, pp. 526–572) that is capable to handle equality and inequality constraints was adopted. The problem gradients were estimated using first order finite differences with an step-size equal to the square-root of machine epsilon (Press et al. 2007, pp 8–11).

3.5 Design optimization of a case study

The aim of this section is to assess the optimization methodology proposed in this work. To this aim, the model was applied to optimize two axial turbine reference cases from Macchi et al. (2017). The two cases consider pentafluoroethane (R125) expanding from 155 °C and 36.2 bar (stagnation properties) to 15.85 bar (static pressure). The mass flow rate is selected to achieve an isentropic power of 250 kW in the first case and 5000 kW in the second case. These cases are representative of a small-scale and a large-scale Rankine cycle used to generate power from a low-temperature heat source (Colonna et al. 2015).

The values of the fixed parameters, design variable bounds, and constrains used to formulate the optimization problem are summarized in Table 3.3 and the total-to-static isentropic efficiency was set as objective function. The minimum hub-to-tip ratio constraint is always active at the exit of the last stage, see Section 3.6.3, and its value has a great influence on the optimal angular speed and diameter. For this reason, the comparison of optimal speed and diameter will only be fair if the minimum hub-to-tip ratio is the same as in the reference case. The value $\lambda_{\text{min}} = 0.60$ reported in Table 3.3 is the same value used by Macchi et al. (2017)[3].

The results of the optimization for the two cases considered are shown in Table 3.4. It can be observed that the optimal angular speed and diameter of the reference case agree well with the results obtained with the turbine model presented in this work and that the maximum relative deviation is less than 6%.

[2]Some of the loss model equations are are not differentiable (e.g., piece-wise functions or functions involving absolute values), see Appendix B. Despite these non-smooth points, experience showed that the optimization problem can be solved reliably using gradient-based methods.

[3]In fact, the minimum-hub-to tip ratio used in Macchi et al. (2017) was not reported in the original publication, but it was confirmed by M. Astolfi in a personal communication.

Table 3.3: Optimization problem formulation and definition of the reference cases.

Fixed parameters				
Number of stages	N	=	1	–
Isentropic power output	$\dot{W}_s$	=	250 | 5000	kW
Turbine inlet stagnation temperature	T_{01}	=	155	°C
Turbine inlet stagnation pressure	p_{01}	=	36.2	bar
Turbine outlet static pressure	p_2	=	15.85	bar
Tip clearance gap	t_{cl}	=	0.50	mm
First stator inlet flow angle	α_{in}	=	0.0	deg
Diffuser mean cant angle	ϕ	=	30.0	deg
Diffuser divergence semi-angle	δ	=	5.0	deg
Diffuser area ratio	AR	=	2.5	–
Diffuser skin friction coefficient	C_{f}	=	0.010	–
Independent variables				
Specific speed	Ω_{s}	$\in$	[0.10, 10.0]	–
Specific diameter	d_{s}	$\in$	[0.10, 10.0]	–
Normalized first stator inlet velocity	v_{in}/v_0	$\in$	[0.01, 1.00]	–
Normalized outlet relative velocity[a]	w_{out}/v_0	$\in$	[0.01, 1.00]	–
Outlet relative flow angle (stator)[a]	$\beta_{\mathrm{out,S}}$	$\in$	[+40.0, +80.0]	deg
Outlet relative flow angle (rotor)[a]	$\beta_{\mathrm{out,R}}$	$\in$	[−80.0, −40.0]	deg
Normalized outlet entropy[a,c]	$s_{\mathrm{out}}/s_{\mathrm{in}}$	$\in$	[1.00, $s_{\mathrm{ref}}/s_{\mathrm{in}}$]	–
Aspect ratio[a]	H/c	$\in$	[1.00, 2.00]	–
Pitch to chord ratio[a]	s/c	$\in$	[0.75, 1.10]	–
Trailing edge thickness to opening ratio[a]	t_{te}/o	$\in$	[0.05, 0.40]	–
Nonlinear constraints				
Inlet relative flow angle (stator)[a]	$\beta_{\mathrm{in,S}}$	$\leq$	+15.0	deg
Inlet relative flow angle (rotor)[a]	$\beta_{\mathrm{in,R}}$	$\geq$	−15.0	deg
Flaring angle[a]	δ_{fl}	$\in$	[−10.0, +10.0]	deg
Hub-to-tip ratio[b]	λ	$\in$	[0.60, 0.95]	–
Cascade pressure ratio[a]	PR_{c}	$\geq$	1.00	–
Diffuser inlet meridional Mach number	$\mathrm{Ma}^{\mathrm{diff}}_{m,\mathrm{in}}$	$\leq$	1.00	–
Outlet static pressure error	p_{error}	=	0.00	–
Cascade loss coefficient error[a]	Y_{error}	=	0.00	–

[a] One value per cascade (rotor or stator).
[b] Two values per cascade (inlet and outlet).
[c] s_{ref} corresponds the outlet entropy assuming $\eta_{\mathrm{ts}}^{\mathrm{ref}} = 50\%$.

Table 3.4: Output of the optimization methodology for the two reference cases.

Isentropic power	Variable	Macchi et al. (2017)	Present work	Deviation
$\dot{W}_s = 250$ kW	Ω	31000 rpm	29231 rpm	-5.71%
	d	0.086 m	0.087 m	1.27%
	$\dot{W}$	219.3 kW	224.4 kW	2.36%
	η_{ts}	87.70%	89.77%	2.07 points
$\dot{W}_s = 5000$ kW	Ω	6000 rpm	6144 rpm	2.40%
	d	0.420 m	0.395 m	-5.87%
	$\dot{W}$	4535.0 kW	4576.5 kW	0.92%
	η_{ts}	90.70%	91.53%	0.83 points

In addition, the model presented in this work captures the trend of the optimal angular speed and diameter as the power output changes. The values of total-to-static efficiency from the reference case and the ones obtained in the present work are comparable, although there are is a difference of 2.07 and 0.83 percentage points in the small scale and large scale cases, respectively. This difference is not surprising considering that the Craig et al. (1971) loss model was used in the reference case while the Kacker et al. (1982) model was used in the present work and that the efficiency prediction uncertainty of these empirical loss models is approximately ± 1.5 percentage points, if not higher (Kacker et al. 1982).

3.6 Sensitivity analysis

This section contains a sensitivity analysis of the 5000 kW reference case analyzed in the previous section to gain insight about the impact of several input parameters on turbine performance. The next subsections investigate the influence of the: (1) isentropic power output, (2) tip clearance gap, (3) minimum hub-to-tip ratio, (4) diffuser area ratio, (5) diffuser skin friction coefficient, (6) total-to-static pressure ratio, (7) number of stages and (8) angular speed and mean diameter on the total-to-static isentropic efficiency. Other variables were not considered because they have a secondary influence or because they are inactive constraints. Each sensitivity analysis considers the influence of one variable on the *optimal solution* while the rest of parameters are the same as in the 5000 kW reference case summarized in Table 3.3.

3.6.1 Influence of isentropic power output

The isentropic power output was varied from 10 kW to 10 MW and the maximum attainable total-to-static efficiency is shown in Figures 3.4 and 3.5. This range of power output was selected to cover a wide spectrum of turbine scales. According to the classification for organic Rankine power systems proposed by

Colonna et al. (2015), this range of power output covers the mini, small, medium, and large power capacities. It can be observed that the efficiency increases monotonously with the isentropic power and that the effect is more marked when the power output is small. The reason for this is that the size of the turbine increases and therefore: (1) the blade height H increases and the t_{cl}/H ratio decreases, which in turn reduces the tip clearance losses and (2) the blade chord of the cascades increases, which in turn increases the Reynolds number and reduces the profile losses.

3.6.2 Influence of tip clearance gap

Figure 3.4 shows the total-to-static efficiency as a function of the isentropic power when the tip clearance gap is varied from 0.00 mm (i.e., no clearance) to 1.00 mm (i.e., large clearance). It can be observed that the isentropic efficiency decreases when the tip clearance is increased and that the trend is not linear. For instance, increasing the tip clearance from 0.00 mm to 0.25 mm penalizes the efficiency more than from 0.25 to 0.50 mm. It can also be seen that the efficiency drop due to tip clearance is more marked when the isentropic power is low because the ratio t_{cl}/H is increased due to the reduction in blade height. In addition, the total-to-static efficiency increases with the isentropic power output even for the case when the rotor tip clearance is zero due to the effect of the Reynolds number.

3.6.3 Influence of the hub-to-tip ratio constraint

The influence of the lower limit for the hub-to-tip ratio constraint on the performance of the turbine is depicted in Figure 3.5 as a function of the isentropic power output. The lower value $\lambda = 0.40$ is representative of low-pressure steam turbine stages and the higher value $\lambda = 0.80$ is representative of the high-pressure stages of steam or gas turbines. The results of the optimization showed that the constraint for the minimum hub-to-tip ratio is always active at the outlet of the turbine. In other words, the turbine model proposed in this work predicts that the isentropic efficiency will always increase when the lower limit for the hub-to-tip ratio is decreased. The reason for this is that the blade height is increased when the minimum hub-to-tip ratio decreases and, as a result of this: (1) the tip clearance to blade height ratio t_{cl}/H and the clearance losses decrease and (2) for a fixed aspect ratio, the blade chord and Reynolds number increase and the profile losses are reduced.

In addition, the diffuser height increases according to $\hat{b}_{\mathrm{in}} = H_{\mathrm{out}} / \cos(\phi)$, see Figure 3.1d. This effect reduces the friction losses in the diffuser because the channel height appears in the denominator of the friction terms, Eqs. (3.40) to (3.42). The effect of the hub-to-tip ratio on the friction losses of the diffuser agrees with the results presented in Chapter 2, but its impact on the isentropic efficiency is marginal compared with that of the profile and tip clearance losses.

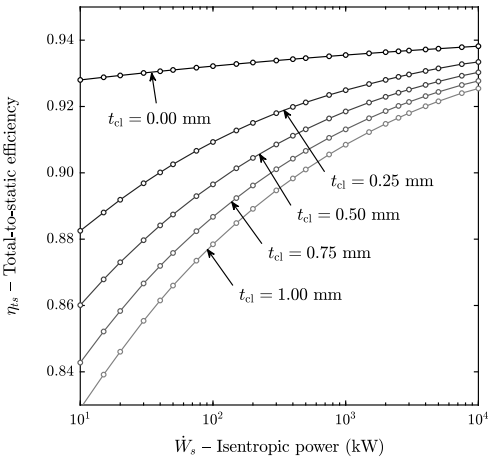

Figure 3.4: Influence of the isentropic power output and tip clearance gap on η_{ts}.

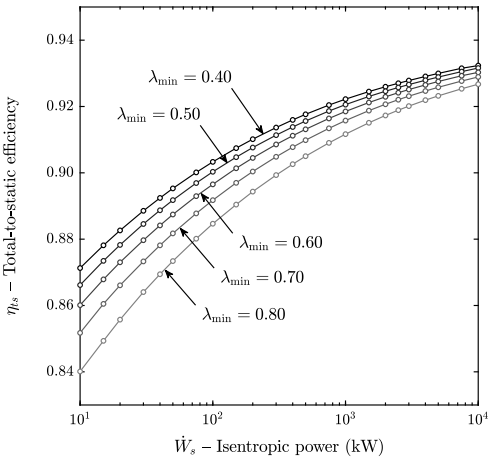

Figure 3.5: Influence of the isentropic power output and hub-to-tip ratio on η_{ts}.

3.6.4 Influence of the diffuser area ratio

The effect of the diffuser area ratio on the total-to-static isentropic efficiency is shown in Figures 3.6 and 3.7. The limits of the area ratio were selected to include cases ranging from the absence of diffuser ($AR = 1$), to cases where a large fraction of the kinetic energy is recovered ($AR = 5$). The upper limit was selected on the basis that, for the case of inviscid, incompressible flow with no inlet swirl, a diffuser with an area ratio of $AR = 5$ would recover 96% of the available dynamic pressure, see Eq. (2.36). Both Figures 3.6 and 3.7 indicate that the isentropic total-to-static efficiency increases with the area ratio in an asymptotic way. A small increase of area ratio from the case with no diffuser ($AR = 1$) increases the total-to-static efficiency significantly, whereas, as the area ratio is higher, the improvement of isentropic efficiency becomes less marked because there is less kinetic energy to recover at the diffuser exit. The results of the optimization showed that adopting an area ratio in the range 2.0–2.5 leads to 70–80% of the maximum efficiency gain. In addition, it was found that the optimum absolute flow angle at the outlet of the last stage was very close to zero (i.e., no swirl) for all cases, regardless of the area ratio of the diffuser.

3.6.5 Influence of the diffuser skin friction coefficient

To the knowledge of the author, there are no correlations available to predict the skin friction coefficient for swirling flow in annular ducts. However it is possible to estimate a reasonable value for the skin friction coefficient based on experimental data from vaneless diffusers without flow separation. Brown (1947) measured the local skin friction coefficient for different vaneless diffusers and obtained values in the range 0.003–0.010. In the absence of better estimates,

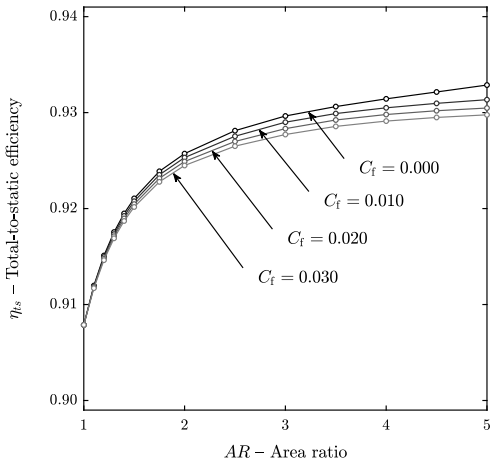

Figure 3.6: Influence of the diffuser area ratio and skin friction coefficient on η_{ts}.

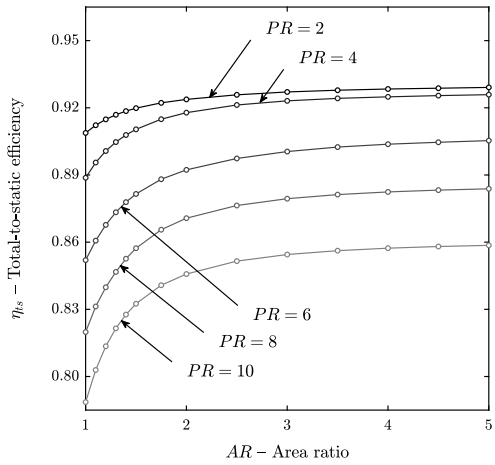

Figure 3.7: Influence of the diffuser area ratio and pressure ratio on η_{ts}.

Johnston et al. (1966) recommend values within the range 0.005-0.010 for the global skin friction coefficient. In a similar way, Dubitsky et al. (2008) suggest 0.010 as a reasonable estimate for the global skin friction coefficient, but noted that values from 0.005 to 0.020 were required to fit experimental data, depending on the application. Based on these considerations, the friction factor was varied from 0.000 (frictionless) to 0.030 (high friction) and the impact on the turbine total-to-static isentropic efficiency as a function of the area ratio is illustrated in Figure 3.6. It can be observed that increasing the friction factor decreases the total-to-static isentropic efficiency in a linear way (i.e., the different curves are equispaced). In addition the impact of friction factor on the efficiency drop is more notable as the area ratio is high because the length of the channel increases. However, the effect of the friction factor has only a modest impact on the total-to-static efficiency as it causes an efficiency drop of about 0.3 percentage points for the worst case considered in Figure 3.6.

3.6.6 Influence of the total-to-static pressure ratio

The effect of the pressure ratio as a function of the diffuser area ratio is depicted in Figure 3.7. The pressure at the outlet of the turbine was kept constant and the pressure at the inlet was varied to achieve pressure ratios ranging from $PR = 2$ (subsonic flow) to $PR = 10$. It can be observed that increasing the pressure ratio from $PR = 2$ to $PR = 4$ causes a small efficiency drop and that further increasing the pressure ratio to $PR = 6$ causes a much larger efficiency drop. The reason for this is that the Mach number at the outlet of the cascades becomes higher than unity when $PR \approx 4$ and the supersonic correction factor of the Kacker et al. (1982) loss system, see Eq. (B.4), penalizes the total-to-static isentropic efficiency. In addition, Figure 3.7 also shows that the total-to-static isentropic

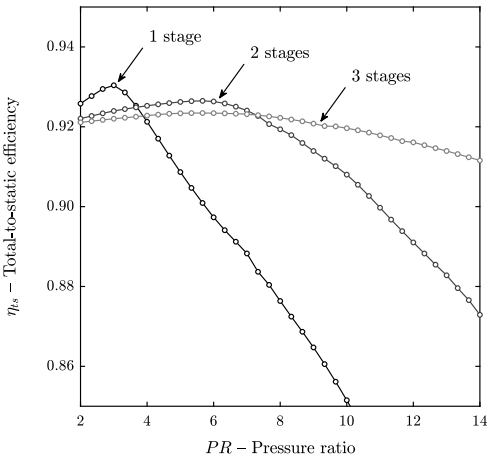

Figure 3.8: Influence of the pressure ratio and number of stages on η_{ts}.

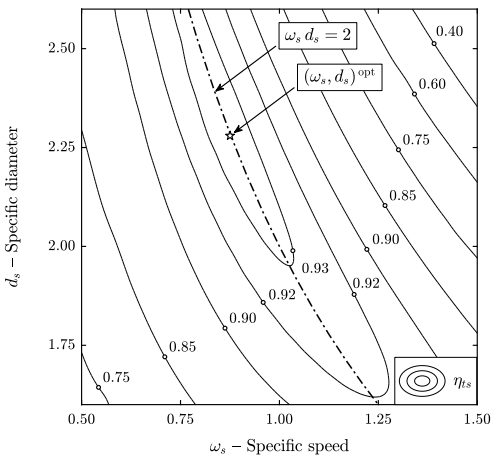

Figure 3.9: Baljé diagram of the reference case and optimal blade speed rule.

efficiency of turbines without diffuser deteriorates rapidly as the pressure ratio is increased. This is because increasing the turbine pressure ratio also increases the flow velocities within the turbine and the amount of kinetic energy that is potentially wasted at the exhaust of the turbine. This highlights the importance of using a diffuser when the pressure ratio is high.

3.6.7 Influence of the number of stages

Figure 3.8 shows the total-to-static efficiency of turbines with one, two, and three stages as a function of the pressure ratio. Again, the pressure ratio was achieved varying the pressure at the inlet of the turbine while keeping the outlet pressure constant. However, in this case, the upper limit of the pressure ratio was increased to $PR = 14$. In can be seen that there is a peak of efficiency and that the performance deteriorates sharply when the pressure ratio increases beyond this point because the flow becomes supersonic and the Mach number correction factor penalizes the profile loss coefficient, see Eq. (B.4). Moreover, the range of pressure ratios for which the isentropic efficiency is high becomes wider as the number of stages increase because the expansion can be distributed over more cascades and the number of optimization variables increases.

3.6.8 Influence of the angular speed and diameter

The results presented in the previous subsections correspond to the optimal angular speed and mean diameter. However, depending on the application, it might not be possible to achieve the point of optimal angular speed and diameter because of technical constraints that were not considered in the analysis such as the frequency of the electrical grid, mechanical stress, or space limitations.

Therefore, the objective of this section is to analyze the impact of using a non-optimal angular speed and diameter on the total-to-static efficiency of the turbine.

Figure 3.9 illustrates the contours of maximum total-to-static isentropic efficiency in the Ω_s–d_s plane for the 5000 kW reference case of Table 3.3. In this diagram, known as Baljé diagram, each point corresponds to a pair of specific speed and diameter, while the rest of the design variables are optimized. It can be observed that there is an optimum combination of specific speed and diameter that maximizes the total-to-static isentropic efficiency. In addition, it can be seen that there is a narrow region where the efficiency is close to its maximum value and that moving away from this region leads to a rapid efficiency drop. Interestingly, the locus of maximum efficiency is approximately given by the hyperbola

$$\frac{1}{2}(\Omega_s\, d_s) = u/\sqrt{\Delta h_s} = 1. \tag{3.51}$$

This suggests that the efficiency penalty away from the point of optimal specific speed and diameter is small if the dimensionless blade velocity $u/\sqrt{\Delta h_s}$ is close to unity. This simple result can be explained from Euler's turbomachinery equation,

$$\Delta h = [u\, v_\theta]_{\,\mathrm{in,R}} - [u\, v_\theta]_{\,\mathrm{out,R}}, \tag{3.52}$$

and the behavior of the solutions that maximize efficiency. On the one hand, close-to-optimal solutions tend to minimize the swirling kinetic energy lost at the exit of the turbine, see Section 3.6.4. As a consequence, the absolute flow angle and tangential velocity at the rotor exit are close to zero ($\alpha_{\mathrm{out}} \to 0$ and $v_{\theta,\,\mathrm{out}} \to 0$). On the other hand, close-to-optimal solutions also tend to have a relative flow angle at the inlet of the rotor that is close to zero ($\beta_{\mathrm{in}} \to 0$) because the Kacker et al. (1982) loss system predicts low profile losses for reaction blades with small relative inlet angles, see Eq. (B.7). As a result, the absolute tangential velocity at the inlet of the rotor approaches the blade velocity ($v_{\theta\,\mathrm{in}} \to u$). Under these conditions, the actual enthalpy change approaches the isentropic enthalpy change ($\Delta h \to \Delta h_s$) and Euler's turbomachinery equation, Eq. (3.52), is reduced to

$$\Delta h_s = u^2 \Rightarrow \frac{u}{\sqrt{\Delta h_s}} = \frac{1}{2}(\Omega_s\, d_s) = 1, \tag{3.53}$$

which corresponds to the hyperbola of maximum efficiencies in the Baljé diagram.

This analysis was valid for single-stage turbines, but it can be extended to turbines with more than one stage. For the case of multistage turbines, the locus of maximum efficiency is approximately given by the hyperbola

$$\frac{1}{2}(\Omega_s\, d_s) = u/\sqrt{\Delta h_s} = \frac{1}{\sqrt{N_{\mathrm{s}}}}, \tag{3.54}$$

where N_{s} is the number of stages. This equation can also be explained from Euler's turbomachinery when $v_{\theta,\,\mathrm{out}} \to 0$ and $v_{\theta,\,\mathrm{in}} \to u$ hold for every stage.

Table 3.5: Comparison of the specific blade speed rule with the optimization results.

Variable	Sample points[a]	Number of stages	Proposed $\frac{1}{2}(\Omega_s\, d_s)^{\text{ref}}$	Optimization[b] $\frac{1}{2}(\Omega_s\, d_s)^{\text{mean}}$	Relative error[c]
$2 \leq PR \leq 14$	37	1	1	0.978	3.22%
	37	2	$1/\sqrt{2}$	0.706	1.56%
	37	3	$1/\sqrt{3}$	0.592	0.90%
$10\,\text{kW} \leq \dot{W}_s \leq 10\,\text{MW}$	23	1	1	1.014	2.05%
	23	2	$1/\sqrt{2}$	0.725	1.42%
	23	3	$1/\sqrt{3}$	0.599	1.29%

[a] Number of points (N) used to sample the PR and $\dot{W}_s$ intervals.

[b] Computed according to $\frac{1}{2N}\sum_{i=1}^{i=N}(\Omega_s\, d_s)_i$.

[c] Computed according to $\frac{1}{(\Omega_s\, d_s)^{\text{ref}}}\sqrt{\frac{1}{N}\sum_{i=1}^{i=N}\left[(\Omega_s\, d_s)_i - (\Omega_s\, d_s)^{\text{ref}}\right]^2}$.

To assess the validity of this result, the optimal blade speed predicted by Eq. (3.54) was compared with the numerical optimization results for different isentropic power outputs ranging between 10 kW and 10 MW and different pressure ratios ranging between 2 and 14, see Table 3.5. It can be observed that location of the point of maximum efficiency predicted by Eq. (3.54) agrees well (relative deviation $< 4\%$) with the optimization results for axial turbines of 1, 2, and 3 stages regardless of the pressure ratio and the isentropic power output.

3.7 Conclusions

A mean-line model and optimization methodology for axial turbines with any number of stages was proposed. The model was formulated in a general way so as to use arbitrary equations of state and empirical loss models and it accounts for the influence of the diffuser using the one-dimensional flow model proposed in Chapter 2. To the knowledge of the author, this is the first time that the coupling of a one-dimensional diffuser model and an axial turbine mean-line model has been documented. The axial turbine preliminary design was formulated as a constrained optimization problem and was solved using a SQP algorithm. Employing a gradient-based algorithm, rather than a gradient-free one, enabled: (1) the optimization of multi-stage design problems with tens of design variables at a low computational cost and (2) the use equality-constraints to integrate the cascade, loss, and diffuser sub-models in a simple way.

The proposed model was validated against experimental data from two test cases documented in the open literature and it was found that the deviation between the data and the model predictions in terms of mass flow rate and power output was less that 1.2% for both cases and that the deviation in total-to-static efficiency was only 0.27 percentage points for the one-stage case and 0.35 points for the two-stage case. It was also concluded that the close match between measured

and predicted efficiencies is within the uncertainty of the efficiencies predicted by the loss model (about ±1.5 percentage points). In addition, the optimization methodology was applied to a case study and a sensitivity analysis was performed to investigate the influence of several design variables on the total-to-static isentropic efficiency, gathering the following conclusions and design guidelines:

- The total-to-static isentropic efficiency increases when the tip clearance gap decreases and this effect is more marked as the isentropic power output of the turbine decreases. This highlights the importance of achieving small tip clearances in small-scale applications.
- The minimum hub-to-tip ratio constraint is always active at the exit of the last stage and the total-to-static isentropic efficiency increases when the value of this constraint is reduced. However, reducing the minimum hub-to-tip ratio also increases the centrifugal and gas bending stresses (Saravanamuttoo et al. 2009). Therefore, the choice of minimum hub-to-tip ratio must be a trade-off between fluid-dynamic and mechanical considerations.
- The total-to-static isentropic efficiency increases with the diffuser area ratio in an asymptotic way, regardless of the value of the diffuser skin friction coefficient, and the numerical optimization results showed that using an area ratio in the range 2.0–2.5 results in 70–80% of the maximum efficiency gain. Using a higher diffuser area ratio will increase the kinetic energy recovery and power output; but it will also increase the turbine footprint, which may be a disadvantage for applications with space limitations.
- The total-to-static isentropic efficiency decreases when the pressure ratio is increased beyond a certain value because the Kacker et al. (1982) loss model predicts a sharp increase of the profile loss coefficient when the flow becomes supersonic. This effect becomes less marked as the number of stages increases because the expansion can be distributed over more cascades. In addition, the total-to-static efficiency of turbines without diffuser deteriorates rapidly when the pressure ratio is increased, highlighting the importance of using a diffuser when the pressure ratio is high.
- The results of the optimization showed that the maximum total-to-static isentropic efficiency is attained when the absolute flow angle at the exit of the last stage is close to zero (i.e., no exit swirl), regardless of the area ratio of the diffuser. This agrees with the conclusions drawn in Chapter 2.
- It was found that the efficiency penalty away from the point of optimal angular speed and diameter (i.e., the peak of the Baljé diagram) is small if the combination of specific speed and diameter is close to the hyperbola given by $\Omega_s \, d_s = 2/\sqrt{N_\mathrm{s}}$. This guideline can be used to select a suitable combination of angular speed and diameter when one of these variables is constrained by technical requirements.

Chapter 4

Unified Geometry Parametrization Method for Turbomachinery Blades

Part of the contents of this chapter appear in:

> R. Agromayor, N. Anand, J.-D. Müller, M. Pini, and L. O. Nord (2021a). "A Unified Geometry Parametrization Method for Turbomachinery Blades". *Computer-Aided Design* 133, pp. 1–16. DOI: https://doi.org/10.1016/j.cad.2020.102987

Abstract

This chapter presents a unified blade parametrization method for axial, radial, and mixed-flow turbomachinery blades. The method is based on conventional engineering design variables and NURBS curves/surfaces and it produces blades that have continuous curvature and rate of change of curvature. In addition, the method is formulated explicitly and it defines the geometry of the blade and flow domain with no trimming or intersection operations. The derivatives of the surface coordinates with respect to the design variables are computed by means of the complex-step method, thereby allowing the integration of the parametrization into gradient-based shape optimization workflows. Furthermore, the method enables the re-parametrization of a blade geometry defined by a cloud of points by solving a two-step optimization problem. The capabilities of the proposed method were demonstrated by replicating the geometry of eight turbomachinery blades in two and three dimensions with an accuracy comparable to the tolerances of current manufacturing technologies.

4.1 Introduction

Driven by ever-increasing requirements in performance, development time, and life-time cost, the aerodynamic design of turbomachinery components is increasingly carried out by means of automated workflows (Verstraete 2019). These workflows integrate geometry parametrization tools, high-fidelity physical models, and numerical optimization to systematically explore the design space. The parametrization of the geometry is an essential aspect of the design chain because it defines the design space where the optimization algorithm can search the optimal solution (Samareh 2001). Ideally, geometry parametrization methods for turbomachinery blades should:

1. Support any type of blade configuration (i.e., axial, radial and mixed-flow) and contain the shapes that achieve the required design objectives.
2. Allow the designer to impose geometric constraints due to mechanical or manufacturing requirements in a simple way.
3. Provide the sensitivity of the shape with respect to the design variables to enable gradient-based shape optimization (Banović et al. 2018).
4. Use conventional engineering design variables with an intuitive geometrical meaning (e.g., chord, metal angles, thickness distribution).
5. Produce smooth geometries with continuous curvature (i.e., G^2 continuity) and continuous rate of change of curvature to avoid velocity spikes that may lead to flow separation (Korakianitis et al. 1993b).
6. Retain compatibility with computer-aided design (CAD) software for further analysis, geometry manipulation, and manufacturing.
7. Be computationally efficient in terms of execution time and memory usage.

Shape parametrization methods can be classified as deformation and constructive methods. Deformation methods are suited to modify an existing geometry (e.g., a mesh or a CAD model) and are widely used in the context of aerodynamic shape optimization. These methods include mesh point displacement (Wu et al. 2005; Walther et al. 2012), CAD model control point displacement (Pini et al. 2014; Xu et al. 2015), superposition of shape functions such as Hicks-Henne bumps (Luo et al. 2013; Walther et al. 2015c), space morphing based on free-form deformation (Vitale et al. 2017; John et al. 2017), or space morphing based on radial basis function interpolation (Tang et al. 2018; Gagliardi et al. 2019). Although these methods offer rich design spaces and lend themselves for differentiation, they are not well-suited to impose geometric constraints (e.g., minimum trailing edge thickness), making it difficult to obtain feasible shapes out of the optimization process. As a notable exception, the NSPCC method proposed by Xu et al. (2015) allows the designer to impose geometric and continuity constraints by evaluating

Table 4.1: Survey of constructive parametrization methods for turbomachinery blades.

Reference	Basis function	Configuration	Cont.[a]	Grad.[b]
Dunham (1974)	Monomial	2D profile	G^1	n.a.
Crouse et al. (1981)	Monomial	3D axial	G^1	n.a
Ye (1984)	Monomial	2D profile	G^2	n.a.
Pritchard (1985)	Monomial	2D profile	G^1	n.a.
Korakianitis (1993a)	Monomial	2D profile	G^2	n.a.
Aungier (2006b)	Monomial	2D profile	G^2	n.a.
Engeli et al. (1974)	Bézier	3D axial	G^2	n.a.
Casey (1983)	Bézier	3D general	G^2	n.a.
Goel et al. (1996)	Bézier	3D axial	G^2	n.a.
Giannakoglou (1999)	Bézier	2D profile	G^1	n.a.
Trigg et al. (1999)	Bézier	2D profile	G^1	n.a.
Pierret et al. (1999)	Bézier	2D profile	G^{2*}	n.a.
Pierret et al. (2000)	Bézier	3D axial	G^{2*}	n.a
Oyama et al. (2004)	B-spline	3D axial	G^1	n.a.
Huppertz et al. (2007)	B-spline	2D profile	G^1	n.a
Verstraete (2010)	B-spline	3D axial	G^{2*}	n.a.
Verstraete (2010)	B-spline	3D general	G^{2*}	n.a.
Siddappaji et al. (2012)	B-spline	3D general	G^2	n.a.
Torreguitart et al. (2018)	B-spline	2D profile	G^{2*}	AD
Mykhaskiv et al. (2018)	B-spline	3D axial	G^2	AD
Miller IV et al. (1996)	NURBS	3D general	G^2	n.a.
Gräsel et al. (2004)	NURBS	3D general	G^2	n.a.
Koini et al. (2009)	NURBS	3D general	G^2	n.a.
Müller et al. (2017)	NURBS	3D general	G^{2*}	CS
Anand et al. (2018)	NURBS	2D profile	G^2	FD
Present work	NURBS	2D/3D general	G^2	CS

[a] Slope continuity (G^1) or curvature continuity (G^2).

[b] Method used to compute the gradient of the shape w.r.t the design variables: not available (n.a.), Finite Differences (FD), Complex-Step (CS), or Algorithmic Differentiation (AD).

[*] The parametrization satisfies curvature continuity everywhere except at the trailing edge.

these constraints at a finite number of test-points and using a projected gradient optimization method to maintain feasibility. In contrast, constructive methods can be used to generate the geometry of a new blade from scratch, or possibly using design variable values obtained during the preliminary design phase. In addition, these methods are suited to impose geometric constraints in a natural and non-intrusive way. Due to these strengths, constructive methods are widely used for turbomachinery blade parametrization and a large number of such methods have been developed over the years. Table 4.1 provides a comprehensive review of constructive blade parametrizations up to the present day.

The early constructive parametrization methods used circular arcs and polynomials in monomial-basis form (i.e., polynomials in the form $\sum_{i=0}^{n} a_i x^i$) to define the geometry of the blades, see Table 4.1. This type of parametrization gained significant popularity among industry practitioners, but it has severe limitations arising from the use of a monomial basis. Specifically: (1) the polynomial coefficients convey little insight about the shape of the blade, (2) ensuring geometric continuity at the connecting points between segments requires the solution of a linear system that may not have a unique solution, (3) the surface of the blade is prone to undesirable inflection points, and (4) the resulting shapes are not compatible with the geometric representation used by modern CAD systems.

To overcome these shortcomings, several authors proposed new constructive parametrizations based on Bézier , B-spline, and NURBS curves and surfaces, see Table 4.1. These mathematical functions have become the standard to represent geometric objects in modern CAD packages due to their favorable mathematical properties and the availability of a wide range of algorithms to define and manipulate curves and surfaces (Piegl et al. 2012; Farin 2001). Currently, most of the constructive CAD-based parametrizations for turbomachinery blades are not suitable for automated design workflows. This is because they do not offer a robust way to handle intersection operations (Taylor 2015) or do not provide sensitivity information required by gradient-based optimization algorithms methods (Banović et al. 2018). In addition, to optimize an existing blade, it is essential to find a parametric representation of the baseline geometry, available, for instance, in the form of a set of points in the Cartesian space. Solving this reverse engineering problem by trial and error is doable for simple cases (Torreguitart et al. 2018), but it becomes impractical for complex blade geometries. Despite the practical relevance of this problem, a robust and automatic method to re-parametrize the geometry of a blade defined by a scattered set of points is still lacking.

In view of the limitations of the existing methods, this work presents a general constructive parametrization method for axial, radial and mixed-flow turbomachinery blades. The method exploits conventional engineering design variables (blade thickness, chord, metal angles, etc.) and NURBS curves and surfaces to define the blade geometry. The method is formulated explicitly and it defines the geometry of the blade and flow domain with no intersection operations. In addition, the blades satisfy G^2 continuity by construction and the sensitivity of the coordinates with respect to the design variables is computed with machine accuracy by means of the complex-step method. Furthermore, the method is capable to re-parametrize the geometry of an existing blade defined by scattered point coordinates. This problem, often referred to as blade matching, is formulated as a two-step optimization problem and it allows one to find the design variable values that best approximates the prescribed geometry in a systematic way. The flexibility and accuracy of the proposed method is demonstrated by replicating the geometry of eight turbomachinery blades in two and three dimensions.

4.2 Background on NURBS curves and surfaces

The origin of Non-Uniform Rational Basis Spline (NURBS) curves and surfaces can be traced back to the research efforts in computer-aided geometric design in the late 60s and early 70s (Piegl 1991). Since then, NURBS have been universally used for geometrical modeling thanks to their intuitive geometrical interpretation, favorable mathematical properties, and efficient computational algorithms. A NURBS curve, see Figure 4.1a, is a parametric curve defined by

$$\mathbf{C}(u) = \frac{\sum_{i=0}^{n} N_{i,p}(u)\, w_i\, \mathbf{P}_i}{\sum_{i=0}^{n} N_{i,p}(u)\, w_i}, \quad \text{with} \quad 0 \le u \le 1, \tag{4.1}$$

where p is the degree of the curve, the coefficients $\mathbf{P}_i$ and w_i are the coordinates and weights of the $n+1$ control points, and $N_{i,p}$ are B-spline basis functions defined on the non-decreasing, clamped knot vector

$$U = [\underbrace{0, \ldots, 0}_{p+1}, \underbrace{u_{p+1}, \ldots, u_n}_{n-p}, \underbrace{1, \ldots, 1}_{p+1}] \in \mathbb{R}^{r+1}, \quad \text{with} \quad r = n + p + 1. \tag{4.2}$$

The B-spline basis functions are given by the recursive relation

$$N_{i,0}(u) = \begin{cases} 1, & \text{if} \quad u_i \le u < u_{i+1} \\ 0, & \text{otherwise} \end{cases} \tag{4.3}$$

$$N_{i,p}(u) = \frac{u - u_i}{u_{i+p} - u_i} N_{i,p-1}(u) + \frac{u_{i+p+1} - u}{u_{i+p+1} - u_{i+1}} N_{i+1,p-1}(u). \tag{4.4}$$

Similarly, a NURBS surface, see Figure 4.1b, is a parametric surface defined by

$$\mathbf{S}(u,v) = \frac{\sum_{i=0}^{n}\sum_{j=0}^{m} N_{i,p}(u) N_{j,q}(v)\, w_{i,j}\, \mathbf{P}_{i,j}}{\sum_{i=0}^{n}\sum_{j=0}^{m} N_{i,p}(u) N_{j,p}(v)\, w_{i,j}}, \quad \text{with} \quad 0 \le u,\, v \le 1, \tag{4.5}$$

where p and q are the degrees of the surface in the u- and v-directions, the coefficients $\mathbf{P}_{i,j}$ and $w_{i,j}$ are bidirectional nets containing the coordinates and weights of the $(n+1) \times (m+1)$ control points, and $N_{i,p}(u)N_{j,q}(v)$ are the product of univariate B-spline basis functions defined on the clamped knot vectors

$$U = [\underbrace{0, \ldots, 0}_{p+1}, \underbrace{u_{p+1}, \ldots, u_n}_{n-p}, \underbrace{1, \ldots, 1}_{p+1}] \in \mathbb{R}^{r+1}, \quad \text{with} \quad r = n + p + 1 \tag{4.6}$$

$$V = [\underbrace{0, \ldots, 0}_{q+1}, \underbrace{v_{q+1}, \ldots, v_n}_{m-q}, \underbrace{1, \ldots, 1}_{q+1}] \in \mathbb{R}^{s+1}, \quad \text{with} \quad s = m + q + 1. \tag{4.7}$$

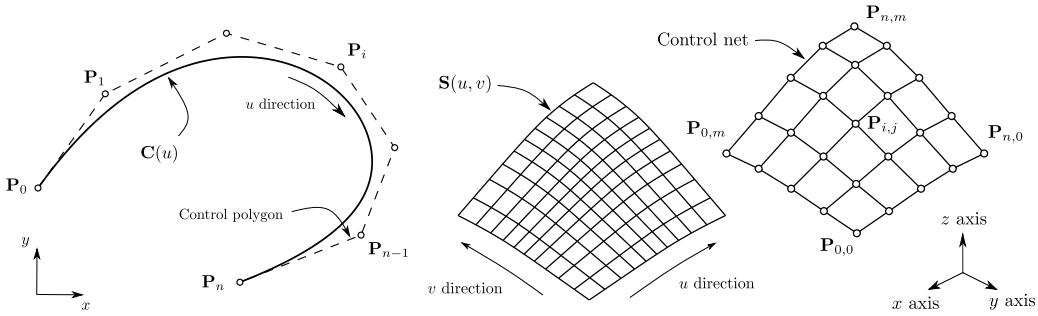

(a) NURBS curve construction. **(b)** NURBS surface construction.

Figure 4.1: Construction of a NURBS curve (left) and surface (right). Note that the NURBS curve interpolates its endpoints and it is tangent to the control polygon at its ends. The control net of the NURBS surface interpolates its four corner points and it was represented at an offset distance in the x-direction for clarity.

The u-direction basis functions $N_{i,p}(u)$ are given by Eqs. (4.3) and (4.4), whereas the v-direction basis functions $N_{i,q}(v)$ are defined in an analogous way replacing the variable u by v and the indices i and p by j and q, respectively.

NURBS curves and surfaces have the following properties that make them particularly suited for geometric modeling (Piegl et al. 2012, pp. 117–139):

- *Affine invariance.* It is possible to apply affine transformations such as rotations, displacements, and scalings to NURBS curves and surfaces by applying the transformation to their control points.
- *Convex hull.* NURBS curves and surfaces are within the convex hull of their control points. When the control points are contained in a certain region of space, this property guarantees that the curve or surface will not blow up arbitrarily far away from this region.
- *Endpoint interpolation* NURBS curves and surfaces coincide with the polytope formed by the control points at the endpoints.
- *Endpoint tangency.* NURBS curves and surfaces are tangent to the polytope formed by the control points at the endpoints.
- *Generalization.* Bézier curves and surfaces are a special case of NURBS when $p = n$ and $q = m$. In addition, B-spline curves and surfaces are an special case of NURBS when all the weights have the same value.

Most of the curves and surfaces used in the proposed blade parametrization method are B-splines. However, the parametrization is formulated in a general way using NURBS so that the designer can include the control point weights as design variables to gain more control over the resulting geometry if desired.

4.3 Blade parametrization in two dimensions

The proposed two-dimensional blade parametrization is based on typical blade design variables which are listed in Table 4.2. The geometry of the blade is generated by defining a camber line and subsequently imposing on it two independent thickness distributions in a way that ensures G^2 continuity at the junction between the upper and the lower sides.

The camber line $\mathbf{C}^{\mathrm{c}}(u)$ is a cubic B-spline curve defined by four control points as shown in Figure 4.2a. The coordinates of the control points are given by

$$\mathbf{P}_0^{\mathrm{c}} = \begin{bmatrix} x_{\mathrm{in}} \\ y_{\mathrm{in}} \end{bmatrix} \tag{4.8}$$

$$\mathbf{P}_1^{\mathrm{c}} = \mathbf{P}_0^{\mathrm{c}} + d_{\mathrm{in}} \begin{bmatrix} c\,\cos(\theta_{\mathrm{in}}) \\ c\,\sin(\theta_{\mathrm{in}}) \end{bmatrix} \tag{4.9}$$

$$\mathbf{P}_2^{\mathrm{c}} = \mathbf{P}_3^{\mathrm{c}} - d_{\mathrm{out}} \begin{bmatrix} c\,\cos(\theta_{\mathrm{out}}) \\ c\,\sin(\theta_{\mathrm{out}}) \end{bmatrix} \tag{4.10}$$

$$\mathbf{P}_3^{\mathrm{c}} = \mathbf{P}_0^{\mathrm{c}} + \begin{bmatrix} c\,\cos(\xi) \\ c\,\sin(\xi) \end{bmatrix}, \tag{4.11}$$

where ξ is the stagger angle, $c_{\mathrm{ax}} = c\,\cos(\xi)$ is the axial chord length, θ_{in} and θ_{out} are the inlet and outlet metal angles, and d_{in} and d_{out} are the inlet and outlet tangent proportions. This construction of the camber line ensures that the blade has the specified axial chord length and that the slope at the leading and trailing edges conforms with the input metal angles thanks to the endpoint tangency property of B-spline curves (Piegl et al. 2012, p. 97). In cases where more control over the shape of the camber line is required, the control point weights could also be adjusted.

Table 4.2: Two-dimensional design variables. Each variable is provided as a scalar value, except for the upper and lower thickness, which are given as sets of control points.

Variable name	Symbol
Spacing	s
Leading edge abscissa and ordinate	$x_{\mathrm{in}}, y_{\mathrm{in}}$
Axial chord length	c_{ax}
Stagger angle	ξ
Inlet and exit metal angles	θ_{in}, θ_{out}
Inlet and exit tangent proportions	d_{in}, d_{out}
Inlet and exit radii of curvature	r_{in}, r_{out}
Upper and lower thickness distributions	t^{u}, t^{l}

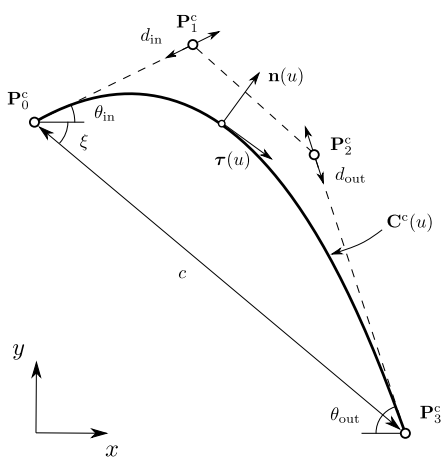

(a) Camber line construction.

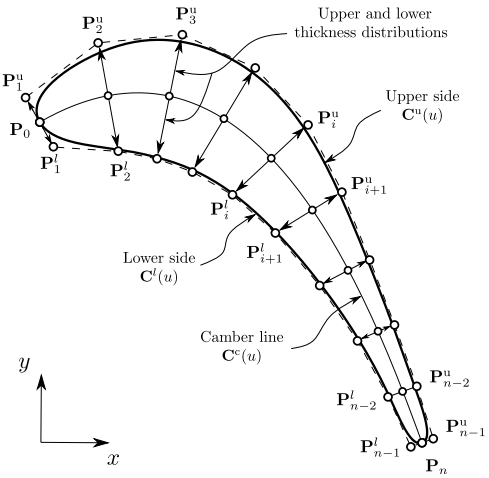

(b) Blade profile construction.

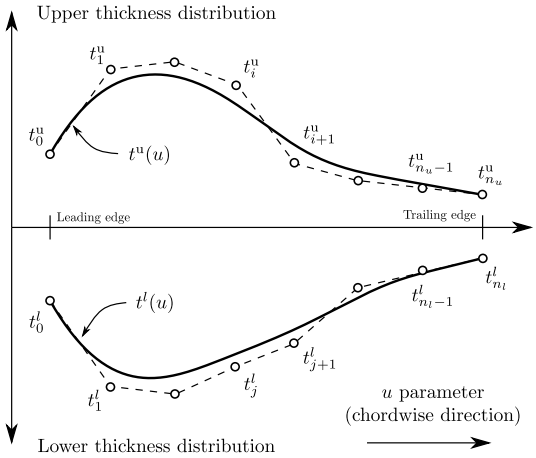

(c) Thickness distribution.

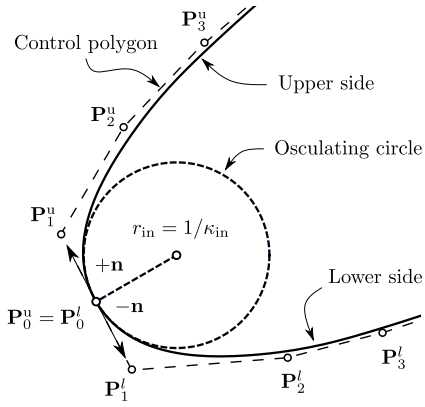

(d) Leading edge construction.

Figure 4.2: Construction of the blade geometry in two dimensions. The upper and lower thickness distributions (bottom-left) are imposed in the direction normal to the camber line (top-left) to compute the location of the blade control points (top-right). The second and second-to-last control points are computed using a different relation to impose the radii of curvature at the leading and trailing edges and to ensure that the blade profile satisfies G^2 continuity (bottom-right).

The upper and lower sides of the blade, $\mathbf{C}^l(u)$ and $\mathbf{C}^{\mathrm{u}}(u)$, are defined as B-spline curves of degree four as it is the lowest degree that guarantees continuous rate of change of curvature at the spline knots. The coordinates of the control points $\{\mathbf{P}_i^l\}$ and $\{\mathbf{P}_i^{\mathrm{u}}\}$, see Figure 4.2b, are computed according to

$$\mathbf{P}_i^l = \begin{cases} \mathbf{C}^{\mathrm{c}}(\hat{u}_i), & \text{for } i = 0 \\ \mathbf{C}^{\mathrm{c}}(\hat{u}_i) - \mathbf{n}(\hat{u}_i) \cdot f(r_{\mathrm{in}}), & \text{for } i = 1 \\ \mathbf{C}^{\mathrm{c}}(\hat{u}_i) - \mathbf{n}(\hat{u}_i) \cdot t^l(\hat{u}_i), & \text{for } i = 2, \ldots, n-2 \\ \mathbf{C}^{\mathrm{c}}(\hat{u}_i) - \mathbf{n}(\hat{u}_i) \cdot g(r_{\mathrm{out}}), & \text{for } i = n-1 \\ \mathbf{C}^{\mathrm{c}}(\hat{u}_i), & \text{for } i = n \end{cases} \tag{4.12}$$

and

$$\mathbf{P}_i^{\mathrm{u}} = \begin{cases} \mathbf{C}^{\mathrm{c}}(\hat{u}_i), & \text{for } i = 0 \\ \mathbf{C}^{\mathrm{c}}(\hat{u}_i) + \mathbf{n}(\hat{u}_i) \cdot f(r_{\mathrm{in}}), & \text{for } i = 1 \\ \mathbf{C}^{\mathrm{c}}(\hat{u}_i) + \mathbf{n}(\hat{u}_i) \cdot t^{\mathrm{u}}(\hat{u}_i), & \text{for } i = 2, \ldots, n-2 \\ \mathbf{C}^{\mathrm{c}}(\hat{u}_i) + \mathbf{n}(\hat{u}_i) \cdot g(r_{\mathrm{out}}), & \text{for } i = n-1 \\ \mathbf{C}^{\mathrm{c}}(\hat{u}_i), & \text{for } i = n \end{cases} \tag{4.13}$$

where the sampling values $\hat{u}_i$ in the above equations are given by

$$\hat{u}_i = \begin{cases} 0, & \text{for } i = 0 \\ \frac{i-1}{n-2}, & \text{for } i = 1, \ldots, n-1 \\ 1, & \text{for } i = n. \end{cases} \tag{4.14}$$

Note that the first and last control points of the upper and lower sides coincide with the endpoints of the camber line.

The upper and lower thickness distributions, $t^{\mathrm{u}}(u)$ and $t^l(u)$, are given by B-spline polynomials of degree three with an arbitrary number of control points, $\{t_i^{\mathrm{u}}\}$ and $\{t_j^l\}$, specified by the designer, see Figure 4.2c. In addition, the unitary vectors normal to the camber line $\mathbf{n}(u)$ are computed from the unitary tangent vector $\boldsymbol{\tau}(u)$ according to

$$\boldsymbol{n}(u) = \begin{bmatrix} n_x \\ n_y \end{bmatrix} = \begin{bmatrix} -\tau_y \\ \tau_x \end{bmatrix}, \qquad \text{with} \qquad \boldsymbol{\tau}(u) = \frac{\dot{\mathbf{C}}^{\mathrm{c}}(u)}{\|\dot{\mathbf{C}}^{\mathrm{c}}(u)\|}, \tag{4.15}$$

where $\dot{\mathbf{C}}^{\mathrm{c}}(u)$ is computed using analytical derivative formulas for B-spline curves (Piegl et al. 2012, pp. 91–100).

The functions $f(r)$ and $g(r)$ appearing in Eqs. (4.12) and (4.13) are used to impose the radii of curvature r_{in} and r_{out} at the leading and trailing edges, ensuring that the parametrization satisfies G^2 continuity by construction, see

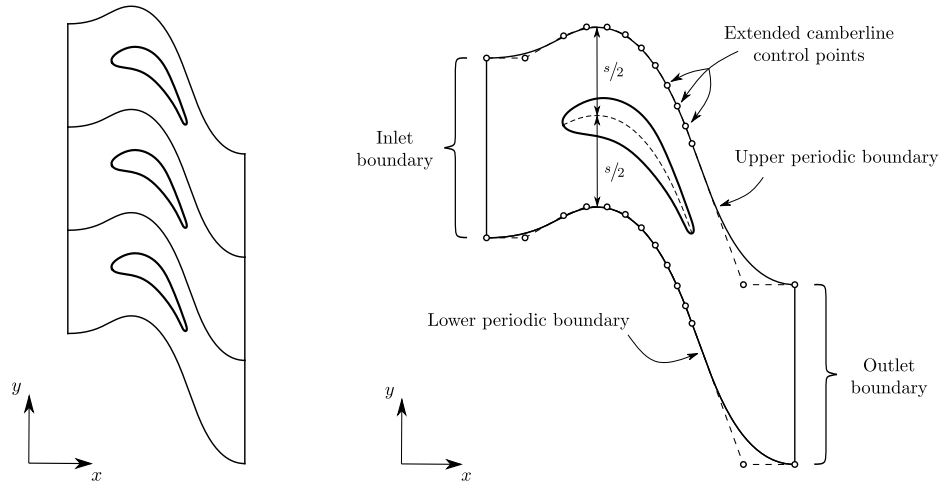

(a) Cascade of blades. **(b)** Construction of the flow domain.

Figure 4.3: Construction of the flow domain in two dimensions. The fluid-dynamic performance of the blade cascade (left) can be evaluated analyzing the flow around a single blade thanks to the periodicity of the problem. The flow domain is defined by four boundaries: inflow, outflow, lower periodic, and upper periodic (right).

Figure 4.2d. This feature is important in the context of aerodynamic design of turbomachinery blades because a sudden change in curvature could cause a spike in the surface pressure distribution or even a local separation bubble (Korakianitis et al. 1993b). The functions $f(r)$ and $g(r)$ are based on the end point curvature formulas for NURBS curves and their derivation is detailed in Appendix C. Once that the upper and lower sides are defined, they can be combined into a single B-spline curve $\mathbf{C}^{\mathrm{b}}(u) = \mathbf{C}^{l} \cup \mathbf{C}^{\mathrm{u}}$ that represents the entire blade profile.

When performing the assessment of the fluid-dynamic performance of the blades via computational fluid dynamics, it is necessary to define the geometry of the flow domain around the blade. For the majority of turbomachinery flow problems one can resort to the periodicity of the flow to reduce the size of the computational domain. In such case, it is sufficient to describe the flow domain around a single blade, which is characterized by the inflow, outflow, and periodic boundaries, as illustrated in Figure 4.3. The periodic boundaries are given by two cubic B-spline curves defined by extending the camber line while keeping zero slope at the inlet and outlet. The periodic boundaries are located at an offset distance of half of the blade spacing, s, with respect to the blade camber line. Finally, the inflow and outflow boundaries are defined as two straight lines connecting the upper and lower periodic boundaries.

The proposed parametrization produces blade profiles that have continuous curvature and rate of change of curvature, therefore reducing the possibility of flow separation (Korakianitis et al. 1993b). This contrasts with most of the

two-dimensional methods described in the open literature, which produce blades with discontinuous curvature (Dunham 1974; Pritchard 1985; Giannakoglou 1999; Trigg et al. 1999; Huppertz et al. 2007), or discontinuous rate of change of curvature (Ye 1984; Aungier 2006b; Korakianitis 1993a; Pierret et al. 1999). As notable exceptions, the second and third methods proposed by Korakianitis (Korakianitis 1993a), see also (Korakianitis 1993b; Korakianitis et al. 1993a), produce blade profiles with continuous curvature and slope-of-curvature. However, the methods proposed by Korakianitis: (1) involve the solution of systems of equations, (2) are not compatible with CAD representations, and (3) are not easily extended from two to three dimensions. In addition, to the knowledge of the author, this is the first time that the endpoint curvature formulas for NURBS curves were used to impose the curvature of turbomachinery blades at the leading and trailing edges. This differs from what is documented in previous publications (Verstraete 2010; Anand et al. 2018; Mykhaskiv et al. 2018), where all the reported methods used the endpoint curvature formulas for Bézier curves to ensure G^2 continuity, with the limitation that the curvature is not imposed exactly when the blades are described by B-spline or NURBS curves.

Application

The flexibility of the proposed two-dimensional blade parametrization method is demonstrated by reconstructing the four blade profiles illustrated in Figure 4.4. Each blade profile was defined using 6 control points for each thickness distribution, resulting in a total of 22 design variables. The LS89 (Arts et al. 1990; Arts et al. 1992) and T106A (Stadtmüller et al. 2001) are representative of high-pressure and low-pressure axial gas turbine blade rows, respectively. In addition, the SIRT profile is typical of a supersonic impulse turbine rotor (Anand et al. 2020) and the STD10 profile is representative of an axial compressor blade derived from a NACA 0006 airfoil profile (Fransson et al. 1993). It can be observed that the parametrization method spans a wide range of shapes and produces blades with smooth curvature variations, which is essential to avoid spikes and dips in the surface-pressure distribution. The numerical values of the design variables used to produce the blade profiles were computed from a set of scattered point coordinates using the method described in Section 4.6.

4.4 Blade parametrization in three dimensions

The proposed three-dimensional parametrization is formulated as an extension of the two-dimensional one and uses the design variables listed in Table 4.3. Similar to the two-dimensional case, the parametrization starts by defining a camber surface and subsequently imposing two independent thickness distributions perpendicular to the camber surface in a way that ensures G^2 continuity.

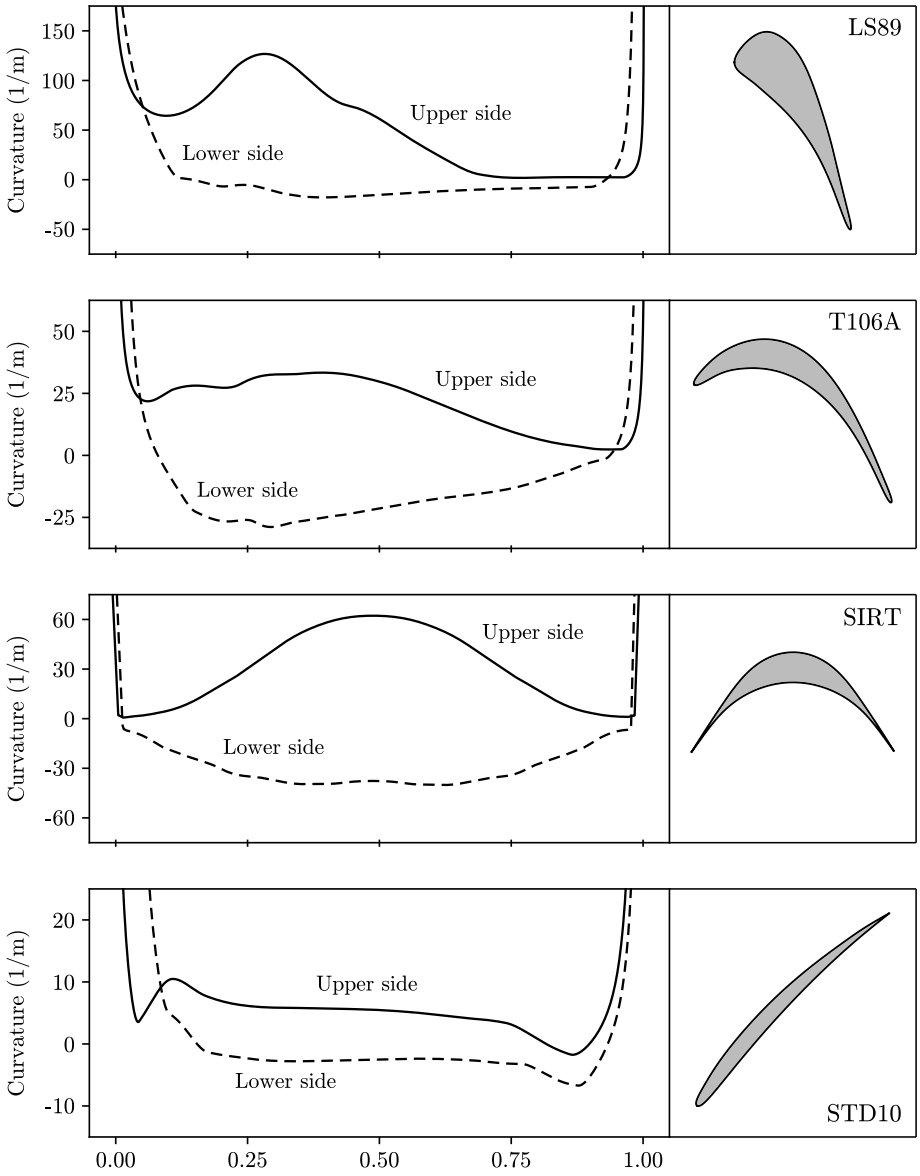

Figure 4.4: Geometry and curvature distribution of the LS89 (Arts et al. 1990; Arts et al. 1992), T106A (Stadtmüller et al. 2001), SIRT (Anand et al. 2020), and STD10 (Fransson et al. 1993) blade profiles. The abscissa of the curvature distribution is the normalized axial length.

Table 4.3: Three-dimensional design variables. Each design variable is provided as a set of control points, except for the number of blades that is a single integer value.

Variable name	Symbol
Number of blades	N_b
Leading edge control points	x_1, z_1
Hub edge control points	x_2, z_2
Trailing edge control points	x_3, z_3
Shroud edge control points	x_4, z_4
Leading edge abscissa*	y_in
Stagger angle*	ξ
Inlet and exit metal angles*	θ_in, θ_out
Inlet and exit tangent proportions*	d_in, d_out
Inlet and exit radii of curvature*	r_in, r_in
Upper and lower thickness distributions	t^u, t^l

* Law of evolution in the spanwise direction.

The camber surface is determined by the shape of the blade in the meridional plane and the spanwise variation of the design variables. The shape of the blade in the meridional plane is described by four curves, namely, leading edge, trailing edge, hub, and shroud, as illustrated in Figure 4.5. Each of these boundaries is defined as a B-spline curve of, at most, degree three with an arbitrary number of control points see Figure 4.6. In contrast with other parametrization methods that are limited to axial turbomachines (Crouse et al. 1981; Engeli et al. 1974; Goel et al. 1996; Pierret et al. 2000; Oyama et al. 2004), the proposed method is suited to describe any kind of turbomachinery configuration, including axial, radial, and mixed-flow machines. The number of control points required to describe the shape of the blade in the meridional plane depends on the complexity of the geometry. For instance, it is possible to define a purely axial turbine using only four control points, but it may be necessary to use 10–20 control points to describe the shape of a mixed-flow machine such as a centrifugal compressor.

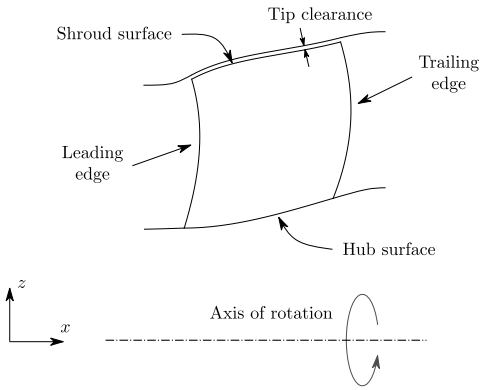

Figure 4.5: Geometry of the blade, hub, and shroud surfaces in the meridional plane.

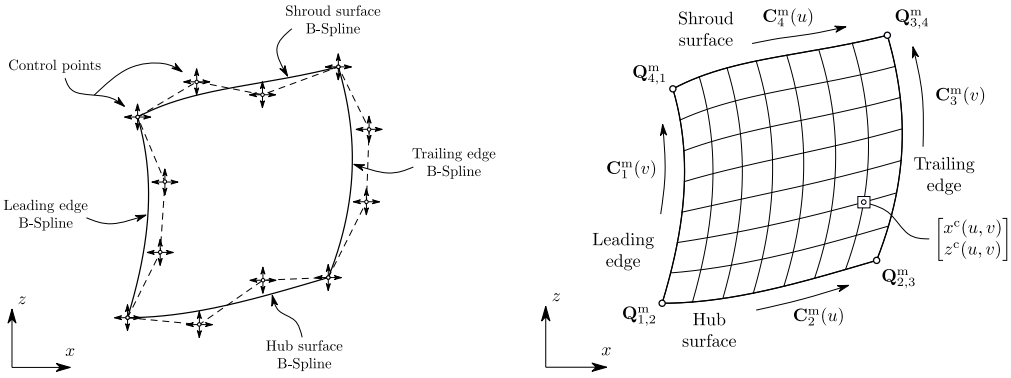

Figure 4.6: Construction of the four B-splines that define the shape of the blade in the meridional plane (left) and point evaluation by transfinite interpolation (right). Note that the corner control points of the B-splines curves are shared.

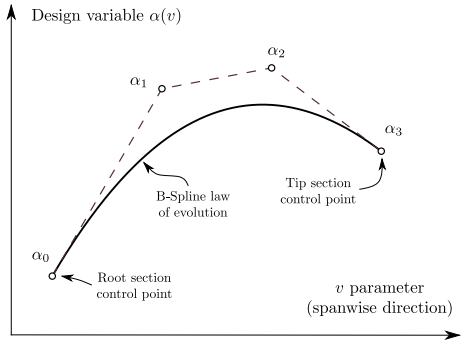

Figure 4.7: Evolution of a design variable along the blade spanwise direction.

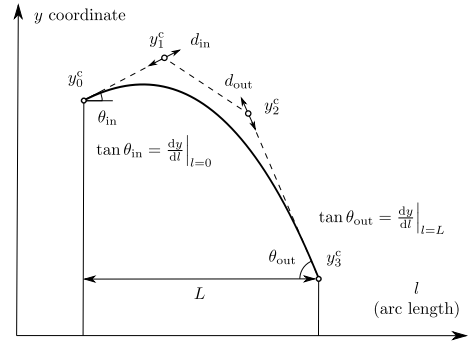

Figure 4.8: B-spline defining the tangential coordinates of the camber line.

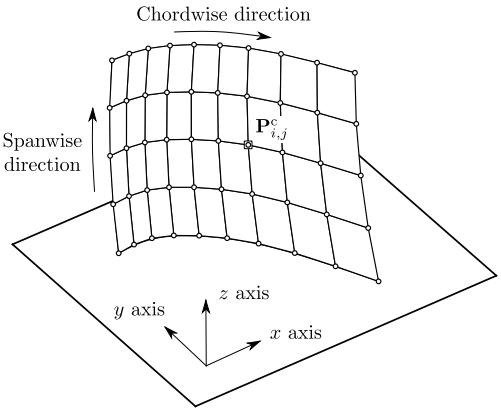

Figure 4.9: Camber surface control points.

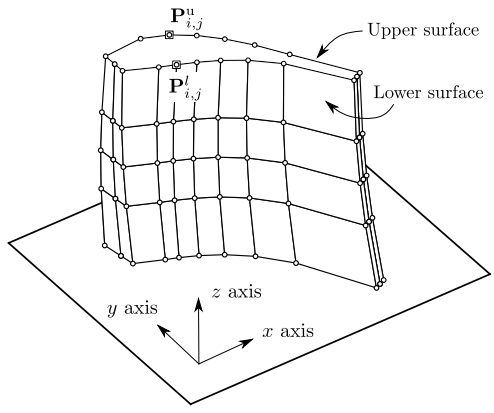

Figure 4.10: Blade surface control points.

The spanwise variation of the some design variables $\alpha(v)$, see Table 4.3 footnote, is defined as law of evolution through a B-spline of, at most, degree three with an arbitrary number of control points as illustrated in Figure 4.7. The number of control points used for each design variable is specified by the designer, and its selection is based on the complexity of the blade geometry. As an example, it is sufficient to use a single constant value to define a prismatic blade, but it might be necessary to use 3–6 control points to describe the geometry of a blade with large twist from the root to the tip.

As illustrated in Figure 4.9, the camber surface $\mathbf{S}^{\mathrm{c}}(u, v)$ is defined as a biquartic B-spline surface with control points $\mathbf{P}^{\mathrm{c}}_{i,j} = [x^{\mathrm{c}}_{i,j},\, y^{\mathrm{c}}_{i,j},\, z^{\mathrm{c}}_{i,j}]$. The coordinates of the control points are computed using the shape of the blade in the meridional plane and the spanwise evolution of the design variables. More specifically, the (x, z) coordinates of the camber surface control points are computed by transfinite interpolation (Gordon et al. 1973) of the four curves that define the meridional plane, see Figure 4.6, and are given by

$$\begin{aligned}\begin{bmatrix} x^{\mathrm{c}}(u,v) \\ z^{\mathrm{c}}(u,v) \end{bmatrix} &= (1-u)\cdot\mathbf{C}^{\mathrm{m}}_1(v) + u\cdot\mathbf{C}^{\mathrm{m}}_3(v) + (1-v)\cdot\mathbf{C}^{\mathrm{m}}_2(u) + v\cdot\mathbf{C}^{\mathrm{m}}_4(u) \\ &\quad - \left[(1-v)(1-u)\cdot\mathbf{Q}^{\mathrm{m}}_{1,2} + v\,u\cdot\mathbf{Q}^{\mathrm{m}}_{3,4} + v\,(1-u)\cdot\mathbf{Q}^{\mathrm{m}}_{4,1} + (1-v)\,u\cdot\mathbf{Q}^{\mathrm{m}}_{2,3}\right],\end{aligned} \tag{4.16}$$

In addition, the y coordinates of the camber surface control points at each spanwise location v are given by a third order cubic B-spline curve $y^{\mathrm{c}}(u, v)$ with control points $\{y^{\mathrm{c}}_0,\, y^{\mathrm{c}}_1,\, y^{\mathrm{c}}_2,\, y^{\mathrm{c}}_3\}$ that are computed according to

$$y^{\mathrm{c}}_0(v) = y_{\mathrm{in}} \tag{4.17}$$

$$y^{\mathrm{c}}_1(v) = y^{\mathrm{c}}_0 + d_{\mathrm{in}}\cdot L\tan\theta_{\mathrm{in}} \tag{4.18}$$

$$y^{\mathrm{c}}_2(v) = y^{\mathrm{c}}_3 - d_{\mathrm{out}}\cdot L\tan\theta_{\mathrm{out}} \tag{4.19}$$

$$y^{\mathrm{c}}_3(v) = y_{\mathrm{in}} + L\tan\xi \tag{4.20}$$

This formulation ensures that the metal angles at the leading and trailing edges, θ_{in} and θ_{out}, are respected, as illustrated in Figure 4.8. The arc length of the blade meridional plane at each span location $L(v)$ is defined as

$$L(v) = \int_{u=0}^{u=1} \sqrt{\left(\frac{\partial x^{\mathrm{c}}}{\partial u}\right)^2 + \left(\frac{\partial z^{\mathrm{c}}}{\partial u}\right)^2}\,\mathrm{d}u \tag{4.21}$$

and it is computed using 8^{th} order Gaussian quadrature (Golub et al. 1969), which provides a satisfactory trade-off between computational speed and accuracy.

The upper and lower sides of the blade, $\mathbf{S}^{l}(u, v)$ and $\mathbf{S}^{\mathrm{u}}(u, v)$, are defined as B-spline surfaces of degree four as it is the lowest degree that guarantees continuous rate of change of curvature at the spline knots. The coordinates of the control

points $\{\mathbf{P}^l_{i,j}\}$ and $\{\mathbf{P}^{\mathrm{u}}_{i,j}\}$, see Figure 4.10, are computed according to

$$\mathbf{P}^l_{i,j} = \begin{cases} \mathbf{S}^{\mathrm{c}}(\hat{u}_i, \hat{v}_j), & \text{for } i = 0 \\ \mathbf{S}^{\mathrm{c}}(\hat{u}_i, \hat{v}_j) - \mathbf{n}(\hat{u}_i, \hat{v}_j) \cdot f(r_{\mathrm{in}}(\hat{v}_j)), & \text{for } i = 1 \\ \mathbf{S}^{\mathrm{c}}(\hat{u}_i, \hat{v}_j) - \mathbf{n}(\hat{u}_i, \hat{v}_j) \cdot t^l(\hat{u}_i, \hat{v}_j), & \text{for } i = 2, \ldots, n-2 \\ \mathbf{S}^{\mathrm{c}}(\hat{u}_i, \hat{v}_j) - \mathbf{n}(\hat{u}_i, \hat{v}_j) \cdot g(r_{\mathrm{out}}(\hat{v}_j)), & \text{for } i = n-1 \\ \mathbf{S}^{\mathrm{c}}(\hat{u}_i, \hat{v}_j), & \text{for } i = n \end{cases} \tag{4.22}$$

and

$$\mathbf{P}^{\mathrm{u}}_{i,j} = \begin{cases} \mathbf{S}^{\mathrm{c}}(\hat{u}_i, \hat{v}_j), & \text{for } i = 0 \\ \mathbf{S}^{\mathrm{c}}(\hat{u}_i, \hat{v}_j) + \mathbf{n}(\hat{u}_i, \hat{v}_j) \cdot f(r_{\mathrm{in}}(\hat{v}_j)), & \text{for } i = 1 \\ \mathbf{S}^{\mathrm{c}}(\hat{u}_i, \hat{v}_j) + \mathbf{n}(\hat{u}_i, \hat{v}_j) \cdot t^{\mathrm{u}}(\hat{u}_i, \hat{v}_j), & \text{for } i = 2, \ldots, n-2 \\ \mathbf{S}^{\mathrm{c}}(\hat{u}_i, \hat{v}_j) + \mathbf{n}(\hat{u}_i, \hat{v}_j) \cdot g(r_{\mathrm{out}}(\hat{v}_j)), & \text{for } i = n-1 \\ \mathbf{S}^{\mathrm{c}}(\hat{u}_i, \hat{v}_j), & \text{for } i = n \end{cases} \tag{4.23}$$

where the sampling values $(\hat{u}_i, \hat{v}_j)$ are given by

$$\hat{u}_i = \begin{cases} 0, & \text{for } i = 0 \\ \frac{i-1}{n-2}, & \text{for } i = 1, \ldots, n-1 \\ 1, & \text{for } i = n \end{cases} \quad \text{and} \quad \hat{v}_j = \frac{j}{m}, \quad \text{for } j = 0, \ldots, m. \tag{4.24}$$

The upper and lower thickness distributions, $t^{\mathrm{u}}(u, v)$ and $t^l(u, v)$, are given by bi-variate B-spline polynomials of degree three with an arbitrary number of control points $\{t^{\mathrm{u}}_{i,j}\}$ and $\{t^l_{i,j}\}$, specified by the designer. In addition, the unitary vectors normal to the camber surface $\mathbf{n}(u, v)$ are computed from the tangent vectors $\boldsymbol{\tau}_u$ and $\boldsymbol{\tau}_v$ according to

$$\mathbf{n} = -\frac{\boldsymbol{\tau}_u \times \boldsymbol{\tau}_v}{\|\boldsymbol{\tau}_u \times \boldsymbol{\tau}_v\|}, \quad \text{with} \quad \boldsymbol{\tau}_u = \frac{\partial \mathbf{S}^{\mathrm{c}}}{\partial u} \quad \text{and} \quad \boldsymbol{\tau}_v = \frac{\partial \mathbf{S}^{\mathrm{c}}}{\partial v}. \tag{4.25}$$

The partial derivatives of the camber surface with respect to u and v are computed analytically using B-spline derivative formulas (Piegl et al. 2012, pp. 110–115).

The functions $f(r)$ and $g(r)$ appearing in Eqs. (4.22) and (4.23) are used to impose the radius of curvature at the leading and trailing edges, ensuring that the upper and lower surfaces of the blade are smoothly joined with G^2 continuity. The derivation of the functions $f(r)$ and $g(r)$ is detailed in Appendix C. Once that the upper and lower sides are defined, they can combined into a single B-spline surface $\mathbf{S}^{\mathrm{b}}(u, v) = \mathbf{S}^l \cup \mathbf{S}^{\mathrm{u}}$ that represents the entire blade.

The parametrization just described is suitable to model linear cascades, which are commonly used for wind tunnel tests. However, in actual turbomachines, the

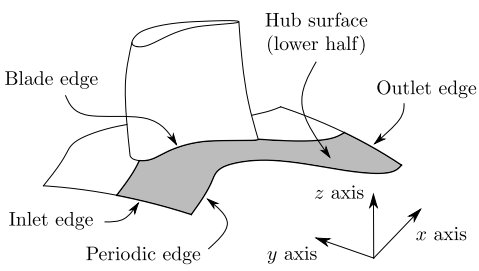

(a) Hub surface as a Coons patch.

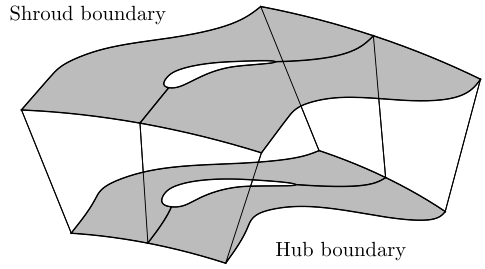

(b) Hub and shroud boundaries.

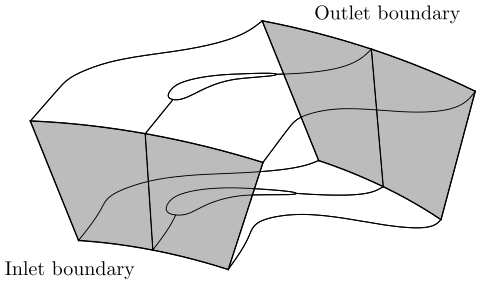

(c) Inlet and outlet boundaries.

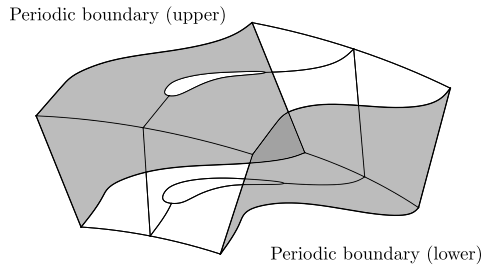

(d) Periodic boundaries.

Figure 4.11: Construction of the blade flow domain in three dimensions.

blades are arranged in an axisymmetric way forming an annular cascade. In order to achieve this, the linear blade configuration is transformed into an annular one with the mapping $\mathcal{H} : \mathbb{R}^3 \to \mathbb{R}^3$ given by

$$\mathbf{P}^{\mathrm{b}}_{\mathrm{annular}} = \mathcal{H}\{\mathbf{P}^{\mathrm{b}}_{\mathrm{linear}}\} = \mathcal{H}\{[x,\, y,\, z]\} = \left[x,\, z \cdot \sin\left(y/z\right),\, z \cdot \cos\left(y/z\right)\right]. \quad (4.26)$$

The rationale behind this transformation is to associate the Cartesian coordinates (x, y, z) of a linear cascade with the cylindrical coordinates $(x, r\theta, r)$ of an annular cascade and then convert from cylindrical to Cartesian coordinates.

The flow domain around a blade is characterized by the hub, shroud, inlet, outlet, and periodic boundaries as illustrated in Figure 4.11. The hub boundary consists of two surfaces that conform with the blade at its root, see Figure 4.11a. Each of these surfaces is defined as a Coons patch (Piegl et al. 2012, pp. 456–507) that is characterized by four edges. The blade edge is given by a B-spline curve formed by extending the lower side of the blade into the upstream and downstream directions following the slope of the camber line at the leading and trailing edges, respectively. The periodic edge is formed by extending the camber line in a similar way and rotating the resulting B-spline about the x-axis through an angle $\theta_{\mathrm{b}}/2$, where $\theta_{\mathrm{b}} = 2\pi/N_{\mathrm{b}}$. Finally, the inlet and outlet edges are defined as NURBS circular arcs that connect the periodic edge with the blade edge. The shroud surface, see Figure 4.11b, is defined in an analogous way and, for the case of

rotor blades, it is possible specify a clearance between the tip of the blade and the shroud. Once that the hub and shroud surfaces are defined, it is straightforward to construct the inlet, outlet and periodic surfaces as ruled surfaces (Piegl et al. 2012, pp. 337–340) that connect the limits of the hub and shroud surfaces as illustrated in Figures 4.11c and 4.11d. Note that the parametrization of the blade and flow domain is watertight by construction and it does not rely on intersection and trimming operations. This contrasts with other blade parametrization methods (Verstraete 2010; Siddappaji et al. 2012; Mykhaskiv et al. 2018; Miller IV et al. 1996; Gräsel et al. 2004; Koini et al. 2009; Müller et al. 2017) that rely on intersection operations between the blade surface and the hub/shroud surfaces and produce trimmed NURBS patches that would have to be specially treated during a shape optimization workflow (Taylor 2015; Xu et al. 2017).

Application

The flexibility of the proposed three-dimensional blade parametrization method is demonstrated by reconstructing the geometry of the four blades illustrated in Figures 4.12 to 4.15. The first example, Figure 4.12, is a prismatic axial turbine stator blade (Stephan et al. 2001). The meridional plane is defined by 4 control points and the design variables are constant in the spanwise direction (i.e., 1 control point), resulting in a total of 26 design variables. Figure 4.13 illustrates the geometry of an axial compressor rotor blade (Pierzga et al. 1985; Pierzga et al. 1989). The blade is highly twisted due to the change in blade speed from root to tip and it was necessary to use 4 control points to describe the spanwise variation of the design variables, resulting in a total of 111 design variables. Similarly Figure 4.14 illustrates the geometry of an aircraft propeller blade (van Arnhem et al. 2020). In this case it was necessary to use 5 control points to describe the twist of the blades, resulting in 113 design variables. Finally, Figure 4.15 shows the geometry of a mixed-flow turbine (radial-inflow, axial-outflow) (Jones 1996; Keep et al. 2017). The complex shape of the blade in the meridional plane was described using 14 control points and the spanwise variation of the blade sections was described using 3 control points per design variable, giving rise to 86 design variables. The numerical values of the design variables used to produce the blades were computed from a set of scattered point coordinates using the method described in Section 4.6.

4.5 Sensitivity computation and verification

One simple way to approximate partial derivatives of a function is by using a finite difference approximation such as forward finite differences given as

$$\frac{\partial F}{\partial \alpha} = \frac{F(\alpha + h) - F(\alpha)}{h} + \mathcal{O}(h), \tag{4.27}$$

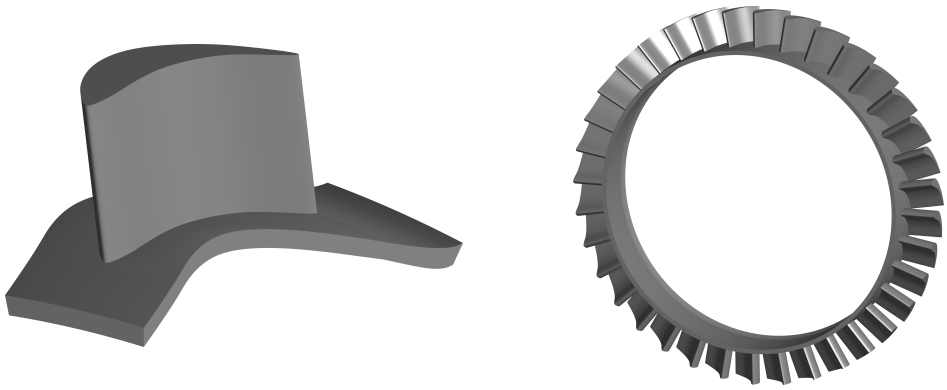

Figure 4.12: Geometry of the AACHEN stator blade (Stephan et al. 2001).

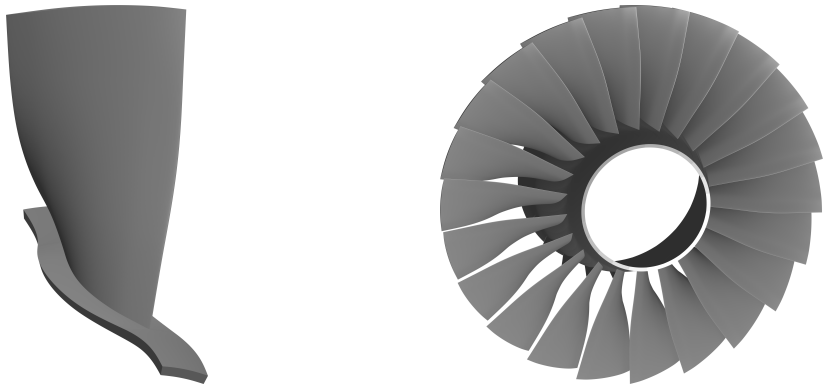

Figure 4.13: Geometry of the NASA R67 blade (Pierzga et al. 1985; Pierzga et al. 1989).

Figure 4.14: Geometry of the XPROP propeller blade (van Arnhem et al. 2020).

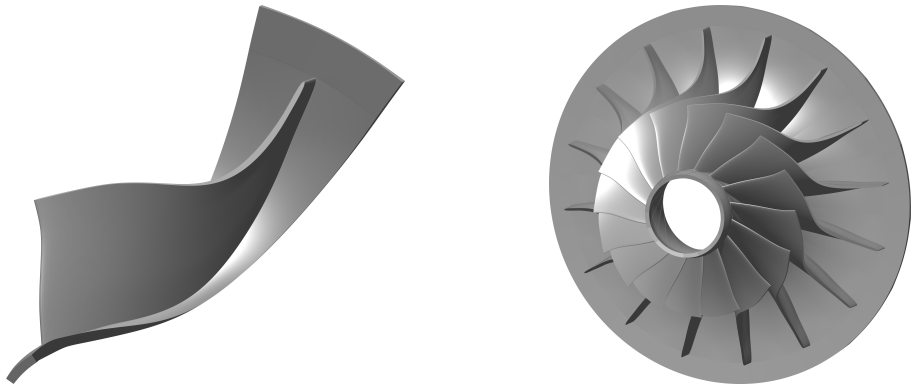

Figure 4.15: Geometry of the APU rotor blade (Jones 1996; Keep et al. 2017).

or central finite differences given as

$$\frac{\partial F}{\partial \alpha} = \frac{F(\alpha + h) - F(\alpha - h)}{2h} + \mathcal{O}(h^2), \tag{4.28}$$

where $F(\alpha)$ can be identified with $\mathbf{C}^{\mathrm{b}}(u, \alpha)$ in two dimensions or $\mathbf{S}^{\mathrm{b}}(u, v, \alpha)$ in three dimensions and h is the step size used for finite difference computation. Finite difference approximations are susceptible to cancellation error when the step size is small because of the subtraction of very similar numbers in the numerator (Press et al. 2007, pp 229–232). As a result, one is faced with the dilemma of selecting a small step size that minimizes the truncation error but does not lead to a large cancellation error.

An alternative method that avoids the occurrence of cancellation error is the complex-step method (Lyness et al. 1967; Squire et al. 1998; Martins et al. 2003). This method uses a complex argument to compute the first derivative of a real-valued function. Indeed, the Taylor series expansion of $F(\alpha)$ in the imaginary axis gives

$$F(\alpha + ih) = F(\alpha) + ih\,\frac{\partial F}{\partial \alpha} - \frac{h^2}{2!}\,\frac{\partial^2 F}{\partial \alpha^2} - \frac{ih^3}{3!}\,\frac{\partial^3 F}{\partial \alpha^3} + \mathcal{O}(h^4). \tag{4.29}$$

Re-arranging the imaginary part of the equation gives

$$\frac{\partial F}{\partial \alpha} = \frac{\operatorname{Im}\big(F(\alpha + i\,h)\big)}{h} + \mathcal{O}(h^2), \tag{4.30}$$

which is the complex-step method formula. In contrast to finite difference approximations, this method *is not* susceptible to subtraction error, therefore allowing one to compute first derivatives accurate to the round-off precision of floating point arithmetic by using an arbitrarily small step size.

Algorithmic Differentiation (AD) provides yet another alternative to compute the derivatives of a function with machine precision (Griewank et al. 2008). AD

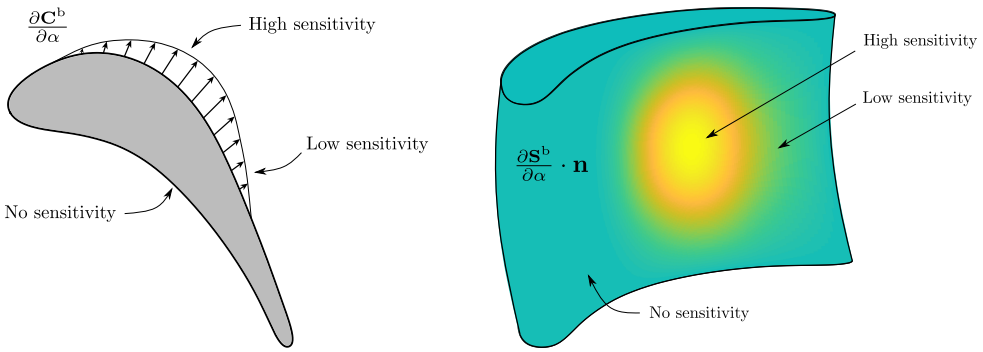

Figure 4.16: Sensitivity of the blade geometry with respect to a thickness distribution control point. The sensitivity of the 2D case (left) is represented as a quiver plot. The sensitivity of the 3D case (right) is represented as a colormap of the scalar field given by the dot product of the sensitivity and the unitary vector normal to the blade surface.

is a set of techniques to numerically evaluate the derivatives of a function specified as a computer program by applying the chain rule of differentiation to each arithmetic operation of the program. This method offers more functionality and computational efficiency (first and higher order derivatives, forward and reverse modes) than the complex-step method (first derivatives and forward mode only), but it is also more difficult to implement (Martins et al. 2003).

In this work, the complex-step method was adopted to compute the sensitivity of the surface coordinates with respect to the design variables due to its accuracy, simplicity, and ease of implementation. Figure 4.16 illustrates the sensitivity of the blade surface with respect to one thickness distribution control point in two and three dimensions. It can be observed that the sensitivity of the blade changes from point to point and that there may be regions where the sensitivity is zero.

To verify the correctness of the sensitivity computation, a convergence study comparing the sensitivities computed using forward finite differences, central finite differences, and the complex-step method was carried out for the NASA rotor 67 test case (Pierzga et al. 1985; Pierzga et al. 1989). The geometry of the NASA rotor 67, see Figure 4.13, was sampled with 10000 uniformly spaced points within the box $(u, v) \in [0, 1] \times [0, 1]$ and the sensitivity was computed with respect to one design variable (the stagger angle at the hub section) for different step sizes in the interval $h \in [10^{-1}, 10^{-15}]$. The error of the sensitivity computation was defined as the mean-square-root deviation between the exact and the estimated sensitivities. The exact sensitivity was assumed to be the sensitivity computed with the complex-step method using an step size $h = 2.22 \cdot 10^{-16}$, which corresponds to the machine precision of double-precision arithmetic (Press et al. 2007, pp 8–11).

The results of the convergence study are shown in Figure 4.17. For the case of the complex-step method (line labeled as CS), reducing the step size decreases the error until the trend flattens to a value close to the machine precision. In

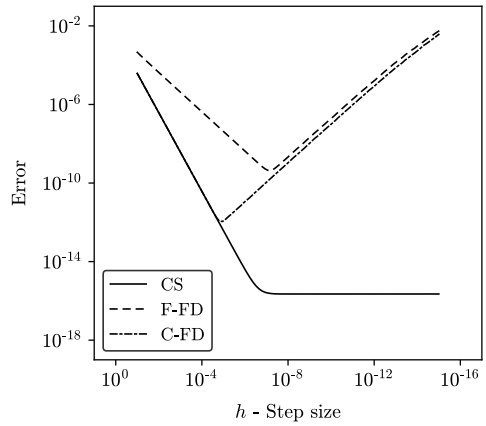

Figure 4.17: Two-norm error of the NASA rotor 67 root-section-stagger-angle sensitivity computation as a function of the step size when using the complex-step method (CS), forward finite differences (F-FD), and central finite differences (C-FD).

contrast, the forward finite difference (line labeled as F-FD) and central finite difference (line labeled as C-FD) errors decrease as the step size decreases down to a minimum value and then increase because the cancellation error becomes more prominent than the truncation error. In addition, it can be observed that the complex-step method and the central finite differences agree in interval when the truncation error dominates ($h \lesssim 10^{-6}$). This verifies that the implementation of the complex-step method is correct. Although not shown here for brevity, the author performed similar convergence studies for all the design variables of each of the test cases summarized in Table 4.4 and obtained similar results.

4.6 Blade matching methodology

In order to optimize the performance of an existing turbomachinery blade, it is essential to find a parametric representation of its geometry, which is usually available as a set of scattered points coordinates $\mathbf{Q}_i$, with $i = 1, 2, ..., N_Q$ obtained from a mesh, from sampling a CAD model, or from laser scan measurements. This section proposes a systematic method to find the set of design variables that best approximates the shape of a prescribed blade geometry. The method can be divided in two phases: (1) the point projection phase and (2) the geometry update phase. It is assumed that the designer starts from an initial guess for the design variables that roughly approximates the existing geometry, see Figure 4.18a.

In the point projection phase, the goal is to find the parametric values u_i, in two dimensions, or (u_i, v_i) in three dimensions, that minimize the distance with respect to each prescribed point $\mathbf{Q}_i$. The two-dimensional point projection

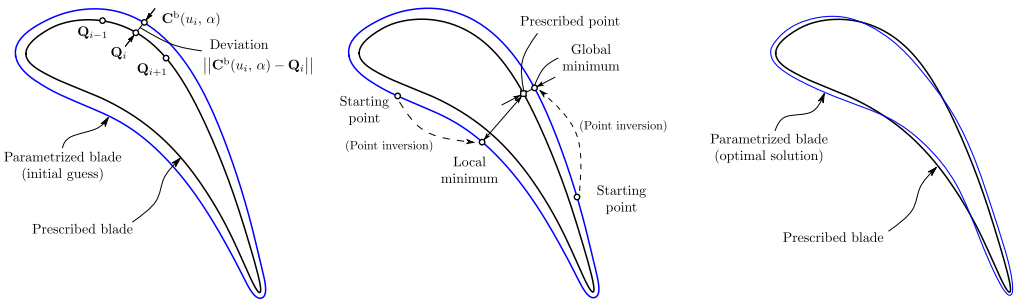

(a) Initial guess. **(b)** Point projection phase. **(c)** Geometry update phase.

Figure 4.18: Illustration of the blade matching problem in two dimensions. The deviation between the prescribed and parametrized blades after the geometry update phase was exaggerated to improve visibility.

problem can be formulated as

$$\begin{aligned} &\underset{u\in\mathbb{R}}{\text{minimize}} \quad J(u) = \frac{1}{2}\left\|\mathbf{C}^{\mathrm{b}}(u) - \mathbf{Q}_i\right\|^2, \\ &\text{subject to} \quad 0 \leq u \leq 1, \end{aligned} \tag{4.31}$$

where J is the distance between the prescribed and the parametrized point. The gradient of the objective function J can be computed analytically as

$$\nabla J = \frac{\partial J}{\partial u} = \left(\mathbf{C}^{\mathrm{b}}(u) - \mathbf{Q}_i\right) \cdot \frac{\partial \mathbf{C}^{\mathrm{b}}}{\partial u}. \tag{4.32}$$

Similarly, in three dimensions, the point projection problem is given by

$$\begin{aligned} &\underset{(u,v)\in\mathbb{R}^2}{\text{minimize}} \quad J(u,v) = \frac{1}{2}\left\|\mathbf{S}^{\mathrm{b}}(u,v) - \mathbf{Q}_i\right\|^2, \\ &\text{subject to} \quad 0 \leq u, v \leq 1 \end{aligned} \tag{4.33}$$

and the gradient of the objective function can be computed according to

$$\nabla J = \begin{bmatrix} \dfrac{\partial J}{\partial u} \\ \dfrac{\partial J}{\partial v} \end{bmatrix} = \begin{bmatrix} \left(\mathbf{S}^{\mathrm{b}}(u,v) - \mathbf{Q}_i\right) \cdot \dfrac{\partial \mathbf{S}^{\mathrm{b}}}{\partial u} \\ \left(\mathbf{S}^{\mathrm{b}}(u,v) - \mathbf{Q}_i\right) \cdot \dfrac{\partial \mathbf{S}^{\mathrm{b}}}{\partial v} \end{bmatrix}. \tag{4.34}$$

Note that the geometry of the parametrized blade *does not change* during the point projection phase. One common pitfall when solving the point projection problem is that the optimization may converge to a local minimum as illustrated in Figure 4.18b. This limitation can be overcome by solving the point projection problem from different starting points and then selecting the global minimum among the various solutions or by sampling the parametrized blade at several

locations and then starting the optimization from the test point that is closest to $\mathbf{Q}_i$ (Piegl et al. 2012, pp. 229-234).

In the geometry update phase, the goal is to find the set of design variables α that minimizes the deviation between the parametrized and the prescribed blades. This can be formulated as an unconstrained minimization problem where the objective function is the sum of the distances between each projected point and the corresponding prescribed point. This optimization problem is given by

$$\underset{\alpha \in \mathbb{R}^{\alpha}}{\text{minimize}} \quad J(\alpha) = \sum_{i=1}^{N_Q} \|\mathbf{C}^{\text{b}}(u_i,\, \alpha) - \mathbf{Q}_i\|^2 \tag{4.35}$$

in two dimensions and by

$$\underset{\alpha \in \mathbb{R}^{\alpha}}{\text{minimize}} \quad J(\alpha) = \sum_{i=1}^{N_Q} \|\mathbf{S}^{\text{b}}(u_i,\, v_i,\, \alpha) - \mathbf{Q}_i\|^2 \tag{4.36}$$

in three dimensions, where α are the design variables listed in Tables 4.2 and 4.3, respectively. The gradient of these objective functions is computed using the complex-step method as described in Section 4.5. In contrast to the point projection phase, the geometry of the parametrized blade *does change* until the deviation with respect to the prescribed geometry is minimized, see Figure 4.18c. In order to improve the matching of $(u,\, v)$ and α, the point projection and geometry update problems can be solved alternatively until the relative deviation between the prescribed and the parametrized blades does not change more than a small tolerance, e.g. 10^{-8}. In this work, the optimization problems posed by the point projection and geometry update phases were solved using the limited-memory BFGS algorithm proposed by Nocedal (1980); Liu et al. (1989).

To demonstrate its flexibility and accuracy, the blade matching method was applied to replicate the geometry of eight exemplary blades. The set of test cases is summarized in Table 4.4 and it was conceived to cover a wide range of turbomachinery blade geometries in two (Figure 4.4) and three dimensions (Figures 4.12 to 4.15). The results of the blade matching in terms of absolute and relative error are summarized in Table 4.4. It can be seen that, the relative matching error was below 0.38% for all cases and the highest absolute error is 0.127 mm for the XPROP test case. This mismatch is of the same order of magnitude as the tolerances used to manufacture axial gas turbine blade profiles, which are about 0.05 mm (Bunker 2009). In addition, the deviation could be further reduced by increasing the number of control points used to parametrize the blade. This is illustrated in the convergence study shown in Figure 4.19, where the number of control points used to describe the thickness distribution of the T106A case is increased from 3 to 10 points. Specifically, the mean deviation is reduced from 0.057 mm to 0.031 mm when the number of control points is increased from 6 to 10. Furthermore, Figure 4.19 also shows the curvature distribution for the T106A

Table 4.4: Summary of the test cases and matching results.

Name	Reference	Dim.	DVs	Error abs.[a] (mm)	Error rel.[b] (%)
LS89	Arts et al. (1990); Arts et al. (1992)	2D	22	0.047	0.067
T106A	Stadtmüller et al. (2001)	2D	22	0.057	0.046
SITR	Anand et al. (2020)	2D	22	0.067	0.087
STD10	Fransson et al. (1993)	2D	22	0.020	0.020
AACHEN	Stephan et al. (2001)	3D	26	0.060	0.084
NASA R67	Pierzga et al. (1985); Pierzga et al. (1989)	3D	99	0.107	0.107
XPROP	van Arnhem et al. (2020)	3D	113	0.127	0.377
APU	Jones (1996); Keep et al. (2017)	3D	86	0.057	0.080

[a] Defined as the arithmetic mean deviation between the prescribed and the matched blades.
[b] Defined as the quotient of the mean error and the arc length of blade camber line (the camber line of the hub section is used in three-dimensional cases).

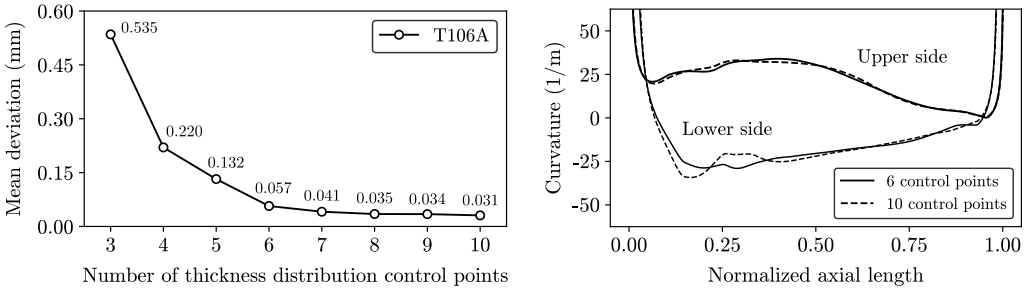

Figure 4.19: Re-parametrization error as a function of the number of thickness distribution control points for the T106A test case (left). Curvature distribution of the T106A profile when the re-parametrization is performed using 6 and 10 control points (right).

blade described using 6 and 10 thickness distribution control points. It can be observed that the curvature variation is smooth for both cases and that increasing the number of control points does not introduce high-frequency undulations that would deteriorate the fluid dynamic performance of the blade. These results indicate that the parametrization and matching methodologies proposed in this work enable the replication of a wide range of geometries with an accuracy comparable to the typical tolerances of modern manufacturing techniques and that the re-parametrization accuracy can be increased by refining the design space.

4.7 Conclusions

A general constructive parametrization method for turbomachinery blades was presented. The method uses typical turbomachinery design variables and NURBS curves and surfaces to produce blade geometries with continuous curvature and rate of change of curvature. In contrast with existing methods, the parametrization of the blade and flow domain were formulated in an explicit way that avoids intersection and trimming operations and the sensitivity of the geometry is computed by means of the complex-step method, allowing the integration of the parametrization into automated, gradient-based shape optimization workflows.

Furthermore, the method enables the systematic re-parametrization of a baseline blade geometry defined by a set of scattered point coordinates by solving a two-step optimization problem. To demonstrate its capabilities, the re-parametrization method was applied to replicate the geometry of eight exemplary blades, showing that the proposed parametrization can reproduce the geometry of a wide range of turbomachinery blades with an accuracy comparable to the tolerances of current manufacturing techniques for axial gas turbine profiles.

Chapter 5

Aerodynamic Design Method for Turbomachinery Blades Operating in NICFD Conditions

Part of the contents of this chapter appear in:

> R. Agromayor, N. Anand, M. Pini, and L. O. Nord (2021b). "Multi-row Adjoint-based Optimization of NICFD Turbomachinery Using a CAD-based Parametrization". *To be submitted to: Journal of Engineering for Gas Turbines and Power*

Abstract

This chapter presents a gradient-based shape optimization framework for the aerodynamic design of turbomachinery blades operating under non-ideal thermodynamic conditions. The proposed design system supports the simultaneous optimization of multiple blade rows in two dimensions and it integrates the CAD-based parametrization presented in Chapter 4 with a real-gas turbomachinery flow solver and its discrete adjoint counterpart. In order to demonstrate the capabilities of the tools developed in this thesis, the preliminary design method presented in Chapter 3 and the aerodynamic design method described herein were applied to carry out the design optimization of a single-stage axial turbine using isobutane (R600a) as working fluid. Notably, the aerodynamic optimization respected the minimum thickness constraint at the trailing edge of the stator and rotor blades and reduced the entropy generation within the turbine by 36%, relative to the baseline, which corresponds to a total-to-total isentropic efficiency increase of about 4 percentage points. The analysis of the flow field revealed that the performance improvement was achieved due to the reduction of the intensity of the wakes downstream of the blades and the elimination of a shock-induced separation bubble at the suction side of the stator cascade.

5.1 Introduction

Automated design workflows are emerging as a powerful tool for the aerodynamic design of turbomachinery components. These workflows integrate geometry parametrization tools, high-fidelity physical models, and numerical optimization techniques to explore large design spaces in a systematic way (Van den Braembussche 2008). This, in turn, allows the designer to obtain higher performance gains and shorten the development time with respect to traditional design workflows based on trial-and-error (Denton 2010). Moreover, automated design workflows offer a great potential for unconventional applications, in which a large body of previous design experience does not yet exist, including ORC turbines (Colonna et al. 2008; Pasquale et al. 2013; Persico et al. 2019), sCO_2 turbines and compressors (Baltadjiev et al. 2015; Romei et al. 2020), and refrigeration and heat-pump turbo-compressors (Mounier et al. 2018; Meroni et al. 2018b).

The optimization methods used within automated workflows can be classified according to the use of derivative information as gradient-free or gradient-based. Gradient-free methods only require the evaluation of the cost function values and they are widely used due to their robustness, simple integration with black-box models, and ability to handle non-smooth or even discontinuous optimization problems (Audet et al. 2017). Over the years, gradient-free methods have been successfully applied for the aerodynamic design of turbines (Mueller et al. 2012; De Servi et al. 2019; Persico et al. 2019) and compressors (Oyama et al. 2004; Samad et al. 2008). However, these methods require a large number of function evaluations to converge to the optimum solution, especially when the number of design variables is large. This, in turn, results in high execution times that hinder the application of gradient-free methods to complex industrial design problems (Verstraete 2019). Gradient-based methods, on the other hand, are particularly suited to solve differentiable problems involving a large number of design variables (Nocedal et al. 2006). These methods require not only the values, but also the gradients of the cost functions to determine the search direction, and they usually converge to a local optimum in a comparatively low number of iterations. Consequently, the aerodynamic design of turbomachinery may benefit significantly from the development of differentiated design chains and the adoption of efficient gradient-based optimization methods (Verstraete 2019).

In the context of fluid-dynamic shape optimization, the adjoint method has emerged as a very efficient way to evaluate the gradient of a cost function with respect to an arbitrary number of design variables (Giles et al. 2000; Peter et al. 2010). The application of this method to external aerodynamics was pioneered by Pironneau (1974) and later revisited and extended by Jameson and coworkers, who used it to optimize airfoils, wings, and complete aircraft configurations (Jameson 1988; Jameson 1995; Reuther et al. 1996). By contrast, the application of the adjoint method to turbomachinery design has lagged behind, arguably, due to the additional complexity involved in the derivation of the adjoint equations and

Table 5.1: Survey of publications using the continuous or discrete adjoint method for the aerodynamic design optimization of turbomachinery blades.

Reference	Dim.	Flow	Adjoint[a]	CEV	Fluid prop.	Blade rows	Param.[b]
Yang et al. (2003)	2D	Euler	Cont.	–	Ideal	Single	Mesh
Wu et al. (2003)	2D	Euler	Cont.	–	Ideal	Single	Mesh
Wu et al. (2005)	3D	RANS	Cont.	Yes	Ideal	Single	Mesh
Arens et al. (2005)	2D	Euler	Cont.	–	Ideal	Single	CAD*
Li et al. (2006)	2D	Euler	Cont.	–	Ideal	Single	CAD*
Papadimitriou et al. (2006)	3D	RANS	Cont.	Yes	Ideal	Single	CAD*
Papadimitriou et al. (2006)	3D	RANS	Cont.	Yes	Ideal	Single	CAD*
Duta et al. (2007)	3D	RANS	Discr.	No	Ideal	Single	CAD
Corral et al. (2008)	3D	RANS	Discr.	Yes	Ideal	Single	Mesh
Wang et al. (2010a)	3D	RANS	Cont.	Yes	Ideal	Multi	Mesh
Wang et al. (2010b)	3D	RANS	Cont.	Yes	Ideal	Multi	Mesh
Luo et al. (2010)	3D	Euler	Cont.	–	Ideal	Single	Mesh
Walther et al. (2012)	2D	RANS	Discr.	Yes	Ideal	Multi	Mesh
Luo et al. (2013)	3D	RANS	Cont.	Yes	Ideal	Single	Mesh
Walther et al. (2014)	3D	RANS	Discr.	Yes	Ideal	Multi	Mesh
Pini et al. (2014)	2D	Euler	Discr.	–	Non-ideal	Single	CAD*
Xu et al. (2015)	3D	RANS	Discr.	No	Ideal	Multi	CAD*
Montanelli et al. (2015)	2D	RANS	Discr.	Yes	Ideal	Single	CAD
Luo et al. (2015)	3D	RANS	Cont.	Yes	Ideal	Single	Mesh
Walther et al. (2015a)	2D	RANS	Discr.	Yes	Ideal	Multi	Mesh
Walther et al. (2015c)	3D	RANS	Discr.	Yes	Ideal	Multi	Mesh
Walther et al. (2015b)	3D	RANS	Discr.	Yes	Ideal	Multi	Mesh
Tang et al. (2018)	3D	RANS	Discr.	Yes	Ideal	Single	Mesh
Müller et al. (2017)	3D	RANS	Discr.	Yes	Ideal	Single	CAD
Vitale et al. (2017)	2D	RANS	Discr.	No	Non-ideal	Single	Mesh
Luers et al. (2018)	3D	RANS	Discr.	No	Ideal	Single	CAD*
Anand et al. (2018)	2D	RANS	Discr.	No	Ideal	Single	Both
Mykhaskiv et al. (2018)	3D	RANS	Discr.	No	Ideal	Single	CAD
Torreguitart et al. (2018)	2D	RANS	Discr.	Yes	Ideal	Single	CAD
Torreguitart et al. (2019)	2D	RANS	Discr.	Yes	Ideal	Single	CAD
Russo et al. (2019)	2D	RANS	Discr.	Yes	Ideal	Single	CAD
Rubino et al. (2020)	2D	RANS	Discr.	No	Non-ideal	Multi	Mesh
Vitale et al. (2020)	3D	RANS	Discr.	No	Non-ideal	Multi	Mesh
Present work	2D	RANS	Discr.	No	Non-ideal	Multi	CAD

[a] Type of adjoint formulation, continuous or discrete.
[b] Type of geometry parametrization, mesh-based or CAD-based.
* This work uses the control points of the NURBS curves or surfaces that define the geometry as design variables. For this special case, the derivatives of the surface displacements can be computed analytically in a simple way.

boundary conditions for internal flow problems. As surveyed in Table 5.1, most of the applications of the adjoint method were limited to the optimization of a single row of blades and used the assumption of Constant Eddy Viscosity (CEV) to avoid the challenges associated with the differentiation of mixing-plane boundary conditions and turbulence models. In addition, with the exception of some notable works (Pini et al. 2014; Vitale et al. 2017; Vitale et al. 2020), all the flow and adjoint solvers assumed that the fluid behaves as an ideal gas, preventing their application to NICFD problems where the thermo-physical behavior of the fluid is modeled by complex equations of state.

Alongside with the choice of optimization method, the success of the aerodynamic design is largely dependent on the geometry parametrization that defines the design space where the optimizer can search for the optimal solution (Samareh 2001). In many cases, see Table 5.1, the geometry of the blades is updated at the level of the computational grid using mesh-based parametrization methods such as grid-point displacement (Walther et al. 2012; Walther et al. 2015a), superposition of Hicks-Henne bumps (Wang et al. 2010a; Wang et al. 2010b), superposition of harmonic functions (Corral et al. 2008; Luo et al. 2015), free-form deformation morphing (Vitale et al. 2017; Vitale et al. 2020), or radial basis function interpolation morphing (Tang et al. 2018). Although these methods offer a lot of flexibility in terms of design space, they are not well-suited for optimization problems involving geometric constraints (e.g., minimum trailing edge thickness) (Vitale et al. 2017; Vitale et al. 2020). In addition, the optimized shape only exists as a surface mesh that needs to be transferred back to a Computer-Aided Design (CAD) format for further analysis or manufacturing. The reconstruction of the CAD-model from the surface mesh, albeit possible, is not an straightforward process and it may introduce fitting errors that can have a detrimental impact on the fluid-dynamic performance of the resulting geometry (Becker et al. 2011; Agromayor et al. 2021a). As an alternative, CAD-based parametrization methods keep a consistent CAD representation of the geometry at every design iteration and, as a result, the optimal shape is directly available in a CAD format (Xu et al. 2015; Mykhaskiv et al. 2018). Moreover, these methods allow the designer to impose geometric constraints in a natural and non-intrusive way, giving more control over the shape to be optimized (Müller et al. 2017; Mykhaskiv et al. 2018). Despite their advantages, CAD-based parametrizations are not widely applied in combination with gradient-based optimization methods, in part, due to the challenges associated with the calculation of the shape derivatives with respect the design variables controlling the CAD model (Banović et al. 2018).

In response to the limitations of the methods currently in use, this work proposes an automated aerodynamic design method for turbomachinery blades operating under non-ideal thermodynamic conditions. The aerodynamic design of each row of row of blades is carried out simultaneously by means of a new gradient-based shape optimization framework that integrates the CAD-based parametrization presented in Chapter 4 with a real-gas turbomachinery flow solver and its discrete adjoint counterpart (Vitale et al. 2020). To demonstrate the capabilities of the tools documented in this thesis, the preliminary design method described in Chapter 3 and the aerodynamic design method presented herein were applied to carry out the design optimization of a single-stage axial turbine usin isobutane (R600a) as working fluid.

5.2 Aerodynamic shape optimization framework

The proposed aerodynamic design method is based on the shape optimization framework illustrated in Figure 5.1. The design system supports constrained and unconstrained design problems involving one or multiple blade rows and it integrates: a CAD-based parametrization, mesh generation and deformation routines, a turbomachinery flow solver and its discrete adjoint counterpart, and a gradient-based optimization algorithm that drives the design process. In what follows, the components of the optimization framework are described in detail.

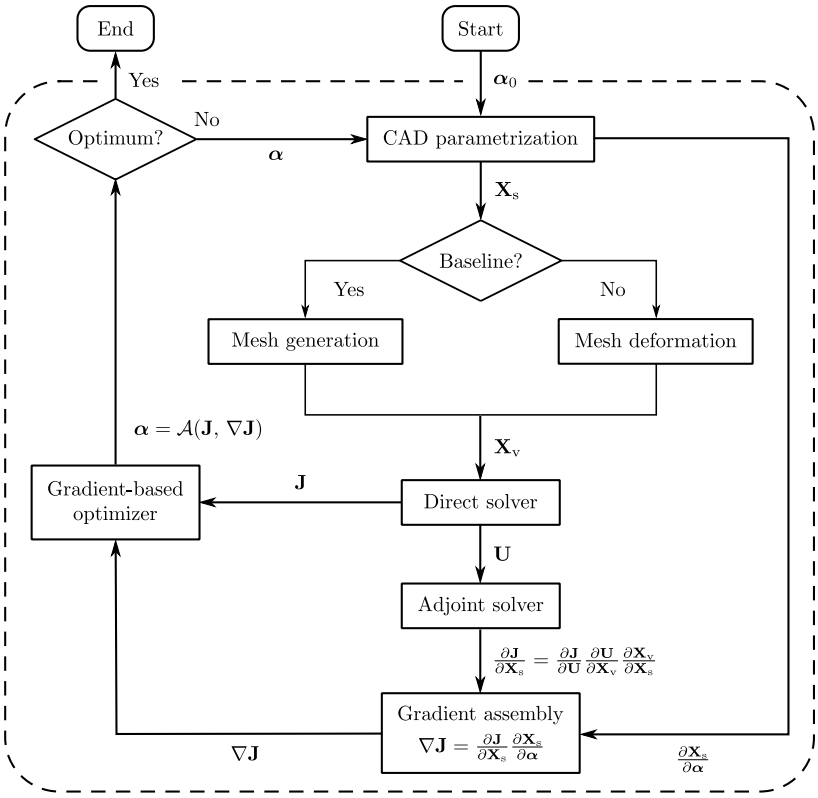

Figure 5.1: Outline of the optimization framework used for the aerodynamic design.

5.2.1 CAD parametrization

The geometry of the blades is defined using the CAD-based parametrization method presented in Chapter 4. This method uses conventional engineering design variables (leading/trailing edge radius, metal angles, blade thickness, etc.) and NURBS curves (Piegl et al. 2012) to represent the geometry of the blade profiles. The design variables used to define one row of blades are listed in Table 5.2. In contrast with most of the two-dimensional methods available in the

Table 5.2: Design variables of the parametric CAD model.

Variable name	Symbol
Spacing	s
Axial chord	c_{ax}
Stagger angle	ξ
Inlet and exit metal angles	θ_{in}, θ_{out}
Inlet and exit tangent proportions	d_{in}, d_{out}
Inlet and exit radii of curvature	r_{in}, r_{out}
Upper and lower thickness distributions*	t^{u}, t^{l}

* In this chapter, each thickness distribution is a cubic B-Spline polynomial defined by 6 control points.

open literature, this parametrization produces blade profiles that have continuous curvature and rate of change of curvature by construction. This feature is important to avoid discontinuities in the surface pressure distribution that may lead to flow separation and deteriorate the fluid-dynamic performance of the cascade (Korakianitis et al. 1993b).

The construction of one blade profile and flow domain is illustrated in Figure 5.2. First, the camber line is determined by the axial chord $c_{\mathrm{ax}} = c\cos\xi$, stagger angle ξ, metal angles θ_{in} and θ_{out}, and tangent proportions d_{in} and d_{out}. After that, two independent thickness distributions t^{u} and t^{l} are imposed normal to the camber line to define the upper and lower sides of the blade. The normal distance for the first and last control points is computed using the end-point curvature equations for NURBS curves to prescribe the radius of curvature at the leading and trailing edges r_{in} and r_{out}. Finally, the flow domain is defined by the inflow and outflow boundaries as well as the two periodic boundaries located an offset distance of half of the blade spacing s with respect to the blade camber line.

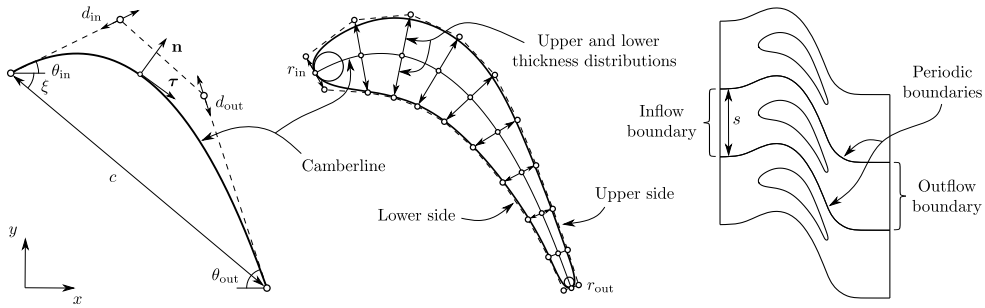

Figure 5.2: Outline of the CAD-based parametrization method used to generate the geometry of the each row of blades and boundary conditions imposed at each edge.

5.2.2 Mesh generation and deformation

The flow domain corresponding to the baseline CAD model is discretized using the unstructured mesh generator proposed by Geuzaine et al. (2009). The mesh is only generated once for the baseline geometry and then deformed each time that the CAD model is updated by a new set of design variables. To this aim, the baseline blade coordinates are mapped into the CAD model using the point projection method described in Chapter 4. Then, at each design cycle, the boundary deformation field given by the difference of updated and initial blade coordinates is propagated into the flow domain using a mesh deformation algorithm based on the linear elasticity equations (Dwight 2009). This approach was adopted instead of mesh re-generation because the latter would change the topology of the unstructured mesh and the discretization error of the flow solution, hindering the convergence of the optimization algorithm.

5.2.3 Direct flow solver

The flow is described by the compressible Reynolds-Averaged Navier-Stokes (RANS) equations (Alfonsi 2009). The RANS equations for a rotating frame of reference with constant angular velocity $\boldsymbol{\Omega}$ can be expressed in differential and conservative form as

$$\frac{\mathrm{d}\mathbf{U}}{\mathrm{d}t} + \nabla \cdot (\mathbf{F}^{\mathrm{c}} - \mathbf{F}^{\mathrm{v}}) - \mathbf{S} = 0, \tag{5.1}$$

where the vector of conservative variables $\mathbf{U}$, vector of convective fluxes $\mathbf{F}^{\mathrm{c}}$, vector of viscous fluxes $\mathbf{F}^{\mathrm{v}}$, and source term $\mathbf{S}$ arising due to Coriolis acceleration are given by

$$\mathbf{U} = \begin{bmatrix} \rho \\ \rho\,\mathbf{v} \\ \rho E \end{bmatrix}, \; \mathbf{F}^{\mathrm{c}} = \begin{bmatrix} \rho\,\mathbf{w} \\ \rho\,\mathbf{v} \otimes \mathbf{w} + p\,\mathbf{I} \\ \rho E\,\mathbf{w} + p\,\mathbf{v} \end{bmatrix}, \; \mathbf{F}^{\mathrm{v}} = \begin{bmatrix} 0 \\ \boldsymbol{\tau} \\ \boldsymbol{\tau} \cdot \mathbf{v} - \dot{\mathbf{q}} \end{bmatrix}, \; \mathbf{S} = \begin{bmatrix} 0 \\ -\rho\,\boldsymbol{\Omega} \times \mathbf{v} \\ 0 \end{bmatrix}. \tag{5.2}$$

In these equations ρ is the fluid density, p is the static pressure, T is the static temperature, $E = e + (\mathbf{v} \cdot \mathbf{v})/2$ is the total energy, and e is the specific internal energy. The density and specific internal energy are utilized as the independent thermodynamic variables, while the rest of the fluid properties are computed using the Peng-Robinson equation of state (Peng et al. 1976) as described in Vitale et al. (2015). Moreover, the absolute velocity vector $\mathbf{v}$ is defined as the sum of the relative velocity $\mathbf{w}$ and the velocity of the rotating frame of reference $\boldsymbol{\Omega} \times \mathbf{X}$. Assuming that the fluid is Newtonian and that the Stokes' hypothesis holds (White 2006, pp. 62–67), the viscous stress tensor is given by

$$\boldsymbol{\tau} = (\mu + \mu_{\mathrm{t}}) \left[\nabla \mathbf{v} + \nabla \mathbf{v}^T - \frac{2}{3} (\nabla \cdot \mathbf{v})\, \mathbf{I} \right], \tag{5.3}$$

where μ is the molecular viscosity and μ_{t} is the turbulence viscosity, which is computed utilizing the two-equation turbulence model proposed by Menter (1994).

In a similar way, the heat flux is given by $\dot{\mathbf{q}} = -(k + k_\mathrm{t})\,\nabla T$, where k is the molecular thermal conductivity and k_t and is the turbulence thermal conductivity.

The continuous partial differential equations governing the flow are discretized in space using an unstructured, vertex-based Finite Volume Method (FVM) (Barth 1991) within the SU2 multi-physics suite (Palacios et al. 2013; Economon et al. 2016). The semi-discretized integral form of the RANS equations is expressed as

$$\Delta V_i \frac{\mathrm{d}\mathbf{U}_i}{\mathrm{d}t} + \sum_j (\mathbf{F}^\mathrm{c}_{ij} - \mathbf{F}^\mathrm{v}_{ij}) \Delta S_{ij} - \Delta V_i\, \mathbf{S}_i = \Delta V_i \frac{\mathrm{d}\mathbf{U}_i}{\mathrm{d}t} + \mathbf{R}_i(\mathbf{U}) = 0, \tag{5.4}$$

where $\mathbf{U}_i$ is the flow solution at node i, $\mathbf{R}_i$ is the numerical residual, $\mathbf{F}^\mathrm{c}_{ij}$ and $\mathbf{F}^\mathrm{v}_{ij}$ are the numerical convective and viscous fluxes, respectively, $\mathbf{S}_i$ is a uniform reconstruction of the source term, ΔV_i is the volume of the dual control volume, and ΔS_{ij} is the area of the face associated with the edge ij. The convective fluxes are computed using a real-gas version of Roe's approximate Riemann solver (Roe 1981; Vinokur et al. 1990) and the numerical dissipation is controlled with the entropy fix proposed by Harten and Hyman (Harten et al. 1983). A Monotonic Upstream-centered Scheme for Conservation Laws (MUSCL) linear reconstruction (van Leer 1979) is used to achieve second order accuracy in space and the van Albada slope limiter (Van Albada et al. 1997; Kemm 2011) is adopted to suppress oscillations near discontinuities such as shock waves. In addition, the convective fluxes of the turbulence model are computed using a first-order scalar upwind scheme and all viscous fluxes are evaluated using a corrected average-gradient method (Weiss et al. 1997). The gradients of the flow variables needed to evaluate the convective and viscous fluxes are calculated using the weighted least-squares method (Mavriplis 2003).

Once discretized in space, the governing equations are driven to steady-state with an implicit Euler pseudo-time integration accelerated by local time-stepping (Palacios et al. 2013). The complete discretization of the RANS equations is thus given by

$$\left(\frac{\Delta V_i}{\Delta t^n_i}\, \delta_{ij} + \frac{\partial \mathbf{R}_i(\mathbf{U}^n)}{\partial \mathbf{U}_j} \right) \Delta \mathbf{U}^n = \mathbf{P}\, \Delta \mathbf{U}^n = -\mathbf{R}(\mathbf{U}^n), \tag{5.5}$$

where $\Delta \mathbf{U}^n = \mathbf{U}^{n+1} - \mathbf{U}^n$ and δ_{ij} is the Kronecker delta function. This linear system can be transformed into a fixed-point equation, such that the steady-state solution of the discretized RANS equations is computed from the iteration

$$\mathbf{U}^{n+1} = \mathbf{U}^n - \mathbf{P}^{-1}\, \mathbf{R}(\mathbf{U}^n) = \mathbf{G}(\mathbf{U}^n), \tag{5.6}$$

where $\mathbf{G}$ is the fixed-point operator. The product $\mathbf{P}^{-1}\, \mathbf{R}$ is computed by solving the sparse linear system given by Eq. (5.5) using a flexible Generalized Minimal Residual (GMRES) method (Saad 2003, pp. 171–193) preconditioned by an incomplete LU factorization with no filling (Saad 2003, pp. 301–319).

With regards to boundary conditions; an adiabatic, non-slip wall condition is used at the surface of the blades. In addition, the inflow and outflow boundaries use an extension of the characteristic-based, non-reflecting boundary conditions proposed by Giles (1990); Giles (1991) that generalizes the original formulation to fluids described by arbitrary equations of state (Vitale et al. 2017). The total pressure, total temperature, flow direction, turbulence intensity, and viscosity ratio are specified at the inlet of the first blade row, whereas the static pressure was prescribed at the exit of the last blade row. The stator and rotor flow domains are coupled using the conservative, non-reflecting mixing plane interface proposed by Saxer et al. (1993); Saxer et al. (1994) with the modifications suggested by Vitale et al. (2020). Finally, periodic boundary conditions are used in the tangential direction to reduce the computational domain to a single blade per row.

5.2.4 Adjoint flow solver and gradient evaluation

Once that the flow equations are solved, the objective function and constraints of the optimization problem (collectively known as cost functions $\mathbf{J}$) can be computed. In addition to their value, the gradient-based optimizer also requires their derivatives with respect to the design variables $\nabla\mathbf{J}$. The dependence of a single cost function J with respect to the design variables can be conceptualized as

$$\boldsymbol{\alpha} \rightarrow \mathbf{X}_\mathrm{s} \rightarrow \mathbf{X}_\mathrm{v} \rightarrow \mathbf{U} \rightarrow J,$$

where $\boldsymbol{\alpha}$ is the set of design variables, $\mathbf{X}_\mathrm{s}$ are the mesh boundary coordinates, $\mathbf{X}_\mathrm{v}$ are the mesh interior coordinates, and $\mathbf{U}$ is the flow solution vector.

The derivatives of the cost function with respect to the surface coordinates $\frac{\partial J}{\partial \mathbf{X}_\mathrm{s}}$ (often known as CFD sensitivities) are computed using the discrete adjoint solver documented in Albring et al. (2016). The adjoint equations associated with the cost function J can be derived from the following optimization problem

$$\begin{aligned} \text{minimize} \quad & J\left(\mathbf{U}(\mathbf{X}_\mathrm{s}),\, \mathbf{X}_\mathrm{v}(\mathbf{X}_\mathrm{s})\right) && (5.7)\\ \text{subject to} \quad & \mathbf{U}(\mathbf{X}_\mathrm{s}) = \mathbf{G}\left(\mathbf{U}(\mathbf{X}_\mathrm{s}),\, \mathbf{X}_\mathrm{v}(\mathbf{X}_\mathrm{s})\right) && (5.8)\\ & \mathbf{X}_\mathrm{v}(\mathbf{X}_\mathrm{s}) = \mathbf{M}(\mathbf{X}_\mathrm{s}), && (5.9) \end{aligned}$$

where Eqs. (5.8) and (5.9) are the constraints imposed by the discretized RANS equations and the mesh deformation equations, respectively. The Lagrangian function associated to this problem is given as

$$\begin{aligned} L = {} & J\left(\mathbf{U}(\mathbf{X}_\mathrm{s}),\, \mathbf{X}_\mathrm{v}(\mathbf{X}_\mathrm{s})\right) \\ & + \left(\mathbf{G}(\mathbf{U}(\mathbf{X}_\mathrm{s}),\, \mathbf{X}_\mathrm{v}(\mathbf{X}_\mathrm{s})) - \mathbf{U}(\mathbf{X}_\mathrm{s})\right)^T \boldsymbol{\lambda} \\ & + \left(\mathbf{M}(\mathbf{X}_\mathrm{s}) - \mathbf{X}_\mathrm{v}(\mathbf{X}_\mathrm{s})\right)^T \boldsymbol{\mu}, \end{aligned} \qquad (5.10)$$

where $\boldsymbol{\lambda}$ and $\boldsymbol{\mu}$ are the Lagrangian multipliers of the problem (also known as adjoint variables). Using the chain rule for differentiation, the derivatives of the

Lagrangian function with respect to the mesh surface coordinates are given by

$$\begin{aligned}\frac{\partial L}{\partial \mathbf{X}_\mathrm{s}} = &\left(\frac{\partial \mathbf{M}}{\partial \mathbf{X}_\mathrm{s}}\right)^T \boldsymbol{\mu} + \left(\frac{\partial J}{\partial \mathbf{U}} + \left(\frac{\partial \mathbf{G}}{\partial \mathbf{U}}\right)^T \boldsymbol{\lambda} - \boldsymbol{\lambda}\right) \frac{\partial \mathbf{U}}{\partial \mathbf{X}_\mathrm{s}} \\ &+ \left(\frac{\partial J}{\partial \mathbf{X}_\mathrm{v}} + \left(\frac{\partial \mathbf{G}}{\partial \mathbf{X}_\mathrm{v}}\right)^T \boldsymbol{\lambda} - \boldsymbol{\mu}\right) \frac{\partial \mathbf{X}_\mathrm{v}}{\partial \mathbf{X}_\mathrm{s}},\end{aligned} \tag{5.11}$$

from which the adjoint equations are derived as

$$\boldsymbol{\lambda} = \frac{\partial J}{\partial \mathbf{U}} + \left(\frac{\partial \mathbf{G}}{\partial \mathbf{U}}\right)^T \boldsymbol{\lambda} \tag{5.12}$$

$$\boldsymbol{\mu} = \frac{\partial J}{\partial \mathbf{X}_\mathrm{v}} + \left(\frac{\partial \mathbf{G}}{\partial \mathbf{X}_\mathrm{v}}\right)^T \boldsymbol{\lambda}. \tag{5.13}$$

If the adjoint variables $\boldsymbol{\lambda}$ and $\boldsymbol{\mu}$ satisfy Eqs. (5.12) and (5.13), then the derivative of the Lagrangian function (and the cost function) with respect to the mesh surface coordinates is simply given by

$$\frac{\partial L}{\partial \mathbf{X}_\mathrm{s}} = \frac{\partial J}{\partial \mathbf{X}_\mathrm{s}} = \left(\frac{\partial \mathbf{M}}{\partial \mathbf{X}_\mathrm{s}}\right)^T \boldsymbol{\mu} \tag{5.14}$$

In order to solve the adjoint equations, $\boldsymbol{\lambda}$ is computed from Eq. (5.12) using the fixed-point iteration

$$\boldsymbol{\lambda}^{n+1} = \frac{\partial J}{\partial \mathbf{U}} + \left(\frac{\partial \mathbf{G}}{\partial \mathbf{U}}\right)^T \boldsymbol{\lambda}^n = \mathbf{N}(\boldsymbol{\lambda}^n) \tag{5.15}$$

and, after that, the converged solution is inserted in Eq. (5.13) to obtain $\boldsymbol{\mu}$. One important feature of the discrete adjoint formulation is that the primal and dual fixed-point iterations satisfy

$$\left\| \frac{\partial \mathbf{N}}{\partial \boldsymbol{\lambda}} \right\| = \left\| \frac{\partial \mathbf{G}}{\partial \boldsymbol{U}} \right\| \tag{5.16}$$

and, as a result, the convergence properties of the RANS solver are preserved in the adjoint solver (Albring et al. 2016).

All the derivatives occurring in the adjoint system, Eqs. (5.12) and (5.13), are obtained by applying the CoDiPack algorithmic differentiation library (Sagebaum et al. 2018; Sagebaum et al. 2019) to the top-level routine of the RANS solver. In this way, all the features of the flow solver such as turbulence models, equations of state, and boundary conditions, are directly inherited by the adjoint solver. This differs with respect to the majority of adjoint solvers described in the open literature, which are derived by manual differentiation or by selective application

of automatic differentiation and often rely on simplifying assumptions such as the CEV approximation to ease their development and implementation, see Table 5.1.

To complete the differentiation chain, the derivatives of the mesh surface coordinates with respect to the design variables $\frac{\partial \mathbf{X}_\mathrm{s}}{\partial \boldsymbol{\alpha}}$ (often known as CAD sensitivities) are computed by applying the complex-step method (Lyness et al. 1967; Squire et al. 1998; Martins et al. 2003) to the parametric CAD model,

$$\frac{\partial \mathbf{X}_\mathrm{s}}{\partial \boldsymbol{\alpha}} = \frac{\mathrm{Im}\left(\mathbf{X}_\mathrm{s}(\boldsymbol{\alpha} + i\,\mathbf{h})\right)}{h} + \mathcal{O}(h^2). \tag{5.17}$$

In contrast to finite differences, the complex-step method *is not* susceptible to subtraction error and it can be used to compute derivatives accurate to round-off precision by setting an arbitrarily small imaginary step size (i.e., $h \to 0$).

Once the CFD and the CAD sensitivities are computed, the gradient of the cost function follows from the application of the chain rule for differentiation,

$$\nabla J = \frac{\partial J}{\partial \mathbf{X}_\mathrm{s}} \frac{\partial \mathbf{X}_\mathrm{s}}{\partial \boldsymbol{\alpha}}. \tag{5.18}$$

5.2.5 Optimization

The optimization framework is driven by a gradient-based optimization algorithm that uses the values and gradients of the cost functions to update the design variables. Formally, this can be represented as

$$\boldsymbol{\alpha}^{k+1} = \mathcal{A}(\mathbf{J}(\boldsymbol{\alpha}^k),\, \nabla\mathbf{J}(\boldsymbol{\alpha}^k)), \tag{5.19}$$

where $\mathcal{A}(\,\cdot\,)$ stands for the algorithmic steps used by the optimizer at the k-th iteration. The new set of design variables is used to update the CAD model, deform the mesh, and re-evaluate the cost functions and gradients. This process is repeated until the optimization algorithm converges to an optimum solution. The optimizer adopted in this work is the SLSQP algorithm (Kraft 1988) implemented in the SciPy library (*SciPy v1.5* 2020), which is a Sequential Quadratic Programming (SQP) algorithm (Nocedal et al. 2006, pp. 526–572) capable to handle general nonlinear constraints as well as bounds for the design variables.

5.3 Validation of the flow solver

Prior to its application for aerodynamic design, the predictive capability of the flow solver was validated against three experimental test cases:

1. The subsonic linear cascade measured by Kiock et al. (1986) at DFVLR Braunschweig. This case is representative of a high-pressure turbine rotor and it features a thick trailing edge characteristic of coolable blades.

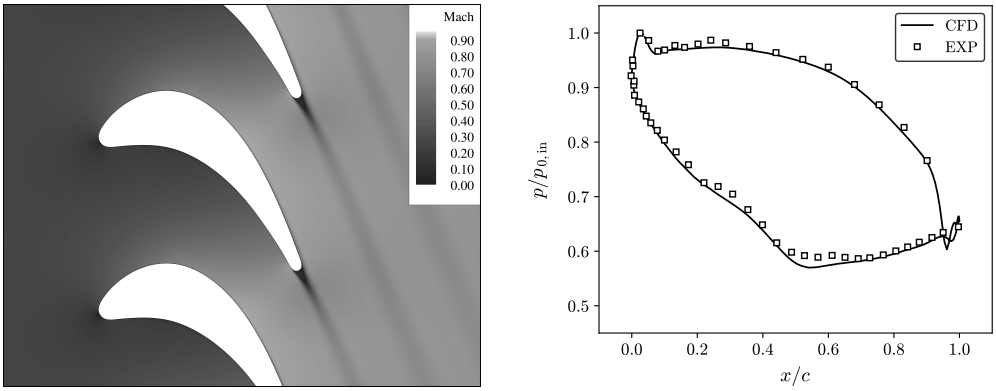

Figure 5.3: Mach number and surface pressure for the Kiock et al. (1986) cascade.

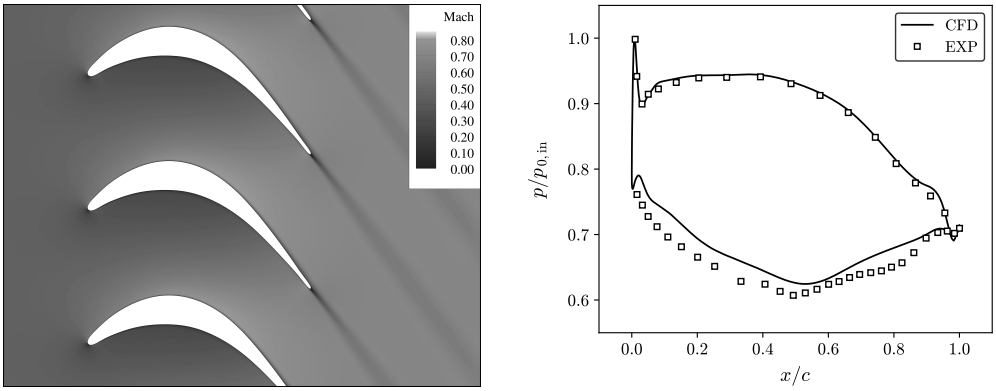

Figure 5.4: Mach number and surface pressure for the Hodson et al. (1987) cascade.

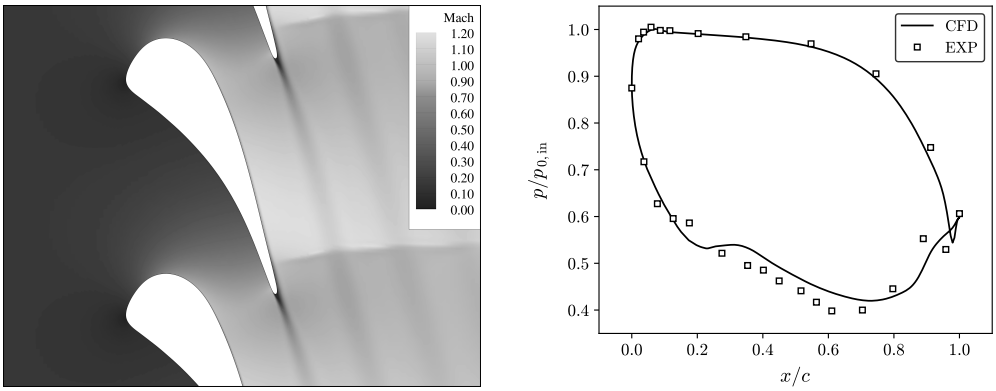

Figure 5.5: Mach number and surface pressure for the Arts et al. (1992) cascade.

Table 5.3: Boundary conditions of the validation test cases.

Reference	α_{in} [°]	$T_{0,in}$ [K]	$p_{0,in}$ [kPa]	p_{out} [kPa]	$I_{t,in}$ [%]	$(\mu_t/\mu)_{in}$ [–]
Kiock et al. (1986)	30.0	313.0	63.8	41.9	0.50	10.0[b]
Hodson et al. (1987)	38.8	298.0[a]	41.4	29.8	0.50	10.0[b]
Arts et al. (1992)	0.0	422.0	160.5	82.8	1.00	10.0[b]

[a] The original publication indicates that the inlet temperature is close to ambient.
[b] Assumed value. The solution has a weak dependence on this variable.

2. The subsonic linear cascade measured by Hodson et al. (1987) at the Whittle Laboratory. This case is representative of the root section of a high-lift, low-pressure turbine rotor with slender blades.

3. The transonic linear cascade measured by Arts et al. (1992) at the Von Karman Institute. This case is representative of a high-pressure turbine stator that features a long semi-bladed region downstream the throat.

The working fluid in all three test cases was air and the boundary conditions that define each case are summarized in Table 5.3. The geometry of the blades was available as a list of point coordinates with a limited number of decimal digits. To avoid the noise introduced by coordinate round-off, the blade geometry was smoothed using the re-parametrization methodology described in Chapter 4.

The flow solution in terms of Mach number and surface pressure distribution along the percentage of chord (not axial chord) are shown in Figures 5.3 to 5.5. The results indicate an excellent agreement between experimental data and the surface pressure distributions predicted by the flow solver for all three cases. In addition, with regards to the third case, the flow solver is able to predict the formation of a normal shock at the rear part of the suction side that agrees with the Schlieren visualizations depicted in the original publication (Arts et al. 1992).

5.4 Application to a case study: EXPAND facility

In order to demonstrate the capabilities of the proposed methods, the preliminary design method described in Chapter 3 and the aerodynamic design method documented in this chapter were applied to the design optimization of a single-stage axial turbine with no diffuser that uses isobutane (R600a) as working fluid. This turbine was specifically designed for experimental testing in the EXPAND facility at the Norwegian University of Science and Technology (Pardiñas et al. 2019) with the aim to provide experimental datasets that contribute towards the validation and refinement of the models currently used to analyze of ORC turbines. To the knowledge of the author, this is the first time that the gradient-based design optimization of a complete ORC turbine stage has been documented.

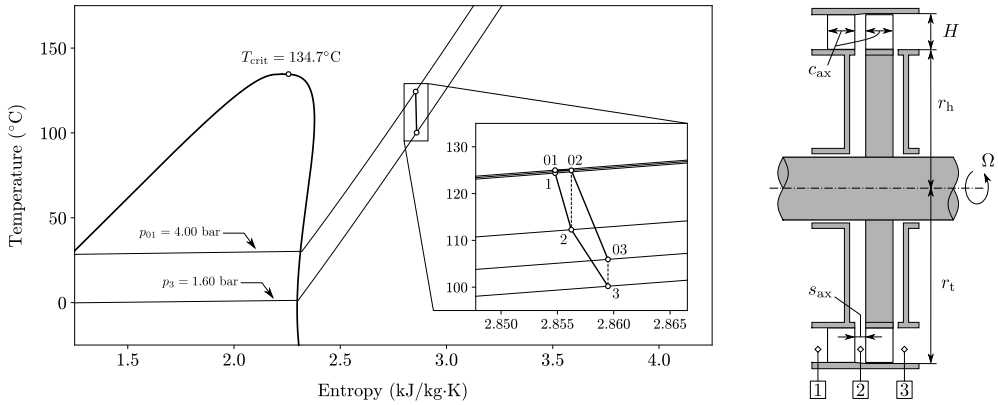

Figure 5.6: T–s diagram of the expansion (left) and cross section of the turbine (right).

5.4.1 Preliminary design

The preliminary turbine design was carried out by means of the mean-line model and optimization methodology documented in Chapter 3. This method assumes that the flow is uniform along the spanwise and circumferential directions and solves the balance equations for mass and rothalpy at the inlet and outlet of each cascade, regardless of the detailed shape of the blades (lumped-parameter approach). In addition, the method uses the Kacker et al. (1982) empirical loss model to estimate the entropy generation in each row of blades. More specifically, the original loss model was modified such that it takes into account the profile and trailing edge losses (2D effects) and neglects the tip-leakage and secondary losses (3D effects). This approach was adopted with the intent that the mean-line model used for the preliminary design and the two-dimensional RANS solver used for the aerodynamic design account for the same loss mechanisms.

The preliminary design was based on the specifications listed in Table 5.4 and it was performed using the total-to-total isentropic efficiency as objective function. This performance metric was adopted because it is an indication of the *blading efficiency* and it does not penalize the kinetic energy that is not recovered at the exhaust of the turbine. To ensure that the new turbine is compatible with the EXPAND facility; the design mass flow rate, inlet total temperature and pressure, outlet static pressure, hub and tip radii, and angular speed were the same as those of an existing turbine designed by an industrial partner. In addition, the axial chord of the stator and rotor blades was set to 10 mm ($H/c_{ax} = 1.27$) to obtain an aspect ratio slightly above unity (Saravanamuttoo et al. 2009, p. 345), and the axial spacing was set to 4 mm ($s_{ax}/c_{ax} = 0.40$) to reduce the vibrational stresses induced in the rotor blades as they pass through the wakes of the stator blades (Saravanamuttoo et al. 2009, p. 333). Furthermore, a trailing edge thickness of 0.50 mm was adopted due to manufacturing requirements.

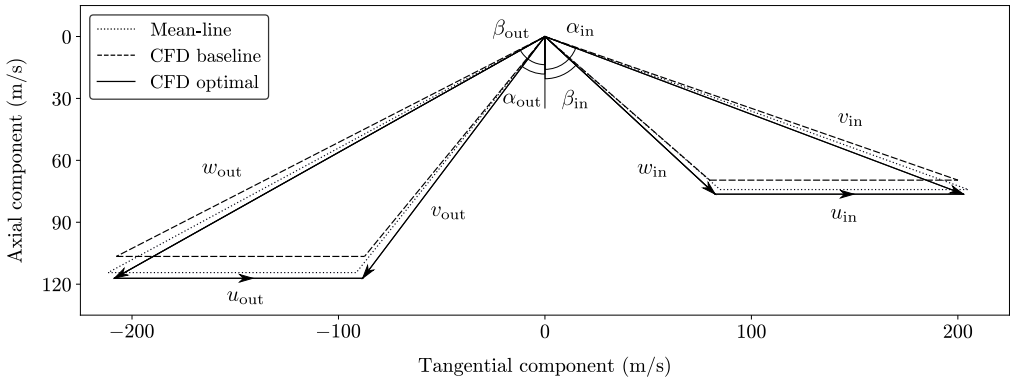

Figure 5.7: Velocity triangles at the inlet and outlet of the rotor cascade.

As depicted in the cross-sectional view of Figure 5.6, the design obtained with the mean-line method is characterized by a constant annulus height and a relatively high hub-to-tip ratio ($r_h/r_t = 0.80$). Under these conditions, the radial variation of the flow is expected to be small (Saravanamuttoo et al. 2009, p. 204) and the use of a two-dimensional flow solver to carry out the detailed blade design is justified. The thermodynamic process within the turbine in the T–s diagram is also illustrated in Figure 5.6, where it can be observed that the expansion takes place in a thermodynamic region close to the vapor saturation line where the fluid departs from ideal gas behavior ($Z_{in} \approx 0.95$). This highlights the importance of using an accurate thermodynamic model to carry out the fluid-dynamic design of the turbine. In addition, the velocity diagrams at the inlet and outlet of the rotor blades are illustrated in Figure 5.7. It is interesting to note that, even if the degree of reaction is $\Lambda = 0.50$, the velocity triangles are not symmetrical because the axial velocity increases along the expansion to satisfy the mass conservation equation. The output of the preliminary design in terms of geometric parameters and operating conditions is reported with a greater level of detail in Appendix D.

5.4.2 Aerodynamic design

Baseline geometry

The baseline geometry of the stator and rotor blades was generated by trial and error with the aim to satisfy the velocity triangles obtained during the preliminary design phase. The boundary conditions used for the aerodynamic design are summarized in Table 5.5 and the parameters used to describe the thermophysical behavior of the fluid are summarized in Table 5.6. The flow domain was discretized using an unstructured grid, see Figure 5.8, and the number of mesh elements was selected in accordance with the results of the mesh independence

Table 5.4: Design specifications used for the preliminary design.

Variable	Symbol	Value	Unit
Working fluid		Isobutane	–
Inlet total temperature	$T_{0,\mathrm{in}}$	125.0	°C
Inlet total pressure	$p_{0,\mathrm{in}}$	400.0	kPa
Outlet static pressure	p_{out}	160.0	kPa
Mass flow rate	$\dot{m}$	1.600	kg/s
Angular speed	Ω	20000	rpm
Radius at the hub	r_{h}	51.05	mm
Radius at the tip	r_{t}	63.75	mm
Axial chord	c_{ax}	10.00	mm
Axial spacing	s_{ax}	4.00	mm
Trailing edge thickness	t_{te}	0.50	mm
Degree of reaction	Λ	0.50	–

Table 5.5: Boundary conditions used for the aerodynamic design.

Variable	Symbol	Value	Unit
Inlet flow angle	α_{in}	0.0	°
Inlet total temperature	$T_{0,\mathrm{in}}$	125.0	°C
Inlet total pressure	$p_{0,\mathrm{in}}$	400.0	kPa
Outlet static pressure	p_{out}	160.0	kPa
Inlet turbulence intensity	$I_{\mathrm{turb,in}}$	1.00	%
Inlet viscosity ratio	$(\mu_{\mathrm{t}}/\mu)_{\mathrm{in}}$	10.0	–

Table 5.6: Thermophysical properties of isobutane (R600a).

Variable	Symbol	Value	Unit
Gas constant	R	143.1	J/kg K
Critical temperature	T_{crit}	407.8	K
Critical pressure	p_{crit}	3629	kPa
Acentric factor	ω	0.1835	–
Heat capacity ratio[a]	γ	1.086	–
Dynamic viscosity[a]	μ	9.918	µPa s
Thermal conductivity[a]	k	28.8	mW/m K

[a] Evaluated at the inlet and assumed to be constant.

All properties were obtained from the CoolProp library (Bell et al. 2014; Bücker et al. 2006; Vogel et al. 2000; Perkins 2002).

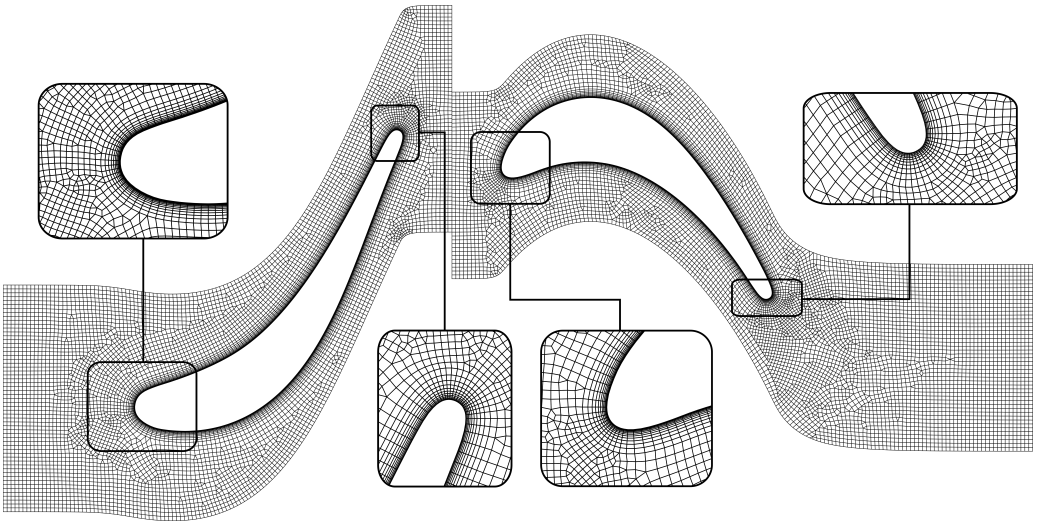

Figure 5.8: Computational grid for the baseline stator and rotor flow domains.

study of Figure 5.9. In addition, the size of the cells in the direction normal to the blade walls was controlled with inflation layers to ensure that the boundary layer is resolved accurately ($y^+ < 1$). The direct and adjoint problems were driven to steady-state using a Courant-Friedrichs-Lewy (CFL) number of 25 and the termination criterion was set to 5000 iterations, which corresponds to a residual reduction of about 9 and 8 orders of magnitude, respectively. The convergence history of the direct and adjoint solvers is shown in Figure 5.10. As expected, both solvers have essentially the same convergence rate.

The flow field for the baseline geometry is illustrated in Figure 5.13 and it is characterized by the presence of a shock wave pattern at the trailing edge of each cascade. Both cascades operate at transonic conditions and the highest relative Mach numbers within the stator and rotor domains are 1.48 and 1.38, respectively. The stator surface pressure distribution, see Figure 5.15 (left), indicates that the flow accelerates monotonously over the entire pressure side and also over the suction side until $x/c \approx 0.58$. At this location, the shock wave originating at the trailing edge of the adjacent stator blade impinges on the suction side, causing a steep increase of the surface pressure. This adverse pressure gradient leads to the formation of a small separation bubble in the region downstream of the impingement, see Figure 5.16 (left). The flow over the rotor blades is similar, but, in this case, the shock wave impinging on the rotor suction side at $x/c \approx 0.73$ is weaker and does not cause flow separation. Instead, the boundary layer remains attached and becomes thicker after the interaction with the shock wave as illutrated in Figure 5.16 (right).

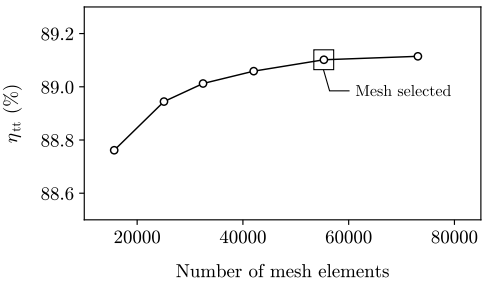

Figure 5.9: Mesh independence study in terms of total-to-total isentropic efficiency.

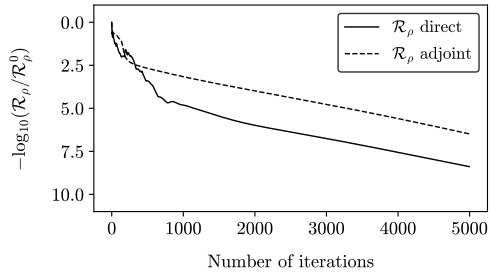

Figure 5.10: Direct and adjoint solver convergence for the baseline geometry.

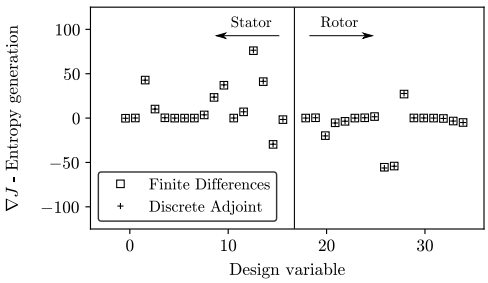

Figure 5.11: Verification of the adjoint-based sensitivities against finite differences.

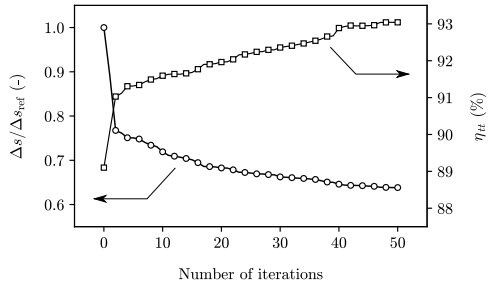

Figure 5.12: Entropy generation and isentropic total-to-total efficiency opt. history.

Optimal geometry

Once the baseline geometry was defined, the aerodynamic shape optimization framework was used to minimize the entropy generation resulting from viscous dissipation and shock waves (Denton 1993). To this aim, the shape of the stator and rotor blades was optimized simultaneously using the CAD model parameters listed in Table 5.2 as design variables. The blade spacing, axial chord, and stagger angle were kept constant to maintain the same number of blades and axial length, resulting in 36 degrees of freedom (18 per blade). In addition, the minimum thickness was constrained to 0.50 mm to respect the manufacturing requirements.

The accuracy of the objective function gradient computation was verified prior to the optimization. Figure 5.11 shows a comparison of the gradient computed using the adjoint-based method against that computed using a forward finite differences applied to the entire evaluation chain. The results indicate an excellent agreement between the adjoint-based and finite difference gradients, confirming that the CAD model and CFD solver are correctly differentiated. In addition, these results demonstrate the superiority of the adjoint-based approach, which only required one direct and one adjoint problem solutions to evaluate the gradient. In contrast, the finite difference gradient evaluation required 36+1 direct problem solutions, one for the baseline and one per perturbed design variable.

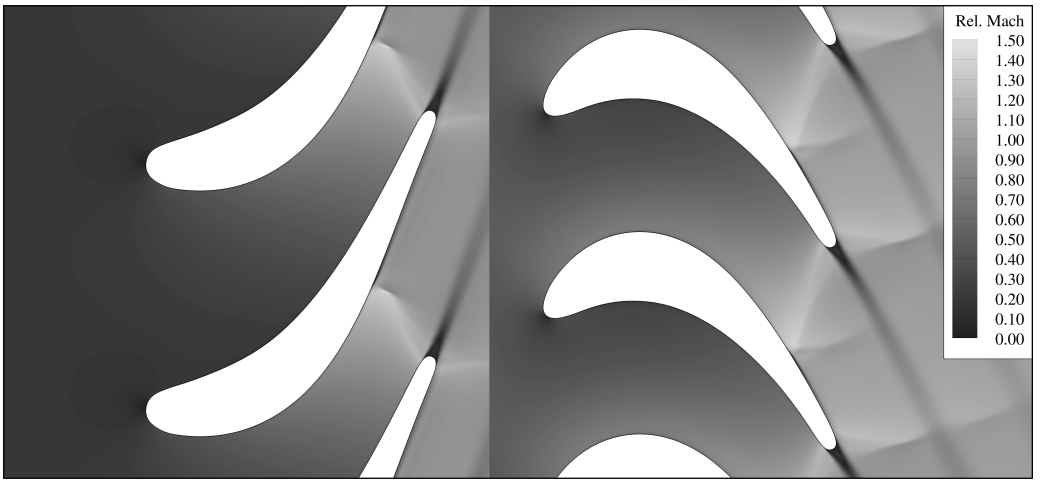

Figure 5.13: Relative Mach number contours of the flow field for the baseline design.

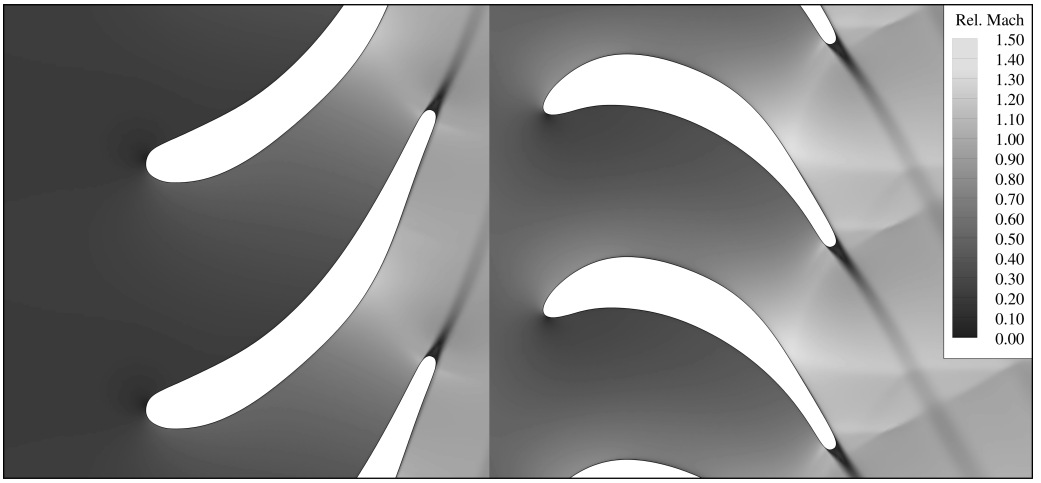

Figure 5.14: Relative Mach number contours of the flow field for the optimal design.

The convergence history of the optimization problem is shown in Figure 5.12. The optimization was stopped after 50 design cycles because the improvement of the objective function value was marginal. The total run-time was approximately 60 hours on a 6 core computer with a CPU rate of 2.2 GHz. The entropy generation within the turbine was reduced by 36.2% relative to the baseline geometry, which corresponds to a total-to-total isentropic efficiency increase of 3.94 percentage points. Notably, 75% of the objective function improvement took place in the first 10 design cycles. In what follows, the causes that produced this fluid-dynamic performance improvement are examined.

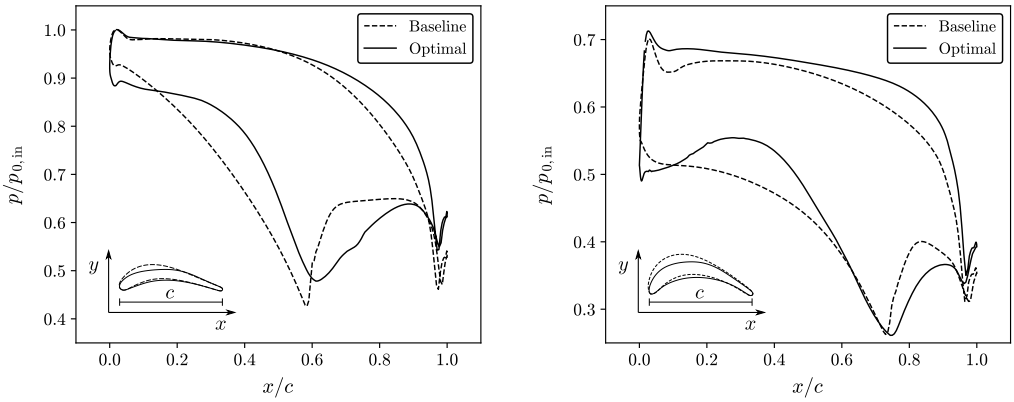

Figure 5.15: Surface pressure distribution over the stator (left) and rotor (right) blades.

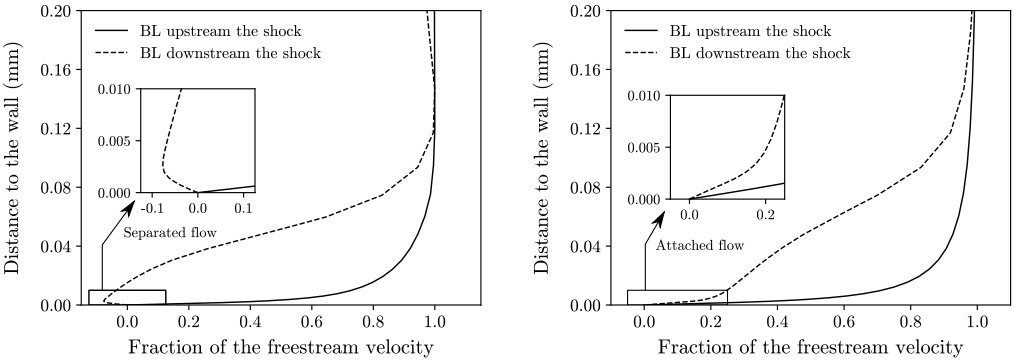

Figure 5.16: Boundary layer profile for the stator (left) and rotor blades (right).

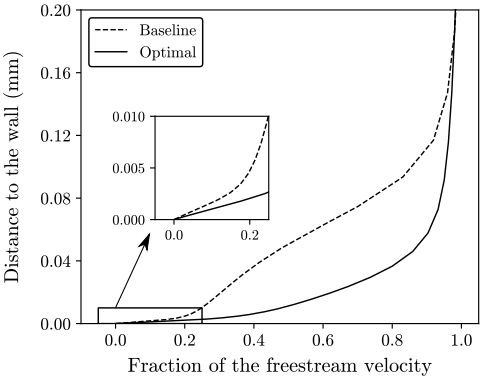

Figure 5.17: Rotor boundary layer downstream the impinging suction side shock.

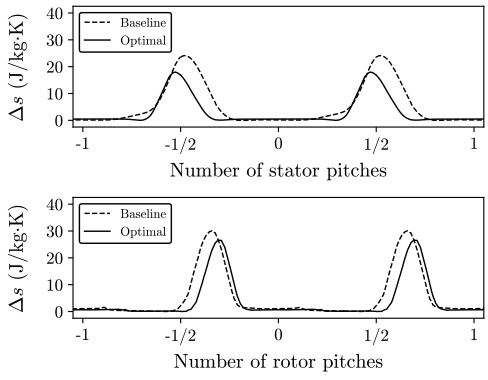

Figure 5.18: Entropy distribution at the plane 2 mm downstream the blades.

The flow field for the optimal geometry is illustrated in Figure 5.14. It can be observed that the optimizer reduced the curvature of the blades, especially at the suction side, and that the minimum thickness constraint was respected. The changes in curvature reduced the maximum Mach number in the stator cascade from 1.48 to 1.17 and, as a result, the trailing edge shock pattern, as well as the separation bubble caused by the shock-boundary layer interaction, were eliminated. For the case of the rotor, the maximum relative Mach number only decreased from 1.38 to 1.35. Despite this, the surface pressure distribution depicted in Figure 5.15 (right) indicates that the shock impinging on the rotor suction side is significantly weaker for the optimal geometry. As a result, the boundary layer downstream of the impinging shock is thinner and more stable than that of the baseline, see Figure 5.17. In addition, the optimizer also reduced the entropy generation due to mixing in the wakes downstream of the blades. Indeed, the area under the entropy distributions shown in Figure 5.18 was reduced by 40.4% for the stator and by 25.0% for the rotor, which is a significant improvement considering that the optimizer respected the minimum trailing edge thickness constraint.

5.5 Conclusions

An aerodynamic design method for turbomachinery blades operating under non-ideal thermodynamic conditions was presented. The method relies on a new gradient-based shape optimization framework that integrates the differentiated CAD-based parametrization developed in Chapter 4 with a real-gas RANS flow solver and its discrete adjoint counterpart. In order to demonstrate the capabilities of the methods developed in this thesis, the preliminary design method presented in Chapter 3 and the aerodynamic design method described in this chapter were applied to carry out the design optimization of a single-stage axial turbine with isobutane (R600a) as working fluid. The following conclusions were drawn from the results of this study:

- The flow solver was validated against three test cases corresponding to linear cascades using air as working fluid. The results showed an excellent agreement between the numerical solution and the experimental data, suggesting that the flow solver is a suitable tool suitable to carry out the fluid dynamic design of the blades.
- The accuracy of the objective function gradients obtained from the adjoint-based method was verified against forward finite differences. The results showed an excellent match between the two methods, confirming that the parametric CAD model and the direct flow solver are correctly differentiated.
- The discrete adjoint solver enabled the evaluation of the objective function gradient with a computational cost that is essentially independent of the

number of design variables, enabling the exploration of a large design space that would be untractable using a gradient-free optimization algorithm.

- The CAD-based parametrization enabled the definition of high-level geometric constraints such as constant axial chord length, minimum trailing edge thickness, and smooth curvature distribution in a straightforward way. This is a significant advantage over mesh-based parametrization methods, which are not well-suited to impose geometric constraints.
- The optimization framework was applied successfully to design the shape of the blades and minimize the entropy generation within the turbine. In particular, the optimizer reduced the entropy generation by 36.2% relative to the baseline geometry in 50 design cycles, which corresponds to a total-to-total isentropic efficiency increase of 3.94 percentage points.
- The aerodynamic design optimization did not only produce a quantitative improvement in performance, but also caused qualitative changes in the flow field. Most notably, the baseline stator cascade featured a trailing edge shock pattern and a shock-induced separation bubble at the suction side that were eliminated as a result of the optimization.

Chapter 6

Conclusions and Further Work

6.1 Conclusions

This PhD thesis proposed a set of automated methods aimed towards the fluid-dynamic design of turbomachinery operating under non-ideal thermodynamic conditions. The proposed methods combine mathematical models and numerical optimization techniques to explore the design space in a systematic way, thereby allowing the designer to achieve higher performance gains and reduce the development time with respect to traditional design workflows based on trial-and-error.

The first contribution of this thesis is a preliminary design method for axial turbines with any number of stages. The proposed method is based on a new mean-line model that accepts arbitrary equations of state to evaluate the thermodynamic properties of the working fluid and empirical loss models to estimate the entropy generation in each row of blades. In addition, the fraction of kinetic energy recovered at the exit of the last stage is predicted using a new one-dimensional annular diffuser model based on the balance equations for mass, momentum, and energy. Even if this work only considered annular diffusers with straight walls, the proposed one-dimensional flow model was formulated in a general way and it can also be used for other annular geometries, such as the U-shaped ducts of multi-stage radial machines. In contrasts with other design methods documented in the literature, the preliminary design problem was formulated as a constrained optimization problem and solved using a gradient-based algorithm. This choice of optimization algorithm enabled: (1) the integration of the turbine, diffuser, and loss models in a simple way by means of equality-constraints and (2) the optimization of multi-stage design problems with tens of design variables at a low computational cost. In the view of the author, this approach represents a significant advantage over gradient-free design strategies which rely on internal iterations to ensure that the model is consistent and require a large number of function evaluations to converge to the optimum. The preliminary design method proposed in this work was developed for the particular case of axial turbines. However, the problem formulation and solution strategy can be easily extended to other types of turbomachines, provided that an appropriate geometry description and empirical loss model are implemented.

The second contribution of this thesis is a general CAD-based parametrization method for axial, radial and mixed flow turbomachinery blades. The proposed parametrization is based on conventional engineering parameters (e.g., chord, metal angles, thickness distribution) and it exploits the mathematical properties of NURBS curves and surfaces to produce blades with continuous curvature and rate of change of curvature. This feature is of interest because sudden changes in curvature can cause spikes in the surface pressure distribution or even local separation bubbles that would deteriorate the aerodynamic performance of the blades. In addition, the method provides the sensitivity of the blade coordinates with respect to the design variables by means of the complex-step method, which allows the integration of the parametrization into automated, gradient-based shape optimization workflows. Furthermore, the proposed method is capable of re-parametrizing the geometry of an existing blade defined by a set of scattered point coordinates. This reverse engineering strategy was formulated as a two-step optimization problem and it allows one to find the design variable values that best approximates the prescribed geometry in a systematic way. Solving this fitting problem is essential in the context of aerodynamic shape optimization because it is necessary to link the CAD representation of the geometry with the surface mesh used for the flow simulations.

The third contribution of this thesis is an aerodynamic design method for turbomachinery blades operating under non-ideal thermodynamic conditions. The proposed method supports the simultaneous optimization of multiple blade rows in two dimensions and it relies on a gradient-based shape optimization framework that integrates the proposed CAD-based parametrization with a multi-row turbomachinery RANS solver and its discrete adjoint counterpart. In the view of the author, the aerodynamic design method developed in this work offers three main advantages with respect to other design systems: (1) the real-gas flow solver enables the optimization of unconventional turbomachinery (e.g., ORC turbines, supercritical CO_2 compressors) in which the fluid deviates from ideal gas behavior, (2) the discrete adjoint solver enables the evaluation of cost function gradients at a computational cost that is essentially independent of the number of design variables, which enables the exploration of large design spaces that would be untractable with gradient-free methods, and (3) compared with mesh-based methods, the CAD-based parametrization allows the designer to impose high-level geometric constraints, such as constant axial chord length, minimum trailing edge thickness, or smooth curvature distribution in a straightforward way.

In order to demonstrate the capabilities of the automated design tools developed in this thesis, the proposed preliminary and aerodynamic design methods were applied to design a new single-stage axial turbine operating with isobutane (R600a) that is is going to be built and tested in the EXPAND facility at the Norwegian University of Science and Technology. The preliminary design method was successfully applied to design a turbine geometry and velocity triangles that

maximize the total-to-total isentropic efficiency of the turbine and satisfy the technical constraints imposed by the EXPAND facility. In addition, the aerodynamic design method was used to define stator and rotor blade shapes that minimize the entropy generation within the turbine and satisfy the design specifications established during the preliminary design phase. In particular, the gradient-based shape optimization framework was able to reduce the entropy generation by 36.2%, relative to the baseline geometry, which corresponds to a total-to-total isentropic efficiency increase of 3.94 percentage points. Furthermore, the aerodynamic optimization did not only produce a quantitative improvement in performance, but also caused qualitative changes in the flow field. Most notably, the baseline stator cascade featured a trailing edge shock pattern and a shock-induced separation bubble that were eliminated as a result of the optimization. To the knowledge of the author, this is the first time that the end-to-end fluid-dynamic design of a complete ORC turbine has been carried out by means of gradient-based methods.

Ultimately, the work presented in this thesis showed that the fluid-dynamic design of turbomachinery can benefit significantly from automated workflows based on mathematical models and numerical optimization. Far from trying to replace the designer, such workflows aim to automate repetitive and error-prone tasks so that the designer is free to focus on the creative aspects of the design process. Nevertheless, the output from such automated workflows should not be accepted blindly. Instead, the results should be carefully judged using previous design experience and a solid understanding of the physical laws, mathematical models, and numerical algorithms involved in the problem.

6.2 Further work

Future work may be devoted to extend the axial turbine mean-line model to other turbomachinery configurations such as radial turbines and axial/radial compressors. In order to do this, it would be necessary to generalize the geometry description and implement a suitable empirical loss model for each type of machine. In addition, the proposed preliminary design method could be extended to predict the performance at off-design conditions or even to account for off-design performance during the design phase (i.e., multi-point design optimization). To this aim, it is recommended to take advantage of the proposed gradient-based solution strategy and use equality constraints to ensure that the model equations are satisfied at each design point.

At the onset of this project, none of the CAD kernels in existence offered functionality to compute the shape derivatives that are required in gradient-based shape optimization workflows. Due to this limitation, the proposed CAD-based parametrization method was implemented using a lightweight NURBS library developed by the author which was differentiated with machine precision using the complex-step method. However, Banović et al. (2018) recently applied algorith-

mic differentiation to the entire OpenCascade CAD kernel and demonstrated its use in the context of gradient-based shape optimization. Considering this step forward, an interesting topic for further work would be to implement the proposed parametrization method into the differentiated version of the OpenCascade kernel. This, in turn, would provide a wide range of algorithms that could be used to model complex geometric features such as blade endwall fillets, shroud seals, or secondary flow systems.

Finally, further studies may be dedicated to extend the proposed shape optimization framework to three-dimensional configurations. Even if the RANS flow solver and CAD-based parametrization already support three-dimensional geometries, further work would be necessary to improve the mesh generation and deformation steps of the design chain. In addition, the shape optimization framework could be extended to account for the influence other disciplines, such as stress analysis, conjugate heat transfer, or aero-elasticity. Such multidisciplinary design chains are expected to play a significant role in the turbomachinery industry as they reduce the interactions between engineering departments and contribute towards a rapid market introduction of new products.

References

Agromayor, R., N. Anand, J.-D. Müller, M. Pini, and L. O. Nord (2021a). "A Unified Geometry Parametrization Method for Turbomachinery Blades". *Computer-Aided Design* 133, pp. 1–16. DOI: https://doi.org/10.1016/j.cad.2020.102987.

Agromayor, R., N. Anand, M. Pini, and L. O. Nord (2021b). "Multi-row Adjoint-based Optimization of NICFD Turbomachinery Using a CAD-based Parametrization". *To be submitted to: Journal of Engineering for Gas Turbines and Power*.

Agromayor, R., B. Müller, and L. O. Nord (2019a). "One-Dimensional Annular Diffuser Model for Preliminary Turbomachinery Design". *International Journal of Turbomachinery, Propulsion and Power* 4.3, pp. 1–31. DOI: https://doi.org/10.3390/ijtpp4030031.

Agromayor, R. and L. O. Nord (2019b). "Preliminary Design and Optimization of Axial Turbines Accounting for Diffuser Performance". *International Journal of Turbomachinery, Propulsion and Power* 4.3, pp. 1–32. DOI: https://doi.org/10.3390/ijtpp4030032.

Agromayor, R. and L. O. Nord (2017a). "Fluid Selection and Thermodynamic Optimization of Organic Rankine Cycles for Waste Heat Recovery Applications". *Energy Procedia* 129, pp. 527–534. DOI: https://doi.org/10.1016/j.egypro.2017.09.180.

Agromayor, R., J. Rúa, and R. Kristoffersen (2017b). "Simulation of Starting and Stopping Vortices of an Airfoil". *Proceedings of the 58th Conference on Simulation and Modelling*, pp. 66–75.

Ainley, D. G. and C. R. Mathieson (1951a). *A Method of Performance Estimation for Axial-Flow Turbines*. Tech. rep. 2974. Aeronautical Research Council Reports and Memoranda, pp. 1–30.

Ainley, D. G. and C. R. Mathieson (1951b). *An Examination of the Flow and Pressure Losses in Blade Rows of Axial-Flow Turbines*. Tech. rep. 2891. Aeronautical Research Council Reports and Memoranda, pp. 1–33.

Al Jubori, A., R. K. A. Dadah, S. Mahmoud, K. M. Khalil, and A. S. B. Ennil (2016). "Development of Efficient Small Scale Axial Turbine for Solar Driven Organic Rankine Cycle". *ASME Turbo Expo: Power for Land, Sea, and Air*, pp. 1–11. DOI: https://doi.org/10.1115/GT2016-57845.

Albring, T. A., M. Sagebaum, and N. R. Gauger (2016). "Efficient Aerodynamic Design using the Discrete Adjoint Method in SU2". *17th AIAA/ISSMO Multidisciplinary Analysis and Optimization Conference*, pp. 1–15. DOI: https://doi.org/10.2514/6.2016-3518.

Alfonsi, G. (2009). "Reynolds-Averaged Navier–Stokes Equations for Turbulence Modeling". *Applied Mechanics Reviews* 62.4, pp. 1–20. DOI: https://doi.org/10.1115/1.3124648.

Anand, N., A. Rubino, P. Colonna, and M. Pini (2020). "Adjoint-Based Aeroelastic Design Optimization Using a Harmonic Balance Method". *ASME Turbo Expo: Turbomachinery Technical Conference and Exposition*, pp. 1–12.

Anand, N., S. Vitale, M. Pini, and P. Colonna (2018). "Assessment of FFD and CAD-Based Shape Parametrization Methods for Adjoint-Based Turbomachinery Shape Optimization". *Proceedings of the Montreal 2018 Global Power and Propulsion Forum*, pp. 1–8.

Arens, K., P. Rentrop, S. Stoll, and U. Wever (2005). "An Adjoint Approach to Otimal Design of Turbine Blades". *Applied Numerical Mathematics* 53.2, pp. 93–105. DOI: https://doi.org/10.1016/j.apnum.2004.11.003.

Arts, T. and M. Lambert de Rouvroit (1992). "Aero-Thermal Performance of a Two-Dimensional Highly Loaded Transonic Turbine Nozzle Guide Vane: A Test Case for Inviscid and Viscous Flow Computations". *Journal of Turbomachinery* 114.1, pp. 147–154. DOI: https://doi.org/10.1115/1.2927978.

Arts, T., M. Lambert de Rouvroit, and A. W. Rutherford (1990). *Aero-Thermal Investigation of a Highly Loaded Transonic Linear Turbine Guide Vane Cascade: a Test Case for Inviscid and Viscous Flow Computations*. Tech. rep. 174. VKI Training Center for Experimental Aerodynamics, pp. 1–97.

Astolfi, M. and E. Macchi (2015). "Efficiency Correlations for Axial Flow Turbines Working with Non-Conventional Fluids". *Proceedings of the 3rd International Seminar on ORC Power Systems*, pp. 1–12.

Audet, C. and W. Hare (2017). *Derivative-Free and Blackbox Optimization*. 1st. Springer. DOI: https://doi.org/10.1007/978-3-319-68913-5.

Aungier, R. H. (2006a). *Turbine Aerodynamics: Axial-Flow and Radial-Flow Turbine Design and Analysis*. 1st. ASME Press. DOI: https://doi.org/10.1115/1.802418.

Aungier, R. H. (2006b). "Turbine Aerodynamics: Axial-Flow and Radial-Flow Turbine Design and Analysis". 1st. ASME Press, pp. 166–183. DOI: https://doi.org/10.1115/1.802418.

Bahamonde, S., M. Pini, C. De Servi, A. Rubino, and P. Colonna (2017). "Method for the Preliminary Fluid Dynamic Design of High-Temperature Mini-Organic Rankine Cycle Turbines". *Journal of Engineering for Gas Turbines and Power* 139.8, pp. 1–14. DOI: https://doi.org/10.1115/1.4035841.

Balje, O. E. and R. L. Binsley (1968a). "Axial Turbine Performance Evaluation. Part A – Loss-Geometry Relationships". *Journal of Engineering for Power* 90.4, pp. 341–348. DOI: https://doi.org/10.1115/1.3609211.

Balje, O. E. and R. L. Binsley (1968b). "Axial Turbine Performance Evaluation. Part B – Optimization With and Without Constraints". *Journal of Engineering for Power* 90.4, pp. 349–359. DOI: https://doi.org/10.1115/1.3609212.

Baltadjiev, N. D., C. Lettieri, and Z. S. Spakovszky (2015). "An Investigation of Real Gas Effects in Supercritical CO_2 Centrifugal Compressors". *Journal of Turbomachinery* 137.9. DOI: https://doi.org/10.1115/1.4029616.

Banović, M., O. Mykhaskiv, S. Auriemma, A. Walther, H. Legrand, and J.-D. Müller (2018). "Algorithmic Differentiation of the Open CASCADE Technology CAD Kernel and its Coupling with an Adjoint CFD Solver". *Optimization Methods and Software* 33.4-6, pp. 813–828. DOI: https://doi.org/10.1080/10556788.2018.1431235.

Barth, T. (1991). "Numerical Aspects of Computing High Reynolds Number Flows on Unstructured Meshes". *29th AIAA Aerospace Sciences Meeting*, pp. 1–19. DOI: https://doi.org/10.2514/6.1991-721.

Becker, G., M. Schäfer, and A. Jameson (2011). "An Advanced NURBS Fitting Procedure for Post-Processing of Grid-Based Shape Optimizations". *49th AIAA Aerospace Sciences Meeting*, pp. 1–19. DOI: https://doi.org/10.2514/6.2011-891.

Bell, I. H., J. Wronski, S. Quoilin, and V. Lemort (2014). "Pure and Pseudo-pure Fluid Thermophysical Property Evaluation and the Open-Source Thermophysical Property Library CoolProp". *Industrial & Engineering Chemistry Research* 53.6, pp. 2498–2508. DOI: https://doi.org/10.1021/ie4033999.

Benner, M. W., S. A. Sjolander, and S. H. Moustapha (1997). "Influence of Leading-Edge Geometry on Profile Losses in Turbines at Off-Design Incidence: Experimental Results and an Improved Correlation". *Journal of Turbomachinery* 119.2, pp. 193–200. DOI: https://doi.org/10.1115/1.2841101.

Brown, W. B. (1947). *Friction Coefficients in a Vaneless Diffuser*. Tech. rep. TN 1311. NACA Flight Propulsion Research Laboratory; Cleveland, OH, United States, pp. 1–100.

Bücker, D. and W. Wagner (2006). "Reference Equations of State for the Thermodynamic Properties of Fluid Phase n-Butane and Isobutane". *Journal of Physical and Chemical Reference Data* 35.2, pp. 929–1019. DOI: https://doi.org/10.1063/1.1901687.

Bunker, R. S. (2009). "The Effects of Manufacturing Tolerances on Gas Turbine Cooling". *Journal of Turbomachinery* 131.4, pp. 1–11. DOI: https://doi.org/10.1115/1.3072494.

Casati, E., S. Vitale, M. Pini, G. Persico, and P. Colonna (2014). "Centrifugal Turbines for Mini-ORC Power Systems". *Journal of Engineering for Gas Turbines and Power* 136.12, pp. 1–11. DOI: https://doi.org/10.1115/1.4027904.

Casey, M. V. (1983). "A Computational Geometry for the Blades and Internal Flow Channels of Centrifugal Compressors". *Journal of Engineering for Power* 105.2, pp. 288–295. DOI: https://doi.org/10.1115/1.3227414.

Cengel, Y. A. (2002). *Heat Transfer: a Practical Approach*. 2nd. McGraw-Hill, New York.

Colonna, P., E. Casati, C. Trapp, T. Mathijssen, J. Larjola, T. Turunen-Saaresti, and A. Uusitalo (2015). "Organic Rankine Cycle Power Systems: From the

Concept to Current Technology, Applications, and an Outlook to the Future". *Journal of Engineering for Gas Turbines and Power* 137.10, pp. 1–19. DOI: http://dx.doi.org/10.1115/1.4029884.

Colonna, P., J. Harinck, S. Rebay, and A. Guardone (2008). "Real-Gas Effects in Organic Rankine Cycle Turbine Nozzles". *Journal of Propulsion and Power* 24.2, pp. 282–294. DOI: https://doi.org/10.2514/1.29718.

Corral, R. and F. Gisbert (2008). "Profiled End Wall Design Using an Adjoint Navier–Stokes Solver". *Journal of Turbomachinery* 130.2, pp. 1–8. DOI: https://doi.org/10.1115/1.2751143.

Craig, H. R. M. and H. J. A. Cox (1971). "Performance Estimation of Axial Flow Turbines". *Proceedings of the Institution of Mechanical Engineers* 185.1, pp. 407–424. DOI: https://doi.org/10.1243/PIME_PROC_1970_185_048_02.

Crouse, J. E. and W. T. Gorrell (1981). *Computer Program for Aerodynamic and Blading Design of Multistage Axial-Flow Compressors*. Tech. rep. TP 1946. NASA Lewis Research Center; Cleveland, OH, United States, pp. 1–110.

Da Lio, L., G. Manente, and A. Lazzaretto (2014). "New Efficiency Charts for the Optimum Design of Axial Flow Turbines for Organic Rankine Cycles". *Energy* 77, pp. 447–459. DOI: https://doi.org/10.1016/j.energy.2014.09.029.

Da Lio, L., G. Manente, and A. Lazzaretto (2016). "Predicting the Optimum Design of Single Stage Axial Expanders in ORC Systems: Is There a Single Efficiency Map for Different Working Fluids?" *Applied Energy* 167, pp. 44–58. DOI: http://dx.doi.org/10.1016/j.apenergy.2016.01.020.

Da Lio, L., G. Manente, and A. Lazzaretto (2017). "A Mean-Line Model to Predict the Design Efficiency of Radial Inflow Turbines in Organic Rankine Cycle (ORC) Systems". *Applied Energy* 205, pp. 187–209. DOI: http://dx.doi.org/10.1016/j.apenergy.2017.07.120.

Dahlquist, A. (2008). "Investigation of Losses Prediction Methods in 1D for Axial Gas Turbines". MA thesis. Lund University.

De Servi, C. M., M. Burigana, M. Pini, and P. Colonna (2019). "Design Method and Performance Prediction for Radial-Inflow Turbines of High-Temperature Mini-Organic Rankine Cycle Power Systems". *Journal of Engineering for Gas Turbines and Power* 141.9, pp. 1–12. DOI: https://doi.org/10.1115/1.4043973.

Denton, J. D. (1993). "The 1993 IGTI Scholar Lecture: Loss Mechanisms in Turbomachines". *Journal of Turbomachinery* 115.4, pp. 621–656. DOI: http://dx.doi.org/10.1115/1.2929299.

Denton, J. D. (2010). "Some Limitations of Turbomachinery CFD". *ASME Turbo Expo: Power for Land, Sea, and Air*, pp. 735–745. DOI: https://doi.org/10.1115/GT2010-22540.

Denton, J. D. and W. N. Dawes (1998). "Computational Fluid Dynamics for Turbomachinery Design". *Proceedings of the Institution of Mechanical Engineers, Part C: Journal of Mechanical Engineering Science* 213.2, pp. 107–124. DOI: https://doi.org/10.1243/0954406991522211.

Denton, J. D. (2017). "Multall – An Open Source, Computational Fluid Dynamics Based, Turbomachinery Design System". *Journal of Turbomachinery* 139.12, pp. 1–12. DOI: https://doi.org/10.1115/1.4037819.

Dixon, S. L. and C. Hall (2013). *Fluid Mechanics and Thermodynamics of Turbomachinery*. 7th. Butterworth-Heinemann.

Dubitsky, O. and D. Japikse (2008). "Vaneless Diffuser Advanced Model". *Journal of Turbomachinery* 130.1, pp. 1–10. DOI: https://doi.org/10.1115/1.2372781.

Dunham, J. (1974). "A Parametric Method of Turbine Blade Profile Design". *ASME Turbo Expo: Power for Land, Sea, and Air*, pp. 1–9. DOI: https://doi.org/10.1115/74-GT-119.

Dunham, J. and P. M. Came (1970). "Improvements to the Ainley-Mathieson Method of Turbine Performance Prediction". *Journal of Engineering for Power* 92.3, pp. 252–256. DOI: https://doi.org/10.1115/1.3445349.

Duta, M. C., S. Shahpar, and M. B. Giles (2007). "Turbomachinery Design Optimization Using Automatic Differentiated Adjoint Code". *ASME Turbo Expo: Power for Land, Sea, and Air*, pp. 1–10. DOI: https://doi.org/10.1115/GT2007-28329.

Dwight, R. P. (2009). "Robust Mesh Deformation Using the Linear Elasticity Equations". *Proceedings of the Fourth International Conference on Computational Fluid Dynamics, ICCFD 2006*, pp. 401–406. DOI: https://doi.org/10.1007/978-3-540-92779-2_62.

Economon, T. D., F. Palacios, S. R. Copeland, T. W. Lukaczyk, and J. J. Alonso (2016). "SU2: An Open-Source Suite for Multiphysics Simulation and Design". *AIAA Journal* 54.3, pp. 828–846. DOI: https://doi.org/10.2514/1.J053813.

Elgammal, A. H. and A. M. Elkersh (1981). "A Method for Predicting Annular Diffuser Performance with Swirling Inlet Flow". *Journal of Mechanical Engineering Science* 23.3, pp. 107–112. DOI: https://doi.org/10.1243/JMES_JOUR_1981_023_023_02.

Encabo-Cáceres, I., R. Agromayor, and L. O. Nord (2017). "Thermodynamic Optimization of an Organic Rankine Cycle for Power Generation From a Low Temperature Geothermal Heat Source". *Proceedings of the 58th Conference on Simulation and Modelling*, pp. 251–262.

Engeli, M., H. J. Zollinger, and J. C. Allemann (1974). "A Computer Program for the Design of Turbomachinery Blades". *ASME Turbo Expo: Power for Land, Sea, and Air*, pp. 1–10. DOI: https://doi.org/10.1115/78-GT-36.

Farin, G. E. (2001). *Curves and Surfaces for CAGD: a Practical Guide*. 5th. Morgan Kaufmann.

Flynn, T. (2004). *Cryogenic Engineering, Revised and Expanded*. 2st. CRC Press.

Fransson, T. H. and J. M. Verdon (1993). "Panel Discussion on Standard Configurations for Unsteady Flow Through Vibrating Axial-Flow Turbomachine-Cascades". *Unsteady Aerodynamics, Aeroacoustics, and Aeroelasticity of Tur-*

bomachines and Propellers, pp. 859–889. DOI: https://doi.org/10.1007/978-1-4613-9341-2.

Gagliardi, F. and K. C. Giannakoglou (2019). "RBF-Based Morphing of B-Rep models for Use in Aerodynamic Shape Optimization". *Advances in Engineering Software* 138, pp. 1–17. DOI: https://doi.org/10.1016/j.advengsoft.2019.102724.

Geuzaine, C. and J.-F. Remacle (2009). "Gmsh: A 3-D Finite Element Mesh Generator with Built-in Pre-and Post-Processing Facilities". *International Journal for Numerical Methods in Engineering* 79.11, pp. 1309–1331. DOI: https://doi.org/10.1002/nme.2579.

Giannakoglou, K. C. (1999). "Designing Turbomachinery Blades Using Evolutionary Methods". *ASME Turbo Expo: Power for Land, Sea, and Air*, pp. 1–9. DOI: https://doi.org/10.1115/99-GT-181.

Giles, M. B. (1990). "Nonreflecting Boundary Conditions for Euler Equation Calculations". *AIAA Journal* 28.12, pp. 2050–2058. DOI: https://doi.org/10.2514/3.10521.

Giles, M. B. (1991). *UNSFLO: A Numerical Method for the Calculation of Unsteady Flow in Turbomachinery*. Tech. rep. GTL 205. Gas Turbine Laboratory, Massachusetts Institute of Technology, pp. 1–101.

Giles, M. B. and N. A. Pierce (2000). "An Introduction to the Adjoint Approach to Design". *Flow, Turbulence and Combustion* 3, pp. 393–415. DOI: https://doi.org/10.1023/A:1011430410075.

Goel, S., I. Cofer John I., and H. Singh (1996). "Turbine Airfoil Design Optimization". *ASME Turbo Expo: Power for Land, Sea, and Air*, pp. 1–10. DOI: https://doi.org/10.1115/96-GT-158.

Goldman, R. (2005). "Curvature Formulas for Implicit Curves and Surfaces". *Computer Aided Geometric Design* 22.7, pp. 632–658. DOI: https://doi.org/10.1016/j.cagd.2005.06.005.

Golub, G. H. and J. H. Welsch (1969). "Calculation of Gauss Quadrature Rules". *Mathematics of Computation* 23.106, pp. 221–230. DOI: https://doi.org/10.2307/2004418.

Gordon, W. J. and C. A. Hall (1973). "Construction of Curvilinear Coordinate Systems and Applications to Mesh Generation". *International Journal for Numerical Methods in Engineering* 7.4, pp. 461–477. DOI: https://doi.org/10.1002/nme.1620070405.

Gräsel, J., A. Keskin, M. Swoboda, H. Przewozny, and A. Saxer (2004). "A Full Parametric Model for Turbomachinery Blade Design and Optimisation". *ASME International Design Engineering Technical Conferences and Computers and Information in Engineering Conference*, pp. 907–914. DOI: https://doi.org/10.1115/DETC2004-57467.

Griewank, A. and A. Walther (2008). *Evaluating Derivatives: Principles and Techniques of Algorithmic Differentiation*. 1st. SIAM.

Hagen, B., R. Agromayor, and P. Nekså (2021). "Equation-Oriented Methods for Design Optimization and Performance Analysis of Radial Inflow Turbines". *Submitted to: Energy*.

Harten, A. and J. M. Hyman (1983). "Self-Adjusting Grid Methods for One-Dimensional Hyperbolic Conservation Laws". *Journal of Computational Physics* 50.2, pp. 235–269. DOI: https://doi.org/10.1016/0021-9991(83)90066-9.

Hodson, H. P. and R. G. Dominy (1987). "Three-Dimensional Flow in a Low-Pressure Turbine Cascade at Its Design Condition". *Journal of Turbomachinery* 109.2, pp. 177–185. DOI: https://doi.org/10.1115/1.3262083.

Huppertz, A., P. M. Flassig, R. J. Flassig, and M. Swoboda (2007). "Knowledge Based 2D Blade Design Using Multi-Objective Aerodynamic Optimization and a Neural Network". *ASME Turbo Expo: Power for Land, Sea, and Air*, pp. 413–423. DOI: https://doi.org/10.1115/GT2007-28204.

Jameson, A. (1988). "Aerodynamic Design via Control Theory". *Journal of Scientific Computing* 3, pp. 233–260. DOI: https://doi.org/10.1007/BF01061285.

Jameson, A. (1995). "Optimum Aerodynamic Design Using CFD and Control Theory". *12th AIAA Computational Fluid Dynamics Conference*, pp. 926–949. DOI: https://doi.org/10.2514/6.1995-1729.

John, A., S. Shahpar, and N. Qin (2017). "Novel Compressor Blade Shaping Through a Free-Form Method". *Journal of Turbomachinery* 139.8, pp. 1–11. DOI: https://doi.org/10.1115/1.4035833.

Johnston, J. P. and R. C. Dean (1966). "Losses in Vaneless Diffusers of Centrifugal Compressors and Pumps: Analysis, Experiment, and Design". *Journal of Engineering for Power* 88.1, pp. 49–60. DOI: https://doi.org/10.1115/1.3678477.

Jones, A. C. (1996). "Design and Test of a Small, High Pressure Ratio Radial Turbine". *Journal of Turbomachinery* 118.2, pp. 362–370. DOI: https://doi.org/10.1115/1.2836651.

Kacker, S. C. and U. Okapuu (1982). "A Mean Line Prediction Method for Axial Flow Turbine Efficiency". *Journal of Engineering for Power* 104.1, pp. 111–119. DOI: https://doi.org/10.1115/1.3227240.

Keep, J. A., S. Vitale, M. Pini, and M. Burigana (2017). "Preliminary Verification of the Open-Source CFD Solver SU2 for Radial-Inflow Turbine Applications". *Energy Procedia* 129, pp. 1071–1077. DOI: https://doi.org/10.1016/j.egypro.2017.09.130.

Kehlhofer, R., F. Hannemann, B. Rukes, and F. Stirnimann (2009). *Combined-Cycle Gas and Steam Turbine Power Plants*. 1st. Pennwell Books.

Kemm, F. (2011). "A Comparative Study of TVD-limiters – Well-known Limiters and an Introduction of New Ones". *International Journal for Numerical Methods in Fluids* 67.4, pp. 404–440. DOI: https://doi.org/10.1002/fld.2357.

Kiock, R., F. Lehthaus, N. C. Baines, and C. H. Sieverding (1986). "The Transonic Flow Through a Plane Turbine Cascade as Measured in Four European Wind

Tunnels". *Journal of Engineering for Gas Turbines and Power* 108.2, pp. 277–284. DOI: https://doi.org/10.1115/1.3239900.

Kline, S. J., D. E. Abbott, and R. W. Fox (1959). "Optimum Design of Straight-Walled Diffusers". *Journal of Basic Engineering* 81.3, pp. 321–329. DOI: https://doi.org/10.1115/1.4008462.

Kluwick, A. (2017). "Non-Ideal Compressible Fluid Dynamics: a Challenge for Theory". *Journal of Physics Conferece Series*. Vol. 821. 1, pp. 1–28. DOI: https://doi.org/10.1088/1742-6596/821/1/012001.

Kofskey, M. G. and W. J. Nusbaum (1972). *Design and Cold-Air Investigation of a Turbine for a Small Low-Cost Turbofan Engine*. Tech. rep. TN D-6967. NASA Lewis Research Center; Cleveland, OH, United States, pp. 1–34.

Koini, G. N., S. S. Sarakinos, and I. K. Nikolos (2009). "A Software Tool for Parametric Design of Turbomachinery Blades". *Advances in Engineering Software* 40.1, pp. 41–51. DOI: https://doi.org/10.1016/j.advengsoft.2008.03.008.

Korakianitis, T. (1993a). "Hierarchical Development of Three Direct-Design Methods for Two-Dimensional Axial-Turbomachinery Cascades". *Journal of Turbomachinery* 115.2, pp. 314–324. DOI: https://doi.org/10.1115/1.2929237.

Korakianitis, T. (1993b). "Prescribed-Curvature-Distribution Airfoils for the Preliminary Geometric Design of Axial-Turbomachinery Cascades". *Journal of Turbomachinery* 115.2, pp. 325–333. DOI: https://doi.org/10.1115/1.2929238.

Korakianitis, T. and P. Papagiannidis (1993a). "Improved Turbine-Blade Design Techniques Using 4th-Order Parametric-Spline Segments". *Computer-Aided Design* 25.5, pp. 289–299. DOI: https://doi.org/10.1016/0010-4485(93)90086-4.

Korakianitis, T. and P. Papagiannidis (1993b). "Surface-Curvature-Distribution Effects on Turbine-Cascade Performance". *Journal of Turbomachinery* 115.2, pp. 334–341. DOI: https://doi.org/10.1115/1.2929239.

Kraft, D. (1988). *A Software Package for Sequential Quadratic Programming*. Tech. rep. DFVLR-FB 88-28. German Test and Research Institute for Aviation and Space Flight, pp. 1–33.

Kumar, D. S. and K. L. Kumar (1980). "Effect of Swirl on Pressure Recovery in Annular Diffusers". *Journal of Mechanical Engineering Science* 22.6, pp. 305–313. DOI: https://doi.org/10.1243/JMES_JOUR_1980_022_056_02.

Lemmon, E. W., M. L. Huber, and M. O. McLinden (2013). *NIST Standard Reference Database 23: Reference Fluid Thermodynamic and Transport Properties-REFPROP, Version 9.1, National Institute of Standards and Technology*. DOI: http://dx.doi.org/10.18434/T4JS3C.

Li, Y., D. Yang, and Z. Feng (2006). "Inverse Problem in Aerodynamic Shape Design of Turbomachinery Blades". *ASME Turbo Expo: Power for Land, Sea, and Air*, pp. 1–9. DOI: https://doi.org/10.1115/GT2006-91135.

Liu, D. C. and J. Nocedal (1989). "On the Limited Memory BFGS Method for Large Scale Optimization". *Mathematical Programming* 45.1-3, pp. 503–528. DOI: https://doi.org/10.1007/BF01589116.

Lohmann, R. P., S. J. Markowski, and E. Brookman (1979). "Swirling Flow Through Annular Diffusers with Conical Walls". *Journal of Fluids Engineering* 101.2, pp. 224–229. DOI: https://doi.org/10.1115/1.3448939.

Lozza, G., E. Macchi, and A. Perdichizzi (1982). "On the Influence of the Number of Stages on the Efficiency of Axial-Flow Turbines". *ASME Turbo Expo: Power for Land, Sea, and Air*, pp. 1–10. DOI: https://doi.org/10.1115/82-GT-43.

Luers, M., M. Sagebaum, S. Mann, J. Backhaus, D. Grossmann, and N. R. Gauger (2018). "Adjoint-Based Volumetric Shape Optimization of Turbine Blades". *AIAA Multidisciplinary Analysis and Optimization Conference*, pp. 1–14. DOI: https://doi.org/10.2514/6.2018-3638.

Luo, J., F. Liu, and I. McBean (2015). "Turbine Blade Row Optimization Through Endwall Contouring by an Adjoint Method". *Journal of Propulsion and Power* 31.2, pp. 1–14. DOI: https://doi.org/10.2514/1.B35152.

Luo, J., J. Xiong, F. Liu, and I. McBean (2010). "Three-Dimensional Aerodynamic Design Optimization of a Turbine Blade by Using an Adjoint Method". *Journal of Turbomachinery* 133.1, pp. 1–11. DOI: https://doi.org/10.1115/1.4001166.

Luo, J., C. Zhou, and F. Liu (2013). "Multipoint Design Optimization of a Transonic Compressor Blade by Using an Adjoint Method". *Journal of Turbomachinery* 136.5, pp. 1–10. DOI: https://doi.org/10.1115/1.4025164.

Lyness, J. N. and C. B. Moler (1967). "Numerical differentiation of analytic functions". *SIAM Journal on Numerical Analysis* 4.2, pp. 202–210. DOI: https://doi.org/10.1137/0704019.

Macchi, E. and M. Astolfi (2017). "Axial Flow Turbines for Organic Rankine Cycle Applications". *Organic Rankine Cycle (ORC) Power Systems: Technologies and Applications*. Ed. by E. Macchi and M. Astolfi. 1st. Woodhead Publising.

Macchi, E. and A. Perdichizzi (1981). "Efficiency Prediction for Axial-Flow Turbines Operating with Nonconventional Fluids". *Journal of Engineering for Power* 103.4, pp. 718–724. DOI: http://dx.doi.org/10.1115/1.3230794.

Martins, J. R. R. A., P. Sturdza, and J. J. Alonso (2003). "The Complex-Step Derivative Approximation". *ACM Transactions on Mathematical Software (TOMS)* 3, pp. 245–262. DOI: https://doi.org/10.1145/838250.838251.

Mavriplis, D. (2003). "Revisiting the Least-Squares Procedure for Gradient Reconstruction on Unstructured Meshes". *16th AIAA Computational Fluid Dynamics Conference*, pp. 1–13. DOI: https://doi.org/10.2514/6.2003-3986.

McDonald, C. F. (2012). "Helium Turbomachinery Operating Experience from Gas Turbine Power Plants and Test Facilities". *Applied Thermal Engineering* 44, pp. 108–142. DOI: https://doi.org/10.1016/j.applthermaleng.2012.02.041.

Menter, F. R. (1994). "Two-Equation Eddy-Viscosity Turbulence Models for Engineering Applications". *AIAA Journal* 32.8, pp. 1598–1605. DOI: https://doi.org/10.2514/3.12149.

Meroni, A., J. Graa, G. Persico, and F. Haglind (2018a). "Optimization of Organic Rankine Cycle Power Systems Considering Multistage Axial Turbine Design". *Applied Energy* 209, pp. 339–354. DOI: https://doi.org/10.1016/j.apenergy.2017.09.068.

Meroni, A., A. La Seta, J. Andreasen, L. Pierobon, G. Persico, and F. Haglind (2016a). "Combined Turbine and Cycle Optimization for Organic Rankine Cycle Power Systems–Part A: Turbine Model". *Energies* 9.5, pp. 1–15. DOI: https://doi.org/10.3390/en9050313.

Meroni, A., A. La Seta, J. Andreasen, L. Pierobon, G. Persico, and F. Haglind (2016b). "Combined Turbine and Cycle Optimization for Organic Rankine Cycle Power Systems–Part B: Case Study". *Energies* 9.5, pp. 1–17. DOI: https://doi.org/10.3390/en9060393.

Meroni, A., B. Zühlsdorf, B. Elmegaard, and F. Haglind (2018b). "Design of Centrifugal Compressors for Heat Pump Systems". *Applied Energy* 232, pp. 139–156. DOI: https://doi.org/10.1016/j.apenergy.2018.09.210.

Miller IV, P. L., J. H. Oliver, D. P. Miller, and D. L. Tweedt (1996). "BladeCAD: An Interactive Geometric Design Tool for Turbomachinery Blades". *ASME Turbo Expo: Power for Land, Sea, and Air*, pp. 1–8. DOI: https://doi.org/10.1115/96-GT-058.

Montanelli, H., M. Montagnac, and F. Gallard (2015). "Gradient Span Analysis Method: Application to the Multipoint Aerodynamic Shape Optimization of a Turbine Cascade". *Journal of Turbomachinery* 137.9, pp. 1–8. DOI: https://doi.org/10.1115/1.4030016.

Mounier, V., C. Picard, and J. Schiffmann (2018). "Data-Driven Predesign Tool for Small-Scale Centrifugal Compressor in Refrigeration". *Journal of Engineering for Gas Turbines and Power* 140.12. DOI: https://doi.org/10.1115/1.4040845.

Moustapha, S. H., S. C. Kacker, and B. Tremblay (1982). "An Improved Incidence Losses Prediction Method for Turbine Airfoils". *Journal of Turbomachinery* 112.2, pp. 267–276. DOI: https://doi.org/10.1115/1.2927647.

Mueller, L., Z. Alsalihi, and T. Verstraete (2012). "Multidisciplinary Optimization of a Turbocharger Radial Turbine". *Journal of Turbomachinery* 135.2, pp. 1–9. DOI: https://doi.org/10.1115/1.4007507.

Müller, L. and T. Verstraete (2017). "CAD Integrated Multipoint Adjoint-Based Optimization of a Turbocharger Radial Turbine". *International Journal of Turbomachinery, Propulsion and Power* 2.3, pp. 1–14. DOI: https://doi.org/10.3390/ijtpp2030014.

Mykhaskiv, O., M. Banović, S. Auriemma, P. Mohanamuraly, A. Walther, H. Legrand, and J.-D. Müller (2018). "NURBS-Based and Parametric-Based Shape Optimization with Differentiated CAD Kernel". *Computer-Aided Design and*

Applications 15.6, pp. 916–926. DOI: https://doi.org/10.1080/16864360.2018.1462881.

Nami, H., I. S. Ertesvåg, R. Agromayor, L. Riboldi, and L. O. Nord (2018). "Gas Turbine Exhaust Gas Heat Recovery by Organic Rankine Cycles (ORC) for Offshore Combined Heat and Power Applications – Energy and Exergy Analysis". *Energy* 165, pp. 1060–1071. DOI: https://doi.org/10.1016/j.energy.2018.10.034.

Nocedal, J. (1980). "Updating Quasi-Newton Matrices with Limited Storage". *Mathematics of Computation* 35.151, pp. 773–782. DOI: https://doi.org/10.2307/2006193.

Nocedal, J. and S. J. Wright (2006). *Numerical Optimization*. 2nd. Springer. DOI: https://doi.org/10.1007/978-0-387-40065-5.

Oyama, A., M.-S. Liou, and S. Obayashi (2004). "Transonic Axial-Flow Blade Optimization: Evolutionary Algorithms/Three-Dimensional Navier-Stokes Solver". *Journal of Propulsion and Power* 20.4, pp. 612–619. DOI: https://doi.org/10.2514/1.2290.

Palacios, F., J. Alonso, K. Duraisamy, M. Colonno, J. Hicken, A. Aranake, A. Campos, S. Copeland, T. Economon, A. Lonkar, T. Lukaczyk, and T. Taylor (2013). "Stanford University Unstructured (SU^2): An Open-Source Integrated Computational Environment for Multi-Physics Simulation and Design". *51st AIAA Aerospace Sciences Meeting including the New Horizons Forum and Aerospace Exposition*, pp. 1–60. DOI: https://doi.org/10.2514/6.2013-287.

Papadimitriou, D. I. and K. C. Giannakoglou (2006). "Compressor Blade Optimization Using a Continuous Adjoint Formulation". *ASME Turbo Expo: Power for Land, Sea, and Air*, pp. 1–9. DOI: https://doi.org/10.1115/GT2006-90466.

Pardiñas, Á. Á., M. Pilarczyk, R. Agromayor, and L. O. Nord (2019). "Design of an Experimental ORC Expander Setup Using Natural Working Fluids". *Proceedings of the 5th International Seminar on ORC Power Systems*, pp. 1–8.

Pasquale, D., A. Ghidoni, and S. Rebay (2013). "Shape Optimization of an Organic Rankine Cycle Radial Turbine Nozzle". *Journal of Engineering for Gas Turbines and Power* 135.4, pp. 1–13. DOI: https://doi.org/10.1115/1.4023118.

Peng, D.-Y. and D. B. Robinson (1976). "A New Two-Constant Equation of State". *Industrial & Engineering Chemistry Fundamentals* 15.1, pp. 59–64. DOI: https://doi.org/10.1021/i160057a011.

Perdichizzi, A. and G. Lozza (1987). "Design Criteria and Efficiency Prediction for Radial Inflow Turbines". *ASME Turbo Expo: Power for Land, Sea, and Air*, pp. 1–9. DOI: https://doi.org/10.1115/87-GT-231.

Perkins, R. A. (2002). "Measurement and Correlation of the Thermal Conductivity of Isobutane from 114 K to 600 K at Pressures to 70 MPa". *Journal of*

Chemical & Engineering Data 47.5, pp. 1272–1279. DOI: https://doi.org/10.1021/je010121u.

Persico, G., P. Rodriguez-Fernandez, and A. Romei (2019). "High-Fidelity Shape Optimization of Non-Conventional Turbomachinery by Surrogate Evolutionary Strategies". *Journal of Turbomachinery* 141.8, pp. 1–11. DOI: https://doi.org/10.1115/1.4043252.

Peter, J. E. V. and R. P. Dwight (2010). "Numerical Sensitivity Analysis for Aerodynamic Optimization: A Survey of Approaches". *Computers & Fluids* 3, pp. 373–391. DOI: https://doi.org/10.1016/j.compfluid.2009.09.013.

Piegl, L. (1991). "On NURBS: a survey". *IEEE Computer Graphics and Applications* 11.1, pp. 55–71. DOI: https://doi.org/10.1109/38.67702.

Piegl, L. and W. Tiller (2012). *The NURBS Book*. 2nd. Springer Science & Business Media. DOI: https://doi.org/10.1007/978-3-642-97385-7.

Pierret, S. and R. A. Van den Braembussche (1999). "Turbomachinery Blade Design Using a Navier-Stokes Solver and Artificial Neural Network". *Journal of Turbomachinery* 121.2, pp. 326–332. DOI: https://doi.org/10.1115/1.2841318.

Pierret, S., A. Demeulenaere, B. Gouverneur, and R. Van den Braembussche (2000). "Designing Turbomachinery Blades with the Function Approximation Concept and the Navier-Stokes Equations". *8th Symposium on Multidisciplinary Analysis and Optimization*, pp. 1–11. DOI: https://doi.org/10.2514/6.2000-4879.

Pierzga, M. J. and J. R. Wood (1985). "Investigation of the Three-Dimensional Flow Field Within a Transonic Fan Rotor: Experiment and Analysis". *Journal of Engineering for Gas Turbines and Power* 107.2, pp. 436–448. DOI: https://doi.org/10.1115/1.3239744.

Pierzga, M. J. and J. R. Wood (1989). *Laser Anemometer Measurements in a Transonic Axial-Flow Fan Rotor*. Tech. rep. TP 2879. NASA Lewis Research Center; Cleveland, OH, United States, pp. 1–216.

Pili, R., N. Siamisiis, R. Agromayor, L. O. Nord, C. Wieland, and H. Spliethoff (2019). "Efficiency Correlations for Off-Design Performance Prediction of ORC Axial-Flow Turbines". *Proceedings of the 5th International Seminar on ORC Power Systems*, pp. 1–8.

Pini, M., G. Persico, D. Pasquale, and S. Rebay (2014). "Adjoint Method for Shape Optimization in Real-Gas Flow Applications". *Journal of Engineering for Gas Turbines and Power* 137.3, pp. 1–13. DOI: https://doi.org/10.1115/1.4028495.

Pini, M. and G. Persico (2017). "Fluid Dynamic Design of Organic Rankine Cycle Turbines". *Organic Rankine Cycle (ORC) Power Systems: Technologies and Applications*. Ed. by E. Macchi and M. Astolfi. 1st. Woodhead Publising.

Pini, M., G. Persico, E. Casati, and V. Dossena (2013). "Preliminary Design of a Centrifugal Turbine for Organic Rankine Cycle Applications". *Journal of*

Engineering for Gas Turbines and Power 135.4, pp. 1–9. DOI: http://dx.doi.org/10.1115/1.4023122.

Pironneau, O. (1974). "On Optimum Design in Fluid Mechanics". *Journal of Fluid Mechanics* 1, pp. 97–110.

Press, W. H., S. A. Teukolsky, W. T. Vetterling, and B. P. Flannery (2007). *Numerical Recipes: The Art of Scientific Computing*. 3rd. Cambridge University Press.

Pritchard, L. J. (1985). "An Eleven Parameter Axial Turbine Airfoil Geometry Model". *ASME Turbo Expo: Power for Land, Sea, and Air*, pp. 1–12. DOI: https://doi.org/10.1115/85-GT-219.

Rahbar, K., S. Mahmoud, R. K. Al-Dadah, and N. Moazami (2015). "Parametric Analysis and Optimization of a Small-Scale Radial Turbine for Organic Rankine Cycle". *Energy* 83, pp. 696–711. DOI: http://dx.doi.org/10.1016/j.energy.2015.02.079.

Reuther, J., A. Jameson, J. Farmer, L. Martinelli, and D. Saunders (1996). "Aerodynamic Shape Optimization of Complex Aircraft Configurations via an Adjoint Formulation". *34th AIAA Aerospace Sciences Meeting and Exhibit*, pp. 1–19. DOI: https://doi.org/10.2514/6.1996-94.

Roe, P. L. (1981). "Approximate Riemann Solvers, Parameter Vectors, and Difference Schemes". *Journal of Computational Physics* 43.2, pp. 357–372. DOI: https://doi.org/10.1016/0021-9991(81)90128-5.

Romei, A., P. Gaetani, A. Giostri, and G. Persico (2020). "The Role of Turbomachinery Performance in the Optimization of Supercritical Carbon Dioxide Power Systems". *Journal of Turbomachinery* 142.7, pp. 1–11. DOI: https://doi.org/10.1115/1.4046182.

Rúa, J., R. Agromayor, M. Hillestad, and L. O. Nord (2020). "Optimal Dynamic Operation of Natural Gas Combined Cycles Accounting for Stresses in Thick-Walled Components". *Applied Thermal Engineering* 170, pp. 1–13. DOI: https://doi.org/10.1016/j.applthermaleng.2019.114858.

Rubino, A., S. Vitale, P. Colonna, and M. Pini (2020). "Fully-Turbulent Adjoint Method for the Unsteady Shape Optimization of Multi-Row Turbomachinery". *Aerospace Science and Technology* 106, pp. 1–12. DOI: https://doi.org/10.1016/j.ast.2020.106132.

Russo, V., S. Orsenigo, L. Mueller, T. Verstraete, and S. Lavagnoli (2019). "Adjoint Based Aerodynamic Optimization of a Multi-Splitter Turbine Vane Frame". *ASME Turbo Expo: Power for Land, Sea, and Air*, pp. 1–13. DOI: https://doi.org/10.1115/GT2019-91608.

Saad, Y. (2003). *Iterative Methods for Sparse Linear Systems*. 2nd. Society for Industrial and Applied Mathematics. DOI: https://doi.org/10.1137/1.9780898718003.

Sagebaum, M., T. Albring, and N. R. Gauger (2018). "Expression Templates for Primal Value Taping in the Reverse Mode of Algorithmic Differentiation".

Optimization Methods and Software 33.4-6, pp. 1207–1231. DOI: https://doi.org/10.1080/10556788.2018.1471140.

Sagebaum, M., T. Albring, and N. R. Gauger (2019). "High-Performance Derivative Computations using CoDiPack". *ACM Transactions on Mathematical Software* 45.4, pp. 1–26. DOI: https://doi.org/10.1145/3356900.

Samad, A., K.-Y. Kim, T. Goel, R. T. Haftka, and W. Shyy (2008). "Multiple Surrogate Modeling for Axial Compressor Blade Shape Optimization". *Journal of Propulsion and Power* 24.2, pp. 301–310. DOI: https://doi.org/10.2514/1.28999.

Samareh, J. A. (2001). "Survey of Shape Parameterization Techniques for High-Fidelity Multidisciplinary Shape Optimization". *AIAA journal* 5, pp. 877–884. DOI: https://doi.org/10.2514/2.1391.

Saravanamuttoo, H. I. H., G. F. C. Rogers, and H. Cohen (2009). *Gas Turbine Theory*. 6th. Pearson Education.

Saxer, A. P. and M. B. Giles (1993). "Quasi-Three-Dimensional Nonreflecting Boundary Conditions for Euler Equations Calculations". *Journal of Propulsion and Power* 9.2, pp. 263–271. DOI: https://doi.org/10.2514/3.23618.

Saxer, A. P. and M. B. Giles (1994). "Predictions of Three-Dimensional Steady and Unsteady Inviscid Transonic Stator/Rotor Interaction With Inlet Radial Temperature Nonuniformity". *Journal of Turbomachinery* 116.3, pp. 347–357. DOI: https://doi.org/10.1115/1.2929421.

SciPy v1.5 (2020). URL: https://scipy.org/.

Shampine, L. F. and M. W. Reichelt (1997). "The MATLAB ODE Suite". *SIAM Journal on Scientific Computing* 18.1, pp. 1–22. DOI: https://doi.org/10.1137/S1064827594276424.

Siddappaji, K., M. G. Turner, and A. Merchant (2012). "General Capability of Parametric 3D Blade Design Tool for Turbomachinery". *ASME Turbo Expo: Power for Land, Sea, and Air*, pp. 1–14. DOI: https://doi.org/10.1115/GT2012-69756.

Squire, W. and G. Trapp (1998). "Using Complex Variables to Estimate Derivatives of Real Functions". *SIAM Review* 40.1, pp. 110–112. DOI: https://doi.org/10.1137/S003614459631241X.

Stadtmüller, P. and L. Fottner (2001). "A Test Case for the Numerical Investigation of Wake Passing Effects on a Highly Loaded LP Turbine Cascade Blade". *ASME Turbo Expo: Power for Land, Sea, and Air*. American Society of Mechanical Engineers Digital Collection, pp. 1–8. DOI: https://doi.org/10.1115/2001-GT-0311.

Stanitz, J. D. (1952). *One-dimensional Compressible Flow in Vaneless Diffusers of Radial- and Mixed-flow Centrifugal Compressors, Including Effects of Friction, Heat Transfer and Area Change*. Tech. rep. TN 2610. NACA Flight Propulsion Research Laboratory; Cleveland, OH, United States, pp. 1–62.

Stephan, B., H. E. Gallus, and R. Niehuis (2001). "Experimental Investigations of Tip Clearance Flow and Its Influence on Secondary Flows in a 1-1/2 Stage

Axial Turbine". *ASME Turbo Expo: Power for Land, Sea, and Air*. American Society of Mechanical Engineers Digital Collection, pp. 1–12. DOI: https://doi.org/10.1115/2000-GT-0613.

Talluri, L. and G. Lombardi (2017). "Simulation and Design Tool for ORC Axial Turbine Stage". *Energy Procedia* 129, pp. 277–284. DOI: https://doi.org/10.1016/j.egypro.2017.09.154.

Tang, X., J. Luo, and F. Liu (2018). "Adjoint Aerodynamic Optimization of a Transonic Fan Rotor Blade with a Localized Two-Level Mesh Deformation Method". *Aerospace Science and Technology* 72, pp. 267–277. DOI: https://doi.org/10.1016/j.ast.2017.11.015.

Taylor, N. J. (2015). "Industrial Perspectives on Geometry Handling for Aerodynamics". *22nd AIAA Computational Fluid Dynamics Conference*, pp. 1–12. DOI: https://doi.org/10.2514/6.2015-3408.

Torreguitart, I., T. Verstraete, and L. Mueller (2019). "CAD and Adjoint Based Multipoint Optimization of an Axial Turbine Profile". *Evolutionary and Deterministic Methods for Design Optimization and Control With Applications to Industrial and Societal Problems*. Ed. by E. Andrés-Pérez, L. M. González, J. Periaux, N. Gauger, D. Quagliarella, and K. Giannakoglou. Springer International Publishing, pp. 35–46. DOI: https://doi.org/10.1007/978-3-319-89890-2_3.

Torreguitart, I., T. Verstraete, and L. Müller (2018). "Optimization of the LS89 Axial Turbine Profile Using a CAD and Adjoint Based approach". *International Journal of Turbomachinery, Propulsion and Power* 3.3, pp. 1–20. DOI: https://doi.org/10.3390/ijtpp3030020.

Tournier, J.-M. and M. S. El-Genk (2010). "Axial Flow, Multi-Stage Turbine and Compressor Models". *Energy Conversion and Management* 51.1, pp. 16–29. DOI: https://doi.org/10.1016/j.enconman.2009.08.005.

Traupel, W. (1982). *Thermische Turbomaschinen*. 3rd. Springer-Verlag, Berlin.

Trigg, M. A., G. R. Tubby, and A. G. Sheard (1999). "Automatic Genetic Optimization Approach to Two-Dimensional Blade Profile Design for Steam Turbines". *Journal of Turbomachinery* 121.1, pp. 11–17. DOI: https://doi.org/10.1115/1.2841220.

Uusitalo, A., T. Turunen-saaresti, J. Honkatukia, and J. Backman (2015). "Combined Thermodynamic and Turbine Design Analysis". *Proceedings of the 3rd International Seminar on ORC Power Systems*, pp. 1–10.

Van Albada, G. D., B. Van Leer, and W. W. Roberts (1997). "A Comparative Study of Computational Methods in Cosmic Gas Dynamics". *Upwind and High-Resolution Schemes*, pp. 95–103. DOI: https://doi.org/10.1007/978-3-642-60543-7_6.

van Arnhem, N., R. de Vries, T. Sinnige, R. Vos, G. Eitelberg, and L. Veldhuis (2020). "Engineering Method to Estimate the Blade Loading of Propellers in Nonuniform Flow". *AIAA Journal* 58.12, pp. 5332–5346. DOI: https://doi.org/10.2514/1.J059485.

Van den Braembussche, R. A. (2008). "Numerical Optimization for Advanced Turbomachinery Design". *Optimization and Computational Fluid Dynamics*. Ed. by D. Thévenin and G. Janiga, pp. 147–189. DOI: https://doi.org/10.1007/978-3-540-72153-6_6.

van Leer, B. (1979). "Towards the Ultimate Conservative Difference Scheme. V. A Second-Order Sequel to Godunov's Method". *Journal of Computational Physics* 32.1, pp. 101–136. DOI: https://doi.org/10.1016/0021-9991(79)90145-1.

Verstraete, T. (2010). "CADO: A Computer Aided Design and Optimization Tool for Turbomachinery Applications". *Proceedings of the 2nd International Conference on Engineering Optimization, Lisbon, Portugal*, pp. 1–10.

Verstraete, T. (2019). "Toward Gradient-Based Optimization of Full Gas Turbines". *Mechanical Engineering* 141.3, pp. 54–55. DOI: https://doi.org/10.1115/1.2019-MAR-7.

Vinokur, M. and J.-L. Montagné (1990). "Generalized Flux-Vector Splitting and Roe Average for an Equilibrium Real Gas". *Journal of Computational Physics* 89.2, pp. 276–300. DOI: https://doi.org/10.1016/0021-9991(90)90145-Q.

Vitale, S., M. Pini, and P. Colonna (2020). "Multistage Turbomachinery Design Using the Discrete Adjoint Method Within the Open-Source Software SU2". *Journal of Propulsion and Power* 36.3, pp. 465–478. DOI: https://doi.org/10.2514/1.B37685.

Vitale, S., T. A. Albring, M. Pini, N. R. Gauger, and P. Colonna (2017). "Fully Turbulent Discrete Adjoint Solver for Non-Ideal Compressible Flow Applications". *Journal of the Global Power and Propulsion Society* 1, pp. 252–270. DOI: https://doi.org/10.22261/JGPPS.Z1FVOI.

Vitale, S., G. Gori, M. Pini, A. Guardone, T. D. Economon, F. Palacios, J. J. Alonso, and P. Colonna (2015). "Extension of the SU2 Open Source CFD Code to the Simulation of Turbulent Flows of Fluids Modelled with Complex Thermophysical Laws". *22nd AIAA Computational Fluid Dynamics Conference*, pp. 1–22. DOI: https://doi.org/10.2514/6.2015-2760.

Vogel, E., C. Küchenmeister, and E. Bich (2000). "Viscosity Correlation for Isobutane Over Wide Ranges of the Fluid Region". *International Journal of Thermophysics* 21.2, pp. 343–356. DOI: https://doi.org/10.1023/A:1006623310780.

Walther, B. and S. Nadarajah (2012). "Constrained Adjoint-Based Aerodynamic Shape Optimization of a Single-Stage Transonic Compressor". *Journal of Turbomachinery* 135.2, pp. 1–10. DOI: https://doi.org/10.1115/1.4007502.

Walther, B. and S. Nadarajah (2014). "An Adjoint-Based Optimization Method for Constrained Aerodynamic Shape Design of Three-Dimensional Blades in Multi-Row Turbomachinery Configurations". *ASME Turbo Expo: Power for Land, Sea, and Air*, pp. 1–16. DOI: https://doi.org/10.1115/GT2014-26604.

Walther, B. and S. Nadarajah (2015a). "Adjoint-Based Constrained Aerodynamic Shape Optimization for Multistage Turbomachines". *Journal of Propulsion and Power* 31.5, pp. 1–22. DOI: https://doi.org/10.2514/1.B35433.

Walther, B. and S. Nadarajah (2015b). "An Adjoint-Based Multi-Point Optimization Method for Robust Turbomachinery Design". *ASME Turbo Expo: Power for Land, Sea, and Air*, pp. 1–12. DOI: https://doi.org/10.1115/GT2015-44142.

Walther, B. and S. Nadarajah (2015c). "Optimum Shape Design for Multirow Turbomachinery Configurations Using a Discrete Adjoint Approach and an Efficient Radial Basis Function Deformation Scheme for Complex Multiblock Grids". *Journal of Turbomachinery* 137.8, pp. 1–20. DOI: https://doi.org/10.1115/1.4029550.

Wang, D. X. and L. He (2010a). "Adjoint Aerodynamic Design Optimization for Blades in Multistage Turbomachines–Part I: Methodology and Verification". *Journal of Turbomachinery* 132.2, pp. 1–14. DOI: https://doi.org/10.1115/1.3072498.

Wang, D. X., L. He, Y. S. Li, and R. G. Wells (2010b). "Adjoint Aerodynamic Design Optimization for Blades in Multistage Turbomachines–Part II: Validation and Application". *Journal of Turbomachinery* 132.2, pp. 1–11. DOI: https://doi.org/10.1115/1.3103928.

Weiss, J., J. Maruszewski, and W. Smith (1997). "Implicit Solution of the Navier-Stokes Equations on Unstructured Meshes". *13th AIAA Computational Fluid Dynamics Conference*, pp. 139–149. DOI: https://doi.org/10.2514/6.1997-2103.

White, F. M. (2006). *Viscous Fluid Flow*. 3rd. McGraw-Hill.

White, F. M. (2011). *Fluid Mechanics*. 7th. McGraw-Hill.

Wu, H.-Y., F. Liu, and H.-M. Tsai (2005). "Aerodynamic Design of Turbine Blades Using an Adjoint Equation Method". *43rd AIAA Aerospace Sciences Meeting and Exhibit*, pp. 1–13. DOI: https://doi.org/10.2514/6.2005-1006.

Wu, H.-Y., S. Yang, F. Liu, and H.-M. Tsai (2003). "Comparisons of Three Geometric Representations of Airfoils for Aerodynamic Optimization". *16th AIAA Computational Fluid Dynamics Conference*, pp. 1–11. DOI: https://doi.org/10.2514/6.2003-4095.

Xu, S., D. Radford, M. Meyer, and J.-D. Müller (2015). "CAD-Based Adjoint Shape Optimisation of a One-Stage Turbine With Geometric Constraints". *ASME Turbo Expo: Power for Land, Sea, and Air*, pp. 1–14. DOI: https://doi.org/10.1115/GT2015-42237.

Xu, S., S. Timme, O. Mykhaskiv, and J.-D. Müller (2017). "Wing-Body Junction Optimisation with CAD-Based Parametrisation Including a Moving Intersection". *Aerospace Science and Technology* 68, pp. 543–551. DOI: https://doi.org/10.1016/j.ast.2017.06.014.

Yang, S., H.-Y. Wu, F. Liu, and H.-M. Tsai (2003). "Optimum Aerodynamic Design of Cascades by Using an Adjoint Equation Method". *41st AIAA Aerospace*

Sciences Meeting and Exhibit, pp. 1–12. DOI: https://doi.org/10.2514/6.2003-1068.

Ye, Z. Q. (1984). "A Systematic Computational Design System for Turbine Cascades, Airfoil Geometry and Blade-to-Blade Analysis". *Journal of Engineering for Gas Turbines and Power*, pp. 598–605. DOI: https://doi.org/10.1115/1.3239612.

Appendix A

Derivation of the Governing Equations for the Flow in an Annular Duct

This appendix contains the derivation the governing equations for steady, one-dimensional flow in an annular channel with area change, heat transfer, and friction for the case of a fluid described by arbitrary equations of state, see Chapter 2.

A.1 Groundwork

The starting point for the derivation of the governing equations is the integral form of the mass, momentum, energy, and entropy balance equations for a fixed control volume. The integral form of these equations can be found in any fluid mechanics textbook such as White (2011). The integral equations are applied to the differential control volume depicted in Figure 2.3 to determine the differential form of the equations. First, the transport equation for mass is derived and then it is used to obtain the transport equation for a general quantity. After this, the general transport equation is used to derive the momentum, energy, and entropy equations in a systematic way. Once the differential equations are found, they are simplified assuming that the flow is steady and axisymmetric to determine the one-dimensional equations used to model the diffuser.

The symbol $\mathbf{e}$ is used to denote the unitary vectors in the different coordinate directions: $\mathbf{e}_\theta$–tangential, $\mathbf{e}_x$–axial, $\mathbf{e}_r$–radial, $\mathbf{e}_m$–meridional, and $\mathbf{e}_n$–normal. The unitary vectors in the meridional–normal plane are related to the unitary vectors in the axial–radial plane according to

$$\mathbf{e}_m = \cos(\phi)\,\mathbf{e}_x + \sin(\phi)\,\mathbf{e}_r \tag{A.1}$$

$$\mathbf{e}_n = -\sin(\phi)\,\mathbf{e}_x + \cos(\phi)\,\mathbf{e}_r. \tag{A.2}$$

The derivatives of the meridional and tangential vectors along the meridional and tangential directions are are given by Eqs. (A.3) to (A.6). These equations can be derived using the chain rule for differentiation and geometric relations between the coordinate directions. Space derivatives of the unitary vectors are

Table A.1: Normal vectors and surface elements of the differential control volume.

Face	Number	$\mathbf{n}$	$\mathrm{d}S$
Front	1	$-\mathbf{e}_m$	$rb\,\mathrm{d}\theta$
Back	2	$+\mathbf{e}_m$	$rb\,\mathrm{d}\theta$
Left	3	$-\mathbf{e}_\theta$	$b\,\mathrm{d}m$
Right	4	$+\mathbf{e}_\theta$	$b\,\mathrm{d}m$
Bottom	5	$-\mathbf{e}_n$	$r\,\mathrm{d}\theta\mathrm{d}m$
Top	6	$+\mathbf{e}_n$	$r\,\mathrm{d}\theta\mathrm{d}m$

non-zero due to the curvature of the coordinate system and they are necessary to derive the momentum transport equation. The term R_m is the radius of curvature of the mean surface of the annular channel and it can be expressed in different ways depending on the parametrization used. However, this term is not of concern because it does not appear on the final equations for one-dimensional flow.

$$\frac{\mathrm{d}\mathbf{e}_m}{\mathrm{d}m} = \frac{\mathrm{d}^2 r}{\mathrm{d}x^2} \cdot \left(1 + \left(\frac{\mathrm{d}r}{\mathrm{d}x}\right)^2\right)^{-\frac{3}{2}} \mathbf{e}_n = \frac{1}{R_m}\,\mathbf{e}_n \tag{A.3}$$

$$\frac{\mathrm{d}\mathbf{e}_m}{\mathrm{d}\theta} = \sin(\phi)\,\mathbf{e}_\theta \tag{A.4}$$

$$\frac{\mathrm{d}\mathbf{e}_\theta}{\mathrm{d}m} = 0 \tag{A.5}$$

$$\frac{\mathrm{d}\mathbf{e}_\theta}{\mathrm{d}\theta} = -\mathbf{e}_r = -\sin(\phi)\,\mathbf{e}_m - \cos(\phi)\,\mathbf{e}_n \tag{A.6}$$

The velocity vector can be expressed in terms of the unitary vectors as

$$\mathbf{v} = v_m\,\mathbf{e}_m + v_\theta\,\mathbf{e}_\theta \tag{A.7}$$

$$\mathbf{v} = v_x\,\mathbf{e}_x + v_r\,\mathbf{e}_r + v_\theta\,\mathbf{e}_\theta \tag{A.8}$$

The volume of the differential control volume is given by $\mathrm{d}V = b\,r\,\mathrm{d}\theta\mathrm{d}m$, while the normal vectors and surface elements of the differential control surface are summarized in Table A.1. These variables are necessary to evaluate the integrals appearing on the balance equations

A.2 Transport equation for mass

The integral form of the mass balance equation is given by Eq. (A.9). This equation indicates that the rate of change of mass within the control volume plus the net mass flow rate leaving the control volume is equal to zero (i.e., mass is conserved).

$$\int_{\mathrm{CV}} \frac{\partial \rho}{\partial t}\,\mathrm{d}V + \int_{\mathrm{CS}} \rho\,(\mathbf{v}\cdot\mathbf{n})\,\mathrm{d}S = 0 \tag{A.9}$$

The accumulation term is approximated by Eq. (A.10).

$$\int_{\mathrm{CV}} \frac{\partial \rho}{\partial t}\,\mathrm{d}V \approx \frac{\partial \rho}{\partial t}\,\mathrm{d}V = \frac{\partial \rho}{\partial t}\,b\,r\mathrm{d}\theta\mathrm{d}m \tag{A.10}$$

The convective term is approximated by Eq. (A.11). This expression is found integrating the mass flux over the six faces of the differential control volume using the normal vectors and surface elements from Table A.1 and the velocity vector given by Eq. (A.7).

$$\begin{aligned}\int_{\mathrm{CS}} \rho\,(\mathbf{v}\cdot\mathbf{n})\;\mathrm{d}S &\approx \sum_{i=1}^{6} \rho_i\,(\mathbf{v}_i\cdot\mathbf{n}_i)\;\mathrm{d}S_i \\ &\approx [\rho v_m r\,b\,\mathrm{d}\theta]_2 - [\rho v_m r\,b\,\mathrm{d}\theta]_1 + [\rho v_\theta b\,\mathrm{d}m]_4 - [\rho v_\theta b\,\mathrm{d}m]_3\end{aligned} \tag{A.11}$$

The different summands of Eq. (A.11) are approximated by a first order Taylor expansion. The Taylor expansions of a generic property β in the meridional and tangential directions are given by Eqs. (A.12) and (A.13), respectively.

$$\beta_2 - \beta_1 = \left(\beta + \frac{\partial \beta}{\partial m}\frac{\mathrm{d}m}{2}\right) - \left(\beta - \frac{\partial \beta}{\partial m}\frac{\mathrm{d}m}{2}\right) + \mathcal{O}(\mathrm{d}m^2) \approx \frac{\partial \beta}{\partial m}\mathrm{d}m \tag{A.12}$$

$$\beta_4 - \beta_3 = \left(\beta + \frac{\partial \beta}{\partial \theta}\frac{\mathrm{d}\theta}{2}\right) - \left(\beta - \frac{\partial \beta}{\partial \theta}\frac{\mathrm{d}\theta}{2}\right) + \mathcal{O}(\mathrm{d}\theta^2) \approx \frac{\partial \beta}{\partial \theta}\mathrm{d}\theta \tag{A.13}$$

Inserting the Taylor expansions into Eq. (A.11) leads to Eq. (A.14).

$$\int_{\mathrm{CS}} \rho\,(\mathbf{v}\cdot\mathbf{n})\;\mathrm{d}S \approx \frac{\partial}{\partial m}\,(\rho v_m r\,b)\;\mathrm{d}m\mathrm{d}\theta + \frac{\partial}{\partial \theta}\,(\rho v_\theta b)\;\mathrm{d}m\mathrm{d}\theta \tag{A.14}$$

Collecting the accumulation and the convective terms and dividing by $\mathrm{d}V$ leads to Eq. (A.15).

$$\frac{\partial \rho}{\partial t} + \frac{1}{b\,r}\frac{\partial}{\partial m}\,(\rho v_m r\,b) + \frac{1}{b\,r}\frac{\partial}{\partial \theta}\,(\rho v_\theta b) = 0 \tag{A.15}$$

Assuming steady and axisymmetric flow Eq. (A.15) reduces to Eq. (A.16), where the partial differentials were replaced by total differentials because the only variation is along the meridional direction.

$$\frac{\mathrm{d}}{\mathrm{d}m}\,(\rho v_m r\,b) = 0 \tag{A.16}$$

The final form of the mass transport equation, Eq. (A.17), is found using the product rule for differentiation and rearranging.

$$\boxed{v_m\frac{\mathrm{d}\rho}{\mathrm{d}m} + \rho\frac{\mathrm{d}v_m}{\mathrm{d}m} = -\frac{\rho v_m}{b\,r}\frac{\mathrm{d}}{\mathrm{d}m}(b\,r)} \tag{A.17}$$

A.3 Transport equation for a general quantity

The integral form of a general balance equation is given by Eq. (A.18). This equation indicates that the rate of change of any intensive quantity η within the control volume plus the net flow rate of η leaving the control volume is equal to the generation of η due to source terms S_η. In general, this quantity η can be a scalar such as energy or entropy or a vector such as the velocity.

$$\int_{\mathrm{CV}} \frac{\partial}{\partial t} \left(\rho\eta\right) \,\mathrm{d}V + \int_{\mathrm{CS}} \rho\eta \left(\mathbf{v}\cdot\mathbf{n}\right) \,\mathrm{d}S = S_\eta \tag{A.18}$$

The accumulation term is approximated by Eq. (A.19).

$$\int_{\mathrm{CV}} \frac{\partial}{\partial t} \left(\rho\eta\right) \,\mathrm{d}V \approx \frac{\partial}{\partial t} \left(\rho\eta\right) \,\mathrm{d}V = \frac{\partial}{\partial t} \left(\rho\eta\right) \, b\, r \mathrm{d}\theta \mathrm{d}m \tag{A.19}$$

The convective term is approximated by Eq. (A.20). This expression is found integrating the η-flux over the six faces of the differential control volume using the normal vectors and surface elements from Table A.1 and the velocity vector given by Eq. (A.7).

$$\begin{aligned} \int_{\mathrm{CS}} \rho\eta \left(\mathbf{v}\cdot\mathbf{n}\right) \,\mathrm{d}S &\approx \sum_{i=1}^{6} \rho_i\eta_i \left(\mathbf{v}_i\cdot\mathbf{n}_i\right) \,\mathrm{d}S_i \\ &\approx \left[\rho\eta v_m r\, b \,\mathrm{d}\theta\right]_2 - \left[\rho\eta v_m r\, b \,\mathrm{d}\theta\right]_1 + \left[\rho\eta v_\theta b \,\mathrm{d}m\right]_4 - \left[\rho\eta v_\theta b \,\mathrm{d}m\right]_3 \end{aligned} \tag{A.20}$$

The different summands of Eq. (A.20) are approximated by first order Taylor expansions, Eqs. (A.12) and (A.13), to find Eq. (A.21).

$$\int_{\mathrm{CS}} \rho\eta \left(\mathbf{v}\cdot\mathbf{n}\right) \,\mathrm{d}S \approx \frac{\partial}{\partial m} \left(\rho\eta v_m r\, b\right) \,\mathrm{d}m\mathrm{d}\theta + \frac{\partial}{\partial \theta} \left(\rho\eta v_\theta b\right) \,\mathrm{d}m\mathrm{d}\theta \tag{A.21}$$

Collecting the accumulation, convective, and source terms leads to Eq. (A.22).

$$\left[\frac{\partial}{\partial t} \left(\rho\eta\right) \, b\, r + \frac{\partial}{\partial m} \left(\rho\eta v_m r\, b\right) + \frac{\partial}{\partial \theta} \left(\rho\eta v_\theta b\right)\right] \mathrm{d}m\mathrm{d}\theta = S_\eta \tag{A.22}$$

Using the product rule for differentiation and the transport equation for mass, Eq. (A.22) can be expressed in non-conservative form as Eq. (A.23), where the differential volume is given by $\mathrm{d}V = b\, r\, \mathrm{d}\theta\mathrm{d}m$.

$$\rho \left[\frac{\partial \eta}{\partial t} + v_m \frac{\partial \eta}{\partial m} + \frac{v_\theta}{r} \frac{\partial \eta}{\partial \theta}\right] \mathrm{d}V = S_\eta \tag{A.23}$$

Eq. (A.23) is used in the next sections to derive the transport equations of momentum, energy and entropy in a systematic way.

A.4 Transport equations for momentum

The integral form of the momentum balance equation is given by Eq. (A.24). This equation indicates that the rate of change of momentum within the control volume plus the net flow rate of momentum leaving the control volume is equal to the net pressure forces acting on the control surfaces plus the body forces acting on the control volume. As discussed below, the viscous forces acting on the walls are modeled as a volume force rather than as a surface force.

$$\int_{\mathrm{CV}} \frac{\partial}{\partial t}\left(\rho \mathbf{v}\right) \mathrm{d}V + \int_{\mathrm{CS}} \rho \mathbf{v}\left(\mathbf{v}\cdot\mathbf{n}\right) \mathrm{d}S = -\int_{\mathrm{CS}} p\mathbf{n}\,\mathrm{d}S + \int_{\mathrm{CV}} \rho \mathbf{f}\,\mathrm{d}V \tag{A.24}$$

The left hand side of Eq. (A.24) is formulated in differential form, Eq. (A.25), by making the identification $\eta = \mathbf{v}$ in the general transport equation, Eq. (A.23).

$$\int_{\mathrm{CV}} \frac{\partial}{\partial t}\left(\rho \mathbf{v}\right) \mathrm{d}V + \int_{\mathrm{CS}} \rho \mathbf{v}\left(\mathbf{v}\cdot\mathbf{n}\right) \mathrm{d}S = \rho\left[\frac{\partial \mathbf{v}}{\partial t} + v_m \frac{\partial \mathbf{v}}{\partial m} + \frac{v_\theta}{r}\frac{\partial \mathbf{v}}{\partial \theta}\right] \mathrm{d}V \tag{A.25}$$

The meridional, tangential, and normal components of the momentum equation are given by Eq. (A.26). This equation found inserting the velocity vector given by Eq. (A.7) and using the product rule to account for the derivatives of the velocity components and the unitary vectors given by Eqs. (A.3) to (A.6).

$$\begin{aligned}\int_{\mathrm{CV}} \frac{\partial}{\partial t}\left(\rho \mathbf{v}\right) \mathrm{d}V + \int_{\mathrm{CS}} \rho \mathbf{v}\left(\mathbf{v}\cdot\mathbf{n}\right) \mathrm{d}S = {} & \mathbf{e}_m \left(\rho\left[\frac{\partial v_m}{\partial t} + v_m \frac{\partial v_m}{\partial m} + \frac{v_\theta}{r}\frac{\partial v_m}{\partial \theta} - \frac{v_\theta^2}{r}\,\sin\left(\phi\right)\right] \mathrm{d}V\right) \\ & + \mathbf{e}_\theta \left(\rho\left[\frac{\partial v_\theta}{\partial t} + v_m \frac{\partial v_\theta}{\partial m} + \frac{v_\theta}{r}\frac{\partial v_\theta}{\partial \theta} + \frac{v_m v_\theta}{r}\,\sin\left(\phi\right)\right] \mathrm{d}V\right) \\ & + \mathbf{e}_n \left(\rho\left[\frac{v_m^2}{R_m} - \frac{v_\theta^2}{r}\cos\left(\phi\right)\right] \mathrm{d}V\right)\end{aligned} \tag{A.26}$$

The surface integral of the pressure forces can be approximated by Eq. (A.27), where the first equality follows from a variation of the Gauss theorem for the surface integral of a scalar field. The gradient of pressure for the curvilinear coordinates used here is given by Eq. (A.28), see Aungier 2006a (Ch. 3).

$$-\int_{\mathrm{CS}} p\,\mathbf{n}\,\mathrm{d}S = -\int_{\mathrm{CV}} \nabla p\,\mathrm{d}V \approx \nabla p\,\mathrm{d}V \tag{A.27}$$

$$\nabla p = \frac{\partial p}{\partial m}\,\mathbf{e}_m + \frac{1}{r}\frac{\partial p}{\partial \theta}\,\mathbf{e}_\theta + \frac{\partial p}{\partial n}\,\mathbf{e}_n \tag{A.28}$$

The viscous force is approximated by Eq. (A.29). This force is modeled as a body force pointing in the opposite direction of the velocity vector and with magnitude given by the product of the stress at the walls and the surface of the walls

$\mathrm{d}S = 2r\,\mathrm{d}\theta\mathrm{d}m$. The factor 2 arises to account for the inner and outer surfaces.

$$\int_{\mathrm{CV}} \rho\mathbf{f}\,\mathrm{d}V \approx \boldsymbol{\tau}_{\mathrm{w}}\,\mathrm{d}S = -\tau_{\mathrm{w}}\,\frac{\mathbf{v}}{|\mathbf{v}|}\,\mathrm{d}S = -2\tau_{\mathrm{w}}\left[\cos(\alpha)\,\mathbf{e}_m + \sin(\alpha)\,\mathbf{e}_\theta\right]\,r\,\mathrm{d}\theta\mathrm{d}m \tag{A.29}$$

Collecting all terms and dividing by $\mathrm{d}V$, the meridional and tangential components of the momentum equation are given by Eqs. (A.30) and (A.31), respectively. The normal component is ignored because it is not used in the one-dimensional diffuser model.

$$\rho\left(\frac{\partial v_m}{\partial t} + v_m\frac{\partial v_m}{\partial m} + \frac{v_\theta}{r}\frac{\partial v_m}{\partial \theta} - \frac{v_\theta^2}{r}\,\sin(\phi)\right) = -\frac{\partial p}{\partial m} - \frac{2\tau_{\mathrm{w}}}{b}\cos(\alpha) \tag{A.30}$$

$$\rho\left(\frac{\partial v_\theta}{\partial t} + v_m\frac{\partial v_\theta}{\partial m} + \frac{v_\theta}{r}\frac{\partial v_\theta}{\partial \theta} + \frac{v_m v_\theta}{r}\,\sin(\phi)\right) = -\frac{1}{r}\frac{\partial p}{\partial \theta} - \frac{2\tau_{\mathrm{w}}}{b}\sin(\alpha) \tag{A.31}$$

The final form of the momentum equations, Eqs. (A.32) and (A.33), is found by assuming steady and axisymmetric flow. The partial differentials were replaced by total differentials because the only variation is along the meridional direction.

$$\boxed{\rho v_m\frac{\mathrm{d}v_m}{\mathrm{d}m} + \frac{\mathrm{d}p}{\mathrm{d}m} = \frac{\rho v_\theta^2}{r}\,\sin(\phi) - \frac{2\tau_{\mathrm{w}}}{b}\cos(\alpha)} \tag{A.32}$$

$$\boxed{\rho v_m\frac{\mathrm{d}v_\theta}{\mathrm{d}m} = -\frac{\rho v_\theta v_m}{r}\,\sin(\phi) - \frac{2\tau_{\mathrm{w}}}{b}\sin(\alpha)} \tag{A.33}$$

A.5 Transport equations for energy

A.5.1 Total energy

The integral form of the energy balance equation is given by Eq. (A.34) or by Eq. (A.35). Total energy is given by $E = e + \frac{v^2}{2}$, whereas the term $h_0 = E + \frac{p}{\rho}$ can be recognized as the stagnation enthalpy of the flow. These equations indicate that the rate of change of total energy within the control volume plus the net flow rate of total energy leaving the control volume is equal to the net heat flow rate entering the control volume plus the work done by pressure forces. The work done by viscous forces (modeled as a body force) is neglected to model the no-slip condition at the wall This aspect is is further discussed in the derivation of the entropy transport equation.

$$\int_{\mathrm{CV}}\frac{\partial}{\partial t}(\rho E)\,\mathrm{d}V + \int_{\mathrm{CS}}\rho E\,(\mathbf{v}\cdot\mathbf{n})\,\mathrm{d}S = -\int_{\mathrm{CS}}\dot{\mathbf{q}}\cdot\mathbf{n}\,\mathrm{d}S - \int_{\mathrm{CS}}p\,(\mathbf{v}\cdot\mathbf{n})\,\mathrm{d}S \tag{A.34}$$

$$\int_{\mathrm{CV}}\frac{\partial}{\partial t}(\rho E)\,\mathrm{d}V + \int_{\mathrm{CS}}\rho\left(E + \frac{p}{\rho}\right)(\mathbf{v}\cdot\mathbf{n})\,\mathrm{d}S = -\int_{\mathrm{CS}}\dot{\mathbf{q}}\cdot\mathbf{n}\,\mathrm{d}S \tag{A.35}$$

The left hand side of Eq. (A.35) is formulated in differential form, Eq. (A.36), by making the identification $\eta = E$ in the general transport equation, Eq. (A.23).

$$\int_{\mathrm{CV}} \frac{\partial}{\partial t}\left(\rho E\right) \mathrm{d}V + \int_{\mathrm{CS}} \rho \left(E + \frac{p}{\rho}\right)\left(\mathbf{v}\cdot\mathbf{n}\right) \mathrm{d}S = \rho\left[\frac{\partial E}{\partial t} + v_m \frac{\partial}{\partial m}\left(E + \frac{p}{\rho}\right) + \frac{v_\theta}{r}\frac{\partial}{\partial \theta}\left(E + \frac{p}{\rho}\right)\right] \mathrm{d}V \tag{A.36}$$

The heat flow rate is computed as the surface integral of heat flux into the system at it is given by Eq. (A.37), where the factor 2 arises to account for the inner and outer surfaces. This equation only accounts for the heat flux at the walls $\dot{q}_{\mathrm{w}}$, ignoring the heat transfer in the meridional and tangential directions.

$$-\int_{\mathrm{CS}} \dot{\mathbf{q}}\cdot\mathbf{n}\,\mathrm{d}S \approx 2\dot{q}_{\mathrm{w}}\, r\,\mathrm{d}\theta \mathrm{d}m \tag{A.37}$$

Collecting all terms and dividing by $\mathrm{d}V$, the total energy transport equation is given by Eq. (A.38).

$$\rho\left(\frac{\partial E}{\partial t} + v_m \frac{\partial}{\partial m}\left(E + \frac{p}{\rho}\right) + \frac{v_\theta}{r}\frac{\partial}{\partial \theta}\left(E + \frac{p}{\rho}\right)\right) = \frac{2\dot{q}_{\mathrm{w}}}{b} \tag{A.38}$$

Assuming that the flow is steady and axisymmetric, the total energy equation transport reduces to Eq. (A.39), where the partial differentials were replaced by total differentials because the only variation is along the meridional direction. Eq. (A.39) indicates that in the absence of heat transfer, the stagnation enthalpy of the flow remains constant (see Section 2.3 on model verification).

$$\rho v_m \frac{\mathrm{d}}{\mathrm{d}m}\left(E + \frac{p}{\rho}\right) = \rho v_m \frac{\mathrm{d}}{\mathrm{d}m}\left(e + \frac{v_m^2}{2} + \frac{v_\theta^2}{2} + \frac{p}{\rho}\right) = \frac{2\dot{q}_{\mathrm{w}}}{b} \tag{A.39}$$

The transport equations for mass, momentum, and energy derived so far pose a system of ordinary differential equations that can be solved if an equation of state is provided to relate the density and pressure with enthalpy. Instead of using this set of equations, a new form of the energy transport equation will be derived, Eq. (2.12). This alternative version of the energy equation is used to show that system of equations has a solution when the meridional Mach number of the flow is different than unity.

A.5.2 Mechanical energy

To derive the mechanical energy equation, first multiply the meridional component of the momentum equation by v_m, Eq. (A.40), and the tangential component

of the momentum equation by v_θ, Eq. (A.41). The chain rule for differentiation and some algebraic manipulations were used to obtain these two equations.

$$\rho v_m \left(\frac{\mathrm{d}}{\mathrm{d}m} \left(\frac{v_m^2}{2} \right) - \frac{v_\theta^2}{r} \sin(\phi) \right) + v_m \frac{\mathrm{d}p}{\mathrm{d}m} = -\frac{2\tau_\mathrm{w} v}{b} \cos(\alpha)^2 \tag{A.40}$$

$$\rho v_m \left(\frac{\mathrm{d}}{\mathrm{d}m} \left(\frac{v_\theta^2}{2} \right) + \frac{v_\theta^2}{r} \sin(\phi) \right) = -\frac{2\tau_\mathrm{w} v}{b} \sin(\alpha)^2 \tag{A.41}$$

After that, Eq. (A.42) is found by summing Eqs. (A.40) and (A.41) and it is known as the mechanical energy equation. This equation can be viewed as the transport equation for kinetic energy. The physical interpretation is that the fluid is decelerated (i.e., the kinetic energy decreases) due to positive pressure gradients and viscous forces.

$$\rho v_m \frac{\mathrm{d}}{\mathrm{d}m} \left(\frac{v_m^2}{2} + \frac{v_\theta^2}{2} \right) = -v_m \frac{\mathrm{d}p}{\mathrm{d}m} - \frac{2\tau_\mathrm{w} v}{b} \tag{A.42}$$

A.5.3 Thermal energy

The thermal energy equation is derived subtracting the mechanical energy equation, Eq. (A.42), from the total energy equation, Eq. (A.39).

$$\rho v_m \frac{\mathrm{d}}{\mathrm{d}m} \left(e + \frac{p}{\rho} \right) = v_m \frac{\mathrm{d}p}{\mathrm{d}m} + \frac{2}{b} (\tau_\mathrm{w} v + \dot{q}_\mathrm{w}) \tag{A.43}$$

Eq. (A.43) can be simplified using the quotient rule for differentiation to reach Eq. (A.44).

$$\rho v_m \left(\frac{\mathrm{d}e}{\mathrm{d}m} - \frac{p}{\rho^2} \frac{\mathrm{d}\rho}{\mathrm{d}m} \right) = \frac{2}{b} (\tau_\mathrm{w} v + \dot{q}_\mathrm{w}) \tag{A.44}$$

Eq. (A.44) is known as the thermal energy equation and its physical interpretation is that the internal energy is increased due to viscous dissipation and heat transfer, as well as to the deformation of the fluid (i.e., the product of pressure and density gradient).

The internal energy can be expressed in terms of pressure and density assuming a general equation of state of the form $e = e(p, \rho)$. First consider the Gibbs relation between thermodynamic properties, Eq. (A.45), and insert the exact differential

of internal energy given by Eq. (A.46) to reach Eq. (A.47).

$$T\mathrm{d}s = \mathrm{d}e - \frac{p}{\rho^2}\mathrm{d}\rho \tag{A.45}$$

$$\mathrm{d}e = \left(\frac{\partial e}{\partial p}\right)_\rho \mathrm{d}p + \left(\frac{\partial e}{\partial \rho}\right)_p \mathrm{d}\rho \tag{A.46}$$

$$T\mathrm{d}s = \left(\frac{\partial e}{\partial p}\right)_\rho \mathrm{d}p + \left[\left(\frac{\partial e}{\partial \rho}\right)_p - \frac{p}{\rho^2}\right]\mathrm{d}\rho \tag{A.47}$$

This equation reduces to Eq. (A.48) for an isentropic process and, since the speed of sound is defined as $a^2 = \left(\frac{\partial p}{\partial \rho}\right)_s$, we find that the speed of sound and the derivatives of the internal energy are related according to Eq. (A.49).

$$0 = \left(\frac{\partial e}{\partial p}\right)_\rho \left(\frac{\partial p}{\partial \rho}\right)_s + \left[\left(\frac{\partial e}{\partial \rho}\right)_p - \frac{p}{\rho^2}\right] \tag{A.48}$$

$$a^2 = \frac{\left(\frac{\partial e}{\partial \rho}\right)_p - \frac{p}{\rho^2}}{\left(\frac{\partial e}{\partial p}\right)_\rho} \tag{A.49}$$

Eq. (A.49) can be used to simplify the thermal energy equation given by Eq. (A.44). First, replace the differential of internal energy given by Eq. (A.46) to find Eq. (A.50).

$$\rho v_m \left(\left(\frac{\partial e}{\partial p}\right)_\rho \frac{\mathrm{d}p}{\mathrm{d}m} + \left[\left(\frac{\partial e}{\partial \rho}\right)_p - \frac{p}{\rho^2}\right]\frac{\mathrm{d}\rho}{\mathrm{d}m}\right) = \frac{2}{b}(\tau_\mathrm{w} v + \dot{q}_\mathrm{w}) \tag{A.50}$$

Now divide this expression by $\left(\frac{\partial e}{\partial p}\right)_\rho$ and use Eq. (A.49) to find Eq. (A.51), which is the alternative version of the energy equation that we wanted to prove.

$$\boxed{\rho v_m \frac{\mathrm{d}p}{\mathrm{d}m} - \rho v_m\, a^2 \frac{\mathrm{d}\rho}{\mathrm{d}m} = \frac{2(\tau_\mathrm{w} v + \dot{q}_\mathrm{w})}{b\left(\frac{\partial e}{\partial p}\right)_\rho}} \tag{A.51}$$

A.6 Transport equation for entropy

The transport equation for entropy is not required to model the flow within the diffuser. However, it is interesting to consider this equation to compute the rate of entropy generation. This is useful to: (1) check that the entropy generation is caused by viscous forces and heat transfer at a finite temperature difference and

(2) assess that the computation of entropy using the rate of entropy generation and the equations of state is consistent (see Section 2.3 on model verification).

The integral form of the entropy balance equation is given by Eq. (A.52). This equation indicates that the rate of change of entropy within the control volume plus the net flow rate of entropy leaving the control volume is equal to the net flow rate of entropy entering the control volume due to heat transfer plus the rate of entropy generation due to irreversibilities.

$$\int_{\mathrm{CV}} \frac{\partial}{\partial t}\left(\rho s\right)\,\mathrm{d}V + \int_{\mathrm{CS}} \rho s\left(\mathbf{v}\cdot\mathbf{n}\right)\,\mathrm{d}S = -\int_{\mathrm{CS}} \frac{1}{T}\left(\dot{\mathbf{q}}\cdot\mathbf{n}\right)\,\mathrm{d}S + \int_{\mathrm{CV}} \dot{\sigma}\,\mathrm{d}V \tag{A.52}$$

The left hand side of Eq. (A.52) is formulated in differential form, Eq. (A.53), by making the identification $\eta = s$ in the general transport equation, Eq. (A.23).

$$\int_{\mathrm{CV}} \frac{\partial}{\partial t}\left(\rho s\right)\,\mathrm{d}V + \int_{\mathrm{CS}} \rho s\left(\mathbf{v}\cdot\mathbf{n}\right)\,\mathrm{d}S = \rho\left[\frac{\partial s}{\partial t} + v_m\frac{\partial s}{\partial m} + \frac{v_\theta}{r}\frac{\partial s}{\partial \theta}\right]\mathrm{d}V \tag{A.53}$$

The entropy flow due to heat transfer is computed according to Eq. (A.54). This equation only accounts for the heat flux at the walls $\dot{q}_{\mathrm{w}}$ at temperature T_{w} and ignores the heat transfer in the meridional and tangential directions.

$$-\int_{\mathrm{CS}} \frac{1}{T}\left(\dot{\mathbf{q}}\cdot\mathbf{n}\right)\,\mathrm{d}S \approx \frac{2\dot{q}_{\mathrm{w}}}{T_{\mathrm{w}}}\,r\,\mathrm{d}\theta\mathrm{d}m \tag{A.54}$$

The entropy generation term is approximated according to Eq. (A.55).

$$\int_{\mathrm{CV}} \dot{\sigma}\,\mathrm{d}V \approx \dot{\sigma}\,\mathrm{d}V \tag{A.55}$$

Collecting all terms and dividing by $\mathrm{d}V$, the entropy transport equation is given by Eq. (A.56).

$$\rho\left(\frac{\partial s}{\partial t} + v_m\frac{\partial s}{\partial m} + \frac{v_\theta}{r}\frac{\partial s}{\partial \theta}\right) = \frac{2}{b}\,\frac{\dot{q}_{\mathrm{w}}}{T_{\mathrm{w}}} + \dot{\sigma} \tag{A.56}$$

The final form of the entropy transport equation, Eq. (A.57), is found assuming that the flow is steady and axisymmetric. The partial differentials were replaced by total differentials because the only variation is along the meridional direction.

$$\rho v_m\frac{\partial s}{\partial m} = \frac{2}{b}\,\frac{\dot{q}_{\mathrm{w}}}{T_{\mathrm{w}}} + \dot{\sigma} \tag{A.57}$$

Entropy generation

Inserting the entropy, Eq. (A.57), and energy, Eq. (A.44), transport equations intro the Gibbs relation, Eq. (A.45), it is possible to find the expression for the rate of entropy generation, Eq. (A.58).

$$\dot{\sigma} = \frac{2}{b\,T}\left[\left(\tau_{\mathrm{w}} v + \left(1 - \frac{T}{T_{\mathrm{w}}}\right)\dot{q}_{\mathrm{w}}\right.\right] \tag{A.58}$$

Eq. (A.58) indicates that the one-dimensional model predicts that the entropy generation is caused by viscous stress and heat transfer at a finite temperature difference. This is satisfactory, as these are the two mechanisms that lead to entropy generation in the real flow that is being modeled. It is interesting to note that if the work done by viscous stress at the walls was not neglected, the viscous stress would not lead to entropy generation. Clearly, an unsatisfactory result. The reason for this is that the friction force was modeled as a body force and body forces do not lead to entropy generation, for instance, gravity force or Coriolis acceleration.

Appendix B

Kacker–Okapuu Loss Model

This appendix describes the loss model proposed by Kacker et al. (1982) to compute aerodynamic losses in axial turbines, see Chapter 3.

B.1 Overview of the method

The Kacker et al. (1982) loss system is a refinement of the correlations proposed by Ainley et al. (1951a); Ainley et al. (1951b) and by Dunham et al. (1970). The general form of the loss model is given by

$$Y = f_{\mathrm{Re}}\, f_{\mathrm{Ma}}\, Y_{\mathrm{p}} + Y_{\mathrm{s}} + Y_{\mathrm{cl}} + Y_{\mathrm{te}} \tag{B.1}$$

The expressions used to compute each term as a function of the cascade geometry and flow variables are presented in the next sections. Some of the signs from the original correlations were modified to comply with the angle conventions used in this work. These modifications are explicitly mentioned in the text.

B.2 Reynolds number correction factor

The term f_{Re} accounts for the effects of the Reynolds number and it is computed according to Eq. (B.2).

$$f_{\mathrm{Re}} = \begin{cases} (\frac{\mathrm{Re}}{2\cdot 10^5})^{-0.40} & \text{for} \quad \mathrm{Re} < 2\cdot 10^5 \\ 1 & \text{for} \quad 2\cdot 10^5 < \mathrm{Re} < 1\cdot 10^6 \\ (\frac{\mathrm{Re}}{1\cdot 10^6})^{-0.20} & \text{for} \quad \mathrm{Re} > 1\cdot 10^6 \end{cases} \tag{B.2}$$

The Reynolds number is given by Eq. (B.3) and it is defined in terms of the chord length and the density, viscosity, and relative velocity at the outlet of the cascade.

$$\mathrm{Re} = \frac{\rho_{\mathrm{out}}\, w_{\mathrm{out}}\, c}{\mu_{\mathrm{out}}} \tag{B.3}$$

B.3 Mach number correction factor

The term f_{Ma} accounts for losses associated with supersonic flows at the trailing edge of the blades and it is computed according to Eq. (B.4).

$$f_{\mathrm{Ma}} = \begin{cases} 1 & \text{for} \quad \mathrm{Ma}_{\mathrm{out}}^{\mathrm{rel}} \leq 1 \\ 1 + 60 \cdot (\mathrm{Ma}_{\mathrm{out}}^{\mathrm{rel}} - 1)^2 & \text{for} \quad \mathrm{Ma}_{\mathrm{out}}^{\mathrm{rel}} > 1 \end{cases} \tag{B.4}$$

The Mach number is given by Eq. (B.5) and it is defined by the relative velocity and the speed of sound at the outlet of the cascade.

$$\mathrm{Ma}_{\mathrm{out}}^{\mathrm{rel}} = w_{\mathrm{out}} / a_{\mathrm{out}} \tag{B.5}$$

B.4 Profile loss coefficient

The profile loss coefficient Y_{p} is computed according to Eq. (B.6).

$$Y_{\mathrm{p}} = 0.914 \cdot \left(\frac{2}{3} \cdot Y'_{\mathrm{p}} \cdot K_{\mathrm{p}} + Y_{\mathrm{shock}} \right) \tag{B.6}$$

The term Y'_{p} is given by Eq. (B.7), where the terms, $Y_{\mathrm{p,\,reaction}}$ and $Y_{\mathrm{p,\,impulse}}$ are be obtained from the graphical data reproduced in Figures B.1 and B.2. The subscript *reaction* refers to blades with zero inlet metal angle (i.e., axial entry) and the subscript *impulse* refers to blades that have an inlet metal angle with the same magnitude but opposite sign as the exit relative flow angle. The second term of the right-hand side of Eq. (B.7) is a correction factor that accounts for the effects of the maximum blade thickness. The sign of β_{out} in Eq. (B.7) was changed with respect to the original work of Kacker–Okappu to comply with the angle convention used in this paper.

$$Y'_{\mathrm{p}} = \left[Y_{\mathrm{p,\,reaction}} - \left(\frac{\theta_{\mathrm{in}}}{\beta_{\mathrm{out}}} \right) \left| \frac{\theta_{\mathrm{in}}}{\beta_{\mathrm{out}}} \right| \cdot (Y_{\mathrm{p,\,impulse}} - Y_{\mathrm{p,\,reaction}}) \right] \cdot \left(\frac{t_{\mathrm{max}}/c}{0.20} \right)^{-\frac{\theta_{\mathrm{in}}}{\beta_{\mathrm{out}}}} \tag{B.7}$$

The factor K_p from Eq. (B.6) accounts for compressible flow effects when the Mach number within the cascade is subsonic and approaches unity. These effects tend to accelerate the flow, make the boundary layers thinner, and decrease the profile losses. K_p is a function on the inlet and outlet relative Mach numbers and it is computed from Eqs. (B.8) to (B.10).

$$K_{\mathrm{p}} = 1 - K_2 \cdot (1 - K_1) \tag{B.8}$$

$$K_1 = \begin{cases} 1 & \text{for} \quad \mathrm{Ma}_{\mathrm{out}}^{\mathrm{rel}} < 0.20 \\ 1 - 1.25 \cdot (\mathrm{Ma}_{\mathrm{out}}^{\mathrm{rel}} - 0.20) & \text{for} \quad 0.20 < \mathrm{Ma}_{\mathrm{out}}^{\mathrm{rel}} < 1.00 \\ 0 & \text{for} \quad \mathrm{Ma}_{\mathrm{out}}^{\mathrm{rel}} > 1.00 \end{cases} \tag{B.9}$$

$$K_2 = \left(\frac{\mathrm{Ma}_{\mathrm{in}}^{\mathrm{rel}}}{\mathrm{Ma}_{\mathrm{out}}^{\mathrm{rel}}} \right)^2 \tag{B.10}$$

The term Y_{shock} from Eq. (B.6) accounts for the relatively weak shock waves that may occur at the leading edge of the cascade due to the acceleration of the flow. After some algebra, the equations proposed in the Kacker–Okapuu method can be condensed as Eq. (B.11), where f_{hub} is given graphically in Figure B.3 and it is a function of the hub-to-tip ratio only. Note that the nomenclature used in Kacker et al. (1982) is different than that used in this work, in particular $q \equiv p_{0\mathrm{rel}} - p$ and $\Delta P \equiv p_{0\mathrm{rel,in}} - p_{0\mathrm{rel,out}}$.

$$Y_{\mathrm{shock}} = 0.75 \cdot \left(f_{\mathrm{hub}} \cdot \mathrm{Ma}_{\mathrm{in}}^{\mathrm{rel}} - 0.40 \right)^{1.75} \cdot \left(\frac{r_{\mathrm{hub}}}{r_{\mathrm{tip}}} \right)_{\mathrm{in}} \cdot \left(\frac{p_{0\mathrm{rel,in}} - p_{\mathrm{in}}}{p_{0\mathrm{rel,out}} - p_{\mathrm{out}}} \right) \tag{B.11}$$

B.5 Secondary loss coefficient

The secondary loss coefficient Y_{s} is computed according to Eq. (B.12).

$$Y_{\mathrm{s}} = 1.2 \cdot K_{\mathrm{s}} \cdot \left[0.0334 \cdot f_{\mathrm{AR}} \cdot Z \cdot \left(\frac{\cos(\beta_{\mathrm{out}})}{\cos(\theta_{\mathrm{in}})} \right) \right] \tag{B.12}$$

The factor 1.2 is included to correct the secondary loss for blades with zero trailing edge thickness. Trailing edge losses are accounted independently.

The factor K_{s} accounts for compressible flow effects present when the Mach number approaches unity. These effects tend to accelerate the flow, make the end wall boundary layers thinner, and decrease the secondary losses. K_{s} is computed from Eq. (B.13), where K_{p} is given by Eq. (B.8) and K_3 is given by Eq. (B.14)). K_3 is a function of the axial aspect ratio H/b only.

$$K_{\mathrm{s}} = 1 - K_3 \cdot \left(1 - K_{\mathrm{p}} \right) \tag{B.13}$$

$$K_3 = \left(\frac{1}{H/b} \right)^2 \tag{B.14}$$

f_{AR} accounts for the blade aspect ratio H/c and it is given by Eq. (B.15).

$$f_{\mathrm{AR}} = \begin{cases} \dfrac{1 - 0.25 \cdot \sqrt{2 - H/c}}{H/c} & \text{for} \quad H/c < 2 \\ \dfrac{1}{H/c} & \text{for} \quad H/c > 2 \end{cases} \tag{B.15}$$

The Ainley-Mathieson loading parameter Z is given by Eqs. (B.16) to (B.18), where the sign of β_{out} was changed with respect to the original work of Kacker

et al. (1982) to comply with the angle convention used in this paper.

$$Z = \left(\frac{C_\mathrm{L}}{s/c}\right)^2 \frac{\cos(\beta_\mathrm{out})^2}{\cos(\beta_\mathrm{m})^3} \tag{B.16}$$

$$\left(\frac{C_\mathrm{L}}{s/c}\right) = 2\cos(\beta_\mathrm{m}) \left[\tan(\beta_\mathrm{in}) - \tan(\beta_\mathrm{out})\right] \tag{B.17}$$

$$\tan(\beta_\mathrm{m}) = \frac{1}{2}\left[\tan(\beta_\mathrm{in}) + \tan(\beta_\mathrm{out})\right] \tag{B.18}$$

B.6 Tip clearance loss coefficient

The clearance loss coefficient Y_cl is computed according to Eq. (B.19), where the influence of the number of seals is neglected.

$$Y_\mathrm{cl} = B \cdot Z \cdot \left(\frac{c}{H}\right) \cdot \left(\frac{t_\mathrm{cl}}{H}\right)^{0.78} \tag{B.19}$$

In this equation, Z is given by Eqs. (B.16) to (B.18). The Kacker-Okapuu loss system proposes $B = 0.37$ for rotor blades with shrouded tips, and $B = 0.00$ for stator blades. In addition, Kacker and Okapuu warn that using $B = 0.47$, as suggested by Dunham et al. (1970), over-predicts the loss for rotor blades with plain tips.

B.7 Trailing edge loss coefficient

The trailing edge loss coefficient Y_te is computed according to Eq. (B.20).

$$Y_\mathrm{te} \approx \zeta = \frac{1}{\phi^2} - 1 = \frac{1}{1 - \Delta\phi^2} - 1 \tag{B.20}$$

Where the pressure loss coefficient Y was approximated by the enthalpy loss coefficient ζ and then related to the kinetic energy loss coefficients ϕ^2 and $\Delta\phi^2$. See the work by Dahlquist (2008) for details about the definitions of the different loss coefficients and the relations among them. The parameter $\Delta\phi^2$ is computed by interpolation of impulse and reaction blades according to Eq. (B.21). The sign of β_out in Eq. (B.21) was changed with respect to the original work of Kacker–Okappu to comply with the angle convention used in this paper.

$$\Delta\phi^2 = \Delta\phi^2_\mathrm{reaction} - \left(\frac{\theta_\mathrm{in}}{\beta_\mathrm{out}}\right)\left|\frac{\theta_\mathrm{in}}{\beta_\mathrm{out}}\right| \cdot (\Delta\phi^2_\mathrm{impulse} - \Delta\phi^2_\mathrm{reaction}) \tag{B.21}$$

$\Delta\phi^2_\mathrm{reaction}$ and $\Delta\phi^2_\mathrm{impulse}$ are the kinetic energy loss coefficients of reaction and impulse blades and they are a function of the trailing edge thickness to opening ratio t_te/o only. The functional relation was published in graphical form, and it is reproduced in Figure B.4.

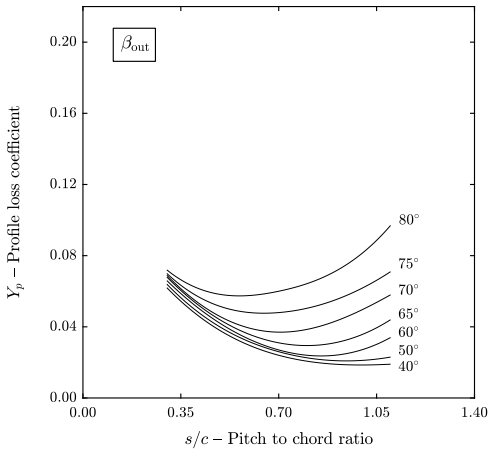

Figure B.1: Profile loss for reaction blades as a function of the exit flow angle.

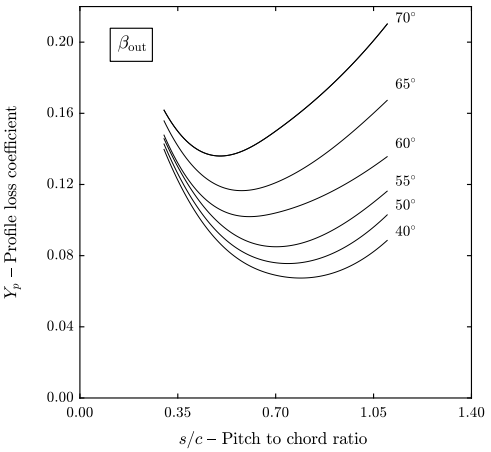

Figure B.2: Profile loss for impulse blades as a function of the exit flow angle.

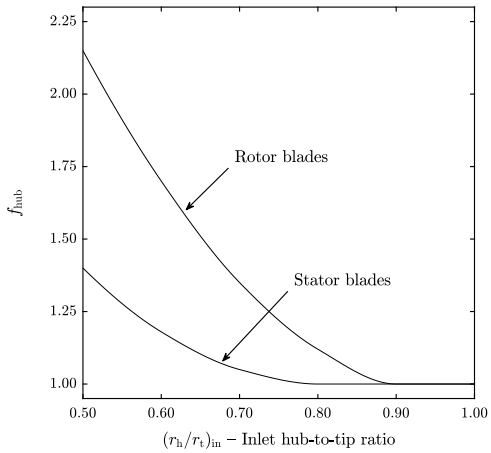

Figure B.3: Ratio of Mach number at the hub to Mach number at the mean radius.

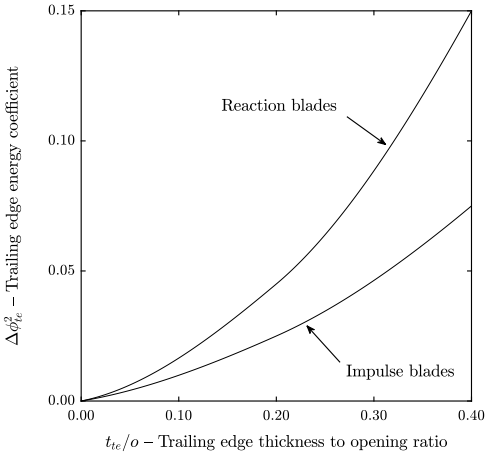

Figure B.4: Trailing edge energy loss coefficient for impulse and reaction blades.

Appendix C

Derivation of the Curvature Formulas at the Leading and Trailing Edges of a Blade Profile

This appendix contains the derivation of the functions $f(r_{\text{in}})$ and $g(r_{\text{out}})$ that are used to impose the radii of curvature r_{in} and r_{out} at the leading and trailing edges of turbomachinery blades, see Chapter 4.

Following Goldman (2005), the curvature of a curve $\mathbf{C}(u)$ is given by

$$\kappa(u) = \frac{\left\| \ddot{\mathbf{C}}(u) \times \dot{\mathbf{C}}(u) \right\|}{\left\| \dot{\mathbf{C}}(u) \right\|^3}. \tag{C.1}$$

In addition, it can be shown (Piegl et al. 2012, pp. 125–127), that the first and second derivatives of a NURBS curve at its *start point* are given by

$$\dot{\mathbf{C}}(u=0) = \left(\frac{p}{u_{p+1}}\right)\left(\frac{w_1}{w_0}\right)(\mathbf{P}_1 - \mathbf{P}_0) \tag{C.2}$$

$$\begin{aligned}\ddot{\mathbf{C}}(u=0) = &+ \frac{p(p-1)}{u_{p+1}}\left(\frac{1}{u_{p+2}}\right)\left(\frac{w_2}{w_0}\right)(\mathbf{P}_2 - \mathbf{P}_0) + \\ &- \frac{p(p-1)}{u_{p+1}}\left(\frac{1}{u_{p+1}} + \frac{1}{u_{p+2}}\right)\left(\frac{w_1}{w_0}\right)(\mathbf{P}_1 - \mathbf{P}_0) + \\ &+ \frac{2p^2}{u_{p+1}^2}\left(\frac{w_1}{w_0}\right)\left(1 - \frac{w_1}{w_0}\right)(\mathbf{P}_1 - \mathbf{P}_0),\end{aligned} \tag{C.3}$$

where p is the degree of the curve, u_k are the knot values, $\mathbf{P}_k$ are the control point coordinates, and w_k are the control point weights. Inserting these expressions into the curvature definition and using the fact that the vector cross product of two

parallel vectors is zero we find

$$\kappa(u=0) = \left(\frac{p-1}{p}\right)\left(\frac{u_{p+1}}{u_{p+2}}\right)\left(\frac{w_0\, w_2}{w_1^2}\right)\frac{\left\|(\mathbf{P}_2-\mathbf{P}_0)\times(\mathbf{P}_1-\mathbf{P}_0)\right\|}{\left\|\mathbf{P}_1-\mathbf{P}_0\right\|^3}. \tag{C.4}$$

Noting that unitary vector perpendicular to the camber line at the leading edge ($\mathbf{n}$) points from $\mathbf{P}_0$ to $\mathbf{P}_1$, see Figure 4.2d, the previous equation simplifies to

$$\kappa_{\text{in}} = \frac{1}{r_{\text{in}}} = \left(\frac{p-1}{p}\right)\left(\frac{u_{p+1}}{u_{p+2}}\right)\left(\frac{w_0\, w_2}{w_1^2}\right)\frac{\left\|(\mathbf{P}_2-\mathbf{P}_0)\times\mathbf{n}\right\|}{\left\|\mathbf{P}_1-\mathbf{P}_0\right\|^2}. \tag{C.5}$$

Solving for $\|\mathbf{P}_1-\mathbf{P}_0\|$, the location of the control point $\mathbf{P}_1$ that guarantees that the radius of curvature at the leading edge is r_{in} is given by

$$\mathbf{P}_1 = \mathbf{P}_0 \pm \|\mathbf{P}_1-\mathbf{P}_0\|\cdot\mathbf{n} = \mathbf{P}_0 \pm f(r_{\text{in}})\cdot\mathbf{n}, \tag{C.6}$$

where the plus and minus signs correspond to the upper and lower sides of the blade, respectively, and the function $f(r_{\text{in}})$ is given by

$$f(r_{\text{in}})^2 = r_{\text{in}}\left(\frac{p-1}{p}\right)\left(\frac{u_{p+1}}{u_{p+2}}\right)\left(\frac{w_0\, w_2}{w_1^2}\right)\left\|(\mathbf{P}_2-\mathbf{P}_0)\times\mathbf{n}\right\|. \tag{C.7}$$

The derivation for the trailing edge is analogous. The first and second derivatives of a NURBS curve at its *end point* are given by

$$\dot{\mathbf{C}}(u=1) = \left(\frac{p}{1-u_n}\right)\left(\frac{w_{n-1}}{w_n}\right)(\mathbf{P}_n-\mathbf{P}_{n-1}) \tag{C.8}$$

$$\begin{aligned}\ddot{\mathbf{C}}(u=1) = &+\frac{p\,(p-1)}{1-u_n}\left(\frac{1}{1-u_{n-1}}\right)\left(\frac{w_{n-2}}{w_n}\right)(\mathbf{P}_{n-2}-\mathbf{P}_n)+\\ &-\frac{p\,(p-1)}{1-u_n}\left(\frac{1}{1-u_n}+\frac{1}{1-u_{n-1}}\right)\left(\frac{w_{n-1}}{w_n}\right)(\mathbf{P}_{n-1}-\mathbf{P}_n)+\\ &+\frac{2p^2}{(1-u_n)^2}\left(\frac{w_{n-1}}{w_n}\right)\left(1-\frac{w_{n-1}}{w_n}\right)(\mathbf{P}_{n-1}-\mathbf{P}_n),\end{aligned} \tag{C.9}$$

respectively. Inserting these expressions into the curvature definition we find

$$\kappa(u=1) = \left(\frac{p-1}{p}\right)\left(\frac{1-u_n}{1-u_{n-1}}\right)\left(\frac{w_n\, w_{n-2}}{w_{n-1}^2}\right)\frac{\left\|(\mathbf{P}_{n-2}-\mathbf{P}_n)\times(\mathbf{P}_{n-1}-\mathbf{P}_n)\right\|}{\left\|\mathbf{P}_{n-1}-\mathbf{P}_n\right\|^3}. \tag{C.10}$$

Noting that unitary vector perpendicular to the camber line at the trailing edge ($\mathbf{n}$) points from $\mathbf{P}_n$ to $\mathbf{P}_{n-1}$, the previous equation simplifies to

$$\kappa_{\text{out}} = \frac{1}{r_{\text{out}}} = \left(\frac{p-1}{p}\right)\left(\frac{1-u_n}{1-u_{n-1}}\right)\left(\frac{w_n\, w_{n-2}}{w_{n-1}^2}\right)\frac{\left\|(\mathbf{P}_{n-2}-\mathbf{P}_n)\times\mathbf{n}\right\|}{\left\|\mathbf{P}_{n-1}-\mathbf{P}_n\right\|^2}. \tag{C.11}$$

Solving for $\|\mathbf{P}_{n-1} - \mathbf{P}_n\|$, the location of the control point $\mathbf{P}_{n-1}$ that guarantees that the radius of curvature at the trailing edge is r_{out} is given by

$$\mathbf{P}_{n-1} = \mathbf{P}_n \pm \|\mathbf{P}_{n-1} - \mathbf{P}_n\| \cdot \mathbf{n} = \mathbf{P}_n \pm g(r_{\text{out}}) \cdot \mathbf{n}, \tag{C.12}$$

where the plus and minus signs correspond to the upper and lower sides of the blade, respectively, and the function $g(r_{\text{out}})$ is given by

$$g(r_{\text{out}})^2 = r_{\text{out}} \left(\frac{p-1}{p} \right) \left(\frac{1-u_n}{1-u_{n-1}} \right) \left(\frac{w_n \, w_{n-2}}{w_{n-1}^2} \right) \left\| (\mathbf{P}_{n-2} - \mathbf{P}_n) \times \mathbf{n} \right\|. \tag{C.13}$$

Note that this construction guarantees that the blade is G^2 continuous at the leading and trailing edges since the radius of curvature is the same at the points connecting the upper and lower sides of the blade.

Appendix D

Design Data of the EXPAND Turbine

This appendix summarizes the main geometric parameters and operating conditions of the single-stage axial turbine considered in Chapter 5. The variables reported only at index (1) refer to the turbine as a whole, whereas those reported at indices (1,2) refer to the stator and rotor rows, and those reported at indices (1,2,3) refer to the flow stations indicated in Figure 5.6. The operating conditions of the *baseline geometry* and *optimal geometry* columns were computed from area-averaged quantities obtained by post-processing the CFD solution.

Table D.1: Preliminary and aerodynamic design of EXPAND test rig turbine.

Variable	Unit	Mean-line model			Aerodynamic baseline			Aerodynamic optimal		
		1	2	3	1	2	3	1	2	3
Ω	rpm	20000	—	—	20000	—	—	20000	—	—
$\dot{m}$	kg/s	1.600	—	—	1.507	—	—	1.660	—	—
$\dot{W}$	kW	57.02	—	—	52.58	—	—	58.41	—	—
η_{ts}	%	72.75	—	—	71.66	—	—	72.44	—	—
η_{tt}	%	93.11	—	—	89.10	—	—	93.04	—	—
Λ	–	0.500	—	—	0.493	—	—	0.492	—	—
Y	–	0.061	0.072	—	0.124	0.118	—	0.066	0.089	—
N_{b}	–	42	51	—	42	51	—	42	51	—
c	mm	12.20	10.06	—	14.32	10.98	—	14.32	10.98	—
c_{ax}	mm	10.00	10.00	—	10.00	10.00	—	10.00	10.00	—
s	mm	8.59	7.07	—	8.59	7.07	—	8.59	7.07	—
o	mm	2.92	3.36	—	2.95	3.34	—	3.16	3.57	—
t_{te}	mm	0.50	0.50	—	0.50	0.50	—	0.50	0.50	—
r_{h}	mm	51.05	51.05	51.05	51.05	51.05	51.05	51.05	51.05	51.05
r_{t}	mm	63.75	63.75	63.75	63.75	63.75	63.75	63.75	63.75	63.75
p	kPa	391.4	252.4	160.0	392.4	251.5	159.9	390.8	252.2	159.9
T	°C	124.4	112.5	100.6	124.4	111.0	97.9	124.2	110.4	97.0
a	m/s	238.2	237.4	235.8	238.9	237.6	235.5	238.9	237.4	235.2
Z	–	0.959	0.971	0.980	0.955	0.968	0.978	0.955	0.968	0.978
Ma	–	0.204	0.918	0.621	0.191	0.892	0.585	0.211	0.913	0.624
$\mathrm{Ma}_{\mathrm{rel}}$	–	0.204	0.475	1.020	0.191	0.446	0.991	0.211	0.474	1.017
α	°	0.00	70.12	-38.62	0.00	70.82	-39.35	0.00	69.35	-37.01
β	°	0.00	48.83	-61.61	0.00	48.92	-62.83	0.00	47.19	-60.67

Appendix E

Publications

Publication I

R. Agromayor, B. Müller, and L. O. Nord (2019a). "One-Dimensional Annular Diffuser Model for Preliminary Turbomachinery Design". *International Journal of Turbomachinery, Propulsion and Power* 4.3, pp. 1–31. DOI: https://doi.org/10.3390/ijtpp4030031.

Publication II

R. Agromayor and L. O. Nord (2019b). "Preliminary Design and Optimization of Axial Turbines Accounting for Diffuser Performance". *International Journal of Turbomachinery, Propulsion and Power* 4.3, pp. 1–32. DOI: https://doi.org/10.3390/ijtpp4030032.

Publication III

R. Agromayor, N. Anand, J.-D. Müller, M. Pini, and L. O. Nord (2021a). "A Unified Geometry Parametrization Method for Turbomachinery Blades". *Computer-Aided Design* 133, pp. 1–16. DOI: https://doi.org/10.1016/j.cad.2020.102987.

Publication IV

R. Agromayor, N. Anand, M. Pini, and L. O. Nord (2021b). "Multi-row Adjoint-based Optimization of NICFD Turbomachinery Using a CAD-based Parametrization". *To be submitted to: Journal of Engineering for Gas Turbines and Power.*

International Journal of
Turbomachinery
Propulsion and Power

MDPI

Article

One-Dimensional Annular Diffuser Model for Preliminary Turbomachinery Design

Roberto Agromayor *, Bernhard Müller and Lars O. Nord

Department of Energy and Process Engineering, NTNU—The Norwegian University of Science and Technology, Kolbj. Hejes v. 1B, NO-7491 Trondheim, Norway
* Correspondence: roberto.agromayor@ntnu.no

Received: 19 May 2019; Accepted: 10 September 2019; Published: 17 September 2019

Abstract: Annular diffusers are frequently used in turbomachinery applications to recover the discharge kinetic energy and increase the total-to-static isentropic efficiency. Despite its strong influence on turbomachinery performance, the diffuser is often neglected during the preliminary design. In this context, a one-dimensional flow model for annular diffusers that accounts for the impact of this component on turbomachinery performance was developed. The model allows use of arbitrary equations of state and to account for the effects of area change, heat transfer, and friction. The mathematical problem is formulated as an implicit system of ordinary differential equations that can be solved when the Mach number in the meridional direction is different than one. The model was verified against a reference case to assess that: (1) the stagnation enthalpy is conserved and (2) the entropy computation is consistent and it was found that the error of the numerical solution was always smaller than the prescribed integration tolerance. In addition, the model was validated against experimental data from the literature, finding that deviation between the predicted and measured pressure recovery coefficients was less than 2% when the best-fit skin friction coefficient is used. Finally, a sensitivity analysis was performed to investigate the influence of several input parameters on diffuser performance, concluding that: (1) the area ratio is not a suitable optimization variable because the pressure recovery coefficient increases asymptotically when this variable tends to infinity, (2) the diffuser should be designed with a positive mean wall cant angle to recover the tangential fraction of kinetic energy, (3) the mean wall cant angle is a critical design variable when the maximum axial length of the diffuser is constrained, and (4) the performance of the diffuser declines when the outlet hub-to-tip ratio of axial turbomachines is increased because the channel height is reduced.

Keywords: axial; radial; centrifugal; turbine; compressor; pump; vaneless; organic rankine cycle; steam turbine; gas turbine; supercritical carbon dioxide

1. Introduction

A diffuser is a device used to decelerate a flow and increase the static pressure of the fluid. Annular diffusers are frequently used in turbomachinery applications to recover the kinetic energy at the discharge of compressors and turbines to increase their total-to-static isentropic efficiency [1]. The design of an effective diffuser is a challenging task due to the presence of adverse pressure gradients. If the adverse pressure gradient is strong enough, the boundary layer close to the wall will separate and lead to flow reversal, reducing the pressure recovery [1]. The performance of a diffuser is often measured using the pressure recovery coefficient given by Equation (1), which reduces to Equation (2) for the limiting case of incompressible flow [2] (pp. 404–408).

$$C_p = \frac{p_{\text{out}} - p_{\text{in}}}{p_{0,\text{in}} - p_{\text{in}}} \quad (1)$$

$$C_p = \frac{p_{\text{out}} - p_{\text{in}}}{\frac{1}{2}\rho v_{\text{in}}^2} \quad (2)$$

The performance of the diffuser has a strong influence on the efficiency and design of turbomachinery. Specifically, Macchi and Perdichizzi [3] showed that the optimal design (maximum efficiency) of axial turbines depends on the amount of kinetic energy that can be recovered from the last stage. In addition, the work of Bahamonde et al. [4] indicates that the discharge kinetic energy can be one of the main mechanisms of efficiency loss when the influence of the diffuser is not accounted during the preliminary design. Despite this, the impact of the diffuser on the overall performance of turbomachines is often neglected or modeled in a very simple way during the preliminary design (mean-line models).

Table 1 summarizes the treatment of the diffuser in several publications about the preliminary design of turbines. Many works ignore the influence of the diffuser while others account for the impact of the diffuser in a simplistic way by assuming that an arbitrary fraction of the outlet kinetic energy is recovered. In addition, some of the works assumed that only the meridional fraction of the kinetic energy can be recovered when, in fact, most annular diffusers also recover the swirling kinetic energy (the tangential component of velocity decreases as the radius of the diffuser increases [1]). However, none of the works contained in Table 1 considered the influence of the diffuser design on the kinetic energy recovery and, to the knowledge of the authors, there are no studies that propose a methodology that accounts for the design of the diffuser during the preliminary turbine design.

Table 1. Treatment of the diffuser in the literature about turbine preliminary design.

Reference	Turbine Type	Diffuser Modeling
Macchi and Perdichizzi [3]	Axial flow	Fixed recovery [a]
Lozza et al. [5]	Axial flow	Fixed recovery [a]
Da Lio et al. [6]	Axial flow	Fixed recovery [b]
Astolfi and Macchi [7]	Axial flow	Fixed recovery [b]
Da Lio et al. [8]	Axial flow	Fixed recovery [b]
Al Jubori et al. [9]	Axial flow	Not considered
Talluri and Lombardi [10]	Axial flow	Not considered
Tournier and El-Genk [11]	Axial flow	Not considered
Meroni et al. [12]	Axial flow	Not considered
Meroni et al. [13]	Axial flow	Not considered
Meroni et al. [14]	Axial flow	Fixed recovery [b]
Perdichizzi and Lozza [15]	Radial inflow	Fixed recovery [a]
Uusitalo et al. [16]	Radial inflow	Not considered
Rahbar et al. [17]	Radial inflow	Not considered
Da Lio et al. [18]	Radial inflow	Not considered
Pini et al. [19]	Radial outflow	Fixed recovery [a]
Casati et al. [20]	Radial outflow Axial flow	Fixed recovery [a]
Bahamonde et al. [4]	Radial inflow Radial outflow	Not considered

[a] Fixed recovery of the total kinetic energy. [b] Fixed recovery of the meridional kinetic energy.

The diffuser performance can be predicted and optimized using detailed flow modes based on CFD simulations and shape optimization, but this approach is unpractical during the preliminary turbomachinery design. Instead, simplified one-dimensional flow models that account for the main features of the flow such as the effects of geometry (area change), heat transfer, and friction are better suited for the level of detail required during the preliminary design. There are several one-dimensional models for the flow within annular diffusers including the ones proposed by Stanitz [21], Johnston

and Dean [22], Elgammal and Elkersh [23], and Dubitsky and Japikse [24], see Table 2 . These models were developed for the vaneless diffuser of compressors and pumps, but they can also be used for turbine diffusers because the flow is governed by the same equations.

Table 2. One-dimensional diffuser models in the open literature.

Reference	Friction	Heat Transfer	Fluid Properties
Stanitz [21]	Yes	Yes	Perfect gas
Johnston and Dean [22]	Yes	No	Incompressible
Elgammal and Elkersh [23]	Yes	No	Incompressible
Dubitsky and Japikse [24]	Yes	No	General
Present work	Yes	Yes	General

Ideally, the diffuser model should accept any equation of state and account for the effects of area change, heat transfer, and friction. None of the models available in the literature meets all these requirements. The model proposed by Stanitz [21] accounts for the effects of area change, heat transfer, and friction, but it assumes that the fluid behaves as a perfect gas. Similarly, the models proposed by Johnston and Dean [22] and Elgammal and Elkersh [23], also account for the effects of area change and friction, but they assume that the flow is adiabatic and incompressible. Finally, the model proposed by Dubitsky and Japikse [24] is the most advanced. It is formulated as a two–zone model that accounts for real gas effects, area change, and friction (although it neglects heat transfer). One limitation of the model proposed by Dubitsky and Japikse [24] is that it is necessary to specify several ad-hoc parameters that might not be known in the early design phase such as the *turbulent mixing loss coefficient* or the *secondary flow area fraction*.

The purpose of this paper is to propose a one-dimensional flow model and solution algorithm for annular diffusers that can be coupled with the preliminary design of turbomachinery (pumps, compressors, and turbines). The flow equations are similar to those presented in previous works, refer to Table 2, but are formulated in a general way to account for heat transfer, friction, and arbitrary geometry and equations of state. The solution algorithm and discussion of the mathematical properties in terms of the meridional Mach number of the flow are original and they are presented in Section 2. In addition, the detailed derivation of the equations (omitted in other works) and the physical interpretation of the different terms are presented in the Appendix A. The model was verified against a reference case in Section 3 to assess that: (1) the stagnation enthalpy is conserved, (2) the computation of entropy is consistent. In addition, the model was validated against experimental data from the literature. Finally, a sensitivity analysis with respect to (1) the skin friction coefficient, (2) inlet hub-to-tip ratio, (3) mean wall cant angle, (4) inlet swirl angle, and (5) inlet Mach number was performed and presented in Section 4 to gain insight into the impact of these variables on diffuser performance and design. The authors would like to mention that the source code of the diffuser model proposed in this work is openly available in an online repository [25], see Supplementary Materials.

2. Diffuser Model

This section describes the diffuser model proposed in this work. First, the geometry of annular diffusers and the conventions for the velocity vector are described. After that, the treatment for the equations of state is presented. Finally, the mathematical model for the flow within the diffuser and the solution algorithm are explained.

2.1. Diffuser Geometry

A sectioned view of a general annular diffuser geometry is shown in Figure 1a. The kinetic energy decreases and the static pressure increases as the fluid flows within the annular duct defined by the inner and outer surfaces. For the case of subsonic diffusers, the meridional component of velocity

decreases when the flow area increases and the tangential component of velocity decreases when the mean radius of the channel increases [1].

In general, the meridional direction m will not be exactly aligned with the axial x or the radial r directions. This is illustrated in Figure 1b, where an axial–radial view of the diffuser is presented. The mean line of the diffuser can be parametrized as $r = r(m)$ and $x = x(m)$ such that the meridional, radial, and axial directions are related by the angle ϕ given by Equation (3).

$$\tan\phi = \frac{\mathrm{d}r}{\mathrm{d}x} = \left(\frac{\mathrm{d}r}{\mathrm{d}m}\right) \cdot \left(\frac{\mathrm{d}x}{\mathrm{d}m}\right)^{-1} \tag{3}$$

With this geometry the flow area is given by Equation (4), where r is the mean radius of the annular channel and b is height of the channel, measured normal to the meridional direction. The channel height can be prescribed as an arbitrary function of the meridional direction $b = b(m)$. The area ratio is defined as the ratio of outlet to inlet areas and is given by Equation (5).

$$A = 2\pi r\, b \tag{4}$$

$$AR = \frac{A_{\text{out}}}{A_{\text{in}}} \tag{5}$$

This section described the geometry of a general annular diffuser. The particular geometry of straight wall annular diffusers is described under the heading *geometry model*.

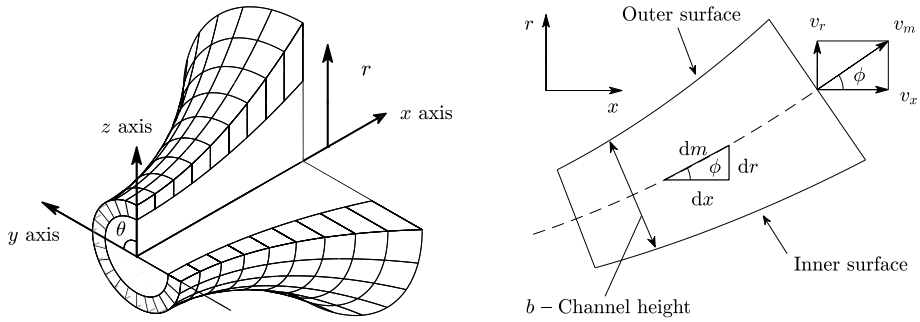

(a) Three-dimensional view **(b)** Axial–radial view.

Figure 1. Geometry of a general annular diffuser

2.2. *Velocity Vector*

In this work, the velocity is denoted by the symbol v, and the components are denoted by the subscripts θ—tangential, m—meridional, x—axial, and r—radial. The velocity vector is illustrated in Figure 2 and the different components are given by Equations (6)–(9). The angle α is measured from the meridional towards the tangential direction.

$$v_m = v\cos(\alpha) \tag{6}$$

$$v_\theta = v\sin(\alpha) \tag{7}$$

$$v_x = v_m\cos(\phi) = v\cos(\phi)\cos(\alpha) \tag{8}$$

$$v_r = v_m\sin(\phi) = v\sin(\phi)\cos(\alpha) \tag{9}$$

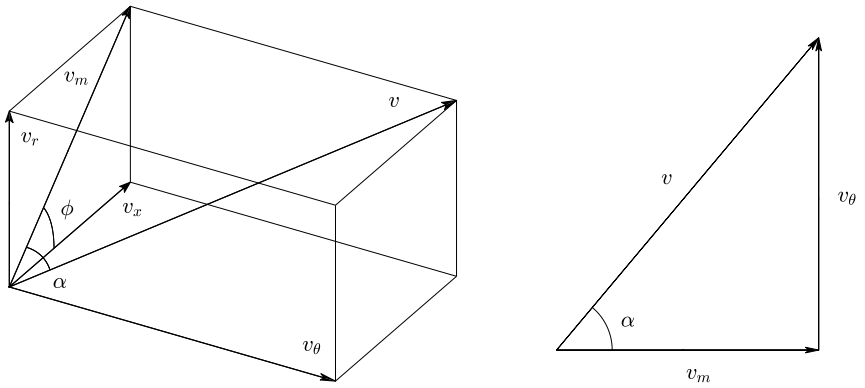

Figure 2. Decomposition of the velocity vector.

2.3. Equations of State

The diffuser model was formulated in a general way and the thermodynamic properties of the working fluid can be computed with any set of equations of state that support pressure–density function calls. In this work, the REFPROP fluid library [26] was used for the computation of thermodynamic properties. The partial derivatives of fluid properties were computed using finite differences.

2.4. Mathematical Model

The diffuser model presented in this work is based on the transport equations for mass, meridional and tangential momentum, and energy in an annular channel. It assumes that the flow is one-dimensional (in the meridional direction), steady (no time variation), and axisymmetric (no circumferential variation). The model can use arbitrary equations of state and it accounts for effects of area change, heat transfer, and friction. Under these conditions the governing equations of the flow are given by Equations (10)–(13). These equations can be derived considering the mass, momentum, and energy balances for the infinitesimal control volume shown in Figure 3. The detailed derivation of these equations and a discussion of the physical meaning of the different terms is presented in the Appendix A.

$$v_m \frac{\mathrm{d}\rho}{\mathrm{d}m} + \rho \frac{\mathrm{d}v_m}{\mathrm{d}m} = -\frac{\rho v_m}{b\,r} \frac{\mathrm{d}}{\mathrm{d}m}(b\,r) \tag{10}$$

$$\rho v_m \frac{\mathrm{d}v_m}{\mathrm{d}m} + \frac{\mathrm{d}p}{\mathrm{d}m} = \frac{\rho v_\theta^2}{r} \sin(\phi) - \frac{2\tau_\mathrm{w}}{b} \cos(\alpha) \tag{11}$$

$$\rho v_m \frac{\mathrm{d}v_\theta}{\mathrm{d}m} = -\frac{\rho v_\theta v_m}{r} \sin(\phi) - \frac{2\tau_\mathrm{w}}{b} \sin(\alpha) \tag{12}$$

$$\rho v_m \frac{\mathrm{d}p}{\mathrm{d}m} - \rho v_m a^2 \frac{\mathrm{d}\rho}{\mathrm{d}m} = \frac{2(\tau_\mathrm{w} v + \dot{q}_\mathrm{w})}{b \left(\frac{\partial e}{\partial p}\right)_\rho} \tag{13}$$

Equations (10)–(13) pose a system of ordinary differential equations (ODE) that can be expressed more compactly in matrix form as given by Equation (14). The solution vector U, coefficient matrix A, and source term vector S are given by Equation (15).

$$A\frac{\mathrm{d}U}{\mathrm{d}m} = S \tag{14}$$

$$A = \begin{bmatrix} \rho & 0 & v_m & 0 \\ \rho v_m & 0 & 0 & 1 \\ 0 & \rho v_m & 0 & 0 \\ 0 & 0 & -\rho v_m\, a^2 & \rho v_m \end{bmatrix} \quad U = \begin{bmatrix} v_m \\ v_\theta \\ \rho \\ p \end{bmatrix} \quad S = \begin{bmatrix} -\frac{\rho v_m}{b\,r}\frac{\mathrm{d}}{\mathrm{d}m}(b\,r) \\ \frac{\rho v_\theta^2}{r}\sin(\phi) - \frac{2\tau_\mathrm{w}}{b}\cos(\alpha) \\ -\frac{\rho v_\theta v_m}{r}\sin(\phi) - \frac{2\tau_\mathrm{w}}{b}\sin(\alpha) \\ \frac{2(\tau_\mathrm{w} v + \dot{q}_\mathrm{w})}{b\left(\frac{\partial e}{\partial p}\right)_\rho} \end{bmatrix} \tag{15}$$

It can be readily shown that the determinant of matrix A is given by Equation (16). This means that if the Mach number in the meridional direction is different than one, the matrix A can be inverted to compute the vector of derivatives $\frac{\mathrm{d}U}{\mathrm{d}m}$ according to Equation (17). In practice, matrix A is not inverted, instead the linear system of equations given by Equation (14) is solved using Gaussian elimination. It can be shown that the condition $\mathrm{Ma}_m = 1$ corresponds to a choked diffuser. This means that the diffuser can only be choked due to the meridional component of velocity and that the tangential component of velocity can be decelerated from supersonic to subsonic velocities without shock waves [21].

$$\det(A) = \rho^3 v_m^2\, a^2 \left(\frac{v_m^2}{a^2} - 1\right) = \rho^3 v_m^2\, a^2 \left(\mathrm{Ma}_m^2 - 1\right) \tag{16}$$

$$\frac{\mathrm{d}U}{\mathrm{d}m} = A^{-1} S \tag{17}$$

The vector $\frac{\mathrm{d}U}{\mathrm{d}m}$ can be computed in this way for any integration step and then used as input for an explicit numerical method to solve ordinary differential equations. The integration starts from the initial values (see Section 2.5) and stops when the prescribed value of the outlet to inlet area ratio AR is reached. In this work, the MATLAB function *ode45* [27] was used to perform the numerical integration. This function uses an automatic-stepsize-control solver that combines fourth and fifth order Runge–Kutta methods.

To compute the source term vector, it is necessary to prescribe the geometry of the diffuser, i.e., the variation of the channel height $b(m)$ and radius $r(m)$ in the meridional direction, and to provide models for the shear stress τ_w and the heat flux $\dot{q}_\mathrm{w}$ at the walls.

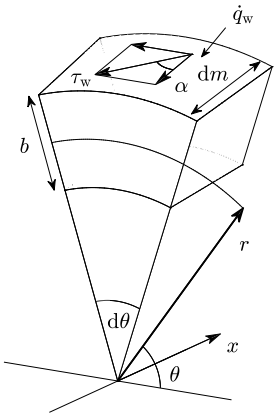

Figure 3. Differential control volume used to derive the diffuser governing equations.

2.4.1. Geometry Sub-Model

The diffuser model was formulated in a general way such that the geometry can be described by any set of arbitrary functions $r = r(m)$, $x = x(m)$, and $b = b(m)$. Although the one-dimensional

model presented in this work can accept any geometry as input, it is not able to predict flow features such as boundary layer separation. For this reason, this type of simplified model is not well suited for a detailed geometry design of the diffuser.

Despite this, one-dimensional models can give a good indication of the expected performance of a well-designed diffuser (in terms of the pressure recovery coefficient). For this reason, the main purpose of the diffuser model presented in this paper is to serve as a realistic boundary condition at the outlet of turbomachinery that reacts to changes in the design variables during the preliminary design and optimization. In addition, the diffuser geometry obtained from this type of analysis can be used as the starting point for a more detailed diffuser design such as a CFD-based shape optimization. Within this context, the geometry of the diffuser was modeled in a simple way assuming that the inner and outer surfaces are straight. These types of diffusers are known as conical wall annular diffusers (also as straight wall annular diffusers) and their geometry is shown in Figure 4.

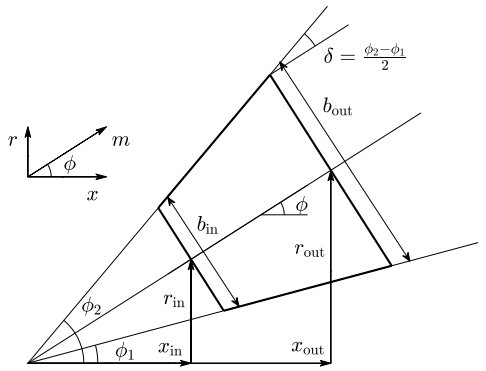

Figure 4. Axial–radial view of an annular diffuser with straight walls.

For this particular geometry, the angle ϕ is constant and it is given as the arithmetic mean of the inner and outer wall cant angles, $\phi = (\phi_1 + \phi_2)/2$. The relations $r = r(m)$, $x = x(m)$, and $b = b(m)$ can be deduced from Figure 4 and they are given by Equations (18)–(20), where $\delta = (\phi_2 - \phi_1)/2$ is the divergence semi-angle.

$$r(m) = r_{\text{in}} + m \sin(\phi) \tag{18}$$

$$x(m) = x_{\text{in}} + m \cos(\phi) \tag{19}$$

$$b(m) = b_{\text{in}} + 2m \tan(\delta) \tag{20}$$

2.4.2. Friction Sub-Model

The friction is modeled as a body force that does not do work (this models the no-slip condition at the walls). This is the approach often used in one-dimensional flow models because they cannot take into account the velocity gradient in the direction normal to the wall [21,24].

The viscous stress at the wall τ_w is computed in terms of the skin friction coefficient C_f as given by Equation (21). The viscous force is assumed to have the opposite direction as the velocity vector such that the friction components in the meridional and tangential direction are given by $-\tau_w \cos(\alpha)$ and $-\tau_w \sin(\alpha)$, respectively, see Figure 3.

$$\tau_w = C_f \frac{\rho v^2}{2} \tag{21}$$

To the knowledge of the authors there are no available correlations to predict the skin friction coefficient in annular channels with swirling flow. Using ordinary skin friction correlations for internal flows is discouraged because they do not consider the influence of swirl on the shear stress at the wall.

However, it is possible to estimate a reasonable value for the skin friction coefficient based on experimental data from existing vaneless diffusers. Brown [28] measured the local skin friction coefficient for different vaneless diffusers and obtained values in the range 0.003–0.010. In the absence of better estimates, Johnston–Dean [22] recommend values within the range 0.005–0.010 for the global skin friction coefficient. In a similar way, Dubitsky–Japikse [24] suggest 0.010 as a reasonable estimate for the global skin friction coefficient, but noted that values from 0.005 to 0.020 were required to fit experimental data, depending on the application. The values that were reported in this paragraph are meaningful for well-designed diffusers without flow separation.

2.4.3. Heat Transfer Sub-Model

The universal approach in the design and analysis of diffusers for turbomachinery applications is to neglect heat transfer and assume that the flow is adiabatic $\dot{q}_\mathrm{w} = 0$. To the knowledge of the authors, Stanitz [21] is the only reference that accounts for the effect of heat transfer in the energy transport equation. Although heat transfer is usually neglected, the heat transfer modeling is discussed in this section for the sake of completeness.

Stanitz [21] suggests that the heat flux is proportional to the temperature difference between the fluid and the wall as given by Equation (22), where the wall temperature is prescribed as a function of the meridional direction $T_\mathrm{w}(m)$. This equation uses the stagnation temperature of the fluid instead of the static temperature because the fluid is at rest at the wall (a recovery factor of unity is assumed).

$$\dot{q}_\mathrm{w} = U\,(T_\mathrm{w} - T_0) \tag{22}$$

In addition, Stanitz [21] suggests to use the Reynolds analogy given by Equations (23) and (24), to obtain an approximate value for the heat transfer coefficient in terms of the skin friction coefficient, where the usual definitions for the Nusselt number $\mathrm{Nu} = \frac{UD_\mathrm{h}}{k}$, Reynolds number $\mathrm{Re} = \frac{\rho v D_\mathrm{h}}{k}$, and Prandtl number $\mathrm{Pr} = \frac{c_p \mu}{k}$ are used. The hydraulic diameter of an annular duct is given by the channel height ($D_\mathrm{h} = b$), but it is immaterial for the computation of the heat transfer coefficient.

$$\mathrm{Nu} = \frac{1}{2}\,\mathrm{C_f}\,\mathrm{Re}\,\mathrm{Pr} \tag{23}$$

$$U = \frac{\rho v c_p}{2}\,\mathrm{C_f} \tag{24}$$

It is also possible to use the Chilton–Colburn analogy [29] (pp. 358–360) given by Equations (25) and (26) to estimate the heat transfer coefficient. This analogy extends the Reynolds analogy to fluids with a Prandtl number different from one.

$$\mathrm{Nu} = \frac{1}{2}\,\mathrm{C_f}\,\mathrm{Re}\,\mathrm{Pr}^{1/3} \tag{25}$$

$$U = \frac{\rho v c_p}{2}\,\mathrm{C_f}\,\mathrm{Pr}^{-2/3} \tag{26}$$

Both these analogies can be used to get a rough estimate of the heat transfer coefficient from a known value of the skin friction coefficient. Using ordinary heat transfer correlations for internal flows is discouraged, because they do not take into account the impact of the swirl into the heat transfer process.

2.5. Connection with a Turbomachinery Model

This section describes the link between the diffuser model presented in this work and a generic turbomachinery model. The initial conditions for the integration of the diffuser model are given by

Equation (27), where it is assumed that the thermodynamic state and velocity vector do not change from the turbomachine outlet to the diffuser inlet.

$$U^0 = \begin{bmatrix} v_m \\ v_\theta \\ \rho \\ p \end{bmatrix}^0 = \begin{bmatrix} v_m \\ v_\theta \\ \rho \\ p \end{bmatrix}^{\text{out}} \tag{27}$$

To describe the geometry of the diffuser, the mean radius r_{in} and the channel height b_{in} at the inlet are obtained from the turbomachine outlet radius R_{out} and blade height H_{out} as given by Equations (28) and (29), see Figure 5.

$$r_{\text{in}} = R_{\text{out}} \tag{28}$$

$$b_{\text{in}} = H_{\text{out}} / \cos(\phi) \tag{29}$$

In addition, it is necessary to prescribe the area ratio AR as the termination criterion for the integration of the ODE system and the inner ϕ_1 and outer ϕ_2 wall angles. Equivalently, it is possible to prescribe the mean cant angle $\phi = (\phi_1 + \phi_2)/2$ and the divergence semi-angle $\delta = (\phi_2 - \phi_1)/2$. These geometric parameters can be specified as fixed parameters or independent variables during the preliminary design and optimization of a turbomachine.

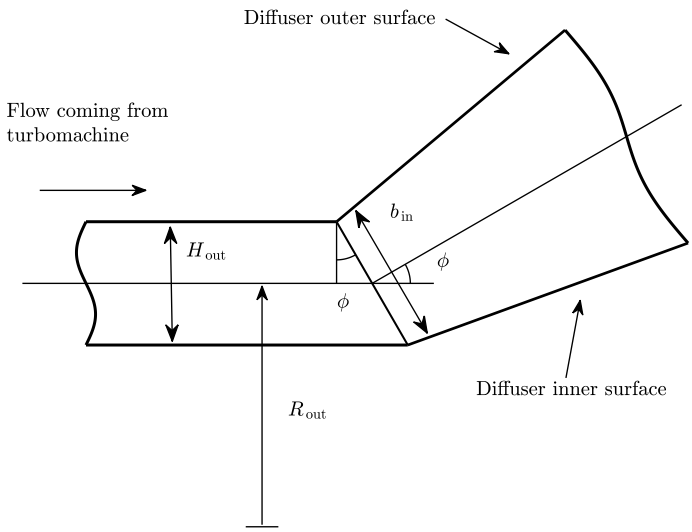

Figure 5. Connection of the diffuser model with a generic turbomachine model.

3. Verification and Validation of the Model

The aim of this section is the *verification* (solving the equations right) and *validation* (solving the right equations) of the diffuser model and solution algorithm proposed in this work. To verify the model, the reference case summarized in Table 3 was analyzed and the error of the numerical solution in terms of stagnation enthalpy and entropy was assessed. The case study proposed considers a subsonic flow of air within the annular diffuser at the outlet of an axial turbine or compressor. The skin friction coefficient was assumed to be $C_f = 0.010$ based on the suggestions from [22,24,28] and the heat transfer was neglected.

In the absence of heat transfer, the stagnation enthalpy of the flow remains constant, see the Appendix A, and any change in stagnation enthalpy is due to numerical error. The relative stagnation enthalpy error was evaluated using Equations (30) and (31) and it is shown as a function of the diffuser area ratio in Figure 6. It can be seen that the stagnation enthalpy is properly conserved and the relative error is of the order of 10^{-9}, which is smaller than the prescribed relative tolerance of 10^{-6} for the integration of the ODE system.

$$h_{0,\text{error}} = \frac{|h_0 - h_{0,\text{in}}|}{h_{0,\text{in}}} \tag{30}$$

$$h_0 = h(p,\rho) + \frac{v_m^2}{2} + \frac{v_\theta^2}{2} \tag{31}$$

In a similar way, the entropy error was analyzed. The entropy of the flow was computed using pressure–density function calls to the equation of state (EoS) at each integration step, Equation (32), and also evaluated integrating the transport equation for entropy given by Equation (33), where $\dot{\sigma}$ is the rate of entropy generation per unit volume due to friction. See the Appendix A for the details about the derivation of the transport equation for entropy. The entropy error was evaluated using Equation (34) and it is shown as a function of the diffuser area ratio in Figure 6. It can be observed that the relative entropy error is of the order of 10^{-7}, which is smaller than the prescribed integration tolerance of 10^{-6}. As both the stagnation enthalpy and entropy errors are smaller than the prescribed tolerance, we can conclude that the solution algorithm solves the flow equations satisfactorily.

$$s_{\text{EoS}} = s(p,\rho) \tag{32}$$

$$\rho v_m \left(\frac{\mathrm{d}s_{\text{gen}}}{\mathrm{d}m}\right) = \dot{\sigma} = 2\frac{\tau_w v}{b\,T} \tag{33}$$

$$s_{\text{error}} = \frac{|s_{\text{EoS}} - s_{\text{gen}}|}{s_{\text{EoS}}} \tag{34}$$

In addition, the diffuser model was validated against the annular diffuser experimental data from Kumar and Kumar [30]. The conditions that define this case are summarized in Table 4 and the experimental and computed pressure recovery coefficients are compared in Table 5 and in Figure 7. The heat transfer was neglected for the validation ($U = 0$) because the experimental data from Kumar and Kumar [30] corresponds to a low-speed annular diffuser where the difference between fluid temperature and wall temperature is expected to be very small. The skin friction coefficient was fitted to minimize the two-norm of the error between the experimental data and the model output. In addition, the range of variation of the pressure recovery coefficient for skin friction coefficients ranging between $\pm 20\%$ of the best-fit value is shown as a shaded area to illustrate the impact of this parameter on the diffuser performance.

Ignoring the point corresponding to $AR = 1.082$, it can be observed that the relative deviation of the pressure recovery coefficient is always less than 2% when the best-fit skin friction coefficient ($C_f = 0.029$) is used. It is plausible that the deviation between experiment and model when $AR = 1.082$ is due to the development of the flow at the inlet of the diffuser. This analysis shows that the model can be used to make accurate predictions when skin friction coefficient can be fitted to experimental data or approximate predictions in cases where there is no experimental data available.

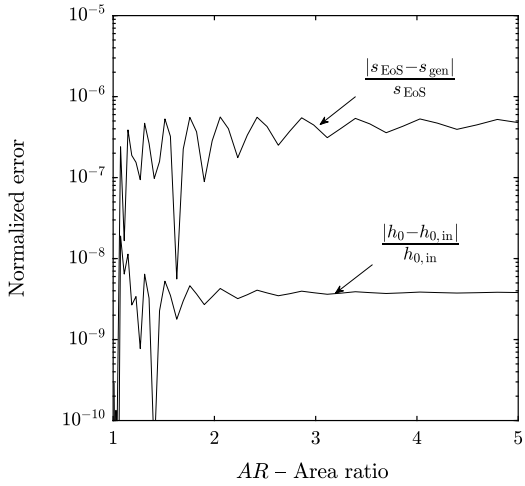

Figure 6. Enthalpy and entropy error analyses for the reference case defined in Table 3.

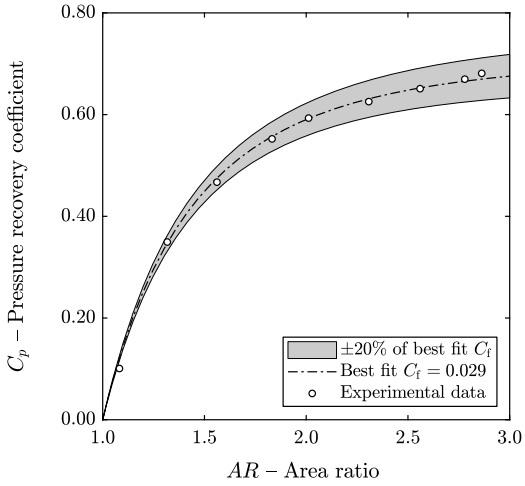

Figure 7. Comparison of model output with the data from Kumar and Kumar [30].

Table 3. Definition of the reference case.

Variable	Symbol	Value
Working fluid	-	Air
Inlet static pressure	p_{in}	101.3 kPa
Inlet static temperature	T_{in}	20.0 °C
Inlet meridional Mach	$\mathrm{Ma}_{\mathrm{m,in}}$	0.30
Inlet swirl angle	α_{in}	30.0°
Turbomachine outlet radius	R_{out}	1.0 m
Outlet hub-to-tip ratio	$(r_{\mathrm{h}}/r_{\mathrm{t}})_{\mathrm{out}}$	0.7
Mean wall cant angle	ϕ	30.0°
Divergence semi-angle	δ	5.0°
Diffuser area ratio	AR	1.0–5.0
Skin friction coefficient	C_{f}	0.010
Heat transfer coefficient	U	0 $\mathrm{W/m^2{\cdot}K}$

Table 4. Definition of the validation case from Kumar and Kumar [30].

Variable	Symbol	Value
Working fluid	-	Air
Inlet static pressure	p_{in}	101.3 kPa
Inlet static temperature	T_{in}	20.0 °C
Inlet meridional Mach	$Ma_{m,in}$	0.07
Inlet swirl angle	α_{in}	0.0°
Inlet mean radius	r_{in}	57.8 mm
Inlet channel height	b_{in}	39.5 mm
Mean wall cant angle	ϕ	15.0°
Divergence semi-angle	δ	0.0°
Diffuser area ratio	AR	1.0–3.0
Skin friction coefficient	C_f	Fitted to data
Heat transfer coefficient	U	0 $W/m^2 \cdot K$

Table 5. Comparison of the model output with the experimental data from Kumar and Kumar [30].

AR	C_p^{exp}	C_p^{model}	Relative Error
1.082	0.101	0.122	21.27%
1.317	0.349	0.347	−0.64%
1.561	0.467	0.475	1.73%
1.832	0.552	0.557	0.89%
2.012	0.593	0.592	−0.14%
2.308	0.626	0.631	0.89%
2.560	0.651	0.653	0.23%
2.779	0.670	0.666	−0.58%
2.863	0.681	0.670	−1.67%

4. Sensitivity Analysis

This section contains a sensitivity analysis of the reference case from Table 3 to gain insight about the impact of several input parameters on diffuser performance. The next sections investigate the influence of: (1) skin friction coefficient, (2) inlet hub-to-tip ratio, (3) mean wall cant angle, (4) inlet swirl angle, and (5) inlet meridional Mach number on the pressure recovery coefficient as a function of diffuser area ratio. The divergence semi-angle was not included in the analysis because increasing this parameter may lead to boundary layer separation close to the walls and the model used in this work cannot predict this phenomenon (Kline et al. [31] provide stability maps that can be used to predict flow separation for straight-walled and conical diffusers as a function of divergence semi-angle and area ratio. However, the authors are not aware of similar maps for annular diffusers in the open literature). Each of the analyses studies the influence of one variable while the other parameters are the same as in the reference case (one-at-a-time sensitivity analysis) and the ranges of the variables were selected to cover the flow conditions typical of most turbomachinery applications.

In addition, the influence of heat transfer on diffuser performance was analyzed for different wall temperatures using the Chilton–Colburn analogy to estimate the heat transfer coefficient. As expected, heat addition accelerates the flow and penalizes the pressure recovery coefficient. The details of the heat transfer investigations are not reported because the influence of heat addition was secondary compared to that of the other input parameters.

4.1. Influence of the Skin Friction Coefficient

As discussed in Section 2, to the knowledge of the authors, there are no correlations available to predict the skin friction coefficient in annular channels with swirling flow, but it is possible to estimate a realistic value based on the existing literature. The friction factor was varied from 0.000 (frictionless) to 0.030 (high friction) and the impact on the pressure recovery coefficient as a function of the area ratio is shown in Figure 8.

It can be observed that increasing the friction factor decreases the pressure recovery in a *linear* way (the different curves are equispaced) and that the effect is more notable when the area ratio increases (since the length of the channel increases). For the reference case considered, the pressure recovery increases with the area ratio in a monotonous manner and has an asymptotic behavior, irrespective of the numerical value of the friction coefficient. This suggest that an optimum value of the area ratio that maximizes the pressure recovery does not exist and that the pressure recovery always increases with the area ratio up to a limiting value.

This, perhaps counter-intuitive, result may be explained as the consequence of two conflicting effects. On the one hand, when the area ratio increases the diffuser length and wetted surface increase. However, as the area ratio increases the velocity and shear stress at the wall are reduced (the shear stress is proportional to the dynamic pressure). If this second effect dominates, friction becomes negligible and the pressure recovery increases asymptotically as the area ratio tends to infinity.

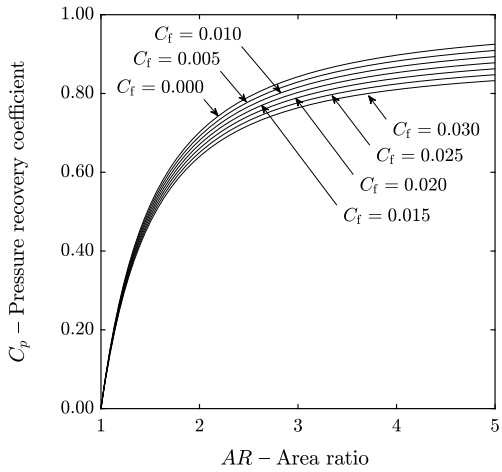

Figure 8. Influence of skin friction coefficient.

4.2. Influence of the Inlet Hub-to-Tip Ratio

To accommodate the density change, the hub-to-tip ratio is usually high at the outlet of axial compressors and low at the outlet of axial turbines. In this section, the hub-to-tip ratio at the inlet of the diffuser was varied between 0.50 and 0.95 and the results were plotted in Figure 9. It can be observed that the diffuser performance is penalized as the hub-to-tip ratio increases and that the effect is not linear: the pressure recovery coefficient is reduced more rapidly at high hub-to-tip ratios.

The reason for this behavior is that when the hub-to-tip ratio increases, the channel height of the diffuser is reduced according to Equation (35) and, since the channel height appears in the denominator of the friction terms of the momentum equations, Equations (11) and (12), the diffuser performance declines. Another interpretation based on physical intuition is that the channel height is the hydraulic diameter of the annular diffuser and that reducing this parameter will increase the friction losses.

$$b_{\text{in}} = H_{\text{out}} / \cos(\phi) = 2\, R_{\text{out}} \left(\frac{1 - (r_{\text{h}}/r_{\text{t}})}{1 + (r_{\text{h}}/r_{\text{t}})} \right)_{\text{out}} / \cos(\phi) \tag{35}$$

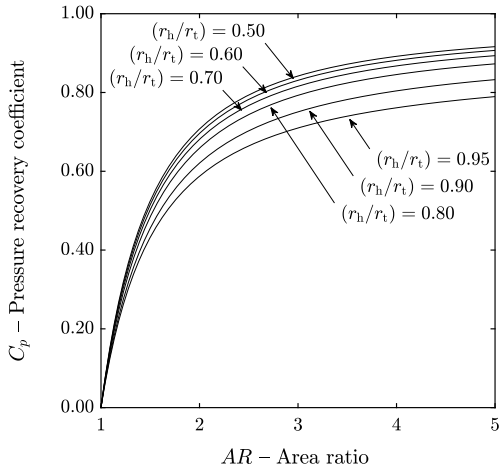

Figure 9. Influence of the hub-to-tip ratio.

4.3. Influence of the Mean Wall Cant Angle

Figure 10a shows the pressure recovery coefficient as a function of the area ratio when the mean cant angle is varied from 0° to 40°. It can be seen that the pressure recovery coefficient is very low when $\phi = 0°$ because the radius of the diffuser remains constant and the tangential component of velocity is not recovered and that it increases very quickly as the mean cant angle increases (for instance from 0° to 10°). Further increasing the mean wall cant angle will only improve the pressure recovery marginally (the change from 30° to 40° is almost inappreciable).

The same results are plotted as a function of the normalized axial length (instead of the area ratio) in Figure 10b. The end of the lines corresponds to the point where $AR = 5$. It can be observed that for a fixed diffuser axial length, the pressure recovery coefficient increases as the mean wall cant angle increases because both the area and the mean radius of the channel increase.

These results illustrate that the mean cant angle is not a critical parameter when there are no space limitations, but that adopting a high mean wall cant angle is advantageous when the maximum axial length of the diffuser is constrained.

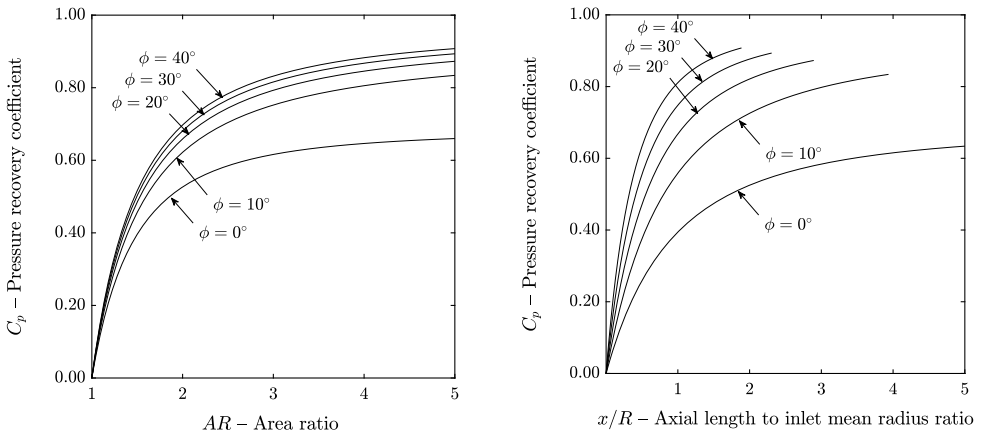

Figure 10. Influence of the mean wall cant angle on the pressure recovery coefficient as a function of the area ratio (**a**) and as a function of the axial length (**b**).

4.4. Influence of the Inlet Swirl Angle

In this section, the influence of the inlet swirl angle for a fixed meridional velocity was investigated. The results from Figure 11 show that increasing the inlet swirl angle decreases the pressure recovery coefficient of the diffuser and that this effect is more marked at higher swirl angles. The reason for this is that the presence of swirl increases the available dynamic pressure at the inlet and, for this reason, the area ratio required to reach the same pressure recovery coefficient as for the case $\alpha = 0°$ is higher. Moreover, the presence of swirl leads to wall shear stress in the circumferential direction that increases the friction losses.

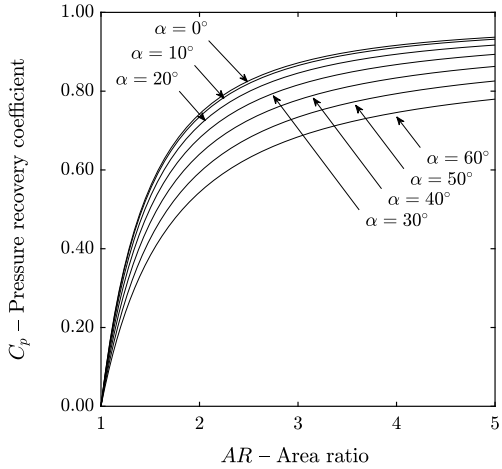

Figure 11. Influence of the inlet swirl angle.

4.5. Influence of the Inlet Mach Number

The influence of the inlet Mach number (compressibility effects) on the diffuser performance, including the limiting case of incompressible flow, is shown in Figure 12. The analysis presented on this section was performed assuming frictionless flow instead of $C_f = 0.010$ in order to compare the results at different inlet Mach numbers with the analytical results for inviscid, incompressible flow given by Equation (36). This equation is a well-known result [1,22] that can be proved integrating the mass and momentum equations, Equations (10)–(12), for constant density and zero wall shear stress.

It can be observed that the model predicts a modest increase on the pressure recovery coefficient as the inlet Mach number increases. In addition, the results obtained when the inlet meridional Mach number is 0.30 or lower (low-speed flow) are consistent with the analytical results for incompressible flow. This result can be regarded as part of the model verification.

$$C_{p,\text{incompressible}} = 1 - \frac{\tan(\alpha_{\text{in}})^2 + \left(\frac{b_{\text{in}}}{b}\right)^2}{1 + \tan(\alpha_{\text{in}})^2} \cdot \left(\frac{r_{\text{in}}}{r}\right)^2 \tag{36}$$

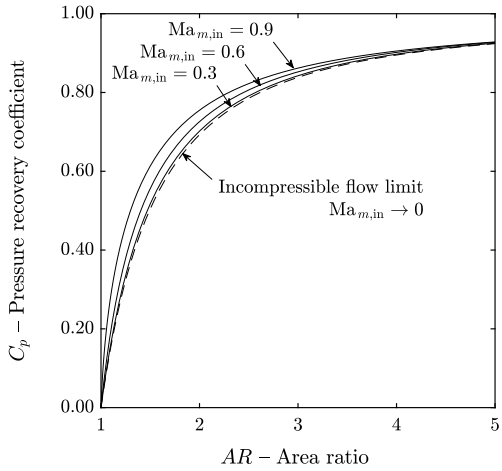

Figure 12. Influence of the inlet Mach number.

5. Conclusions

A one-dimensional flow model for annular diffusers was proposed and the connection of this model with the preliminary design and optimization of turbomachinery was discussed. The model formulation is more general than that of previous literature as it is possible to use arbitrary equations of state and include the effects of area change, heat transfer, and friction. The mathematical model poses a system of ordinary differential equations and it was shown that: (1) the solution is undetermined when the Mach number in the meridional direction is one (the flow is choked) and (2) the Mach number in the circumferential direction does not compromise the solution. In addition, the detailed derivation of the equations (omitted in other works) was presented in the Appendix A to provide physical insight about the flow in annular channels.

The model was *verified* against a reference case assessing that: (1) the stagnation enthalpy is conserved, (2) the entropy generation computed using the equation of state and using the second law of thermodynamics is consistent and it was found that the error of the numerical solution was always smaller than the prescribed integration tolerance. In addition, the model was *validated* against the experimental data from Kumar and Kumar [30], finding that the relative deviation between the predicted and measured pressure recovery coefficients was always less than 2% when the best-fit skin friction coefficient is used.

A sensitivity analysis was performed to investigate the influence of the: (1) skin friction coefficient, (2) inlet hub-to-tip ratio, (3) mean wall cant angle, (4) inlet swirl angle, and (5) inlet meridional Mach number on the diffuser performance. The ranges of these variables were selected to cover the flow conditions typical of most turbomachinery applications. The following conclusions were gathered:

- The pressure recovery coefficient increases asymptotically as the area ratio tends to infinity, regardless of the value of the skin friction coefficient. This suggest that the area ratio is not a suitable optimization variable during the diffuser design when the size of the diffuser is not constrained.
- The inlet hub-to-tip ratio has a strong impact on the pressure recovery because it is closely related to the channel height of the diffuser. The pressure recovery is penalized when the hub-to-tip ratio increases, and the trend is nonlinear: the pressure recovery coefficient is reduced more rapidly at high hub-to-tip ratios. This implies that in general, the design of efficient diffusers for axial compressors (high hub-to-tip ratios and short blades at the last stage) is more challenging than that of axial turbines (low hub-to-tip ratios and long blades at the last stage).
- The pressure recovery is very low when the mean wall cant angle is zero because the radius of the diffuser remains constant and the tangential component of velocity is not recovered. This shows

that the diffuser should be designed with an increasing mean radius to recover the kinetic energy of swirling flows effectively.

- Assuming that there is no flow separation, increasing the mean wall cant angle always improves the pressure recovery. However, for a given area ratio the mean wall cant angle has only a small impact on the pressure recovery, while for a given axial length increasing the mean wall cant angle improves the pressure recovery significantly. This implies that the mean wall cant angle is not a critical parameter when there are no space limitations, but that adopting a high mean wall cant angle is advantageous when the maximum axial length of the diffuser is constrained.
- Increasing the swirl angle at the inlet of the diffuser reduces the pressure recovery coefficient because the wall shear stress in the circumferential direction is increased. This implies that the diffuser performance will be improved if the velocity triangle of the last turbomachinery stage is designed so that the absolute velocity has a small tangential component.
- The pressure recovery coefficient increases as the inlet meridional Mach number increases. The effect on the inlet Mach number has only a modest impact on the pressure recovery, compared with the other variables. In addition, it was found that when the inlet meridional Mach number is lower than 0.30 the results from the compressible and incompressible analyses are almost identical.

Supplementary Materials: The source code of the diffuser model proposed in this work is openly available in an online repository (doi:10.5281/zenodo.2634095).

Author Contributions: Conceptualization, R.A. and L.O.N.; methodology, R.A.; software, R.A; validation, R.A.; resources, L.O.N.; writing–original draft preparation, R.A.; writing–review and editing, R.A., L.O.N. and B.M.

Funding: The authors gratefully acknowledge the financial support from the Research Council of Norway (EnergiX grant no. 255016) for the COPRO project, and the user partners Equinor, Hydro, Alcoa, GE Power Norway, and FrioNordica.

Conflicts of Interest: All authors of the article, Roberto Agromayor, Bernhard Müller, and Lars O. Nord, declare that they have no conflict of interest.

Nomenclature

Latin symbols

A	Annulus area or coefficient matrix	m^2
a	Speed of sound	m/s
AR	Area ratio	–
b	Diffuser channel height	m
C_f	Skin friction coefficient	–
C_p	Pressure recovery coefficient	–
c_p	Specific heat capacity at constant pressure	J/kg K
D_h	Hydraulic diameter	m
e	Internal energy	J/kg
h	Static specific enthalpy	J/kg
h_0	Stagnation specific enthalpy	J/kg
H_{out}	Outlet turbomachinery blade height	m
k	Heat conductivity	W/m K
Nu	Nusselt number	–
p	Static pressure	Pa
p_0	Stagnation pressure	Pa
Pr	Prandtl number	–
$\dot{q}_w$	Heat flux at the wall	W/m^2
r	Mean radius	m
R_{out}	Outlet turbomachinery radius	m
Re	Reynolds number	–
S	Source term vector	–
s	Specific entropy	J/kg K

T	Static temperature	K
T_0	Stagnation temperature	K
T_w	Temperature at the wall	K
U	Solution vector or heat transfer coefficient	$W/m^2 K$
v	Velocity	m/s
x	Axial distance	m

Greek symbols

α	Angle between the velocity vector the meridional direction	°
δ	Divergence semi-angle	°
θ	Tangential angle	°
ρ	Density	kg/m^3
$\dot{\sigma}$	Entropy generation per unit volume	$W/m^3 K$
τ_w	Shear stress at the wall	Pa
ϕ	Mean wall cant angle or angle between the radial a meridional directions	°
ϕ_1	Inner wall cant angle	°
ϕ_2	Outer wall cant angle	°

Abbreviations

CFD	Computational Fluid Dynamics
EOS	Equation of State
ODE	Ordinary Differential Equation

Subscripts

gen	Refers to entropy generation
in	Refers to the inlet
m	Refers to the meridional direction
out	Refers to the outlet
r	Refers to the radial direction
x	Refers to the axial direction
θ	Refers to the tangential direction

Appendix A. Derivation of the Governing Equations

This appendix contains the derivation the governing equations for the one-dimensional flow in an annular channel with area change, heat transfer, and friction using arbitrary equations of state. The final version of the equations derived in this appendix were presented within a box and they correspond to Equations (10)–(13) in the main text.

Appendix A.1. Groundwork

The starting point for the derivation of the governing equations is the integral form of the mass, momentum, energy, and entropy balance equations for a fixed control volume. The integral form of these equations can be found in any fluid mechanics textbook such as [2]. The integral equations are applied to the differential control volume shown in Figure 3 to determine the differential form of the equations. First, the transport equation for mass is derived and then it is used to obtain the transport equation for a general quantity. After this, the general transport equation is used to derive the momentum, energy, and entropy equations in a systematic way. Once the differential equations are found, they are simplified assuming that the flow is steady and axisymmetric to determine the one-dimensional equations used to model the diffuser.

The additional notation used in this appendix was not included in the nomenclature. Instead, it was preferred to introduce the new notation along the way to make the derivations easier to follow. The symbol **e** (vector quantities were typeset in boldface) is used to denote the unitary vectors in the different coordinate directions: $\mathbf{e}_\theta$—tangential, $\mathbf{e}_x$—axial, $\mathbf{e}_r$—radial, $\mathbf{e}_m$—meridional,

and $\mathbf{e}_n$—normal. The unitary vectors in the meridional–normal plane are related to the unitary vectors in the axial–radial plane according to Equations (A1) and (A2).

$$\mathbf{e}_m = \cos(\phi)\,\mathbf{e}_x + \sin(\phi)\,\mathbf{e}_r \tag{A1}$$

$$\mathbf{e}_n = -\sin(\phi)\,\mathbf{e}_x + \cos(\phi)\,\mathbf{e}_r \tag{A2}$$

The derivatives of the meridional and tangential vectors along the meridional and tangential directions are given by Equations (A3)–(A6). These equations are given without proof, but they can be derived using the chain rule for differentiation and geometric relations between the coordinate directions. Space derivatives of the unitary vectors are non-zero due to the curvature of the coordinate system and they are necessary to derive the momentum transport equation. The term R_m is the radius of curvature of the mean surface of the annular channel and it can be expressed in different ways depending on the parametrization used (we will not be concerned about this term because it does not appear on the final equations of the diffuser model).

$$\frac{\mathrm{d}\mathbf{e}_m}{\mathrm{d}m} = \frac{\mathrm{d}^2 r}{\mathrm{d}x^2} \cdot \left(1 + \left(\frac{\mathrm{d}r}{\mathrm{d}x}\right)^2\right)^{-\frac{3}{2}} \mathbf{e}_n = \frac{1}{R_m}\,\mathbf{e}_n \tag{A3}$$

$$\frac{\mathrm{d}\mathbf{e}_m}{\mathrm{d}\theta} = \sin(\phi)\,\mathbf{e}_\theta \tag{A4}$$

$$\frac{\mathrm{d}\mathbf{e}_\theta}{\mathrm{d}m} = 0 \tag{A5}$$

$$\frac{\mathrm{d}\mathbf{e}_\theta}{\mathrm{d}\theta} = -\mathbf{e}_r = -\sin(\phi)\,\mathbf{e}_m - \cos(\phi)\,\mathbf{e}_n \tag{A6}$$

The velocity vector can be expressed in terms of the unitary vectors according to Equations (A7) and (A8).

$$\mathbf{v} = v_m\,\mathbf{e}_m + v_\theta\,\mathbf{e}_\theta \tag{A7}$$

$$\mathbf{v} = v_x\,\mathbf{e}_x + v_r\,\mathbf{e}_r + v_\theta\,\mathbf{e}_\theta \tag{A8}$$

The volume of the differential control volume is given by $\mathrm{d}V = b\,r\,\mathrm{d}\theta\mathrm{d}m$, while the normal vectors and surface elements of the differential control surface are summarized in Table A1. These parameters are necessary to evaluate the integrals appearing on the balance equations

Table A1. Normal vectors and surface elements of the differential control volume.

Number	Face	n	d*S*
1	Front	$-\mathbf{e}_m$	$rb\,\mathrm{d}\theta$
2	Back	$+\mathbf{e}_m$	$rb\,\mathrm{d}\theta$
3	Left	$-\mathbf{e}_\theta$	$b\,\mathrm{d}m$
4	Right	$+\mathbf{e}_\theta$	$b\,\mathrm{d}m$
5	Bottom	$-\mathbf{e}_n$	$r\,\mathrm{d}\theta\mathrm{d}m$
6	Top	$+\mathbf{e}_n$	$r\,\mathrm{d}\theta\mathrm{d}m$

Appendix A.2. Transport Equation for Mass

The integral form of the mass balance equation is given by Equation (A9). This equation indicates that the rate of change of mass within the control volume plus the net mass flow rate leaving the control volume is equal to zero (mass is conserved).

$$\int_{\mathrm{CV}} \frac{\partial \rho}{\partial t}\,\mathrm{d}V + \int_{\mathrm{CS}} \rho\,(\mathbf{v}\cdot\mathbf{n})\,\mathrm{d}S = 0 \tag{A9}$$

The accumulation term is approximated by Equation (A10).

$$\int_{\mathrm{CV}} \frac{\partial \rho}{\partial t}\,\mathrm{d}V \approx \frac{\partial \rho}{\partial t}\,\mathrm{d}V = \frac{\partial \rho}{\partial t}\,b\,r\mathrm{d}\theta\mathrm{d}m \tag{A10}$$

The convective term is approximated byEquation (A11). This expression is found integrating the mass flux over the six faces of the differential control volume using the normal vectors and surface elements from Table A1 and the velocity vector given by Equation (A7).

$$\begin{aligned}\int_{\mathrm{CS}} \rho\,(\mathbf{v}\cdot\mathbf{n})\;\mathrm{d}S &\approx \sum_{i=1}^{6} \rho_i\,(\mathbf{v}_i\cdot\mathbf{n}_i)\;\mathrm{d}S_i \\ &\approx [\rho v_m r\,b\,\mathrm{d}\theta]_2 - [\rho v_m r\,b\,\mathrm{d}\theta]_1 + [\rho v_\theta b\,\mathrm{d}m]_4 - [\rho v_\theta b\,\mathrm{d}m]_3\end{aligned} \tag{A11}$$

The different summands of Equation (A11) are approximated by a first order Taylor expansion. The Taylor expansions of a generic property β in the meridional and tangential directions are given by Equations (A12) and (A13), respectively.

$$\beta_2 - \beta_1 = \left(\beta + \frac{\partial \beta}{\partial m}\frac{\mathrm{d}m}{2}\right) - \left(\beta - \frac{\partial \beta}{\partial m}\frac{\mathrm{d}m}{2}\right) + \mathcal{O}(\mathrm{d}m^2) \approx \frac{\partial \beta}{\partial m}\mathrm{d}m \tag{A12}$$

$$\beta_4 - \beta_3 = \left(\beta + \frac{\partial \beta}{\partial \theta}\frac{\mathrm{d}\theta}{2}\right) - \left(\beta - \frac{\partial \beta}{\partial \theta}\frac{\mathrm{d}\theta}{2}\right) + \mathcal{O}(\mathrm{d}\theta^2) \approx \frac{\partial \beta}{\partial \theta}\mathrm{d}\theta \tag{A13}$$

Inserting the Taylor expansions into Equation (A11) leads to Equation (A14).

$$\int_{\mathrm{CS}} \rho\,(\mathbf{v}\cdot\mathbf{n})\;\mathrm{d}S \approx \frac{\partial}{\partial m}\,(\rho v_m r\,b)\;\mathrm{d}m\mathrm{d}\theta + \frac{\partial}{\partial \theta}\,(\rho v_\theta b)\;\mathrm{d}m\mathrm{d}\theta \tag{A14}$$

Collecting the accumulation and the convective terms and dividing by $\mathrm{d}V$ leads to Equation (A15).

$$\frac{\partial \rho}{\partial t} + \frac{1}{b\,r}\frac{\partial}{\partial m}\,(\rho v_m r\,b) + \frac{1}{b\,r}\frac{\partial}{\partial \theta}\,(\rho v_\theta b) = 0 \tag{A15}$$

Assuming steady and axisymmetric flow Equation (A15) reduces to Equation (A16), where the partial differentials were replaced by total differentials because the only variation is along the meridional direction.

$$\frac{\mathrm{d}}{\mathrm{d}m}\,(\rho v_m r\,b) = 0 \tag{A16}$$

The final form of the mass transport equation, Equation (A17), is found using the product rule for differentiation and rearranging.

$$\boxed{v_m\frac{\mathrm{d}\rho}{\mathrm{d}m} + \rho\frac{\mathrm{d}v_m}{\mathrm{d}m} = -\frac{\rho v_m}{b\,r}\frac{\mathrm{d}}{\mathrm{d}m}(b\,r)} \tag{A17}$$

Appendix A.3. Transport Equation for A General Quantity

The integral form of a general balance equation is given by Equation (A18). This equation indicates that the rate of change of any intensive quantity η within the control volume plus the net flow rate of η leaving the control volume is equal to the generation of η due to source terms S_η. In general, this quantity η can be a scalar such as energy or entropy or a vector such as the velocity.

$$\int_{\mathrm{CV}} \frac{\partial}{\partial t}\,(\rho\eta)\;\mathrm{d}V + \int_{\mathrm{CS}} \rho\eta\,(\mathbf{v}\cdot\mathbf{n})\;\mathrm{d}S = S_\eta \tag{A18}$$

The accumulation term is approximated by Equation (A19).

$$\int_{\mathrm{CV}} \frac{\partial}{\partial t}\left(\rho\eta\right)\,\mathrm{d}V \approx \frac{\partial}{\partial t}\left(\rho\eta\right)\,\mathrm{d}V = \frac{\partial}{\partial t}\left(\rho\eta\right)\,b\,r\mathrm{d}\theta\mathrm{d}m \tag{A19}$$

The convective term is approximated by Equation (A20). This expression is found integrating the η-flux over the six faces of the differential control volume using the normal vectors and surface elements from Table A1 and the velocity vector given by Equation (A7).

$$\begin{aligned}\int_{\mathrm{CS}} \rho\eta\left(\mathbf{v}\cdot\mathbf{n}\right)\,\mathrm{d}S &\approx \sum_{i=1}^{6}\rho_i\eta_i\left(\mathbf{v}_i\cdot\mathbf{n}_i\right)\,\mathrm{d}S_i \\ &\approx \left[\rho\eta v_m r\,b\,\mathrm{d}\theta\right]_2 - \left[\rho\eta v_m r\,b\,\mathrm{d}\theta\right]_1 + \left[\rho\eta v_\theta b\,\mathrm{d}m\right]_4 - \left[\rho\eta v_\theta b\,\mathrm{d}m\right]_3\end{aligned} \tag{A20}$$

The different summands of Equation (A20) are approximated by first order Taylor expansions, Equations (A12) and (A13), to find Equation (A21).

$$\int_{\mathrm{CS}} \rho\eta\left(\mathbf{v}\cdot\mathbf{n}\right)\,\mathrm{d}S \approx \frac{\partial}{\partial m}\left(\rho\eta v_m r\,b\right)\,\mathrm{d}m\mathrm{d}\theta + \frac{\partial}{\partial\theta}\left(\rho\eta v_\theta b\right)\,\mathrm{d}m\mathrm{d}\theta \tag{A21}$$

Collecting the accumulation, convective, and source terms leads to Equation (A22).

$$\left[\frac{\partial}{\partial t}\left(\rho\eta\right)\,b\,r + \frac{\partial}{\partial m}\left(\rho\eta v_m r\,b\right) + \frac{\partial}{\partial\theta}\left(\rho\eta v_\theta b\right)\right]\mathrm{d}m\mathrm{d}\theta = S_\eta \tag{A22}$$

Using the product rule for differentiation and the transport equation for mass, Equation (A22) can be expressed in non-conservative form as Equation (A23), where $\mathrm{d}V = b\,r\,\mathrm{d}\theta\mathrm{d}m$.

$$\rho\left[\frac{\partial\eta}{\partial t} + v_m\frac{\partial\eta}{\partial m} + \frac{v_\theta}{r}\frac{\partial\eta}{\partial\theta}\right]\mathrm{d}V = S_\eta \tag{A23}$$

Equation (A23) is used in the next sections to derive the transport equations of momentum, energy and entropy in a systematic way.

Appendix A.4. Transport Equations for Momentum

The integral form of the momentum balance equation is given by Equation (A24). This equation indicates that the rate of change of momentum within the control volume plus the net flow rate of momentum leaving the control volume is equal to the net pressure forces acting on the control surfaces plus the body forces acting on the control volume. The viscous forces acting on the walls of the annular channel are modeled as a volume force instead of as a surface force as discussed below.

$$\int_{\mathrm{CV}} \frac{\partial}{\partial t}\left(\rho\mathbf{v}\right)\,\mathrm{d}V + \int_{\mathrm{CS}} \rho\mathbf{v}\left(\mathbf{v}\cdot\mathbf{n}\right)\,\mathrm{d}S = -\int_{\mathrm{CS}} p\mathbf{n}\,\mathrm{d}S + \int_{\mathrm{CV}} \rho\mathbf{f}\,\mathrm{d}V \tag{A24}$$

The left hand side of Equation (A24) is formulated in differential form, Equation (A25), by making the identification $\eta = \mathbf{v}$ in the general transport equation, Equation (A23).

$$\int_{\mathrm{CV}} \frac{\partial}{\partial t}\left(\rho\mathbf{v}\right)\,\mathrm{d}V + \int_{\mathrm{CS}} \rho\mathbf{v}\left(\mathbf{v}\cdot\mathbf{n}\right)\,\mathrm{d}S = \rho\left[\frac{\partial\mathbf{v}}{\partial t} + v_m\frac{\partial\mathbf{v}}{\partial m} + \frac{v_\theta}{r}\frac{\partial\mathbf{v}}{\partial\theta}\right]\mathrm{d}V \tag{A25}$$

The meridional, tangential, and normal components of the momentum equation are given by Equation (A26). This equation found inserting the velocity vector given by Equation (A7) and using

the product rule to account for the derivatives of the velocity components and the unitary vectors that are given by Equations (A3)–(A6).

$$\begin{aligned}\int_{CV} \frac{\partial}{\partial t}(\rho \mathbf{v})\, dV + \int_{CS} \rho \mathbf{v}\,(\mathbf{v}\cdot\mathbf{n})\, dS = \mathbf{e}_m \left(\rho\left[\frac{\partial v_m}{\partial t} + v_m\frac{\partial v_m}{\partial m} + \frac{v_\theta}{r}\frac{\partial v_m}{\partial \theta} - \frac{v_\theta^2}{r}\sin(\phi)\right] dV\right) \\ + \mathbf{e}_\theta \left(\rho\left[\frac{\partial v_\theta}{\partial t} + v_m\frac{\partial v_\theta}{\partial m} + \frac{v_\theta}{r}\frac{\partial v_\theta}{\partial \theta} + \frac{v_m v_\theta}{r}\sin(\phi)\right] dV\right) \\ + \mathbf{e}_n \left(\rho\left[\frac{v_m^2}{R_m} - \frac{v_\theta^2}{r}\cos(\phi)\right] dV\right)\end{aligned} \tag{A26}$$

The surface integral of the pressure forces can be approximated by Equation (A27), where the first equality follows from a variation of the Gauss theorem for the surface integral of a scalar field. The gradient of pressure for the curvilinear coordinates used here is given by Equation (A28), see [32] (Ch. 3).

$$-\int_{CS} p\mathbf{n}\, dS = -\int_{CV} \nabla p\, dV \approx \nabla p\, dV \tag{A27}$$

$$\nabla p = \frac{\partial p}{\partial m}\mathbf{e}_m + \frac{1}{r}\frac{\partial p}{\partial \theta}\mathbf{e}_\theta + \frac{\partial p}{\partial n}\mathbf{e}_n \tag{A28}$$

The viscous force is approximated by Equation (A29). This force is modeled as a body force pointing in the opposite direction of the velocity vector and with magnitude given by the product of the stress at the walls and the surface of the walls $dS = 2r\, d\theta dm$. The factor 2 arises to account for the inner and outer surfaces.

$$\int_{CV} \rho \mathbf{f}\, dV \approx \boldsymbol{\tau}_w\, dS = -\tau_w \frac{\mathbf{v}}{|\mathbf{v}|} dS = -2\tau_w \left[\cos(\alpha)\mathbf{e}_m + \sin(\alpha)\mathbf{e}_\theta\right] r\, d\theta dm \tag{A29}$$

Collecting all terms and dividing by dV, the meridional and tangential components of the momentum equation are given by Equations (A30) and (A31), respectively. The normal component is ignored because it is not used in the one-dimensional diffuser model.

$$\rho\left(\frac{\partial v_m}{\partial t} + v_m\frac{\partial v_m}{\partial m} + \frac{v_\theta}{r}\frac{\partial v_m}{\partial \theta} - \frac{v_\theta^2}{r}\sin(\phi)\right) = -\frac{\partial p}{\partial m} - \frac{2\tau_w}{b}\cos(\alpha) \tag{A30}$$

$$\rho\left(\frac{\partial v_\theta}{\partial t} + v_m\frac{\partial v_\theta}{\partial m} + \frac{v_\theta}{r}\frac{\partial v_\theta}{\partial \theta} + \frac{v_m v_\theta}{r}\sin(\phi)\right) = -\frac{1}{r}\frac{\partial p}{\partial \theta} - \frac{2\tau_w}{b}\sin(\alpha) \tag{A31}$$

The final form of the momentum equations, Equations (A32) and (A33), is found assuming steady and axisymmetric flow. The partial differentials were replaced by total differentials because the only variation is along the meridional direction.

$$\boxed{\rho v_m \frac{dv_m}{dm} + \frac{dp}{dm} = \frac{\rho v_\theta^2}{r}\sin(\phi) - \frac{2\tau_w}{b}\cos(\alpha)} \tag{A32}$$

$$\boxed{\rho v_m \frac{dv_\theta}{dm} = -\frac{\rho v_\theta v_m}{r}\sin(\phi) - \frac{2\tau_w}{b}\sin(\alpha)} \tag{A33}$$

Appendix A.5. Transport Equations for Energy

Appendix A.5.1. Total Energy

The integral form of the energy balance equation is given by Equation (A34) or by Equation (A35). Total energy is given by $E = e + \frac{v^2}{2}$ and the term $h_0 = E + \frac{p}{\rho}$ can be recognized as the stagnation

enthalpy of the flow. These equations indicate that the rate of change of total energy within the control volume plus the net flow rate of total energy leaving the control volume is equal to the net heat flow rate entering the control volume plus the work done by pressure forces. The work done by viscous forces (modeled as a body force) is neglected to model the no-slip condition at the wall (this is further discussed in the derivation of the entropy transport equation).

$$\int_{CV} \frac{\partial}{\partial t}(\rho E)\, \mathrm{d}V + \int_{CS} \rho E\, (\mathbf{v}\cdot\mathbf{n})\, \mathrm{d}S = -\int_{CS} \dot{\mathbf{q}}\cdot\mathbf{n}\, \mathrm{d}S - \int_{CS} p\, (\mathbf{v}\cdot\mathbf{n})\, \mathrm{d}S \tag{A34}$$

$$\int_{CV} \frac{\partial}{\partial t}(\rho E)\, \mathrm{d}V + \int_{CS} \rho \left(E + \frac{p}{\rho}\right)(\mathbf{v}\cdot\mathbf{n})\, \mathrm{d}S = -\int_{CS} \dot{\mathbf{q}}\cdot\mathbf{n}\, \mathrm{d}S \tag{A35}$$

The left hand side of Equation (A35) is formulated in differential form, Equation (A36), by making the identification $\eta = E$ in the general transport equation, Equation (A23).

$$\int_{CV} \frac{\partial}{\partial t}(\rho E)\, \mathrm{d}V + \int_{CS} \rho \left(E + \frac{p}{\rho}\right)(\mathbf{v}\cdot\mathbf{n})\, \mathrm{d}S = \rho \left[\frac{\partial E}{\partial t} + v_m \frac{\partial}{\partial m}\left(E + \frac{p}{\rho}\right) + \frac{v_\theta}{r}\frac{\partial}{\partial \theta}\left(E + \frac{p}{\rho}\right)\right] \mathrm{d}V \tag{A36}$$

The heat flow rate is computed as the surface integral of heat flux into the system at it is given by Equation (A37), where the factor 2 arises to account for the inner and outer surfaces. This equation only accounts for the heat flux at the walls $\dot{q}_w$, ignoring the heat transfer in the meridional and tangential directions.

$$-\int_{CS} \dot{\mathbf{q}}\cdot\mathbf{n}\, \mathrm{d}S \approx 2\dot{q}_w\, r\, \mathrm{d}\theta \mathrm{d}m \tag{A37}$$

Collecting all terms and dividing by $\mathrm{d}V$, the total energy transport equation is given by Equation (A38).

$$\rho\left(\frac{\partial E}{\partial t} + v_m \frac{\partial}{\partial m}\left(E + \frac{p}{\rho}\right) + \frac{v_\theta}{r}\frac{\partial}{\partial \theta}\left(E + \frac{p}{\rho}\right)\right) = \frac{2\dot{q}_w}{b} \tag{A38}$$

Assuming that the flow is steady and axisymmetric, the total energy equation transport reduces to Equation (A39), where the partial differentials were replaced by total differentials because the only variation is along the meridional direction. Equation (A39) indicates that in the absence of heat transfer, the stagnation enthalpy of the flow remains constant. This result is used in the main body of the paper to verify the numerical solution of the model, see Section 3.

$$\rho v_m \frac{\mathrm{d}}{\mathrm{d}m}\left(E + \frac{p}{\rho}\right) = \rho v_m \frac{\mathrm{d}}{\mathrm{d}m}\left(e + \frac{v_m^2}{2} + \frac{v_\theta^2}{2} + \frac{p}{\rho}\right) = \frac{2\dot{q}_w}{b} \tag{A39}$$

The transport equations for mass, momentum, and energy derived so far pose a system of ordinary differential equations that can be solved if an equation of state is provided to relate the density and pressure with enthalpy. Instead of using this set of equations, a new form of the energy transport equation will be derived, Equation (13). This alternative version of the energy equation is used to show that system of equations has a solution when the meridional Mach number of the flow is different than one (see Section 2).

Appendix A.5.2. Mechanical Energy

To derive the mechanical energy equation, first multiply the meridional component of the momentum equation by v_m, Equation (A40), and the tangential component of the momentum equation by v_θ, Equation (A41). The chain rule for differentiation and some algebraic manipulations were used to obtain these two equations.

$$\rho v_m \left(\frac{\mathrm{d}}{\mathrm{d}m} \left(\frac{v_m^2}{2} \right) - \frac{v_\theta^2}{r} \sin(\phi) \right) + v_m \frac{\mathrm{d}p}{\mathrm{d}m} = -\frac{2\tau_w v}{b} \cos(\alpha)^2 \tag{A40}$$

$$\rho v_m \left(\frac{\mathrm{d}}{\mathrm{d}m} \left(\frac{v_\theta^2}{2} \right) + \frac{v_\theta^2}{r} \sin(\phi) \right) = -\frac{2\tau_w v}{b} \sin(\alpha)^2 \tag{A41}$$

Equation (A42) is found summing both expressions and it is known as the mechanical energy equation. This equation can be viewed as the transport equation for kinetic energy. The physical interpretation is that the fluid is decelerated (decreasing kinetic energy) by positive pressure gradients and viscous forces.

$$\rho v_m \frac{\mathrm{d}}{\mathrm{d}m} \left(\frac{v_m^2}{2} + \frac{v_\theta^2}{2} \right) = -v_m \frac{\mathrm{d}p}{\mathrm{d}m} - \frac{2\tau_w v}{b} \tag{A42}$$

Appendix A.5.3. Thermal Energy

The thermal energy equation is derived subtracting the mechanical energy equation, Equation (A42), from the total energy equation, Equation (A39).

$$\rho v_m \frac{\mathrm{d}}{\mathrm{d}m} \left(e + \frac{p}{\rho} \right) = v_m \frac{\mathrm{d}p}{\mathrm{d}m} + \frac{2}{b} (\tau_w v + \dot{q}_w) \tag{A43}$$

Equation (A43) can be simplified using the quotient rule for differentiation to reach Equation (A44).

$$\rho v_m \left(\frac{\mathrm{d}e}{\mathrm{d}m} - \frac{p}{\rho^2} \frac{\mathrm{d}\rho}{\mathrm{d}m} \right) = \frac{2}{b} (\tau_w v + \dot{q}_w) \tag{A44}$$

Equation (A44) is known as the thermal energy equation and its physical interpretation is that the internal energy is increased due to viscous dissipation and heat transfer, as well as to the deformation of the fluid (product of pressure and density gradient).

The internal energy can be expressed in terms of pressure and density assuming a general equation of state of the form $e = e(p, \rho)$. First consider the Gibbs relation between thermodynamic properties, Equation (A45), and insert the exact differential of internal energy given by Equation (A46) to reach Equation (A47).

$$T\mathrm{d}s = \mathrm{d}e - \frac{p}{\rho^2} \mathrm{d}\rho \tag{A45}$$

$$\mathrm{d}e = \left(\frac{\partial e}{\partial p} \right)_\rho \mathrm{d}p + \left(\frac{\partial e}{\partial \rho} \right)_p \mathrm{d}\rho \tag{A46}$$

$$T\mathrm{d}s = \left(\frac{\partial e}{\partial p} \right)_\rho \mathrm{d}p + \left[\left(\frac{\partial e}{\partial \rho} \right)_p - \frac{p}{\rho^2} \right] \mathrm{d}\rho \tag{A47}$$

This equation reduces to Equation (A48) for an isentropic process and, since the speed of sound is defined as $a^2 = \left(\frac{\partial p}{\partial \rho} \right)_s$, we find that the speed of sound and the derivatives of the internal energy are related according to Equation (A49).

$$0 = \left(\frac{\partial e}{\partial p} \right)_\rho \left(\frac{\partial p}{\partial \rho} \right)_s + \left[\left(\frac{\partial e}{\partial \rho} \right)_p - \frac{p}{\rho^2} \right] \tag{A48}$$

$$a^2 = \frac{\left(\frac{\partial e}{\partial \rho} \right)_p - \frac{p}{\rho^2}}{\left(\frac{\partial e}{\partial p} \right)_\rho} \tag{A49}$$

Equation (A49) can be used to simplify the thermal energy equation given by Equation (A44). First, replace the differential of internal energy given by Equation (A46) to find Equation (A50).

$$\rho v_m \left(\left(\frac{\partial e}{\partial p} \right)_\rho \frac{\mathrm{d}p}{\mathrm{d}m} + \left[\left(\frac{\partial e}{\partial \rho} \right)_p - \frac{p}{\rho^2} \right] \frac{\mathrm{d}\rho}{\mathrm{d}m} \right) = \frac{2}{b} (\tau_\mathrm{w} v + \dot{q}_\mathrm{w}) \tag{A50}$$

Now divide this expression by $\left(\frac{\partial e}{\partial p} \right)_\rho$ and use Equation (A49) to find Equation (A51), which is the alternative version of the energy equation that we wanted to prove.

$$\boxed{\rho v_m \frac{\mathrm{d}p}{\mathrm{d}m} - \rho v_m a^2 \frac{\mathrm{d}\rho}{\mathrm{d}m} = \frac{2(\tau_\mathrm{w} v + \dot{q}_\mathrm{w})}{b \left(\frac{\partial e}{\partial p} \right)_\rho}} \tag{A51}$$

Appendix A.6. Transport Equation for Entropy

The transport equation for entropy is not required to model the flow within the diffuser. However, it is interesting to consider this equation to compute the rate of entropy generation. This is useful to: (1) check that the entropy generation is caused by viscous forces and heat transfer at a finite temperature difference and (2) assess that the computation of entropy using the rate of entropy generation and the equations of state is consistent (see Section 3 on model verification).

The integral form of the entropy balance equation is given by Equation (A52). This equation indicates that the rate of change of entropy within the control volume plus the net flow rate of entropy leaving the control volume is equal to the net flow rate of entropy entering the control volume due to heat transfer plus the rate of entropy generation due to irreversibilities.

$$\int_\mathrm{CV} \frac{\partial}{\partial t} (\rho s) \, \mathrm{d}V + \int_\mathrm{CS} \rho s \, (\mathbf{v} \cdot \mathbf{n}) \, \mathrm{d}S = - \int_\mathrm{CS} \frac{1}{T} \, (\dot{\mathbf{q}} \cdot \mathbf{n}) \, \mathrm{d}S + \int_\mathrm{CV} \dot{\sigma} \, \mathrm{d}V \tag{A52}$$

The left hand side of Equation (A52) is formulated in differential form, Equation (A53), by making the identification $\eta = s$ in the general transport equation, Equation (A23).

$$\int_\mathrm{CV} \frac{\partial}{\partial t} (\rho s) \, \mathrm{d}V + \int_\mathrm{CS} \rho s \, (\mathbf{v} \cdot \mathbf{n}) \, \mathrm{d}S = \rho \left[\frac{\partial s}{\partial t} + v_m \frac{\partial s}{\partial m} + \frac{v_\theta}{r} \frac{\partial s}{\partial \theta} \right] \mathrm{d}V \tag{A53}$$

The entropy flow due to heat transfer is computed according to Equation (A54). This equation only accounts for the heat flux at the walls $\dot{q}_\mathrm{w}$ at temperature T_w and ignores the heat transfer in the meridional and tangential directions.

$$- \int_\mathrm{CS} \frac{1}{T} \, (\dot{\mathbf{q}} \cdot \mathbf{n}) \, \mathrm{d}S \approx \frac{2 \dot{q}_\mathrm{w}}{T_\mathrm{w}} \, r \, \mathrm{d}\theta \mathrm{d}m \tag{A54}$$

The entropy generation term is approximated according to Equation (A55).

$$\int_\mathrm{CV} \dot{\sigma} \, \mathrm{d}V \approx \dot{\sigma} \, \mathrm{d}V \tag{A55}$$

Collecting all terms and dividing by $\mathrm{d}V$, the entropy transport equation is given by Equation (A56).

$$\rho \left(\frac{\partial s}{\partial t} + v_m \frac{\partial s}{\partial m} + \frac{v_\theta}{r} \frac{\partial s}{\partial \theta} \right) = \frac{2}{b} \frac{\dot{q}_\mathrm{w}}{T_\mathrm{w}} + \dot{\sigma} \tag{A56}$$

The final form of the entropy transport equation, Equation (A57), is found assuming that the flow is steady and axisymmetric. The partial differentials were replaced by total differentials because the only variation is along the meridional direction.

$$\rho v_m \frac{\partial s}{\partial m} = \frac{2}{b} \frac{\dot{q}_w}{T_w} + \dot{\sigma} \tag{A57}$$

Entropy Generation

Inserting the entropy, Equation (A57), and energy, Equation (A44), transport equations intro the Gibbs relation, Equation (A45), it is possible to find the expression for the rate of entropy generation, Equation (A58).

$$\dot{\sigma} = \frac{2}{b\,T} \left[(\tau_w v + \left(1 - \frac{T}{T_w}\right) \dot{q}_w \right] \tag{A58}$$

Equation (A58) indicates that the one-dimensional model predicts that the entropy generation is caused by viscous stress and heat transfer at a finite temperature difference. This is satisfactory, as these are the two mechanisms that lead to entropy generation in the real flow that we are tying to model. It is interesting to note that if the work done by viscous stress at the walls was not neglected, the viscous stress would not lead to entropy generation (clearly, an unsatisfactory result). This is because the friction force was modeled as a body force and body forces do not lead to entropy generation, for instance, gravity force or Coriolis acceleration.

References

1. Lohmann, R.; Markowski, S.; Brookman, E. Swirling Flow Through Annular Diffusers with Conical Walls. *J. Fluids Eng.* **1979**, *101*, 224–229. [CrossRef]
2. White, F.M. *Fluid Mechanics*, 7th ed.; McGraw-Hill: New York, NY, USA, 2011.
3. Macchi, E.; Perdichizzi, A. Efficiency Prediction for Axial-Flow Turbines Operating with Nonconventional Fluids. *J. Eng. Power* **1981**, *103*, 718–724. [CrossRef]
4. Bahamonde, S.; Pini, M.; De Servi, C.; Rubino, A.; Colonna, P. Method for the Preliminary Fluid Dynamic Design of High-Temperature Mini-Organic Rankine Cycle Turbines. *J. Eng. Gas Turbines Power* **2017**, *139*, 1–14. [CrossRef]
5. Lozza, G.; Macchi, E.; Perdichizzi, A. On the Influence of the Number of Stages on the Efficiency of Axial-Flow Turbines. In Proceedings of the International Gas Turbine Conference and Exhibition, London, UK, 18–22 April 1982; pp. 1–10.
6. Da Lio, L.; Manente, G.; Lazzaretto, A. New Efficiency Charts for the Optimum Design of Axial Flow Turbines for Organic Rankine Cycles. *Energy* **2014**, *77*, 447–459. [CrossRef]
7. Astolfi, M.; Macchi, E. Efficiency Correlations for Axial Flow Turbines Working with Non-Conventional Fluids. In Proceedings of the 3rd International Seminar on ORC Power System, ASME-ORC2015, Brussels, Belgium, 12–14 October 2015; pp. 1–12.
8. Da Lio, L.; Manente, G.; Lazzaretto, A. Predicting the Optimum Design of Single Stage Axial Expanders in ORC Systems: Is There a Single Efficiency Map for Different Working Fluids? *Appl. Energy* **2016**, *167*, 44–58. [CrossRef]
9. Al Jubori, A.; Dadah, R.K.A.; Mahmoud, S.; Khalil, K.M.; Ennil, A.S.B. Development of Efficient Small Scale Axial Turbine for Solar Driven Organic Rankine Cycle. In Proceedings of the ASME Turbo Expo 2016, Seoul, Korea, 13–17 June 2016; pp. 1–11.
10. Talluri, L.; Lombardi, G. Simulation and Design Tool for ORC Axial Turbine Stage. *Energy Procedia* **2017**, *129*, 277–284. [CrossRef]
11. Tournier, J.M.; El-Genk, M.S. Axial Flow, Multi-Stage Turbine and Compressor Models. *Energy Convers. Manag.* **2010**, *51*, 16–29. [CrossRef]
12. Meroni, A.; La Seta, A.; Andreasen, J.; Pierobon, L.; Persico, G.; Haglind, F. Combined Turbine and Cycle Optimization for Organic Rankine Cycle Power Systems–Part A: Turbine Model. *Energies* **2016**, *9*, 313. [CrossRef]

13. Meroni, A.; La Seta, A.; Andreasen, J.; Pierobon, L.; Persico, G.; Haglind, F. Combined Turbine and Cycle Optimization for Organic Rankine Cycle Power Systems–Part B: Case Study. *Energies* **2016**, *9*, 393. [CrossRef]
14. Meroni, A.; Graa, J.; Persico, G.; Haglind, F. Optimization of Organic Rankine Cycle Power Systems Considering Multistage Axial Turbine Design. *Appl. Energy* **2018**, *209*, 339–354. [CrossRef]
15. Perdichizzi, A.; Lozza, G. Design Criteria and Efficiency Prediction for Radial Inflow Turbines. In Proceedings of the International Gas Turbine Conference and Exhibition, Anaheim, CA, USA, 31 May–4 June 1987; pp. 1–9.
16. Uusitalo, A.; Turunen-saaresti, T.; Honkatukia, J.; Backman, J. Combined Thermodynamic and Turbine Design Analysis. In Proceedings of the 3rd International Seminar on ORC Power System, ASME-ORC2015, Brussels, Belgium, 12–14 October 2015; pp. 1–10.
17. Rahbar, K.; Mahmoud, S.; Al-Dadah, R.K.; Moazami, N. Parametric Analysis and Optimization of a Small-Scale Radial Turbine for Organic Rankine Cycle. *Energy* **2015**, *83*, 696–711. [CrossRef]
18. Da Lio, L.; Manente, G.; Lazzaretto, A. A Mean-Line Model to Predict the Design Efficiency of Radial Inflow Turbines in Organic Rankine Cycle (ORC) Systems. *Appl. Energy* **2017**, *205*, 187–209. [CrossRef]
19. Pini, M.; Persico, G.; Casati, E.; Dossena, V. Preliminary Design of a Centrifugal Turbine for Organic Rankine Cycle Applications. *J. Eng. Gas Turbines Power* **2013**, *135*, 042312. [CrossRef]
20. Casati, E.; Vitale, S.; Pini, M.; Persico, G.; Colonna, P. Centrifugal Turbines for Mini-ORC Power Systems. *J. Eng. Gas Turbines Power* **2014**, *136*, 11. [CrossRef]
21. Stanitz, J.D. *One-Dimensional Compressible Flow in Vaneless Diffusers of Radial- and Mixed-Flow Centrifugal Compressors, Including Effects of Friction, Heat Transfer and Area Change*; National Advisory Committee for Aeronautics: Washington, DC, USA, 1952.
22. Johnston, J.P.; Dean, R.C. Losses in Vaneless Diffusers of Centrifugal Compressors and Pumps: Analysis, Experiment, and Design. *J. Eng. Power* **1966**, *88*, 49–60. [CrossRef]
23. Elgammal, A.; Elkersh, A. A Method for Predicting Annular Diffuser Performance with Swirling Inlet Flow. *J. Mech. Eng. Sci.* **1981**, *23*, 107–112. [CrossRef]
24. Dubitsky, O.; Japikse, D. Vaneless Diffuser Advanced Model. *J. Turbomach.* **2008**, *130*, 1–10. [CrossRef]
25. Agromayor, R.; Nord, L.O. AnnularDiffuser1D—A One-Dimensional Model for the Performance Prediction of Annular Diffusers. 2019. Available online: https://doi.org/10.5281/zenodo.2634095 (accessed on 13 September 2019) .
26. Lemmon, E.W.; Huber, M.L.; McLinden, M.O. *NIST Standard Reference Database 23: Reference Fluid Thermodynamic and Transport Properties-REFPROP, Version 9.1*; National Institute of Standards and Technology: Gaithersburg, MD, USA, 2013.
27. Shampine, L.F.; Reichelt, M.W. The MATLAB ODE Suite. *SIAM J. Sci. Comput.* **1997**, *18*, 1–22. [CrossRef]
28. Brown, W.B. *Friction Coefficients in a Vaneless Diffuser*; National Advisory Committee for Aeronautics: Washington, DC, USA, 1947.
29. Cengel, Y.A. *Heat Transfer: A Practical Approach*, 2nd ed.; McGraw-Hill: New York, NY, USA, 2002.
30. Kumar, D.S.; Kumar, K.L. Effect of Swirl on Pressure Recovery in Annular Diffusers. *J. Mech. Eng. Sci.* **1980**, *22*, 305–313. [CrossRef]
31. Kline, S.J.; Abbott, D.E.; Fox, R.W. Optimum Design of Straight-Walled Diffusers. *J. Basic Eng.* **1959**, *81*, 321–329. [CrossRef]
32. Aungier, R.H. *Turbine Aerodynamics*, 1st ed.; ASME Press: New York, NY, USA, 2006.

International Journal of
Turbomachinery
Propulsion and Power

MDPI

Article

Preliminary Design and Optimization of Axial Turbines Accounting for Diffuser Performance

Roberto Agromayor * and Lars O. Nord

Department of Energy and Process Engineering, NTNU—The Norwegian University of Science and Technology, Kolbj. Hejes v. 1B, NO-7491 Trondheim, Norway; lars.nord@ntnu.no
* Correspondence: roberto.agromayor@ntnu.no

Received: 19 May 2019; Accepted: 11 September 2019; Published: 18 September 2019

Abstract: Axial turbines are the most common turbine configuration for electric power generation and propulsion systems due to their versatility in terms of power capacity and range of operating conditions. Mean-line models are essential for the preliminary design of axial turbines and, despite being covered to some extent in turbomachinery textbooks, only some scientific publications present a comprehensive formulation of the preliminary design problem. In this context, a mean-line model and optimization methodology for the preliminary design of axial turbines with any number of stages is proposed. The model is formulated to use arbitrary equations of state and empirical loss models and it accounts for the influence of the diffuser on turbine performance using a one-dimensional flow model. The mathematical problem was formulated as a constrained, optimization problem, and solved using gradient-based algorithms. In addition, the model was validated against two test cases from the literature and it was found that the deviation between experimental data and model prediction in terms of mass flow rate and power output was less than 1.2% for both cases and that the deviation of the total-to-static efficiency was within the uncertainty of the empirical loss models. Moreover, the optimization methodology was applied to a case study from the literature and a sensitivity analysis was performed to investigate the influence of several variables on turbine performance, concluding that: (1) the minimum hub-to-tip ratio constraint is always active at the outlet of the last rotor and that its value should be selected as a trade-off of aerodynamic performance and mechanical integrity; (2) that the total-to-static isentropic efficiency of turbines without diffuser deteriorates rapidly when the pressure ratio is increased; and (3) that there exist a loci of maximum efficiency in the specific speed and specific diameter plane (Baljé diagram) that can be predicted with a simple analytical expression.

Keywords: turbomachinery; mean-line; multistage; annular diffuser; gradient-based; loss model; baljé diagram; organic rankine cycle; cryogenic; supercritical carbon dioxide

1. Introduction

Axial turbines are the most common turbine configuration for electric power generation and propulsion systems, including: open Brayton cycles [1], closed Brayton cycles using helium [2] or carbon dioxide at supercritical conditions [3], and Rankine cycles using steam [4] or organic working fluids [5]. In addition, they are also used in cryogenic applications such as gas separation processes and liquefaction of natural gas [6]. Arguably, axial turbines owe their popularity to their versatility in terms of power capacity and range of operating conditions. The power capacity of axial turbines can vary from tens of kilowatts for small-scale Rankine power systems using organic fluids to hundreds of megawatts for large-scale steam and gas turbine power plants. In addition, the operating temperatures range from below -200 °C in some cryogenic applications to temperatures in excess of 1500 °C for some advanced gas turbines, whereas the operating pressures can vary from a few millibars at the

exhaust of some steam turbines to hundreds of bars at the inlet of supercritical steam and carbon dioxide power systems.

The fluid-dynamic or aerodynamic design of axial turbines can be divided in several steps involving mathematical models of different levels of complexity ranging from low-fidelity models for the preliminary design (mean-line and through-flow models) to high-fidelity models for the detailed blade shape definition (solution of the Navier–Stokes equations with turbulence models) [7]. Even if mean-line models are the simplest approach to analyze the thermodynamics and fluid dynamics of turbomachinery, they are still an essential step of the fluid-dynamic design chain because they provide the information required to use more advanced flow models [8]. Mean-line models assume that the flow is uniform at a mean radius and evaluate the conditions at the inlet and outlet of each cascade using the balance equations for mass and rothalpy, a set of equations of state to compute thermodynamic and transport properties, and empirical loss models to evaluate the entropy generation within the turbine [9]. In addition, to automate the preliminary design, it is possible to formulate the mean-line model as an optimization problem. This is especially advantageous to design new turbine concepts because it allows exploration of the design space in a systematic way and account for technical limitations in the form of constraints [7].

Despite mean-line models being covered to some extent in turbomachinery textbooks [1,9], only some scientific publications present a comprehensive formulation of the preliminary design problem. Table 1 contains a non-exhaustive survey of mean-line axial turbine models in the open literature. Some of the differences in the model formulation include: considering single-stage or multistage turbines, using restrictive assumptions such as repeating stages or not, using simplified equations of state or real gas fluid properties, and whether or not to account for the influence of the diffuser on turbine performance. In addition, some works formulate the preliminary design as an optimization problem and then solve it using gradient-based or direct search optimization algorithms, while other works formulate the design problem as system of equations and then do parametric studies to explore the design space. One of the recurring limitations of the scientific literature is that most mean-line models have not been validated against experimental data or CFD simulations. Finally, to the knowledge of the authors, no publication has made the mean-line model source code openly available to the research community and industry, with the notable exception of the *Meangen* code by Denton [8].

In this work, a mean-line model and optimization methodology for the preliminary design of axial turbines with any number of stages is proposed. The model is presented in Section 2 and it was formulated to use arbitrary equations of state and empirical loss models and to account for the influence of the diffuser on turbine performance using a one-dimensional flow model from a previous publication [10]. In addition, Section 3 contains the validation of the model against experimental data from two well-documented test cases reported in the literature. After that, the design problem is formulated as a constrained optimization problem in Section 4 and the proposed optimization methodology was applied to a case study from the literature in Section 5 to assess the optimal design in terms of total-to-static efficiency, angular speed, and mean diameter. Finally, Section 6 contains a sensitivity analysis of the case study with respect to: (1) isentropic power output, (2) tip clearance height, (3) minimum hub-to-tip ratio, (4) diffuser area ratio, (5) diffuser skin friction coefficient, (6) total-to-static pressure ratio, (7) number of stages and (8) angular speed and mean diameter to gain insight about the impact of these variables on the performance of the turbine and to extract general design guidelines. The authors would like to mention that the source code with the implementation of the mean-line model and optimization methodology described in this paper is available in an online repository [11], see Supplementary Materials.

Table 1. Non-exhaustive survey of axial turbine mean-line models.

Reference	Optimization [a]	Stages [b]	Repeating [c]	Diffuser [d]	Properties [e]	Validation [f]
Balje and Binsley [12]	Direct	1	No	No	Incompressible	Exp.
Macchi and Perdichizzi [13]	Direct	1	No	Fixed	Perfect gas	No
Lozza et al. [14]	Direct	1, 2, 3	No	Fixed	Perfect gas	No
Astolfi and Macchi [15]	Direct	1, 2, 3	No	Fixed	Real gas	No
Tournier and El-Genk [16]	No	Any	Yes	No	Real gas	Exp.
Da Lio et al. [17]	No	1	Yes	Fixed	Real gas	No
Da Lio et al. [18]	No	1	Yes	Fixed	Real gas	No
Meroni et al. [19]	Direct	1	No	Fixed	Real gas	Exp./CFD
Meroni et al. [20]	Direct	Any	No	Fixed	Real gas	Exp./CFD
Bahamonde et al. [21]	Direct	Any	No	No	Real Gas	CFD
Talluri and Lombardi [22]	Direct	1	Yes	No	Real gas	No
Denton [8]	No	Any	Optional	No	Perfect gas	CFD
Present work	Gradient	Any	Optional	1D model	Real gas	Exp.

[a] If applicable, type of optimization algorithm used (gradient-based or direct search). [b] Number of turbine stages that the model can handle. [c] Whether or not the model uses the repeating-stage assumption (this reduces the design space significantly). [d] Whether the model accounts for the influence of the diffuser or not. The models that accounted for the diffuser assumed a *fixed fraction* of kinetic energy recovery and did not model the flow within the diffuser. [e] Equation of state used to compute the properties of the fluid. [f] Whether or not the model has been validated with experimental data or CFD simulations.

2. Axial Turbine Model

Axial turbines are rotary machines that convert the energy from a fluid flow into work. An axial turbine is composed of one or more stages in series and each stage consists of one cascade of stator blades that accelerate the flow and one cascade of rotor blades that deflect the flow, converting the enthalpy of the fluid into work as a result of the net change of angular momentum. The kinetic energy of the flow at the outlet of the last stage can be significant and, for this reason, it is possible to install a diffuser to recover the kinetic energy and increase the turbine power output.

This section describes the axial turbine model proposed in this work. First, the geometry of axial turbines and the variables involved in the model are introduced. After that, the conventions used for the velocity triangles are explained. Finally, the design specifications (boundary conditions) and the mathematical model for the axial turbine is described. This mathematical model is composed of three sub-models that are used as building blocks: (1) the cascade model, (2) the loss model, and (3) the diffuser model. In Section 4 these sub-models are used to formulate the turbine preliminary design as a nonlinear, constrained optimization problem.

2.1. Axial Turbine Geometry

The geometry of a turbine blade is shown in Figure 1a. Blades are characterized by a mean camber line halfway between the suction and the pressure surfaces. The most forward point of the camber line is the leading edge and the most rearward point is the trailing edge. The blade chord c is the length of the straight line connecting the leading and the trailing edges. The blade thickness is the distance between the pressure and suction surfaces, measured perpendicular to the camber line. The aerodynamic performance of a blade is influenced by the maximum thickness $t_{\max}$ and the trailing edge thickness t_{te}. The angle between the axial direction and the tangent to the camber line is the metal angle θ and the difference between inlet and outlet metal angles is the camber angle $\Delta\theta = |\theta_{\text{in}} - \theta_{\text{out}}|$.

The axial–tangential view of a turbine stage is shown in Figure 1b. The blade pitch or spacing s is the circumferential separation between two contiguous blades and the opening o is defined as the distance between the trailing edge of one blade and the suction surface of the next one, measured perpendicular to the direction of the outlet metal angle. The angle between the axial direction and the chord line is the stagger angle or setting angle ξ and the projection of the chord onto the axial direction is known as the axial chord b. The cascade spacing s_{c} is the axial separation between one blade cascade and the next one.

The axial–radial view of a three-stage axial turbine is shown in Figure 1c. The working fluid flows parallel to the shaft within the annular duct defined by the inner and outer diameters. The hub is the surface defined by the inner diameter and the shroud is the surface defined by the outer diameter. The blade height H is defined as the difference between the blade radius at the tip r_t and the blade radius at the hub r_h and the spacing between the tip of the rotor blades and the shroud is known as clearance gap height t_{cl}. The mean radius r is often defined as the arithmetic mean of the hub and tip radii, although other definitions are possible. The blade height can vary along the turbine, but the flaring angle δ_{fl} should be limited to avoid flow separation close to the annulus walls. The geometry of an annular diffuser is shown in Figure 1d. The fluid leaving the last stage of the turbine enters the annular channel and it reduces its meridional component of velocity as the flow area increases (for subsonic flow) and its tangential component of velocity as the mean radius of the channel increases. The flow area of the diffuser is given by $A = 2\pi\hat{r}\,\hat{b}$, where $\hat{r}$ is the mean radius of the diffuser and $\hat{b}$ is the channel height of the diffuser. The area ratio is defined as the ratio of outlet to inlet areas, $AR = A_{out}/A_{in}$. When the inner and outer walls of the diffuser are straight, the diffuser is known as a conical-wall annular diffuser and its geometry can be parametrized in terms of the mean wall cant angle ϕ and the divergence semi-angle δ.

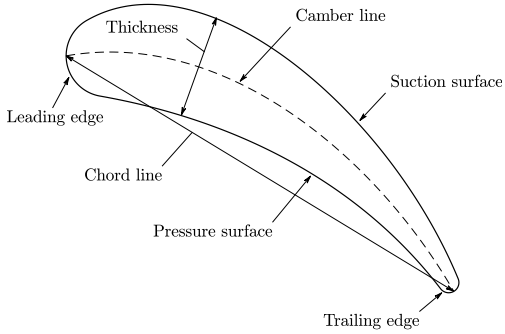

(**a**) Geometry of a blade section.

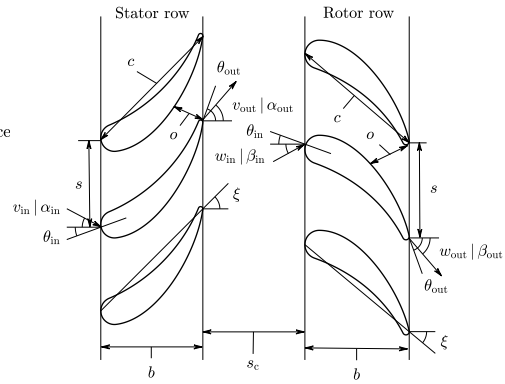

(**b**) Axial-tangential view of a cascade.

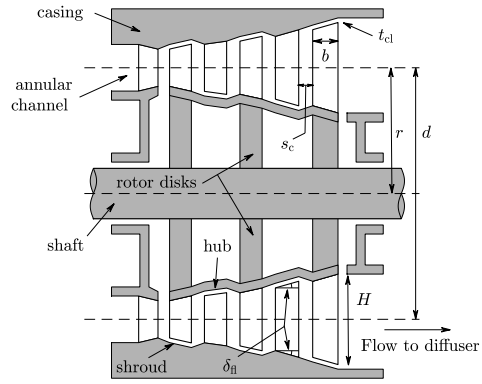

(**c**) Axial-radial view of an axial turbine.

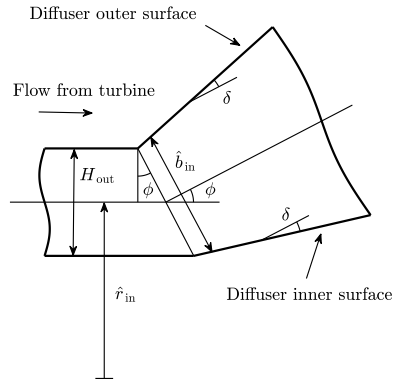

(**d**) Annular diffuser geometry.

Figure 1. Geometry of a general axial turbine and exhaust diffuser.

2.2. Velocity Vector Conventions

In this work the symbol v is used for the absolute velocity, w for the relative velocity, and u for the blade velocity. The components of velocity in the tangential and meridional directions are denoted with the subscripts θ and m, respectively. For the case of axial turbines, the meridional direction coincides with the axial direction. Regarding the sign convention for the velocity components, the positive axial direction is taken along the shaft axis from the inlet of the turbine to the outlet and the positive radial direction is taken as the turbine radius increases. The positive circumferential direction is taken in the direction of the blade speed.

The symbol α is used to denote the absolute flow angle while β is used for the relative flow angle. As shown in the velocity triangle of Figure 2, all angles are measured from the meridional towards the tangential direction. This is the usual convention in the gas turbine industry and it bounds the flow angles to the interval $[-\frac{\pi}{2}, \frac{\pi}{2}]$ [1] (p. 316). The advantage of this angle convention is that it is possible to use single-input inverse trigonometric functions directly. In addition, the same sign convention is used for stator and rotor blades for the sake of consistency. However, the loss model that is used in this paper [23] employs a different sign convention for stator and rotor blades and some of the formulas of the loss model had to be adapted, see Appendix A.

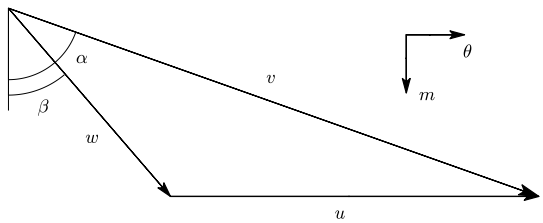

Figure 2. Velocity triangle showing the notation and conventions used in this work.

2.3. Design Specifications

A turbine is a component of a larger system that will impose some requirements on the turbine design, including: (1) stagnation state at the inlet of the turbine, (2) static pressure at the outlet of the turbine, and (3) mass flow rate. Alternatively, it is possible to specify the isentropic power output instead of the mass flow rate because both are related according to Equation (1), where the subscripts 1 and 2 refer to the states at the inlet and outlet of the turbine, respectively, and the subscript s refers to an isentropic expansion.

$$\dot{W}_s = \dot{m}\ (h_{01} - h_{2s}) = \dot{m}\,\Delta h_s \tag{1}$$

These design requirements can be regarded as the thermodynamic boundary conditions for the expansion and they are given inputs for the turbine model.

2.4. Cascade Model

This section describes the equations used to model the flow within stator and rotor cascades. All flow variables are evaluated at constant mean radius at the inlet and outlet of each cascade (mean-line model). The cascade model presented in this section is solved sequentially and it contains three blocks: (1) computation of the velocity triangles, (2) determination of the thermodynamic properties using the principle of conservation of rothalpy and equations of state, and (3) calculation of the cascade geometry.

2.4.1. Velocity Triangles

The equations used to compute the velocity diagrams for rotor and stator sections are the same, provided that the blade velocity is given by $u = 0$ for the stators and $u = \omega\, r$ for the rotors, where the angular speed ω and mean radius r are given as input variables.

The velocity triangles at the inlet of each cascade are computed according to Equations (2)–(7), where the subscripts that refer to inlet conditions have been dropped for simplicity. For the first stator, the absolute velocity v and flow angle α are given as inputs. For the rest of cascades, the absolute velocity and flow angle are obtained from the outlet of the previous cascade.

$$v_\theta = v\, \sin(\alpha) \tag{2}$$

$$v_m = v\, \cos(\alpha) \tag{3}$$

$$w_\theta = v_\theta - u \tag{4}$$

$$w_m = v_m \tag{5}$$

$$w = \sqrt{w_\theta^2 + w_m^2} \tag{6}$$

$$\beta = \arctan\left(\frac{w_\theta}{w_m}\right) \tag{7}$$

The velocity triangles at the outlet of each cascade are computed according to Equations (8)–(13), where the subscripts that refer to outlet conditions have been dropped for simplicity. The relative velocity w and flow angle β at the outlet of each cascade are provided as an input for the model.

$$w_\theta = w\, \sin(\beta) \tag{8}$$

$$w_m = w\, \cos(\beta) \tag{9}$$

$$v_\theta = w_\theta + u \tag{10}$$

$$v_m = w_m \tag{11}$$

$$v = \sqrt{v_\theta^2 + v_m^2} \tag{12}$$

$$\alpha = \arctan\left(\frac{v_\theta}{v_m}\right) \tag{13}$$

2.4.2. Thermodynamic Properties

The axial turbine model was formulated in a general way and the thermodynamic properties of the working fluid can be computed with any set of equations of state that supports enthalpy–entropy function calls. In this work, the REFPROP fluid library was used for the computation of thermodynamic and transport properties [24].

The stagnation state at the inlet of the first stator (for instance temperature and pressure) is an input for the model and the corresponding static state is determined according to Equations (14) and (15). The remaining static properties at the inlet of the first stator are determined with enthalpy–entropy function calls to the REFPROP library, see Equation (16). The static thermodynamic properties at the inlet of all the other cascade are obtained from the outlet of the previous cascade.

$$h_{\text{in}} = h_{0,\text{in}} - \frac{1}{2} v_{\text{in}}^2 \tag{14}$$

$$s_{\text{in}} = s\left(p_{0,\text{in}},\, h_{0,\text{in}}\right) \tag{15}$$

$$[T,\, p,\, \rho,\, a,\, \mu]_{\text{in}} = [T,\, p,\, \rho,\, a,\, \mu]\left(h_{\text{in}},\, s_{\text{in}}\right) \tag{16}$$

The thermodynamic properties at the outlet of each cascade are computed using the fact that rothalpy is conserved both in rotor and stator cascades [9] (pp. 10–11). For purely axial turbines (constant mean radius), the conservation of rothalpy is reduced to the conservation of relative

stagnation enthalpy, and the static enthalpy at the outlet of each cascade can be computed according to Equation (17). In addition, the entropy at the outlet of each cascade is provided as an input to the model. Therefore, any other static thermodynamic property can be determined with enthalpy–entropy function calls to the REFPROP library, Equation (18).

$$h_{\text{out}} = h_{\text{in}} + \frac{1}{2}w_{\text{in}}^2 - \frac{1}{2}w_{\text{out}}^2 \tag{17}$$

$$[T,\, p,\, \rho,\, a,\, \mu]_{\text{out}} = [T,\, p,\, \rho,\, a,\, \mu]\,(h_{\text{out}},\, s_{\text{out}}) \tag{18}$$

2.4.3. Cascade Geometry

The geometry of the annulus is obtained from the principle of conservation of mass and geometric relations, Equations (19)–(23), where the mass flow rate $\dot{m}$ is given as an input for the model. These equations are valid both for the inlet and outlet of the cascade and the subscripts were not included for simplicity.

$$A = \frac{\dot{m}}{\rho\, v_m} \tag{19}$$

$$H = \frac{A}{2\pi r} \tag{20}$$

$$r_{\text{h}} = r - H/2 \tag{21}$$

$$r_{\text{t}} = r + H/2 \tag{22}$$

$$\lambda = \frac{r_{\text{h}}}{r_{\text{t}}} \tag{23}$$

The mean blade height of the cascade is determined as the arithmetic mean of the blade height at the inlet and outlet of the cascade,

$$H = \frac{1}{2}\,(H_{\text{in}} + H_{\text{out}}) \tag{24}$$

The blade chord is determined from the blade aspect ratio (input variable) and the mean blade height using Equation (25). Similarly, the blade pitch (also known as spacing) is determined from the pitch to chord ratio (input variable) and the blade chord according to Equation (26).

$$c = \frac{H}{(H/c)} \tag{25}$$

$$s = c \cdot (s/c) \tag{26}$$

The incidence i and deviation δ angles are assumed to be zero and, therefore, the metal angle at the inlet and outlet of each cascade are given by Equations (27) and (28), respectively.

$$\theta_{\text{in}} = \beta_{\text{in}} - i = \beta_{\text{in}} \tag{27}$$

$$\theta_{\text{out}} = \beta_{\text{out}} - \delta = \beta_{\text{out}} \tag{28}$$

The blade opening is given by Equation (29). This equation is an approximation that neglects the effect or the curvature of the blade suction surface [1] (pp. 343–344).

$$o \approx s \cdot \cos\,(\theta_{\text{out}}) \tag{29}$$

The maximum blade thickness is computed according to the formula proposed by Kacker and Okapuu [23] that correlates the blade maximum thickness to chord ratio with the camber angle as given by Equation (30). The blade camber angle is defined as $\Delta\theta = |\theta_{in} - \theta_{out}|$.

$$(t_{max}/c) = \begin{cases} 0.15 & \text{for} \quad \Delta\theta \leq 40^\circ \\ 0.15 + 1.25 \cdot 10^{-3} \cdot (\theta - 40) & \text{for} \quad 40^\circ \leq \Delta\theta \leq 120^\circ \\ 0.25 & \text{for} \quad \Delta\theta \geq 120^\circ \end{cases} \tag{30}$$

The stagger angle is computed according to Equation (31), which assumes that circular-arc blades are used, Dixon and Hall [9] (p. 72). Alternatively, the stagger angle could be computed using the graphical relation proposed by Kacker and Okapuu [23] or given as an input for the model. The axial chord of the blades is determined using the geometric relation given by Equation (32).

$$\xi = \frac{1}{2}(\theta_{in} + \theta_{out}) \tag{31}$$

$$b = c \cdot \cos(\xi) \tag{32}$$

The axial chord and blade height difference between inlet and outlet are used to compute the flaring angle of the cascade according to Equation (33).

$$\tan(\delta_{fl}) = \frac{H_{out} - H_{in}}{2\,b} \tag{33}$$

The trailing edge thickness is computed using the trailing edge thickness to opening ratio (input variable) and the cascade opening according to Equation (34).

$$t_{te} = o \cdot (t_{te}/o) \tag{34}$$

In addition, the axial spacing between cascades s_c can be computed as fraction of the axial chord. However, this variable does not affect the performance predicted by the model because the Kacker and Okapuu [23] loss correlations neglect the influence of this parameter. Saravanamuttoo et al. [1] (pp. 332–333) suggests that axial spacing to chord ratios between 0.20 and 0.50 are satisfactory. Finally, the tip clearance height of the rotor blades t_{cl} is given as a fixed input to the model that depends on manufacturing limits. The geometry relations presented in this section allow a description of the turbine geometry in a level of detail that is adequate for preliminary design purposes. A more detailed design of the turbine geometry, such as the definition of the shape of the blades, requires more advanced mathematical models based on the fluid dynamics within the turbine rather than the algebraic loss models used in this work.

2.5. Loss Model

During the preliminary design phase, it is common to use empirical correlations to estimate the losses within the turbine. These sets of empirical correlations are known as loss models. Losses can be interpreted as any mechanism that leads to entropy generation within the turbine (which in turn reduces the power output), such as viscous friction in boundary layers or shock waves. See the work by Denton [25] for a detailed description of loss mechanisms in turbomachinery.

Perhaps, the most popular loss model for axial turbines is the one proposed by Ainley and Mathieson [26,27] and its subsequent refinements by Dunham and Came [28] and Kacker and Okapuu [23]. The Kacker–Okapuu loss model has been further refined to account for off-design performance by Moustapha et al. [29] and by Benner et al. [30]. One of the remarkable aspects of the Ainley–Mathieson family of loss methods is that it has been updated with new experimental data several times since the first version of the method was published. This was not the case for

other loss prediction methods such as the ones proposed by Balje and Binsley [31], Craig and Cox [32], Traupel [33], or Aungier [34]. A comprehensive review of different loss models is given by Wei [35].

In this work, the Kacker and Okapuu [23] loss model was selected because of its popularity and maturity. The improvements of this loss model to account for off-design performance were not considered because the axial turbine methodology proposed in this paper is meant for the optimization of design performance. The Kacker–Okapuu loss model is described in detail in Appendix A. The formulation of the loss model has been adapted to the nomenclature and sign conventions used in this work for the convenience of the reader.

As described by Denton [25] and by Dahlquist [36], there are several definitions for the loss coefficient. In this work, the stagnation pressure loss coefficient was used because the Kacker–Okapuu loss model was developed using this definition. This loss coefficient is meaningful for cascades with a constant mean radius and it is defined as the ratio of relative stagnation pressure drop across the cascade to relative dynamic pressure at the outlet of the cascade, Equation (35). This definition is valid for both rotor and stator cascades.

$$Y = \frac{p_{0\mathrm{rel,in}} - p_{0\mathrm{rel,out}}}{p_{0\mathrm{rel,out}} - p_{\mathrm{out}}} \tag{35}$$

In general, the loss coefficient computed from its definition, Equation (35), and the loss coefficient computed using the loss model, Appendix A, will not match for an arbitrary set of input parameters. In Section 4, the turbine design is formulated as an optimization problem that uses equality constraints to ensure that the value of both loss coefficients matches for each cascade. The loss coefficient error is given by Equation (36).

$$Y_{\mathrm{error}} = Y_{\mathrm{definition}} - Y_{\mathrm{loss\,model}} \tag{36}$$

2.6. Diffuser Model

The diffuser model is based on the transport equations for mass, meridional and tangential momentum, and energy in an annular channel. It assumes that the flow is one-dimensional (in the meridional direction), steady (no time variation), and axisymmetric (no tangential variation). The model can use arbitrary equations of state and it accounts for effects of area change, heat transfer, and friction. Under these conditions, the governing equations of the flow are given by Equations (37)–(40). The detailed derivation of these equations and a discussion of the physical meaning of the different terms is presented in the Appendix of Agromayor et al. [10].

$$v_m \frac{\mathrm{d}\rho}{\mathrm{d}m} + \rho \frac{\mathrm{d}v_m}{\mathrm{d}m} = -\frac{\rho v_m}{\hat{b}\,\hat{r}} \frac{\mathrm{d}}{\mathrm{d}m}(\hat{b}\,\hat{r}) \tag{37}$$

$$\rho v_m \frac{\mathrm{d}v_m}{\mathrm{d}m} + \frac{\mathrm{d}p}{\mathrm{d}m} = \frac{\rho v_\theta^2}{\hat{r}} \sin(\phi) - \frac{2\tau_{\mathrm{w}}}{\hat{b}} \cos(\alpha) \tag{38}$$

$$\rho v_m \frac{\mathrm{d}v_\theta}{\mathrm{d}m} = -\frac{\rho v_\theta v_m}{\hat{r}} \sin(\phi) - \frac{2\tau_{\mathrm{w}}}{\hat{b}} \sin(\alpha) \tag{39}$$

$$\rho v_m \frac{\mathrm{d}p}{\mathrm{d}m} - \rho v_m a^2 \frac{\mathrm{d}\rho}{\mathrm{d}m} = \frac{2(\tau_{\mathrm{w}} v + \dot{q}_{\mathrm{w}})}{\hat{b}\left(\frac{\partial e}{\partial p}\right)_\rho} \tag{40}$$

The viscous term is modeled using a constant skin friction coefficient C_{f} such that $\tau_{\mathrm{w}} = C_{\mathrm{f}} \frac{\rho v^2}{2}$ and heat transfer is neglected, $\dot{q}_{\mathrm{w}} = 0$. The geometry of the diffuser was modeled in a simple way assuming that the inner and outer surfaces are straight, see Figure 1d. For this particular geometry, the diffuser channel height $\hat{b}$ and mean radius $\hat{r}$ are given by Equations (41) and (42), where the mean cant angle ϕ and divergence semi-angle δ are given as input parameters.

$$\hat{r}(m) = \hat{r}_{\mathrm{in}} + m \sin(\phi) = r + m \sin(\phi) \tag{41}$$

$$\hat{b}(m) = \hat{b}_{\mathrm{in}} + 2m \tan(\delta) = H_{\mathrm{out}} / \cos(\phi) + 2m \tan(\delta) \tag{42}$$

The initial conditions required to integrate the system of ordinary differential equations (ODE) are prescribed assuming that the thermodynamic state and velocity vector do not change from the turbine outlet to the diffuser inlet. The integration starts from the initial conditions and stops when the prescribed value of outlet to inlet area ratio AR is reached. In this work, the MATLAB function *ode45* was used to perform the numerical integration [37]. This function uses an automatic-stepsize-control solver that combines fourth and fifth order Runge–Kutta methods to control the error of the solution.

In general, the static pressure that is given as a design specification from a system analysis will not match the pressure at the outlet of the diffuser computed by the model. In Section 4, the turbine design is formulated as an optimization problem that uses an equality constrain to ensure that the static pressure at the outlet of the diffuser and the target pressure match. The dimensionless outlet static pressure error is given by Equation (43).

$$p_{\text{error}} = \frac{p_{\text{out}}^{\text{diff}} - p_{\text{target}}}{p_{\text{target}}} \tag{43}$$

3. Validation of the Axial Turbine Model

The aim of this section is to validate the axial turbine model presented in Section 2 using the experimental data of the one- and two-stage turbines reported by Kofskey and Nusbaum [38]. The flow in both turbines is subsonic and they use air as working fluid. To validate the model, the geometry and operating conditions reported by Kofskey and Nusbaum [38] were replicated and the design-point performance of both test cases was compared with the output of the model, see Table 2. The inlet thermodynamic state, angular speed, and total-to-static pressure ratio were matched at the design point and the validation was performed analyzing the deviation in mass flow rate, power output, and total-to-static isentropic efficiency. This approach is consistent with the definition of the design point given by Kofskey and Nusbaum [38]. The data reported in Table 2 shows that the agreement between the predicted and measured mass flow rates and power outputs is satisfactory and that the relative deviation is less than 1.2% for both turbines. In addition, the deviation of total-to-static isentropic efficiency between model and experiment is 1.15 percentage points for the one-stage turbine and 0.60 points for the two-stage turbine, which is within the efficiency-prediction uncertainty of the loss model of ± 1.5 percentage points [23]. The turbines reported in [38] did not have a diffuser to recover the exhaust kinetic energy and therefore could not be used to validate the diffuser model. Nevertheless, the diffuser model used in this work has been validated in a previous publication [10].

The analysis presented in this section showed that the axial turbine model can be used to predict the design-point performance of turbines with one or more stages. However, the validation was restricted to subsonic turbines using air as working fluid and it is likely that the efficiency predictions will not be as accurate for turbines with transonic–supersonic cascades or when the fluid behavior deviates from ideal gas, such as in Rankine cycles using organic fluids with high molecular mass or in supercritical carbon dioxide power systems.

Table 2. Validation of the axial turbine model against experimental data.

Number of Stages	Variable [a,b,c]	Kofskey and Nusbaum [38]	Present Work	Deviation
1 stage	T_{01}	22.5 °C	Same	n.a.
	p_{01}	1.380 bar	Same	n.a.
	PR	2.298	Same	n.a.
	ω	15,533 rpm	Same	n.a.
	$\dot{m}$	2.695 kg/s	2.729 kg/s	0.91%
	$\dot{W}$	136.17 kW	135.03 kW	−0.42%
	η_{ts}	80.00%	78.85%	1.15 points
2 stages	T_{01}	25.8 °C	Same	n.a.
	p_{01}	1.240 bar	Same	n.a.
	PR	4.640	Same	n.a.
	ω	15,619 rpm	Same	n.a.
	$\dot{m}$	2.407 kg/s	2.434 kg/s	1.12%
	$\dot{W}$	212.06 kW	211.10 kW	−0.46%
	η_{ts}	82.00%	81.40%	0.60 points

[a] Kofskey and Nusbaum [38] reported the turbine performance in terms of *equivalent* variables. These were converted to ordinary variables using ambient conditions at sea level (101.325 kPa and 288.15 K). [b] The power output is computed from the measured torque and angular speed. [c] The total-to-static isentropic efficiency is a dependent variable that is computed from the thermodynamic conditions, mass flow rate, and power output.

4. Optimization Problem Formulation

The sub-models presented in Section 2 can be integrated to formulate the design of the turbine as a nonlinear, constrained optimization problem. To formulate this problem, it is necessary to specify: (1) the objective function to be optimized, (2) the independent variables and fixed parameters, and (3) the inequality and equality constraints that limit the design space. Once the problem is formulated, it is possible to find the optimal solution that satisfies the constraints using a numerical algorithm.

4.1. Objective Function

The objective function is any indicator of interest that must be minimized or maximized. In this work the total-to-static isentropic efficiency was used as objective function because it is assumed that the kinetic energy at the outlet of the diffuser is wasted [9] (pp. 23–24). The total-to-static isentropic efficiency is given by Equation (44), where the subscripts 1 and 2 refer to the states at the inlet and outlet of the turbine, respectively, and the subscript s refers to an isentropic expansion.

$$\eta_{ts} = \frac{h_{01} - h_{02}}{h_{01} - h_{2s}} \tag{44}$$

4.2. Independent Variables

The choice of independent variables is not unique and different sets of variables can be used to formulate the same problem. Ideally, it should be easy to provide a set of independent variables and this set should allow computation of the dependent variables in a sequential way, avoiding iterations when the model is evaluated. In addition, it is preferable to use a set of independent variables that is not poorly scaled, Nocedal and Wright [39] (pp. 26–27). An appropriate scaling of the problem increases the convergence rate of some algorithms and will reduce the numerical rounding error when the gradient of the objective function and constraints are evaluated using finite differences.

Table 3 shows the set of independent variables adopted in this work as well as the lower and upper bounds that were used to formulate the optimization problem for the case study discussed in Section 5. This formulation uses 6 independent variables per cascade (or 12 independent variables per stage) plus three additional global independent variables. This set of independent variables is well-scaled (all variables have a similar order of magnitude) and it allows evaluation of the turbine model in a sequential way without inner iterations from the inlet of the first stator to the exit of the

diffuser. The lower and upper bounds of the independent variables were selected to span a large design space that respects the range of applicability of the Kacker and Okapuu [23] loss system.

The specific speed and specific diameter were selected as independent variables instead of the angular speed and mean diameter because they have an order of magnitude of unity and it is easier to provide a reasonable initial guess since they are independent of the scale of the problem [31]. The definitions of the specific speed and diameter are given by Equations (45) and (46). The angular speed and mean diameter can be readily obtained from their specific counterparts.

Table 3. Optimization problem formulation and definition of the reference cases.

Fixed parameters				
Number of stages	N	=	1	–
Isentropic power output	$\dot{W}_s$	=	250|5000	kW
Turbine inlet stagnation temperature	T_{01}	=	155	°C
Turbine inlet stagnation pressure	p_{01}	=	36.2	bar
Turbine outlet static pressure	p_2	=	15.85	bar
Tip clearance height	t_{cl}	=	0.50	mm
First stator inlet flow angle	α_{in}	=	0.0	deg
Diffuser mean cant angle	ϕ	=	30.0	deg
Diffuser divergence semi-angle	δ	=	5.0	deg
Diffuser area ratio	AR	=	2.5	–
Diffuser skin friction coefficient	C_{f}	=	0.010	–
Independent variables				
Specific speed	ω_{s}	$\in$	[0.10, 10.0]	–
Specific diameter	d_{s}	$\in$	[0.10, 10.0]	–
Normalized first stator inlet velocity	v_{in}/v_0	$\in$	[0.01, 1.00]	–
Normalized outlet relative velocity [a]	w_{out}/v_0	$\in$	[0.01, 1.00]	–
Outlet relative flow angle (stator) [a]	$\beta_{\mathrm{out,S}}$	$\in$	[+40.0, +80.0]	deg
Outlet relative flow angle (rotor) [a]	$\beta_{\mathrm{out,R}}$	$\in$	[−80.0, −40.0]	deg
Normalized outlet entropy [a,c]	$s_{\mathrm{out}}/s_{\mathrm{in}}$	$\in$	[1.00, $s_{\mathrm{ref}}/s_{\mathrm{in}}$]	–
Aspect ratio [a]	H/c	$\in$	[1.00, 2.00]	–
Pitch to chord ratio [a]	s/c	$\in$	[0.75, 1.10]	–
Trailing edge thickness to opening ratio [a]	t_{te}/o	$\in$	[0.05, 0.40]	–
Nonlinear constraints				
Inlet relative flow angle (stator) [a]	$\beta_{\mathrm{in,S}}$	$\leq$	+15.0	deg
Inlet relative flow angle (rotor) [a]	$\beta_{\mathrm{in,R}}$	$\geq$	−15.0	deg
Flaring angle [a]	δ_{fl}	$\in$	[−10.0, +10.0]	deg
Hub-to-tip ratio [b]	λ	$\in$	[0.60, 0.95]	–
Cascade pressure ratio [a]	PR_{c}	$\geq$	1.00	–
Diffuser inlet meridional Mach number	$\mathrm{Ma}^{\mathrm{diff}}_{m,\mathrm{in}}$	$\leq$	1.00	–
Outlet static pressure error	p_{error}	=	0.00	–
Cascade loss coefficient error [a]	Y_{error}	=	0.00	–

[a] One value per cascade (rotor or stator). [b] Two values per cascade (inlet and outlet). [c] s_{ref} corresponds the outlet entropy assuming $\eta_{ts}^{\mathrm{ref}} = 50\%$.

$$\omega_{\mathrm{s}} = \omega \frac{\left(\dot{m}/\rho_{2s}\right)^{1/2}}{\left(h_{01} - h_{2s}\right)^{3/4}} \tag{45}$$

$$d_s = d \frac{\left(h_{01} - h_{2s}\right)^{1/4}}{\left(\dot{m}/\rho_{2s}\right)^{1/2}} \tag{46}$$

In addition, the flow velocities were normalized using the isentropic velocity (also known as spouting velocity), see Equation (47), and the entropies were normalized using a reference entropy value computed assuming an isentropic turbine efficiency, see Equations (48) and (49).

$$v_0 = \sqrt{2\ (h_{01} - h_{2s})} \tag{47}$$

$$s_{\text{ref}} = s(p_2, h_{\text{ref}}) \tag{48}$$

$$h_{\text{ref}} = h_{01} - \eta_{\text{ref}} \cdot (h_{01} - h_{2s}) \tag{49}$$

The remaining independent variables did not need to be scaled.

4.3. Fixed Parameters

To compute the dependent variables, it is also necessary to provide several fixed parameters that will not change during the optimization. Table 3 contains the set of fixed parameters that are used as input for the axial turbine model as well as the numerical values used for the case study.

The isentropic power output, given by Equation (1), and thermodynamic boundary conditions are kept constant because they are given by the system design requirements, see Section 2.3. It is interesting to note that the set of independent variables is dimensionless and that the isentropic power output (or the mass flow rate) is the variable that scales-up the problem.

The flow angle at the inlet of the first stator was not selected as an optimization variable because it was assumed that there is no swirl at the inlet of the turbine and the tip clearance height was set as a fixed parameter because it is given by manufacturing limits. Finally, the diffuser model inputs were set as fixed parameters because the total-to-static isentropic efficiency is a monotonic function of these variables, see Agromayor et al. [10].

4.4. Constraints

In addition to the bounds for the degrees of freedom, the axial turbine model includes nonlinear equality and inequality constraints to guarantee that the model is consistent and that the design is feasible. These constraints and the numerical values used for the case study are summarized in Table 3. Depending on each application, it is possible to implement additional constraints for the model or to ignore some of the constraints suggested in Table 3. The pressure ratio in each cascade was constrained to avoid compression within the turbine (this is equivalent to constrain the degree of reaction between zero and one) and the constraint on the flaring angle was set to avoid flow separation close to the annulus walls [26]. In addition, the constrains for the inlet relative flow angles were imposed to avoid blades with too low deflection [23]. The meridional component of the Mach number at the inlet of the diffuser was constrained to ensure that the ODE system of the diffuser model, Equations (37)–(40), is not singular [10].

The constrain for the hub-to-tip ratio was set because the hub-to-tip ratio is a dependent variable that the designer might want to control since it has a great influence on the optimal angular speed and diameter, on the aerodynamic design of the blades (radial variation of flow angles), and on the centrifugal and gas bending stresses [1].

Finally, as discussed in Sections 2.5 and 2.6, equality constrains were imposed on the loss coefficient error and the outlet static pressure error to ensure that the model is consistent.

4.5. Optimization Algorithm

The are two main families of optimization methods, gradient-based method and direct search or derivative-free methods. Gradient-based methods are suitable for problems that are continuous and smooth, and they use derivative information of the objective function and constraints to determine the next iterate, while direct search methods use only sampled values of the objective function and constraints. For this reason, direct search methods can be used when gradient information

is not available or to solve non-smooth or even discontinuous problems. However, direct search methods have slower convergence rates and they are not well suited to handle problems with equality constraints [39] (pp. 220–223).

The axial turbine model proposed in this work is continuous and smooth, except for some of the equations of the loss model that are not differentiable (piece-wise functions or functions involving absolute values), see Appendix A. Despite these non-smooth points, experience shows that the optimization problem can be solved successfully using gradient-based optimization algorithms. In particular, the sequential quadratic programming algorithm of the MATLAB Optimization Toolbox was used to optimize the axial turbine design [40].

4.6. Optimization Strategy

Once the optimization problem is formulated it is possible to find the optimal solution that satisfies the constraints using a numerical algorithm. The optimization strategy for axial turbines is summarized in Figure 3. The optimization requires an initial guess for the independent variables and the values of the fixed parameters listed in Table 3. In addition, it is necessary to specify the choice of optimization algorithm and the tolerances for the termination criteria. In the first iteration, the optimization algorithm uses the initial guess to evaluate the axial turbine model. Once the axial turbine model is evaluated, the gradients of the objective function and the constraints are calculated by finite differences and they are used by the optimization algorithm to determine the values of the independent variables in the next iteration. This process is repeated until the solution meets the termination criteria and the optimal turbine design is saved.

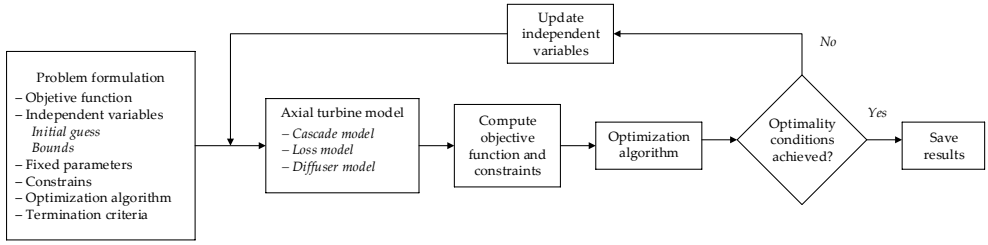

Figure 3. Axial turbine optimization strategy flow diagram.

5. Optimization of a Case Study

The aim of this section is to assess the optimization methodology proposed in this work. To do this, the model was tested against two reference axial turbine optimization problems presented in Macchi and Astolfi [41]. The two cases consider pentaflueroethane (R125) expanding from 155 °C and 36.2 bar (stagnation properties) to 15.85 bar (static pressure). The mass flow rate is selected to achieve an isentropic power of 250 kW in the first case and 5000 kW in the second case. These two case studies are representative of a small-scale and a large-scale Rankine cycles used to generate power from a low-temperature heat source as in a geothermal, solar, biomass, or waste heat recovery application [5].

The values of the fixed parameters, bounds of the optimization variables, and the nonlinear constrains used to formulate the optimization problem are summarized in Table 3. The minimum hub-to-tip ratio constraint is always active at the exit of the last rotor, see Section 6.3, and it has a great influence on the optimal angular speed and diameter. For this reason, the comparison of optimal speed and diameter will only be fair if the minimum hub-to-tip ratio is the same as in the reference case. The value $\lambda_{\text{min}} = 0.60$ reported in Table 3 is the same value used by Macchi and Astolfi [41] (the minimum-hub-to tip ratio used by Macchi and Astolfi was not reported in the original publication, but it was confirmed by M. Astolfi in a personal communication).

The results of the optimization for the two cases considered are shown in Table 4. It can be observed that the optimal angular speed and diameter of the reference case agree well with the results obtained with the turbine model presented in this work and that the maximum relative deviation is less than 6%. In addition, the model presented in this work captures the trend of the angular speed and diameter as the power output changes. The values of total-to-static efficiency from the reference case and the ones obtained in the present work are comparable although there are is a difference of 2.07 and 0.83 percentage points in the small-scale and large-scale cases, respectively. This difference is not surprising considering that the Craig and Cox [32] loss model was used in the reference case while the Kacker and Okapuu [23] model was used in the present work and that the efficiency-prediction uncertainty of these empirical loss models is approximately ± 1.5 percentage points, if not higher [23].

Table 4. Output of the optimization methodology for two reference optimization problems.

Isentropic Power	Variable	Macchi and Astolfi [41]	Present Work	Deviation
$\dot{W}_s = 250$ kW	ω	31,000 rpm	29,231 rpm	−5.71%
	d	0.086 m	0.087 m	1.27%
	$\dot{W}$	219.3 kW	224.4 kW	2.36%
	η_{ts}	87.70%	89.77%	2.07 points
$\dot{W}_s = 5000$ kW	ω	6000 rpm	6144 rpm	2.40%
	d	0.420 m	0.395 m	−5.87%
	$\dot{W}$	4535.0 kW	4576.5 kW	0.92%
	η_{ts}	90.70%	91.53%	0.83 points

6. Sensitivity Analysis

This section contains a sensitivity analysis of the 5000 kW reference case analyzed in the previous section to gain insight about the impact of several input parameters on turbine performance. The next subsections investigate the influence of: (1) isentropic power output, (2) tip clearance height, (3) minimum hub-to-tip ratio, (4) diffuser area ratio, (5) diffuser skin friction coefficient, (6) total-to-static pressure ratio, (7) number of stages and (8) angular speed and mean diameter on the total-to-static isentropic efficiency. Each of the analyses of this section studies the influence of these variables on the optimal solution while all other fixed parameters are the same as in the 5000 kW reference case summarized in Table 3. The ranges of the variables were selected to cover a wide span of flow conditions and they are justified in each subsection. Other variables were not considered for the sensitivity analysis because they have a secondary influence on turbine performance or because they are inactive constraints.

6.1. Influence of Isentropic Power

The isentropic power output was varied from 10 kW to 10 MW and the maximum attainable total-to-static efficiency is shown in Figure 4a,b. This range of power output was selected to cover a wide spectrum of turbine scales. According to the classification for Rankine power systems using organics working fluids proposed by Colonna et al. [5], this range of power output covers the mini, small, medium, and large power capacities.

It can be observed that the efficiency increases monotonously with the isentropic power and that the effect is more marked when the power output is small. The reason for this is that the size of the turbine increases and therefore: (1) the blade height H increases and the t_{cl}/H ratio decreases, which in turn reduces the tip clearance loss coefficient, see Equation (A19), and (2) the blade chord of the cascades increases, which in turn increases the Reynolds number and reduces the profile loss coefficient, see Equation (A1).

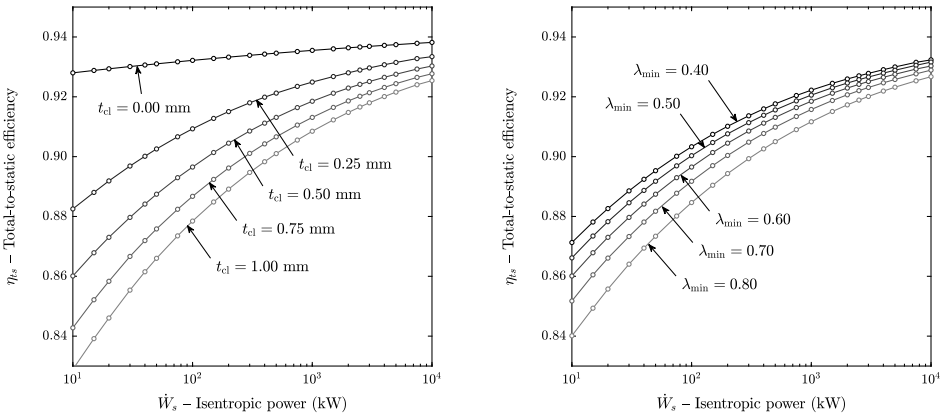

(**a**) Influence of the tip clearance height. (**b**) Influence of the minimum hub-to-tip ratio constraint.

Figure 4. Total-to-static isentropic efficiency as a function of the isentropic power output and (**a**) tip clearance height or (**b**) minimum hub-to-tip ratio constraint.

6.2. Influence of Tip Clearance

Figure 4a shows the total-to-static efficiency as a function of the isentropic power when the tip clearance height is varied from 0.00 mm (no clearance) to 1.00 mm (high clearance). It can be observed that the isentropic efficiency decreases when the tip clearance is increased and that the trend is not linear. For instance, increasing the tip clearance from 0.00 mm to 0.25 mm penalizes the efficiency more than from 0.25 to 0.50 mm.

It can also be seen that the efficiency drop due to tip clearance is more marked when the isentropic power is low because the ratio t_{cl}/H is increased both due to blade height reduction and tip clearance increase. In addition, note that total-to-static efficiency increases with the isentropic power output even for the case when the rotor tip clearance is zero due to Reynolds number effects.

6.3. Influence of the Hub-to-Tip Ratio

The influence of the lower limit for the hub-to-tip ratio constraint on the turbine performance as a function of the isentropic power is shown in Figure 4b, where the low value $\lambda = 0.40$ is representative of low-pressure steam turbine stages and the high value $\lambda = 0.80$ is representative of gas turbines or high-pressure steam turbine stages. The results of the optimization showed that the constraint for the minimum hub-to-tip ratio is always active at the outlet of the turbine, i.e., the turbine model proposed in this work predicts that the isentropic efficiency will always increase when the allowable lower limit for the hub-to-tip ratio is decreased.

The reason for this is that the blade height is increased when the minimum hub-to-tip ratio decreases and, as a result of this, (1) the tip clearance to blade height ratio t_{cl}/H and the clearance loss coefficient decrease and (2) for a fixed aspect ratio, the blade chord and Reynolds number increase and the profile loss coefficient is reduced. In addition, the channel height of the diffuser increases according to $\hat{b}_{in} = H_{out} / \cos(\phi)$, see Figure 1d. This in turn reduces the friction losses in the diffuser because the channel height appears in the denominator of the friction terms of the diffuser model, Equations (38)–(40). The effect of the hub-to-tip ratio on the friction losses of the diffuser agrees with the results obtained by the authors in a previous work [10], but its impact on the isentropic efficiency is marginal compared with the impact of profile and tip clearance losses.

6.4. Influence of the Diffuser Area Ratio

The effect of the diffuser area ratio on the total-to-static isentropic efficiency is shown in Figure 5a,b. The limits of the area ratio were selected to include cases ranging from the absence of diffuser $(AR = 1)$,

to cases where a large fraction of the kinetic energy is recovered ($AR = 5$). This upper limit was selected because, for the case of inviscid, incompressible flow with no inlet swirl, a diffuser with an area ratio of $AR = 5$ would recover 96% of the available dynamic pressure [10].

Both Figure 5a,b show that the isentropic total-to-static efficiency increases with the area ratio in an asymptotic way. A small increase of area ratio from the case with no diffuser ($AR = 1$) increases the total-to-static efficiency significantly, whereas, as the area ratio is higher, the improvement of isentropic efficiency becomes less marked because there is less kinetic energy to recover at the diffuser exit. The results of the optimization showed that using an area ratio in the range 2.0–2.5 achieves 70–80% of the maximum efficiency gain. In addition, it was found that the optimum absolute flow angle at the outlet of the last rotor was very close to zero (no swirl) for all cases, regardless of the area ratio of the diffuser.

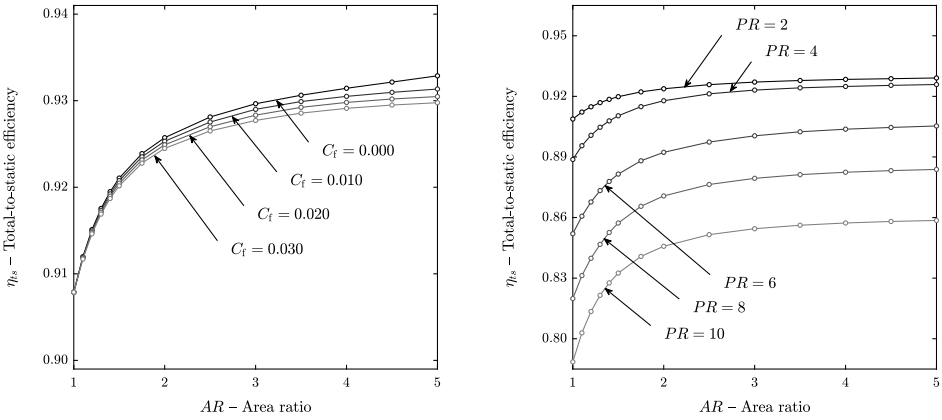

(**a**) Influence of the skin friction coefficient.

(**b**) Influence of the pressure ratio.

Figure 5. Total-to-static isentropic efficiency as a function of the diffuser area ratio and (**a**) skin friction coefficient or (**b**) pressure ratio.

6.5. Influence of the Skin Friction Coefficient

To the knowledge of the authors, there are no correlations available to predict the skin friction coefficient for annular channels with swirling flow. However, it is possible to estimate a reasonable value for the skin friction coefficient based on experimental data from vaneless diffusers without flow separation. Brown [42] measured the local skin friction coefficient for different vaneless diffusers and obtained values in the range 0.003–0.010. In the absence of better estimates, Johnston and Dean [43] recommend values within the range 0.005–0.010 for the global skin friction coefficient. In a similar way, Dubitsky and Japikse [44] suggest 0.010 as a reasonable estimate for the global skin friction coefficient, but noted that values from 0.005 to 0.020 were required to fit experimental data, depending on the application.

In this section, the friction factor was varied from 0.000 (frictionless) to 0.030 (high friction) and the impact on the turbine total-to-static isentropic efficiency is shown in Figure 5a as a function of the area ratio. This range of skin friction factor is representative of well-designed diffusers with attached boundary layers. If the adverse pressure gradient is too high and causes flow separation, the friction losses in the diffuser would increase significantly reducing the pressure recovery and the turbine total-to-static isentropic efficiency [45].

It can be observed that increasing the friction factor decreases the total-to-static isentropic efficiency in a linear way (the different curves are equispaced). In addition, the impact of friction factor on the efficiency drop is more notable as the area ratio is high because the length of the channel increases. However, the effect of the friction factor has only a modest impact on the total-to-static efficiency as it causes an efficiency drop of ∼0.3 percentage points for the worst case of Figure 5a.

6.6. Influence of the Total-to-Static Pressure Ratio

The effect of the pressure ratio as a function of the diffuser area ratio is shown in Figure 5b. The pressure at the outlet of the turbine was kept constant and the pressure at the inlet was varied to achieve pressure ratios ranging from $PR = 2$ (subsonic flow) to $PR = 10$. It can be observed that increasing the pressure ratio from $PR = 2$ to $PR = 4$ causes a small efficiency drop and that further increasing the pressure ratio to $PR = 6$ causes a much larger efficiency drop. The reason for this is that the Mach number at the outlet of the cascades becomes higher than unity when $PR \approx 4$ and the supersonic correction factor of the Kacker and Okapuu [23] loss system, see Equation (A4), penalizes the total-to-static isentropic efficiency.

In addition, Figure 5b also shows that the total-to-static isentropic efficiency of turbines without diffuser deteriorates rapidly when the pressure ratio is increased. This is because increasing the turbine pressure ratio increases the flow velocities within the turbine and the amount of kinetic energy that is potentially wasted at the outlet. This highlights the importance of using a diffuser when the pressure ratio is high.

6.7. Influence of the Number of Stages

Figure 6 shows the total-to-static efficiency of turbines with one, two, and three stages as a function of the pressure ratio. Again, the pressure ratio was achieved varying the pressure at the inlet of the turbine while keeping the outlet pressure constant. However, in this case, the upper limit of the pressure ratio increased to $PR = 14$.

In can be seen that there is a peak of efficiency and that the performance deteriorates rapidly when the pressure ratio increases beyond this point because the flow becomes supersonic and the Mach number correction factor penalizes the profile loss coefficient, see Equation (A4). Moreover, the range of pressure ratios for which the isentropic efficiency is high becomes wider as the number of stages increase because the expansion can be distributed over more cascades and the number of optimization variables increases.

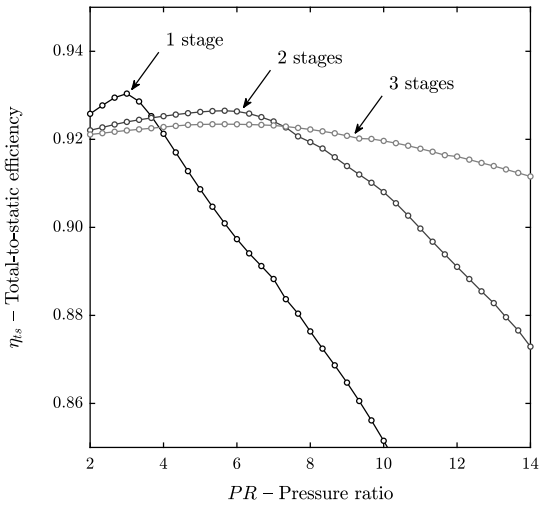

Figure 6. Influence of the pressure ratio and number of stages.

6.8. Influence of the Angular Speed and Diameter

The results presented in the previous subsections correspond to the optimal values of angular speed and diameter because the specific speed and specific diameter were independent optimization variables with inactive upper and lower bounds. Depending on the application, it might not be

possible to achieve the point of optimal angular speed and diameter because of technical constraints that were not considered in the analysis such as the frequency of the electrical grid, mechanical stress, or space limitations. The objective of this section is to analyze the impact of using a non-optimal angular speed and diameter on the total-to-static efficiency of the turbine. To make the conclusions general, the analysis is presented in terms of dimensionless variables.

Figure 7 shows the contours of maximum total-to-static isentropic efficiency in the ω_s-d_s plane for the 5000 kW reference case of Table 3. In this diagram, often referred as Baljé diagram, the specific speed and specific diameter are regarded as fixed parameters while the rest of the independent optimization variables are free. It can be observed that there exist an optimum specific speed and specific diameter that maximize the total-to-static isentropic efficiency. In addition, there is a narrow region where the efficiency is close to its maximum value and that moving away from this region leads to a rapid decrease in efficiency. Interestingly, the loci of maximum efficiencies are approximately given by the hyperbola of Equation (50).

$$\frac{1}{2}(\omega_s\, d_s) = u/\sqrt{\Delta h_s} = 1 \tag{50}$$

This suggests that the efficiency penalty away from the point of optimal specific speed and specific diameter is small if the dimensionless blade velocity $u/\sqrt{\Delta h_s}$ is close to unity. This simple result can be explained from Euler's turbomachinery equation and the behavior of the solutions that maximize efficiency. On the one hand, close-to-optimal solutions tend to minimize the swirling kinetic energy lost at the exit of the turbine, see Section 6.4. As a consequence, the absolute flow angle and tangential velocity at the rotor exit are close to zero ($\alpha_{\text{out}} \to 0$ and $v_{\theta,\,\text{out}} \to 0$). On the other hand, close-to-optimal solutions also tend to have a relative flow angle at the inlet of the rotor that is close to zero ($\beta_{\text{in}} \to 0$) because the Kacker and Okapuu [23] loss system predicts low profile losses for reaction blades with small relative inlet angles, see Equation (A7). As a result, of this, the absolute tangential velocity at the inlet of the rotor approaches the blade velocity ($v_{\theta\,\text{in}} \to u$).

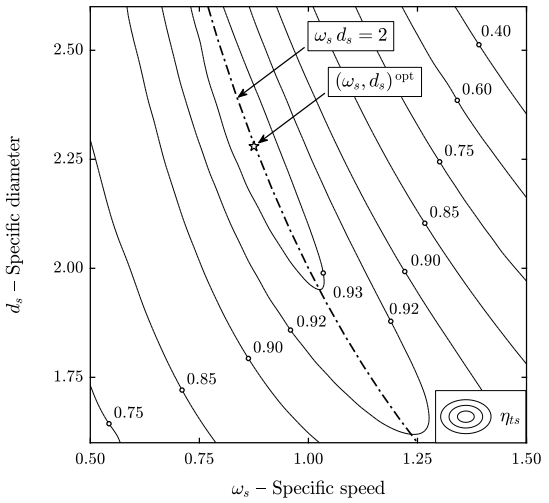

Figure 7. Balje diagram of the reference case.

Under these conditions, the actual enthalpy change approaches the isentropic enthalpy change ($\Delta h \to \Delta h_s$) and Euler's turbomachinery equation, Equation (51), is reduced to Equation (52), which corresponds to the hyperbola of maximum efficiencies in the Baljé diagram.

$$\Delta h = [u\, v_\theta]_{\text{in,R}} - [u\, v_\theta]_{\text{out,R}} \tag{51}$$

$$\Delta h_s = u^2 \Rightarrow \frac{u}{\sqrt{\Delta h_s}} = \frac{1}{2}(\omega_s\, d_s) = 1 \tag{52}$$

This analysis was valid for single-stage turbines, but it can be extended to turbines with more than one stage. For the case of a multistage turbine, it was observed that the loci of maximum efficiencies are approximately given by the hyperbola of Equation (53). This relation can also be explained from Euler's turbomachinery when $v_{\theta,\text{out}} \to 0$ and $v_{\theta,\text{in}} \to u$ hold for every stage.

$$\frac{1}{2}(\omega_s\, d_s) = u/\sqrt{\Delta h_s} = \frac{1}{\sqrt{N}} \tag{53}$$

To assess the validity of this result, the optimal blade speed predicted by Equation (53) was compared with the results of numerical optimization for different isentropic power outputs ranging between 10 kW and 10 MW and different pressure ratios ranging between 2 and 14, see Table 5. It can be observed that location of the point of maximum efficiency predicted by Equation (53) agrees well (relative deviation <4%) with the optimization results for axial turbines of 1, 2, and 3 stages regardless of the pressure ratio and the isentropic power output.

Table 5. Comparison of the suggested optimal specific blade speed with the optimization results.

Variable	Sample Points [a]	Number of Stages	Proposed $\frac{1}{2}(\omega_s\, d_s)^{\text{ref}}$	Optimization [b] $\frac{1}{2}(\omega_s\, d_s)^{\text{mean}}$	Relative Error [c]
$2 \le PR \le 14$	37	1	1	0.978	3.22%
	37	2	$1/\sqrt{2}$	0.706	1.56%
	37	3	$1/\sqrt{3}$	0.592	0.90%
$10\,\text{kW} \le \dot{W}_s \le 10\,\text{MW}$	23	1	1	1.014	2.05%
	23	2	$1/\sqrt{2}$	0.725	1.42%
	23	3	$1/\sqrt{3}$	0.599	1.29%

[a] Number of points (N) used to sample the PR and $\dot{W}_s$ intervals. [b] Computed according to $\frac{1}{2N}\sum_{i=1}^{i=N}(\omega_s\, d_s)_i$ where the index $i = 1, 2, \ldots, N$ corresponds to each of the sample points. [c] Computed according to $\frac{1}{(\omega_s\, d_s)^{\text{ref}}}\sqrt{\frac{1}{N}\sum_{i=1}^{i=N}\left[(\omega_s\, d_s)_i - (\omega_s\, d_s)^{\text{ref}}\right]^2}$.

7. Conclusions

A mean-line model and optimization methodology for axial turbines with any number of stages was proposed. The model was formulated to use arbitrary equations of state and empirical loss models and it accounts for the influence of the diffuser on turbine performance using a one-dimensional flow model proposed by the authors in a previous publication [10]. To the knowledge of the authors, this was the first time that a diffuser model has been coupled with a mean-line model for the optimization of axial turbines. The axial turbine preliminary design was formulated as a constrained optimization problem and was solved using a sequential quadratic programming algorithm. Employing a gradient-based algorithm (instead of a direct search one) allowed to use equality constraints to integrate the cascade, loss, and diffuser sub-models in a simple way.

The model was validated against two test cases from the literature and it was found that the deviation between experimental data and model prediction in terms of mass flow rate and power output was less than 2.5% for both cases and that the deviation in total-to-static efficiency was only 0.27 percentage points for the one-stage case and 0.35 points for the two-stage case. It was also concluded that the close match between measured and predicted efficiencies is probably incidental because the uncertainty of the efficiencies predicted by the loss model is approximately ±1.5 percentage points. In addition, the optimization methodology was applied to a case study from the literature and a

sensitivity analysis was performed to investigate the influence of several design variables on the total-to-static isentropic efficiency, gathering the following conclusions and design guidelines:

- The total-to-static isentropic efficiency increases when the tip clearance height decreases, and this effect is more marked as the isentropic power output of the turbine decreases. This highlights the importance of using small tip clearances in small-scale applications.
- The total-to-static isentropic efficiency increases when the minimum hub-to-tip ratio constraint is reduced (this constraint is always active at the exit of the last rotor). However, reducing the minimum hub-to-tip ratio also increases the centrifugal and gas bending stresses [1]. Therefore, the choice of minimum hub-to-tip ratio must be a trade-off between the fluid-dynamic and the mechanical designs.
- The total-to-static isentropic efficiency increases with the diffuser area ratio in an asymptotic way, regardless of the value of the diffuser skin friction coefficient, and the results of the optimization showed that using an area ratio in the range 2.0–2.5 achieves 70–80% of the maximum efficiency gain. Using a higher diffuser area ratio will increase the kinetic energy recovery and the power output; but it will also increase the turbine footprint, which may be a disadvantage for applications with space limitations.
- The total-to-static isentropic efficiency decreases when the pressure ratio is increased beyond a certain value because the Kacker and Okapuu [23] loss model predicts an increase of the profile loss coefficient when the flow becomes supersonic. This effect becomes less marked as the number of stages increases because the expansion can be distributed over more cascades. In addition, the total-to-static efficiency of turbines without diffuser deteriorates rapidly when the pressure ratio is increased, highlighting the importance of using a diffuser when the pressure ratio is high.
- The results of the optimization showed that the maximum total-to-static isentropic efficiency is attained when the absolute flow angle at the exit of the last stage is close to zero (no exit swirl), regardless of the area ratio of the diffuser. This agrees with the conclusions drawn in a previous work from the authors where the flow within the diffuser was examined in more detail [10].
- It was found that the efficiency penalty away from the point of optimal angular speed and diameter, peak of the Baljé diagram, is small if the combination of specific speed and diameter is close to the hyperbola given by $\omega_s\, d_s = 2/\sqrt{N}$. This guideline can be used to select a suitable combination of angular speed and diameter when one of these variables is imposed by technical constraints such as the frequency of the electrical grid, mechanical stress, or space limitations.

Supplementary Materials: The source code with the implementation of the mean-line model and optimization methodology described in this paper is available in an online repository (doi:10.5281/zenodo.2635586).

Author Contributions: Conceptualization, R.A. and L.O.N.; methodology, R.A.; software, R.A.; validation, R.A.; resources, L.O.N.; writing–original draft preparation, R.A.; writing–review and editing, R.A., L.O.N.

Funding: The authors gratefully acknowledge the financial support from the Research Council of Norway (EnergiX grant no. 255016) for the COPRO project, and the user partners Equinor, Hydro, Alcoa, GE Power Norway and FrioNordica.

Acknowledgments: The authors gratefully acknowledge the support from Roberto Pili for his help in the validation of the axial turbine model.

Conflicts of Interest: The authors of the article, Roberto Agromayor and Lars O. Nord, declare that they have no conflict of interest.

Nomenclature

Latin symbols

a	Speed of sound	m/s
A	Flow area	m^2
AR	Diffuser area ratio	–
b	Blade axial chord	m
$\hat{b}$	Diffuser channel height	m

c	Blade chord	m
C_f	Diffuser skin friction coefficient	–
d	Turbine mean diameter	m
d_s	Turbine specific diameter	–
h	Static specific enthalpy	J/kg
h_0	Stagnation specific enthalpy	J/kg
Δh_s	Total-to-static isentropic specific enthalpy change	J/kg
H	Blade height	m
$\dot{m}$	Mass flow rate	kg/s
N	Number of turbine stages	–
o	Blade opening	m
p	Static pressure	Pa
p_0	Stagnation pressure	Pa
PR	Total-to-static pressure ratio	–
$\dot{q}_w$	Heat flux at the diffuser wall	W/m^2
r	Turbine mean radius	m
$\hat{r}$	Diffuser mean radius	m
r_h	Radius at the hub of the blades	m
r_t	Radius at the tip of the blades	m
s	Blade pitch or specific entropy	m or J/kg K
s_c	Cascade spacing	m
T	Static temperature	K
T_0	Stagnation temperature	K
t_{cl}	Tip clearance height	m
t_{max}	Maximum blade thickness	m
t_{te}	Trailing edge thickness	m
u	Blade velocity	m/s
v	Absolute flow velocity	m/s
v_0	Isentropic velocity (also known as spouting velocity)	m/s
w	Relative flow velocity	m/s
$\dot{W}$	Actual power output	W
$\dot{W}_s$	Isentropic power output	W
Y	Stagnation pressure loss coefficient	–

Greek symbols

α	Absolute flow angle	$^\circ$
β	Relative flow angle	$^\circ$
δ	Deviation angle or diffuser semi-divergence angle	$^\circ$
δ_{fl}	Blade flaring angle	$^\circ$
η_{ts}	Total-to-static isentropic efficiency	–
$\Delta\theta$	Camber angle	$^\circ$
θ	Metal angle	$^\circ$
i	Incidence angle	$^\circ$
λ	Hub-to-tip radii ratio	–
μ	Dynamic viscosity	Pa s
ξ	Stagger angle (also known as setting angle)	$^\circ$
ρ	Density	kg/m^3
τ_w	Shear stress at the diffuser wall	Pa
ϕ	Diffuser mean wall cant angle or kinetic energy loss coefficient ($\phi^2 + \Delta\phi^2 = 1$)	$^\circ$ or –
ω	Angular speed	rad/s
ω_s	Specific speed	–

Abbreviations

CFD	Computational Fluid Dynamics
ODE	Ordinary Differential Equation

Subscripts

0	Stagnation state
1	Inlet of the turbine
2	Outlet of the turbine
in	Inlet of the cascade
out	Outlet of the cascade
error	Violation of an equality constraint
m	Meridional direction
r	Radial direction
ref	Turbine exit state assuming a reference isentropic efficiency
rel	Relative to the rotating frame of reference
s	Isentropic expansion
x	Axial direction
θ	Tangential direction

Appendix A. Kacker–Okapuu Loss Model

This appendix describes the loss model proposed by Kacker and Okapuu [23] to compute aerodynamic losses in axial turbines. This model is a refinement of the correlations proposed by Ainley and Mathieson [26,27] and by Dunham and Came [28]. The general form of the Kacker-Okapuu loss system given by Equation (A1).

$$Y = f_{\mathrm{Re}}\, f_{\mathrm{Ma}}\, Y_{\mathrm{p}} + Y_{\mathrm{s}} + Y_{\mathrm{cl}} + Y_{\mathrm{te}} \tag{A1}$$

The expressions used to compute each term of this equation as a function of the cascade geometry and the thermodynamic and kinematic variables of the flow are presented in the next subsections. Some of the signs from the original correlations were modified to comply with the angle convention used in this work. These modifications are explicitly mentioned in the text.

Appendix A.1. Reynolds Number Correction Factor

The term f_{Re} accounts for the effects of the Reynolds number and it is computed according to Equation (A2).

$$f_{\mathrm{Re}} = \begin{cases} \left(\frac{\mathrm{Re}}{2\cdot 10^5}\right)^{-0.40} & \text{for} \quad \mathrm{Re} < 2\cdot 10^5 \\ 1 & \text{for} \quad 2\cdot 10^5 < \mathrm{Re} < 1\cdot 10^6 \\ \left(\frac{\mathrm{Re}}{1\cdot 10^6}\right)^{-0.20} & \text{for} \quad \mathrm{Re} > 1\cdot 10^6 \end{cases} \tag{A2}$$

The Reynolds number is given by Equation (A3) and it is defined in terms of the chord length and the density, viscosity, and relative velocity at the outlet of the cascade.

$$\mathrm{Re} = \frac{\rho_{\mathrm{out}}\, w_{\mathrm{out}}\, c}{\mu_{\mathrm{out}}} \tag{A3}$$

Appendix A.2. Mach Number Correction Factor

The term f_{Ma} accounts for losses associated with supersonic flows at the trailing edge of the blades and it is computed according to Equation (A4).

$$f_{\mathrm{Ma}} = \begin{cases} 1 & \text{for} \quad \mathrm{Ma}_{\mathrm{out}}^{\mathrm{rel}} \leq 1 \\ 1 + 60\cdot(\mathrm{Ma}_{\mathrm{out}}^{\mathrm{rel}} - 1)^2 & \text{for} \quad \mathrm{Ma}_{\mathrm{out}}^{\mathrm{rel}} > 1 \end{cases} \tag{A4}$$

The Mach number is given by Equation (A5) and it is defined by the relative velocity and the speed of sound at the outlet of the cascade.

$$\mathrm{Ma}_{\mathrm{out}}^{\mathrm{rel}} = w_{\mathrm{out}} / a_{\mathrm{out}} \tag{A5}$$

Appendix A.3. Profile Loss Coefficient

The profile loss coefficient Y_p is computed according to Equation (A6).

$$Y_p = 0.914 \cdot \left(\frac{2}{3} \cdot Y'_p \cdot K_p + Y_{shock} \right) \tag{A6}$$

The term Y'_p is given by Equation (A7), where the terms, $Y_{p,\,reaction}$ and $Y_{p,\,impulse}$ are be obtained from the graphical data reproduced in Figures A1 and A2. The subscript *reaction* refers to blades with zero inlet metal angle (axial entry) and the subscript *impulse* refers to blades that have an inlet metal angle with the same magnitude but opposite sign as the exit relative flow angle. The second term of the right-hand side of Equation (A7) is a correction factor that accounts for the effect of the maximum blade thickness. The sign of β_{out} in Equation (A7) was changed with respect to the original work of Kacker–Okappu to comply with the angle convention used in this paper.

$$Y'_p = \left[Y_{p,\,reaction} - \left(\frac{\theta_{in}}{\beta_{out}} \right) \left| \frac{\theta_{in}}{\beta_{out}} \right| \cdot \left(Y_{p,\,impulse} - Y_{p,\,reaction} \right) \right] \cdot \left(\frac{t_{max}/c}{0.20} \right)^{-\frac{\theta_{in}}{\beta_{out}}} \tag{A7}$$

The factor K_p from Equation (A6) accounts for compressible flow effects when the Mach number within the cascade is subsonic and approaches unity. These effects tend to accelerate the flow, make the boundary layers thinner, and decrease the profile losses. K_p is a function on the inlet and outlet relative Mach numbers and it is computed from Equations (A8)–(A10).

$$K_p = 1 - K_2 \cdot (1 - K_1) \tag{A8}$$

$$K_1 = \begin{cases} 1 & \text{for} \quad Ma_{out}^{rel} < 0.20 \\ 1 - 1.25 \cdot (Ma_{out}^{rel} - 0.20) & \text{for} \quad 0.20 < Ma_{out}^{rel} < 1.00 \\ 0 & \text{for} \quad Ma_{out}^{rel} > 1.00 \end{cases} \tag{A9}$$

$$K_2 = \left(\frac{Ma_{in}^{rel}}{Ma_{out}^{rel}} \right)^2 \tag{A10}$$

The term Y_{shock} from Equation (A6) accounts for the relatively weak shock waves that may occur at the leading edge of the cascade due to the acceleration of the flow. After some algebra, the equations proposed in the Kacker–Okapuu method can be summarized as Equation (A11), where f_{hub} is given graphically in Figure A3 and it is a function of the hub-to-tip ratio only. Please note that the nomenclature used in Kacker and Okapuu [23] is different than then one used in this work, in particular $q \equiv p_{0rel} - p$ and $\Delta P \equiv p_{0rel,in} - p_{0rel,out}$.

$$Y_{shock} = 0.75 \cdot \left(f_{hub} \cdot Ma_{in}^{rel} - 0.40 \right)^{1.75} \cdot \left(\frac{r_{hub}}{r_{tip}} \right)_{in} \cdot \left(\frac{p_{0rel,in} - p_{in}}{p_{0rel,out} - p_{out}} \right) \tag{A11}$$

Appendix A.4. Secondary Loss Coefficient

The secondary loss coefficient Y_s is computed according to Equation (A12).

$$Y_s = 1.2 \cdot K_s \cdot \left[0.0334 \cdot f_{AR} \cdot Z \cdot \left(\frac{\cos(\beta_{out})}{\cos(\theta_{in})} \right) \right] \tag{A12}$$

The factor 1.2 is included to correct the secondary loss for blades with zero trailing edge thickness. Trailing edge losses are accounted independently.

The factor K_s accounts for compressible flow effects when the Mach number within the cascade is subsonic and approaches unity. These effects tend to accelerate the flow, make the end wall boundary

layers thinner, and decrease the secondary losses. K_s is computed from Equation (A13), where K_p is given by Equation (A8) and K_3 is given by Equation (A14). K_3 is a function of the axial blade aspect ratio H/b only.

$$K_s = 1 - K_3 \cdot \left(1 - K_p\right) \tag{A13}$$

$$K_3 = \left(\frac{1}{H/b}\right)^2 \tag{A14}$$

f_{AR} accounts for the blade aspect ratio H/c and it is given by Equation (A15).

$$f_{AR} = \begin{cases} \frac{1-0.25\cdot\sqrt{2-H/c}}{H/c} & \text{for} \quad H/c < 2 \\ \frac{1}{H/c} & \text{for} \quad H/c > 2 \end{cases} \tag{A15}$$

The Ainley-Mathieson loading parameter Z is given by Equations (A16)–(A18), where the sign of β_{out} was changed with respect to the original work of Kacker and Okapuu [23] to comply with the angle convention used in this paper.

$$Z = \left(\frac{C_L}{s/c}\right)^2 \frac{\cos(\beta_{out})^2}{\cos(\beta_m)^3} \tag{A16}$$

$$\left(\frac{C_L}{s/c}\right) = 2\cos(\beta_m)\ \left[\tan(\beta_{in}) - \tan(\beta_{out})\right] \tag{A17}$$

$$\tan(\beta_m) = \frac{1}{2}\left[\tan(\beta_{in}) + \tan(\beta_{out})\right] \tag{A18}$$

Appendix A.5. Tip Clearance Loss Coefficient

The clearance loss coefficient Y_{cl} is computed according to Equation (A19), where the influence of the number of seals is neglected.

$$Y_{cl} = B \cdot Z \cdot \left(\frac{c}{H}\right) \cdot \left(\frac{t_{cl}}{H}\right)^{0.78} \tag{A19}$$

In this equation, Z is given by Equations (A16)–(A18). The Kacker-Okapuu loss system proposes $B = 0.37$ for rotor blades with shrouded tips, and $B = 0.00$ for stator blades. In addition, Kacker and Okapuu warn that using $B = 0.47$, as suggested by Dunham and Came [28], over-predicts the loss for rotor blades with plain tips.

Appendix A.6. Trailing Edge Loss Coefficient

The trailing edge loss coefficient Y_{te} is computed according to Equation (A20).

$$Y_{te} \approx \zeta = \frac{1}{\phi^2} - 1 = \frac{1}{1 - \Delta\phi^2} - 1 \tag{A20}$$

where the pressure loss coefficient Y was approximated by the enthalpy loss coefficient ζ and then related to the kinetic energy loss coefficients ϕ^2 and $\Delta\phi^2$. See the work by Dahlquist [36] for details about the definitions of the different loss coefficients and the relations among them. The parameter $\Delta\phi^2$ is computed by interpolation of impulse and reaction blades according to Equation (A21). The sign of β_{out} in Equation (A21) was changed with respect to the original work of Kacker–Okappu to comply with the angle convention used in this paper.

$$\Delta\phi^2 = \Delta\phi^2_{reaction} - \left(\frac{\theta_{in}}{\beta_{out}}\right)\left|\frac{\theta_{in}}{\beta_{out}}\right| \cdot \left(\Delta\phi^2_{impulse} - \Delta\phi^2_{reaction}\right) \tag{A21}$$

$\Delta\phi^2_{\text{reaction}}$ and $\Delta\phi^2_{\text{impulse}}$ are the kinetic energy loss coefficients of reaction and impulse blades and they are a function of the trailing edge thickness to opening ratio t_{te}/o only. The functional relation was given graphically, and it is reproduced in Figure A4.

Appendix A.7. Final Remarks

The Kacker–Okapuu loss model was developed to estimate the performance of competent turbine designs and its predictions will not be accurate if the input parameters are outside the range of the experimental data used to develop the correlations. This situation is often encountered before the optimization algorithm converges since, in general, it is not possible to satisfy constraints for each iterate of a nonlinear programming problem. For this reason, some of the variables used within the Kacker–Okapuu loss model were bounded to avoid numerical problems that might prevent the convergence to a feasible solution. For instance, some variables were forced to be non-negative because the correlations were not developed to cover such cases. These modifications do not affect the final results of the optimization and they are not reported in this paper although they are documented in detail within the code.

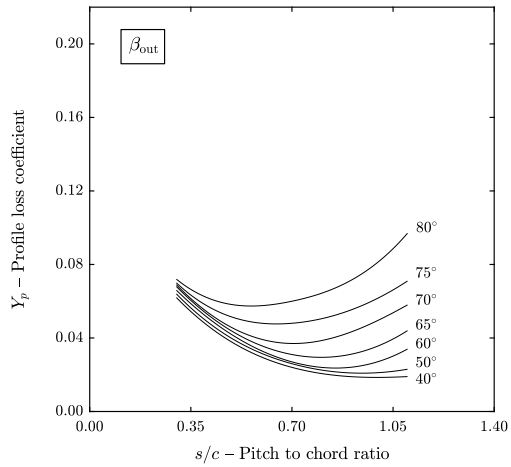

Figure A1. Profile loss of reaction blades (axial entry blades).

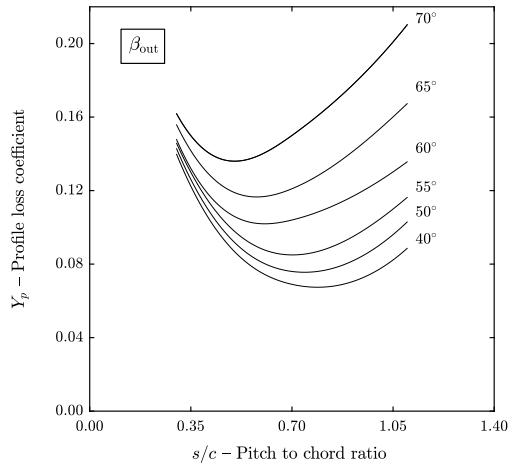

Figure A2. Profile loss of impulse blades.

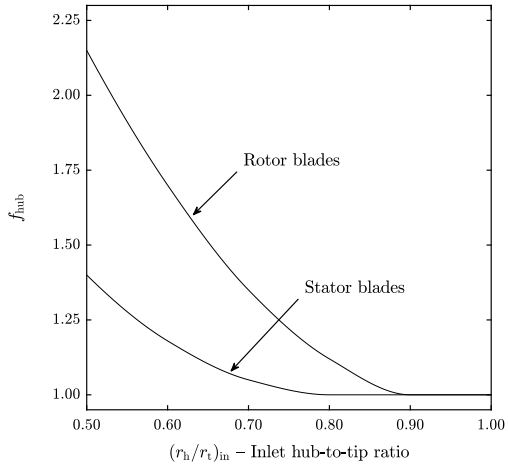

Figure A3. Ratio of Mach number at the hub to Mach number at the mean radius.

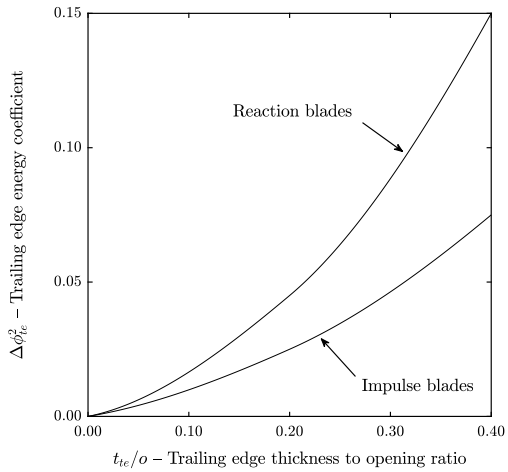

Figure A4. Trailing edge energy loss coefficient for impulse and reaction blades.

References

1. Saravanamuttoo, H.I.H.; Rogers, G.F.C.; Cohen, H. *Gas Turbine Theory*, 6th ed.; Pearson Education: London, UK, 2009.
2. McDonald, C.F. Helium Turbomachinery Operating Experience from Gas Turbine Power Plants and Test Facilities. *Appl. Therm. Eng.* **2012**, *44*, 108–142. [CrossRef]
3. Dostal, V.; Driscoll, M.J.; Hejzlar, P. A Supercritical Carbon Dioxide Cycle for Next Generation Nuclear Reactors. Ph.D. Thesis, Department of Nuclear Engineering, Massachusetts Institute of Technology, Cambridge, MA, USA, 2004.
4. Kehlhofer, R.; Hannemann, F.; Rukes, B.; Stirnimann, F. *Combined-Cycle Gas and Steam Turbine Power Plants*; Pennwell Books: Tulsa, OK, USA, 2009.
5. Colonna, P.; Casati, E.; Trapp, C.; Mathijssen, T.; Larjola, J.; Turunen-Saaresti, T.; Uusitalo, A. Organic Rankine Cycle Power Systems: From the Concept to Current Technology, Applications, and an Outlook to the Future. *J. Eng. Gas Turbines Power* **2015**, *137*, 1–19. [CrossRef]
6. Flynn, T. *Cryogenic Engineering, Revised and Expanded*; CRC Press: Boca Raton, FL, USA, 2004.

7. Pini, M.; Persico, G. Fluid dynamic design of Organic Rankine Cycle turbines. In *Organic Rankine Cycle (ORC) Power Systems: Technologies and Applications*; Macchi, E., Astolfi, M., Eds.; Woodhead Publising: Sawston, UK, 2017.
8. Denton, J.D. Multall—An Open Source, Computational Fluid Dynamics Based, Turbomachinery Design System. *J. Turbomach.* **2017**, *139*, 1–12. [CrossRef]
9. Dixon, S.L.; Hall, C. *Fluid Mechanics and Thermodynamics of Turbomachinery*, 7th ed.; Butterworth-Heinemann: Oxford, UK, 2013.
10. Agromayor, R.; Müller, B.; Nord, L.O. One-Dimensional Annular Diffuser Model for Preliminary Turbomachinery Design. *Int. J. Turbomach. Propuls. Power*. **2019**, *4*, 31. [CrossRef]
11. Agromayor, R.; Nord, L.O. AxialOpt—A Meanline Model for the Design and Optimization of Axial Turbines. *Zenodo Repos.* **2019**. [CrossRef]
12. Balje, O.E.; Binsley, R.L. Axial Turbine Performance Evaluation. Part B—Optimization with and without Constraints. *J. Eng. Power* **1968**, *90*, 349–359.
13. Macchi, E.; Perdichizzi, A. Efficiency Prediction for Axial-Flow Turbines Operating with Nonconventional Fluids. *J. Eng. Power* **1981**, *103*, 718–724. [CrossRef]
14. Lozza, G.; Macchi, E.; Perdichizzi, A. On the Influence of the Number of Stages on the Efficiency of Axial-Flow Turbines. In Proceedings of the ASME 1982 International Gas Turbine Conference and Exhibit, London, UK, 18–22 April 1982; pp. 1–10.
15. Astolfi, M.; Macchi, E. Efficiency Correlations for Axial Flow Turbines Working With Non-Conventional Fluids. In Proceedings of the 3rd International Seminar on ORC Power System (ASME-ORC2015), Brussels, Belgium, 12–14 October 2015; pp. 1–12.
16. Tournier, J.M.; El-Genk, M.S. Axial Flow, Multi-Stage Turbine and Compressor Models. *Energy Convers. Manag.* **2010**, *51*, 16–29. [CrossRef]
17. Da Lio, L.; Manente, G.; Lazzaretto, A. New efficiency charts for the optimum design of axial flow turbines for organic Rankine cycles. *Energy* **2014**, *77*, 447–459. [CrossRef]
18. Da Lio, L.; Manente, G.; Lazzaretto, A. Predicting the Optimum Design of Single Stage Axial Expanders in ORC Systems: Is There a Single Efficiency Map for Different Working Fluids? *Appl. Energy* **2016**, *167*, 44–58. [CrossRef]
19. Meroni, A.; La Seta, A.; Andreasen, J.; Pierobon, L.; Persico, G.; Haglind, F. Combined Turbine and Cycle Optimization for Organic Rankine Cycle Power Systems–Part B: Case Study. *Energies* **2016**, *9*, 313. [CrossRef]
20. Meroni, A.; Graa, J.; Persico, G.; Haglind, F. Optimization of Organic Rankine Cycle Power Systems Considering Multistage Axial Turbine Design. *Appl. Energy* **2018**, *209*, 339–354. [CrossRef]
21. Bahamonde, S.; Pini, M.; De Servi, C.; Rubino, A.; Colonna, P. Method for the Preliminary Fluid Dynamic Design of High-Temperature Mini-Organic Rankine Cycle Turbines. *J. Eng. Gas Turb. Power* **2017**, *139*, 1–14. [CrossRef]
22. Talluri, L.; Lombardi, G. Simulation and Design Tool for ORC Axial Turbine Stage. *Energy Procedia* **2017**, *129*, 277–284. [CrossRef]
23. Kacker, S.C.; Okapuu, U. A Mean Line Prediction Method for Axial Flow Turbine Efficiency. *J. Eng. Power* **1982**, *104*, 111–119. [CrossRef]
24. Lemmon, E.W.; Huber, M.L.; McLinden, M.O. *NIST Standard Reference Database 23: Reference Fluid Thermodynamic and Transport Properties-REFPROP, Version 9.1*; National Institute of Standards and Technology: Gaithersburg, MD, USA, 2013.
25. Denton, J.D. The 1993 IGTI Scholar Lecture: Loss Mechanisms in Turbomachines. *J. Turbomach.* **1993**, *115*, 621–656. [CrossRef]
26. Ainley, D.G.; Mathieson, C.R. An Examination of the Flow and Pressure Losses in Blade Rows of Axial-Flow Turbines. *Aeronaut. Res. Counc. Rep. Memo.* **1951**, *2891*, 1–33.
27. Ainley, D.G.; Mathieson, C.R. A Method of Performance Estimation for Axial-Flow Turbines. *Aeronaut. Res. Counc. Rep. Memo.* **1951**, *2974*, 1–30.
28. Dunham, J.; Came, P.M. Improvements to the Ainley-Mathieson Method of Turbine Performance Prediction. *J. Eng. Power* **1970**, *92*, 252–256. [CrossRef]
29. Moustapha, S.H.; Kacker, S.C.; Tremblay, B. An Improved Incidence Losses Prediction Method for Turbine Airfoils. *J. Turbomach.* **1982**, *112*, 267–276. [CrossRef]

30. Benner, M.W.; Sjolander, S.A.; Moustapha, S.H. Influence of Leading-Edge Geometry on Profile Losses in Turbines at Off-Design Incidence: Experimental Results and an Improved Correlation. *J. Turbomach.* **1997**, *119*, 193–200. [CrossRef]
31. Balje, O.E.; Binsley, R.L. Axial Turbine Performance Evaluation. Part A—Loss-Geometry Relationships. *J. Eng. Power* **1968**, *90*, 341–348.
32. Craig, H.R.M.; Cox, H.J.A. Performance Estimation of Axial Flow Turbines. *Proc. Inst. Mech. Eng.* **1971**, *185*, 407–424. [CrossRef]
33. Traupel, W. *Thermische Turbomaschinen*, 3rd ed.; Springer: Berlin, Germany, 1982.
34. Aungier, R.H. *Turbine Aerodynamics*, 1st ed.; ASME Press: New York, NY, USA, 2006.
35. Wei, N. Significane of Loss Models in Aerothermodynamic Simulation for Axial Turbines. Ph.D. Thesis, Royal Institute of Technology in Stockholm (KTH), Stockholm, Sweden, 2000.
36. Dahlquist, A. Investigation of Losses Prediction Methods in 1D for Axial Gas Turbines. Master's Thesis, Lund University, Lund, Sweden, 2008.
37. Shampine, L.F.; Reichelt, M.W. The MATLAB ODE suite. *SIAM J. Sci. Comput.* **1997**, *18*, 1–22. [CrossRef]
38. Kofskey, M.G.; Nusbaum, W.J. *Design and Cold-Air Investigation of a Turbine for a Small Low-Cost Turbofan Engine*; Technical Report NASA TN D-6967; National Aeronautics and Space Administration: Washington, DC, USA, 1992.
39. Nocedal, J.; Wright, S.J. *Numerical Optimization*, 2nd ed.; Springer: Berlin, Germany, 2006; pp. 22–23.
40. The MathWorks Inc. *MATLAB Version R2016a*; The MathWorks Inc.: Natick, MA, USA, 2016.
41. Macchi, E.; Astolfi, M. Axial flow turbines for Organic Rankine Cycle applications. In *Organic Rankine Cycle (ORC) Power Systems: Technologies and Applications*; Macchi, E., Astolfi, M., Eds.; Woodhead Publising: Sawston, UK, 2017.
42. Brown, W.B. *Friction Coefficients in a Vaneless Diffuser*; National Advisory Committee for Aeronautics: Washington, DC, USA, 1947.
43. Johnston, J.P.; Dean, R.C. Losses in Vaneless Diffusers of Centrifugal Compressors and Pumps: Analysis, Experiment, and Design. *J. Eng. Power* **1966**, *88*, 49–60. [CrossRef]
44. Dubitsky, O.; Japikse, D. Vaneless Diffuser Advanced Model. *J. Turbomach.* **2008**, *130*, 1–10. [CrossRef]
45. Lohmann, R.P.; Markowski, S.J.; Brookman, E.T. Swirling Flow Through Annular Diffusers with Conical Walls. *J. Fluids Eng.* **1979**, *101*, 224–229. [CrossRef]

Computer-Aided Design 133 (2021) 102987

Contents lists available at ScienceDirect

Computer-Aided Design

journal homepage: www.elsevier.com/locate/cad

Application paper

A Unified Geometry Parametrization Method for Turbomachinery Blades☆

Roberto Agromayor [a,*], Nitish Anand [b], Jens-Dominik Müller [c], Matteo Pini [b], Lars O. Nord [a]

[a] Department of Energy and Process Engineering, NTNU – The Norwegian University of Science and Technology, Kolbj. Hejes v. 1B, NO-7491, Trondheim, Norway
[b] Propulsion & Power, Aerospace Engineering Faculty, Delft University of Technology, Kluyverweg 1, 2629 HS, Delft, The Netherlands
[c] School of Engineering and Materials Science, Queen Mary University of London, Mile End Road, E1 4NS London, United Kingdom

ARTICLE INFO

Article history:
Received 29 July 2020
Received in revised form 19 October 2020
Accepted 12 December 2020

Keywords:
Turbine
Compressor
Shape optimization
Gradient
CAD
NURBS

ABSTRACT

Turbomachinery design is increasingly carried out by means of automated workflows based on high-fidelity physical models and optimization algorithms. The parametrization of the blade geometry is an essential aspect of such workflows because it defines the design space in which an optimal solution can be found. Currently, parametrization methods used for this purpose are often tailored to one particular type of turbomachinery blade, do not provide shape derivatives required for gradient-based optimization, or are not suited to re-parametrize a baseline blade geometry defined by a set of scattered point coordinates in a systematic way. This paper thus presents a general blade parametrization method for axial, radial, and mixed flow blades based on typical turbomachinery design variables and NURBS curves and surfaces. The shape derivatives are computed by means of the complex-step method, allowing the integration of the parametrization into gradient-based shape optimization workflows. In addition, the method enables the re-parametrization of a blade geometry defined by a cloud of points by solving a two-step optimization problem. The capabilities of the method are demonstrated by replicating eight blade geometries in two and three dimensions with an accuracy comparable to the tolerances of current manufacturing technologies.

1. Introduction

Driven by the ever-increasing requirements in performance, environmental impact, and life-time cost, turbomachinery design is increasingly carried out by means of automated workflows [1]. These workflows integrate geometry parametrization tools, high-fidelity physical models, and optimization algorithms to systematically explore the design space. The parametrization of the geometry is an essential aspect of the design chain because it defines the design space within which the optimization algorithm can find the optimal solution [2]. Ideally, a parametrization method for turbomachinery blades should:

1. Support any type of blade configuration and contain the shapes that achieve the required design objectives.
2. Allow the designer to impose geometric constraints due to mechanical or manufacturing requirements.
3. Provide the sensitivity of the shape with respect to the design variables to enable gradient-based shape optimization [3].
4. Use conventional engineering parameters with an intuitive geometrical meaning.
5. Produce smooth geometries with continuous curvature (G^2 continuity) and continuous rate of change of curvature to avoid velocity spikes that may lead to flow separation [4].
6. Retain compatibility with Computer-Aided Design (CAD) software for further analysis, geometry manipulation, and manufacturing.
7. Be computationally cheap in terms of execution time and memory usage.

Shape parametrization methods can be classified into deformation and constructive methods. Deformation methods can be used to modify an existing geometry (a mesh or a CAD model) and are widely used in the context of turbomachinery shape optimization. These methods include mesh point displacement [5,6], CAD model control point displacement [7,8], superposition of shape functions such as Hicks–Henne bumps [9,10], and space morphing methods based on Free-Form Deformation (FFD) [11,12] or on Radial Basis Function (RBF) interpolation [13,14]. Although these methods enable the exploration of rich design spaces, they are not suited for an effective handling of geometric constraints, making it difficult to obtain feasible shapes out of the optimization process. As a notable exception, the NSPCC method [8]

☆ This paper has been recommended for acceptance by Xiaoping Qian.
* Corresponding author.
E-mail address: roberto.agromayor@ntnu.no (R. Agromayor).

https://doi.org/10.1016/j.cad.2020.102987

Nomenclature

Latin symbols

c	Chord length (m)
c_{ax}	Axial chord length (m)
$\mathbf{C}(u)$	NURBS curve values (m)
d	Tangent proportion (-)
f, g	NURBS endpoint curvature functions (m)
h	Step size (-)
J	Objective function (m^2)
L	Arc length (m)
N_b	Number of blades (-)
N_Q	Number of prescribed points (-)
$N_{i,p}$, $N_{j,q}$	B-spline basis polynomials (-)
$\mathbf{n}$	Unitary normal vector (-)
n, m	NURBS highest indices (-)
p, q	NURBS degree (-)
$\mathbf{P}_i$, $\mathbf{P}_{i,j}$	NURBS control point coordinates (m)
$\mathbf{Q}_i$	Prescribed point coordinates (m)
r	Radius of curvature or radial direction (m)
$\mathbf{S}(u, v)$	NURBS surface values (m)
s	Blade spacing, also known as pitch (m)
t	Thickness distribution (m)
u, v	NURBS parametric coordinates (-)
$\hat{u}$, $\hat{v}$	NURBS sample points (-)
U, V	NURBS knot vectors (-)
w_i, $w_{i,j}$	NURBS control point weights (-)
x, y, z	Cartesian coordinates (m)

Greek symbols

α	Set of design variables (-)
θ	Metal angle or circumferential angle (°)
κ	Curvature (m^{-1})
ξ	Stagger angle, also known as setting angle (°)
$\boldsymbol{\tau}$	Unitary tangent vector (-)

Abbreviations

AD	Algorithmic Differentiation
B-spline	Basis Spline
BFGS	Broyden–Fletcher–Goldfarb–Shanno
C-FD	Central Finite Differences
CAD	Computed-Aided Design
CS	Complex-Step
F-FD	Forward Finite Differences
FD	Finite Differences
FFD	Free Form Deformation
NSPCC	NURBS-based Parametrization with Complex Constraints
NURBS	Non Uniform Rational Basis Spline
RBF	Radial Basis Functions

Subscripts and superscripts

b	Blade
c	Camber
in, out	Inlet and outlet
l, u	Lower and upper sides
m	Meridional
u, v	u and v parametric directions
1, 2, 3, 4	Meridional channel edges

allows the designer to impose geometric and continuity constraints by evaluating these constraints at a finite number of test-points and using a projected gradient optimization algorithm to maintain feasibility. In contrast, constructive methods can be used to generate the geometry of a new blade from scratch, or possibly using design variable values obtained from preliminary design models such as mean-line [15,16] or throughflow models [17,18]. In addition, they allow one to impose geometric constraints such as minimum blade thickness in a natural and non-intrusive way. Due to these strengths, constructive methods are widely used for turbomachinery blade parametrization and a large number of such methods have been developed over the years. Table 1 provides a comprehensive review of constructive blade parametrizations up to the present day.

The early constructive parametrization methods used circular arcs and polynomials in monomial-basis form (that is, polynomials in the form $\sum_{i=0}^{n} a_i x^i$) to define the geometry of the blades [19–24]. This type of parametrization gained significant popularity among industry practitioners, but it has severe limitations arising from the use of a monomial basis. Specifically: (1) the polynomial coefficients convey little insight about the shape of the blade, (2) ensuring geometric continuity at the connecting points between segments requires the solution of a linear system that may not have a unique solution, (3) the surface of the blade is prone to undesirable inflection points, and (4) the resulting shapes are not compatible with the geometric representation used by modern CAD systems.

To overcome these shortcomings, several authors proposed new constructive parametrizations based on Bézier [25–31], B-spline [32–37], and NURBS [38–42] curves and surfaces. These mathematical functions have become the standard to represent geometric objects in modern CAD packages due to their favorable mathematical properties and the availability of a wide range of algorithms to define and manipulate curves and surfaces [43,44]. Currently, most of the constructive CAD-based parametrizations for turbomachinery blades described in the open literature are not suitable for automated design workflows. This is because they do not offer a robust way to handle trimming and intersection operations [45,46] or do not provide sensitivity information required by gradient-based optimization algorithms [3]. In addition, to optimize an existing blade, it is essential to find a parametric representation of the baseline geometry, available, for instance, in the form of a large set of points in the Cartesian space. Solving this reverse engineering problem by trial and error is doable for simple cases [36,42], but it becomes impractical for complex blade geometries. Despite the practical relevance of this problem, a robust and automatic method to re-parametrize the geometry of a blade defined by a scattered set of points is still lacking.

In response to the limitations of the existing methods, this paper presents a general constructive parametrization method for axial, radial, and mixed-flow turbomachinery blades. The method exploits conventional engineering design variables (leading/trailing edge radius, metal angles, blade thickness, etc.) and NURBS curves and surfaces to represent the blade geometry. The method is formulated in an explicit way that avoids the use of intersection and trimming operations to define the geometry of the blade and flow domain and produces blades satisfying G^2 continuity by construction. The sensitivity of the geometry with respect to the design variables is computed with machine accuracy by means of the complex-step method [47–49]. In addition, the method is also adapted to re-parametrize the geometry of an existing blade defined by a scattered set of point coordinates. This problem, often referred to as blade matching, is formulated as a two-step optimization problem and it allows one to find the set of design variable values that best approximates the prescribed geometry in a systematic way. The flexibility and accuracy of the

Table 1
Review of constructive blade parametrization methods documented in the open literature.

Reference		Basis function	Configuration	Cont.[a]	Grad.[b]
Dunham (1974)	[19]	Monomial	2D profile	G^1	n.a.
Crouse (1981)	[20]	Monomial	3D axial	G^1	n.a
Ye (1984)	[21]	Monomial	2D profile	G^2	n.a.
Pritchard (1985)	[22]	Monomial	2D profile	G^1	n.a.
Korakianitis (1993)	[23]	Monomial	2D profile	G^2	n.a.
Aungier (2006)	[24]	Monomial	2D profile	G^2	n.a.
Engeli et al. (1974)	[25]	Bézier	3D axial	G^2	n.a.
Casey (1983)	[26]	Bézier	3D general	G^2	n.a.
Goel et al. (1996)	[27]	Bézier	3D axial	G^2	n.a.
Giannakoglou (1999)	[28]	Bézier	2D profile	G^1	n.a.
Trigg et al. (1999)	[29]	Bézier	2D profile	G^1	n.a.
Pierret et al. (1999)	[30]	Bézier	2D profile	G^{2c}	n.a.
Pierret et al. (2000)	[31]	Bézier	3D axial	G^{2c}	n.a
Oyama et al. (2004)	[32]	B-spline	3D axial	G^1	n.a.
Huppertz et al. (2007)	[33]	B-spline	2D profile	G^1	n.a
Verstraete (2010)	[34]	B-spline	3D axial	G^{2c}	n.a.
Verstraete (2010)	[34]	B-spline	3D general	G^{2c}	n.a.
Siddappaji et al. (2012)	[35]	B-spline	3D general	G^2	n.a.
Torreguitart et al. (2018)	[36]	B-spline	2D profile	G^{2c}	AD
Mykhaskiv et al. (2018)	[37]	B-spline	3D axial	G^2	AD
Miller et al. (1996)	[38]	NURBS	3D general	G^2	n.a.
Gräsel et al. (2004)	[39]	NURBS	3D general	G^2	n.a.
Koini et al. (2009)	[40]	NURBS	3D general	G^2	n.a.
Müller et al. (2017)	[41]	NURBS	3D general	G^{2c}	CS
Anand et al. (2018)	[42]	NURBS	2D profile	G^2	FD
Present work		NURBS	2D/3D general	G^2	CS

[a]Slope continuity (G^1) or curvature continuity (G^2).
[b]Method used for gradient computation: not available (n.a.), Finite Differences (FD), Complex-Step (CS), or Algorithmic Differentiation (AD).
[c]The parametrization satisfies curvature continuity everywhere except at the trailing edge.

proposed method is demonstrated by replicating the geometry of eight turbomachinery blades in two and three dimensions.

The rest of the paper is organized as follows. Section 2 documents the definition and properties of NURBS curves and surfaces. The blade parametrization in two and three dimensions is described in Sections 3 and 4, respectively, and the computation of the geometry sensitivity using the complex-step method is introduced and verified in Section 5. The blade matching method is presented and applied to replicate a wide range of blade geometries in Section 6. Finally, the software implementation of the method is described in Section 7 and the conclusions are summarized in Section 8.

2. Background on NURBS curves and surfaces

The origin of Non-Uniform Rational Basis Spline (NURBS) curves and surfaces can be traced back to the research efforts in computer-aided geometric design in the late 60s and early 70s [50]. Since then, NURBS curves and surfaces have been universally used for geometrical modeling thanks to their intuitive geometrical interpretation, favorable mathematical properties, and efficient computational algorithms. A NURBS curve, see Fig. 1(a), is a parametric curve defined by

$$\mathbf{C}(u) = \frac{\sum_{i=0}^{n} N_{i,p}(u)\, w_i\, \mathbf{P}_i}{\sum_{i=0}^{n} N_{i,p}(u)\, w_i}, \quad \text{with} \quad 0 \le u \le 1, \tag{1}$$

where p is the degree of the curve, the coefficients $\mathbf{P}_i$ and w_i are the coordinates and weights of the $n+1$ control points, and $N_{i,p}$ are B-spline basis functions defined on the non-decreasing, clamped knot vector

$$U = [\underbrace{0, \ldots, 0}_{p+1}, \underbrace{u_{p+1}, \ldots, u_n}_{n-p}, \underbrace{1, \ldots, 1}_{p+1}] \in \mathbb{R}^{r+1} \tag{2}$$

with $r = n + p + 1$. The B-spline basis functions are given by the recursive relation

$$N_{i,0}(u) = \begin{cases} 1, & \text{if} \quad u_i \le u < u_{i+1} \\ 0, & \text{otherwise} \end{cases} \tag{3}$$

$$N_{i,p}(u) = \frac{u - u_i}{u_{i+p} - u_i} N_{i,p-1}(u) + \frac{u_{i+p+1} - u}{u_{i+p+1} - u_{i+1}} N_{i+1,p-1}(u). \tag{4}$$

Similarly, a NURBS surface, see Fig. 1(b), is a parametric surface defined by

$$\mathbf{S}(u, v) = \frac{\sum_{i=0}^{n} \sum_{j=0}^{m} N_{i,p}(u) N_{j,q}(v)\, w_{i,j}\, \mathbf{P}_{i,j}}{\sum_{i=0}^{n} \sum_{j=0}^{m} N_{i,p}(u) N_{j,p}(v)\, w_{i,j}}, \quad \text{with} \quad 0 \le u,\ v \le 1, \tag{5}$$

where p and q are the degrees of the surface in the u- and v-directions, the coefficients $\mathbf{P}_{i,j}$ and $w_{i,j}$ are bidirectional nets containing the coordinates and weights of the $(n+1) \times (m+1)$ control points, and $N_{i,p}(u)N_{j,q}(v)$ are the product of univariate B-spline basis functions defined on the non-decreasing, clamped knot vectors

$$U = [\underbrace{0, \ldots, 0}_{p+1}, \underbrace{u_{p+1}, \ldots, u_n}_{n-p}, \underbrace{1, \ldots, 1}_{p+1}] \in \mathbb{R}^{r+1} \tag{6}$$

$$V = [\underbrace{0, \ldots, 0}_{q+1}, \underbrace{v_{q+1}, \ldots, v_n}_{m-q}, \underbrace{1, \ldots, 1}_{q+1}] \in \mathbb{R}^{s+1}, \tag{7}$$

with $r = n + p + 1$ and $s = m + q + 1$. The u-direction basis functions $N_{i,p}(u)$ are given by Eqs. (3) and (4), whereas the v-direction basis functions $N_{i,q}(v)$ are defined in an analogous way replacing the variable u by v and the indices i and p by j and q, respectively.

NURBS curves and surfaces have the following mathematical properties that make them particularly suited for geometric modeling [43, pp. 117–139]:

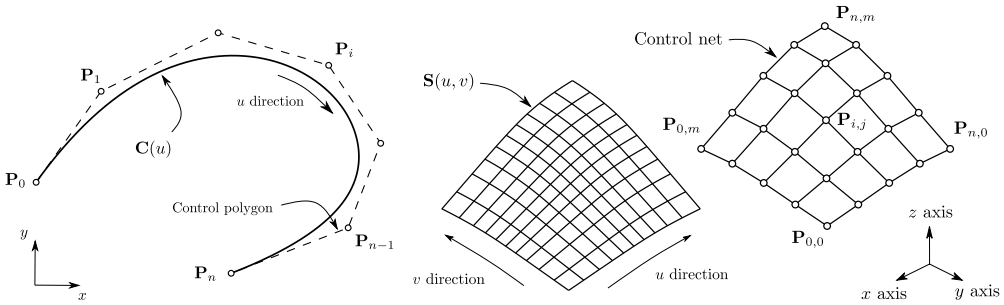

(a) NURBS curve construction (b) NURBS surface construction

Fig. 1. Construction of a NURBS curve (left) and surface (right). Note that the NURBS curve interpolates its endpoints and it is tangent to the control polygon at its ends. The control net of the NURBS surface interpolates its four corner points and it was represented at an offset distance in the x-direction for clarity.

Table 2
Two-dimensional design variables. Each design variable is provided as a scalar value, except for the upper and lower thickness that are given as sets of control points.

Variable name	Symbol
Spacing	s
Leading edge abscissa and ordinate	x_{in}, y_{in}
Axial chord length	c_{ax}
Stagger angle	ξ
Inlet and exit metal angles	θ_{in}, θ_{out}
Inlet and exit tangent proportions	d_{in}, d_{out}
Inlet and exit radii of curvature	r_{in}, r_{out}
Upper and lower thickness distributions	t^u, t^l

- *Affine invariance.* It is possible to apply affine transformations such as rotations, displacements, and scalings to NURBS curves and surfaces by applying the transformation to their control points.
- *Convex hull.* NURBS curves and surfaces are within the convex hull of their control points. When the control points are contained in a certain region of space, this property guarantees that the curve or surface will not blow up arbitrarily far away from this region.
- *Endpoint interpolation* NURBS curves and surfaces coincide with the polytope formed by the control points at the endpoints.
- *Endpoint tangency.* NURBS curves and surfaces are tangent to the polytope formed by the control points at the endpoints.
- *Generalization.* Bézier curves and surfaces are a special case of NURBS when $p = n$ and $q = m$. In addition, B-spline curves and surfaces are an special case of NURBS when all the weights have the same value.

Most of the curves and surfaces used in the proposed blade parametrization method are B-splines. However, the parametrization is formulated in a general way using NURBS so that the user can include the control point weights as design variables to gain more control over the resulting geometry.

3. Blade parametrization in two dimensions

The proposed two-dimensional blade parametrization is based on typical blade design variables which are listed in Table 2. The geometry of the blade is generated by defining a camber line and subsequently imposing on it two independent thickness distributions in a way that ensures G^2 continuity at the junction between the upper and the lower sides.

The camber line $\mathbf{C}^c(u)$ is a cubic B-spline curve defined by four control points as shown in Fig. 2(a). The coordinates of the control points are given by

$$\mathbf{P}_0^c = \begin{bmatrix} x_{\text{in}} \\ y_{\text{in}} \end{bmatrix}, \tag{8}$$

$$\mathbf{P}_1^c = \mathbf{P}_0^c + d_{\text{in}} \begin{bmatrix} c\,\cos(\theta_{\text{in}}) \\ c\,\sin(\theta_{\text{in}}) \end{bmatrix}, \tag{9}$$

$$\mathbf{P}_2^c = \mathbf{P}_3^c - d_{\text{out}} \begin{bmatrix} c\,\cos(\theta_{\text{out}}) \\ c\,\sin(\theta_{\text{out}}) \end{bmatrix}, \tag{10}$$

$$\mathbf{P}_3^c = \mathbf{P}_0^c + \begin{bmatrix} c\,\cos(\xi) \\ c\,\sin(\xi) \end{bmatrix}, \tag{11}$$

where ξ is the stagger angle, $c_{\text{ax}} = c\,\cos(\xi)$ is the axial chord length, θ_{in} and θ_{out} are the inlet and outlet metal angles, and d_{in} and d_{out} are the inlet and outlet tangent proportions. This construction of the camber line ensures that the blade has the specified axial chord length and that the slope at the leading and trailing edges agrees with the input metal angles thanks to the endpoint tangency property of B-spline curves [43, p. 97].

The upper and lower sides of the blade, $\mathbf{C}^l(u)$ and $\mathbf{C}^u(u)$, are defined as B-spline curves of degree four as it is the lowest degree that guarantees continuous rate of change of curvature at the spline knots. The coordinates of the control points $\{\mathbf{P}_i^l\}$ and $\{\mathbf{P}_i^u\}$, see Fig. 2(b), are computed according to

$$\mathbf{P}_i^l = \begin{cases} \mathbf{C}^c(\hat{u}_i), & \text{for } i = 0 \\ \mathbf{C}^c(\hat{u}_i) - \mathbf{n}(\hat{u}_i) \cdot f(r_{\text{in}}), & \text{for } i = 1 \\ \mathbf{C}^c(\hat{u}_i) - \mathbf{n}(\hat{u}_i) \cdot t^l(\hat{u}_i), & \text{for } i = 2 : n-2 \\ \mathbf{C}^c(\hat{u}_i) - \mathbf{n}(\hat{u}_i) \cdot g(r_{\text{out}}), & \text{for } i = n-1 \\ \mathbf{C}^c(\hat{u}_i), & \text{for } i = n \end{cases} \tag{12}$$

and

$$\mathbf{P}_i^u = \begin{cases} \mathbf{C}^c(\hat{u}_i), & \text{for } i = 0 \\ \mathbf{C}^c(\hat{u}_i) + \mathbf{n}(\hat{u}_i) \cdot f(r_{\text{in}}), & \text{for } i = 1 \\ \mathbf{C}^c(\hat{u}_i) + \mathbf{n}(\hat{u}_i) \cdot t^u(\hat{u}_i), & \text{for } i = 2 : n-2 \\ \mathbf{C}^c(\hat{u}_i) + \mathbf{n}(\hat{u}_i) \cdot g(r_{\text{out}}), & \text{for } i = n-1 \\ \mathbf{C}^c(\hat{u}_i), & \text{for } i = n. \end{cases} \tag{13}$$

The sampling values $\hat{u}_i$ are given by

$$\hat{u}_i = \begin{cases} 0, & \text{for } i = 0 \\ \frac{i-1}{n-2}, & \text{for } i = 1 : n-1 \\ 1, & \text{for } i = n. \end{cases} \tag{14}$$

The upper and lower thickness distributions, $t^u(u)$ and $t^l(u)$, are given by B-spline polynomials of degree three with an arbitrary

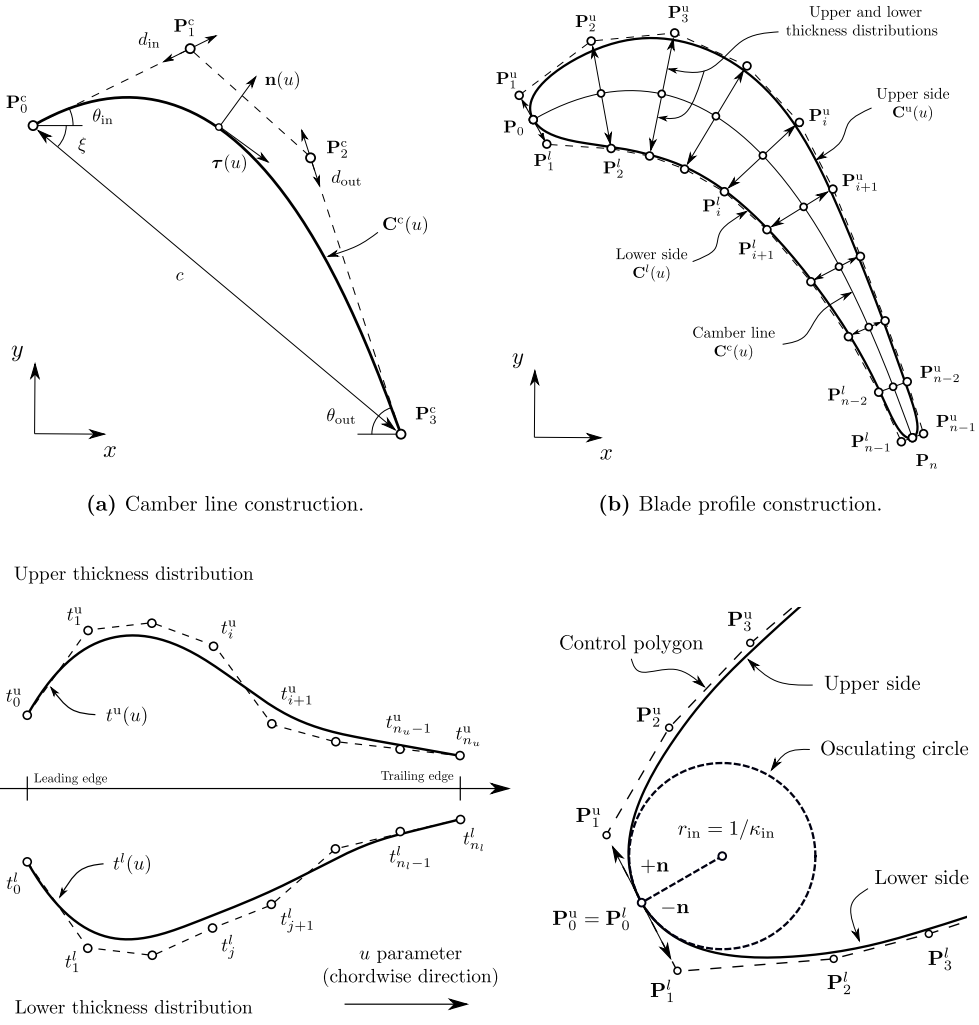

(a) Camber line construction. **(b)** Blade profile construction.

(c) Thickness distribution. **(d)** Leading edge construction.

Fig. 2. Construction of the blade geometry in two dimensions. The upper and lower thickness distributions (bottom-left) are imposed in the direction normal to the camber line (top-left) to compute the location of the blade control points (top-right). The second and second-to-last control points are computed in a special way to impose the radii of curvature at the leading and trailing edges and to ensure that the blade profile is G^2 continuous (bottom-right).

number of control points, $\{t_i^u\}$ and $\{t_j^l\}$, specified by the user, see Fig. 2(c). The unitary vectors normal to the camber line $\mathbf{n}(u)$ are computed from the unitary tangent vector $\boldsymbol{\tau}(u)$ according to

$$\boldsymbol{n}(u) = \begin{bmatrix} n_x \\ n_y \end{bmatrix} = \begin{bmatrix} -\tau_y \\ \tau_x \end{bmatrix}, \text{ with } \boldsymbol{\tau}(u) = \frac{\dot{\mathbf{C}}^c(u)}{\|\dot{\mathbf{C}}^c(u)\|}, \tag{15}$$

where $\dot{\mathbf{C}}^c(u)$ is computed using analytical derivative formulas for B-spline curves [43, pp. 91–100]. The functions $f(r)$ and $g(r)$ appearing in Eqs. (12) and (13) are used to impose the radii of curvature r_{in} and r_{out} at the leading and trailing edges, ensuring that the parametrization satisfies G^2 continuity by construction, see Fig. 2(d). This feature is important for the aerodynamic design of turbomachinery blades because a sudden change in curvature could cause a spike in the surface pressure distribution or even a local separation bubble [4]. The functions $f(r)$ and $g(r)$ are based on the end point curvature formulas for NURBS curves and their derivation is detailed in the Appendix. Once that the upper and lower sides are defined, they can be combined into a single B-spline curve $\mathbf{C}^b(u) = \mathbf{C}^l \cup \mathbf{C}^u$ that represents the entire blade profile.

When performing the assessment of the fluid-dynamic performance of the blades via computational fluid dynamics, it is necessary to define the geometry of the flow domain around the blade. For the majority of turbomachinery flow problems one can resort to the periodicity of the flow to reduce the size of the computational domain. In this case, it is therefore sufficient to describe the flow domain around a single blade, which is characterized by the inflow, outflow, and periodic boundaries, as illustrated in Fig. 3. The periodic boundaries are given by two cubic B-spline curves defined by extending the camber line while keeping zero slope at the inlet and outlet. The periodic boundaries

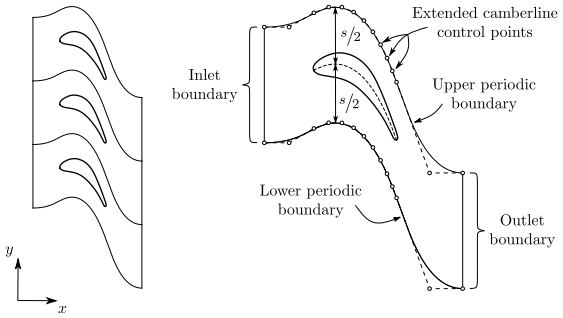

Fig. 3. Construction of the blade flow domain in two dimensions. The fluid-dynamic performance of the blade cascade (left) can be evaluated analyzing the flow around a single blade. The flow domain is defined by four boundaries: inflow, outflow, lower periodic, and upper periodic (right).

are located at an offset distance of half of the blade spacing, s, with respect to the blade camber line. Finally, the inflow and outflow boundaries are defined as two straight lines connecting the upper and lower periodic boundaries.

The proposed parametrization produces blade profiles that have continuous curvature and rate of change of curvature, therefore reducing the possibility of flow separation [4]. This contrasts with most of the two-dimensional methods available in the open literature, which produce blades with discontinuous curvature [19,22,28,29,33], or rate of change of curvature [21,23,24,30]. As a notable exception, the second and third methods proposed by Korakianitis [23], see also [51,52], produce blade profiles with continuous curvature and slope-of-curvature. However, the methods proposed by Korakianitis involve the solution of systems of equations, are not compatible with CAD representations, and are not easily extended from two to three dimensions. In addition, to the knowledge of the authors, it is the first time that the endpoint curvature formulas for NURBS curves are used to impose the curvature of turbomachinery blades at the leading and trailing edges. This is different than what is documented in previous publications [34,37,42], where all the reported methods used the endpoint curvature formulas for Bézier curves to ensure G^2 continuity, with the limitation that the curvature is not imposed exactly when the blades are described by B-spline or NURBS curves.

Application

The flexibility of the proposed two-dimensional blade parametrization method is demonstrated by reconstructing the four blade profiles illustrated in Fig. 4. Each blade profile was defined using 6 control points for each thickness distribution, resulting in a total of 22 design variables. The LS89 [53,54] and T106A [55] are representative of high-pressure and low-pressure axial gas turbine blade rows, respectively. In addition, the SIRT profile is typical of a supersonic impulse turbine rotor [56] and the STD10 profile is representative of an axial compressor blade derived from a NACA 0006 airfoil profile [57]. It can be observed that the parametrization method produces blades with smooth curvature variations, which is essential to avoid spikes and dips in the surface-pressure distribution. The numerical values of the design variables used to produce the blade profiles were computed from a set of scattered point coordinates using the method described in Section 6.

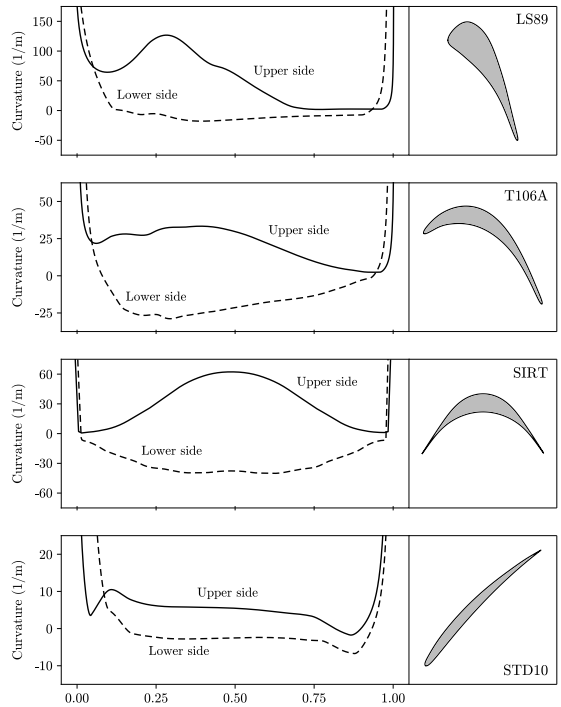

Fig. 4. Geometry and curvature distribution of the two-dimensional test cases. From top to bottom: LS89 [53,54], T106A [55], SIRT [56], and STD10 [57]. The abscissa of the curvature distribution is the normalized axial length.

Table 3
Three-dimensional design variables. Each design variable is provided as a set of control points that defines a continuous variation, except for the number of blades that is a single integer value.

Variable name	Symbol
Number of blades	N_b
Leading edge control points	x_1, z_1
Hub edge control points	x_2, z_2
Trailing edge control points	x_3, z_3
Shroud edge control points	x_4, z_4
Leading edge abscissa[a]	y_{in}
Stagger angle[a]	ξ
Inlet and exit metal angles[a]	θ_{in}, θ_{out}
Inlet and exit tangent proportions[a]	d_{in}, d_{out}
Inlet and exit radii of curvature[a]	r_{in}, r_{in}
Upper and lower thickness distributions	t^u, t^l

[a]Law of evolution in the spanwise direction.

4. Blade parametrization in three dimensions

The proposed three-dimensional parametrization is formulated as an extension of the two-dimensional parametrization and uses the design variables listed in Table 3. Similar to the two-dimensional case, the parametrization starts by defining a camber surface and subsequently imposing two independent thickness distributions perpendicular to the camber surface in a way that ensures G^2 continuity.

The camber surface is determined by the shape of the blade in the meridional plane and the spanwise variation of the design variables. The shape of the blade in the meridional plane is described by four curves, namely, leading edge, trailing edge, hub, and shroud, as illustrated in Fig. 5. In contrast with other

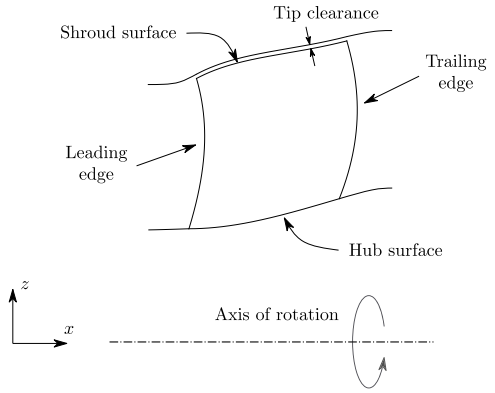

Fig. 5. Geometry of the blade in the meridional plane.

parametrization methods that are limited to axial turbomachines [20,25,27,31,32], the proposed method is suited to describe any kind of turbomachinery configuration, including axial, radial, and mixed-flow machines. The number of control points required to describe the shape of the blade in the meridional plane depends on the complexity of the geometry. For instance, it is possible to define a purely axial turbine using only four control points, but it may be necessary to use 10–20 control points to describe the shape of a mixed-flow machine such as a centrifugal compressor.

The spanwise variation of the some design variables $\alpha(v)$, see Table 3 footnote, is defined as law of evolution through a B-spline of, at most, degree three with an arbitrary number of control points as illustrated in Fig. 7. The number of control points used for each design variable is specified by the user, and its selection is based on the complexity of the blade geometry. As an example, it is sufficient to use a single constant value to define a prismatic blade, but it might be necessary to use 3–6 control points to describe the geometry of a blade with large twist from the root to the tip.

As illustrated in Fig. 9(a), the camber surface $\mathbf{S}^{\mathrm{c}}(u, v)$ is defined as a bi-quartic B-spline surface with control points $\mathbf{P}^{\mathrm{c}}_{i,j} = [x^{\mathrm{c}}_{i,j},\ y^{\mathrm{c}}_{i,j},\ z^{\mathrm{c}}_{i,j}]$. The coordinates of the control points are computed using the shape of the blade in the meridional plane and the spanwise evolution of the design variables. More specifically, the (x, z) coordinates of the camber surface control points are computed by transfinite interpolation [58] of the four curves that define the meridional plane, see Fig. 6, and are given by

$$\begin{aligned}\begin{bmatrix} x^{\mathrm{c}}(u,v) \\ z^{\mathrm{c}}(u,v) \end{bmatrix} &= (1-u)\cdot \mathbf{C}_1{}^{\mathrm{m}}(v) + u\cdot \mathbf{C}_3{}^{\mathrm{m}}(v) \\ &+ (1-v)\cdot \mathbf{C}_2{}^{\mathrm{m}}(u) + v\cdot \mathbf{C}_4{}^{\mathrm{m}}(u) \\ &- (1-v)(1-u)\cdot \mathbf{Q}^{\mathrm{m}}_{1,2} - v\,u\cdot \mathbf{Q}^{\mathrm{m}}_{3,4} \\ &- v\,(1-u)\cdot \mathbf{Q}^{\mathrm{m}}_{4,1} - (1-v)\,u\cdot \mathbf{Q}^{\mathrm{m}}_{2,3},\end{aligned} \tag{16}$$

In addition, the y coordinates of the camber surface control points at each spanwise location v are given by a third order B-spline curve $y^{\mathrm{c}}(u, v)$ with control points $\{y^{\mathrm{c}}_0,\ y^{\mathrm{c}}_1,\ y^{\mathrm{c}}_2,\ y^{\mathrm{c}}_3\}$ that are computed according to

$$y^{\mathrm{c}}_0(v) = y_{\mathrm{in}} \tag{17}$$

$$y^{\mathrm{c}}_1(v) = y^{\mathrm{c}}_0 + d_{\mathrm{in}}\cdot L\tan\theta_{\mathrm{in}} \tag{18}$$

$$y^{\mathrm{c}}_2(v) = y^{\mathrm{c}}_3 - d_{\mathrm{out}}\cdot L\tan\theta_{\mathrm{out}} \tag{19}$$

$$y^{\mathrm{c}}_3(v) = y_{\mathrm{in}} + L\tan\xi \tag{20}$$

This formulation ensures that the metal angles at the leading and trailing edges, θ_{in} and θ_{out}, are respected, as illustrated in Fig. 8. The arc length of the blade meridional plane at each span location $L(v)$ is defined as

$$L(v) = \int_{u=0}^{u=1} \sqrt{\left(\frac{\partial x^{\mathrm{c}}}{\partial u}\right)^2 + \left(\frac{\partial z^{\mathrm{c}}}{\partial u}\right)^2}\,\mathrm{d}u \tag{21}$$

and it is computed using 8th order Gaussian quadrature [59], which provides a satisfactory trade-off between computational speed and accuracy.

The upper and lower sides of the blade, $\mathbf{S}^{l}(u, v)$ and $\mathbf{S}^{u}(u, v)$, are defined as B-spline surfaces of degree four as it is the lowest degree that guarantees continuous rate of change of curvature at the spline knots. The coordinates of the control points $\{\mathbf{P}^{l}_{i,j}\}$ and $\{\mathbf{P}^{u}_{i,j}\}$, see Fig. 9(b), are computed according to

$$\mathbf{P}^{l}_{i,j} = \begin{cases} \mathbf{S}^{\mathrm{c}}(\hat{u}_i,\hat{v}_j), & \text{for } i=0 \\ \mathbf{S}^{\mathrm{c}}(\hat{u}_i,\hat{v}_j) - \mathbf{n}(\hat{u}_i,\hat{v}_j)\cdot f(r_{\mathrm{in}}(\hat{v}_j)), & \text{for } i=1 \\ \mathbf{S}^{\mathrm{c}}(\hat{u}_i,\hat{v}_j) - \mathbf{n}(\hat{u}_i,\hat{v}_j)\cdot t^{l}(\hat{u}_i,\hat{v}_j), & \text{for } i=2:n-2 \\ \mathbf{S}^{\mathrm{c}}(\hat{u}_i,\hat{v}_j) - \mathbf{n}(\hat{u}_i,\hat{v}_j)\cdot g(r_{\mathrm{out}}(\hat{v}_j)), & \text{for } i=n-1 \\ \mathbf{S}^{\mathrm{c}}(\hat{u}_i,\hat{v}_j), & \text{for } i=n \end{cases} \tag{22}$$

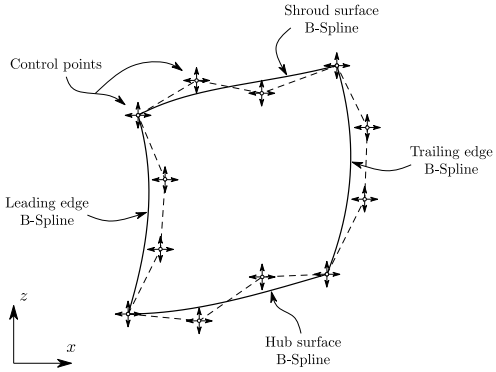

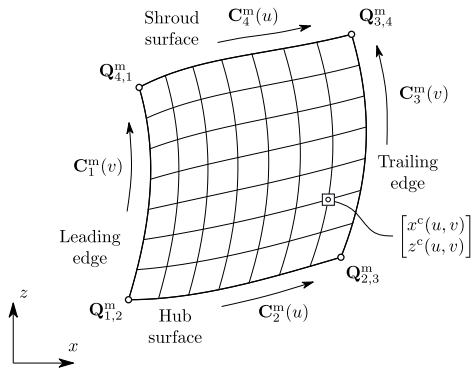

Fig. 6. Construction of the four B-splines that define the shape of the blade in the meridional plane (left) and point evaluation by transfinite interpolation (right). Note that the corner control points of the B-splines are shared.

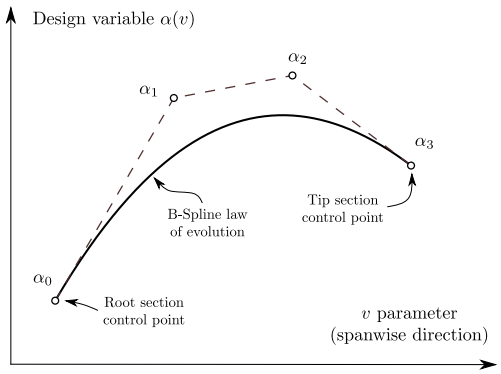

Fig. 7. Spanwise variation of a design variable.

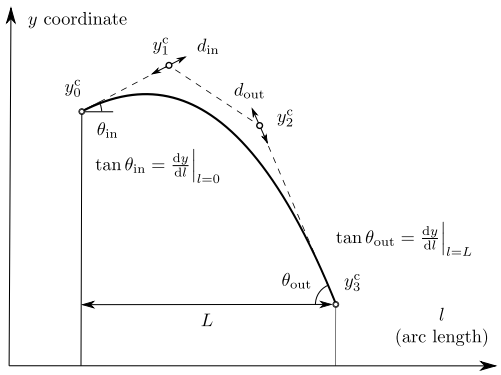

Fig. 8. Tangential camber line coordinate.

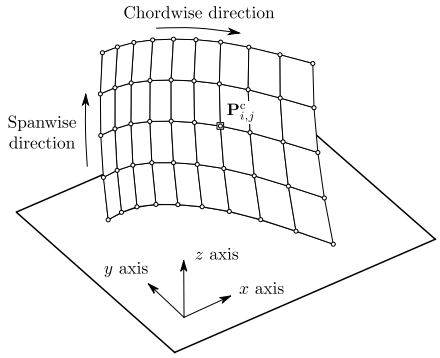

Fig. 9(a). Control points defining the camber surface.

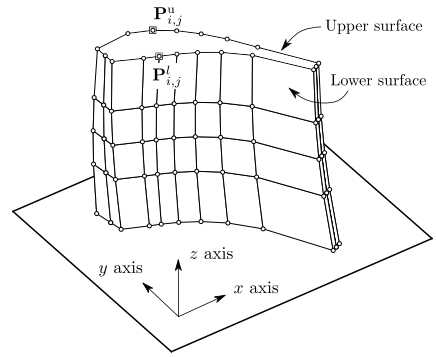

Fig. 9(b). Control points defining the blade surface.

and

$$\mathbf{P}^u_{i,j} = \begin{cases} \mathbf{S}^c(\hat{u}_i, \hat{v}_j), & \text{for } i = 0 \\ \mathbf{S}^c(\hat{u}_i, \hat{v}_j) + \mathbf{n}(\hat{u}_i, \hat{v}_j) \cdot f(r_{\text{in}}(\hat{v}_j)), & \text{for } i = 1 \\ \mathbf{S}^c(\hat{u}_i, \hat{v}_j) + \mathbf{n}(\hat{u}_i, \hat{v}_j) \cdot t^u(\hat{u}_i, \hat{v}_j), & \text{for } i = 2 : n-2 \\ \mathbf{S}^c(\hat{u}_i, \hat{v}_j) + \mathbf{n}(\hat{u}_i, \hat{v}_j) \cdot g(r_{\text{out}}(\hat{v}_j)), & \text{for } i = n-1 \\ \mathbf{S}^c(\hat{u}_i, \hat{v}_j), & \text{for } i = n \end{cases} \tag{23}$$

where the sampling values $(\hat{u}_i, \hat{v}_j)$ are given by

$$\hat{u}_i = \begin{cases} 0, & \text{for } i = 0 \\ \frac{i-1}{n-2}, & \text{for } i = 1 : n-1 \\ 1, & \text{for } i = n \end{cases} \quad \text{and} \tag{24}$$

$$\hat{v}_j = \frac{j}{m}, \quad \text{for } j = 0 : m. \tag{25}$$

The upper and lower thickness distributions, $t^u(u, v)$ and $t^l(u, v)$, are given by bi-variate B-spline polynomials of degree three with an arbitrary number of control points $\{t^u_{i,j}\}$ and $\{t^l_{i,j}\}$, specified by the user. The unitary vectors normal to the camber surface $\mathbf{n}(u, v)$ are computed according to

$$\mathbf{n} = -\frac{\boldsymbol{\tau}_u \times \boldsymbol{\tau}_v}{\|\boldsymbol{\tau}_u \times \boldsymbol{\tau}_v\|}, \tag{26}$$

where the tangent vectors $\boldsymbol{\tau}_u$ and $\boldsymbol{\tau}_v$ are given by

$$\boldsymbol{\tau}_u = \frac{\partial \mathbf{S}^c}{\partial u} \quad \text{and} \quad \boldsymbol{\tau}_v = \frac{\partial \mathbf{S}^c}{\partial v}. \tag{27}$$

The partial derivatives of the camber surface with respect to u and v are computed analytically using B-spline surface derivative formulas [43, pp. 110–115]. In addition, the functions $f(r)$ and $g(r)$ appearing in Eqs. (22) and (23) are used to impose the radius of curvature at the leading and trailing edges, ensuring that the upper and lower surfaces of the blade are smoothly joined with G^2 continuity. The derivation of the functions $f(r)$ and $g(r)$ is detailed in the Appendix. Once that the upper and lower sides are defined, they can combined into a single B-spline surface $\mathbf{S}^b(u, v) = \mathbf{S}^l \cup \mathbf{S}^u$ that represents the entire blade.

The parametrization just described is suitable to model linear cascades, which are commonly used for wind tunnel tests. However, in actual turbomachines, the blades are arranged in an axisymmetric way forming an annular cascade. In order to achieve this, the linear blade configuration is transformed into an annular one with the mapping $\mathcal{H} : \mathbb{R}^3 \to \mathbb{R}^3$ given by

$$\begin{aligned} \mathbf{P}^b_{\text{annular}} &= \mathcal{H}\{\mathbf{P}^b_{\text{linear}}\} = \mathcal{H}\{[x,\ y,\ z]\} \\ &= [x,\ z \cdot \sin(y/z),\ z \cdot \cos(y/z)]\,. \end{aligned} \tag{28}$$

The rationale behind this transformation is to associate the Cartesian coordinates (x, y, z) of a linear cascade with the cylindrical coordinates $(x, r\theta, r)$ of an annular cascade and then convert from cylindrical to Cartesian coordinates.

The flow domain around a blade is characterized by the hub, shroud, inlet, outlet, and periodic boundaries as illustrated in Fig. 10. The hub boundary consists of two surfaces that conform with the blade at its root, see Fig. 10(a). Each of these surfaces is defined as a Coons patch [43, pp. 456–507] that is characterized by four edges. The blade edge is given by a B-spline curve formed by extending the lower side of the blade into the upstream and downstream directions following the slope of the camber line at

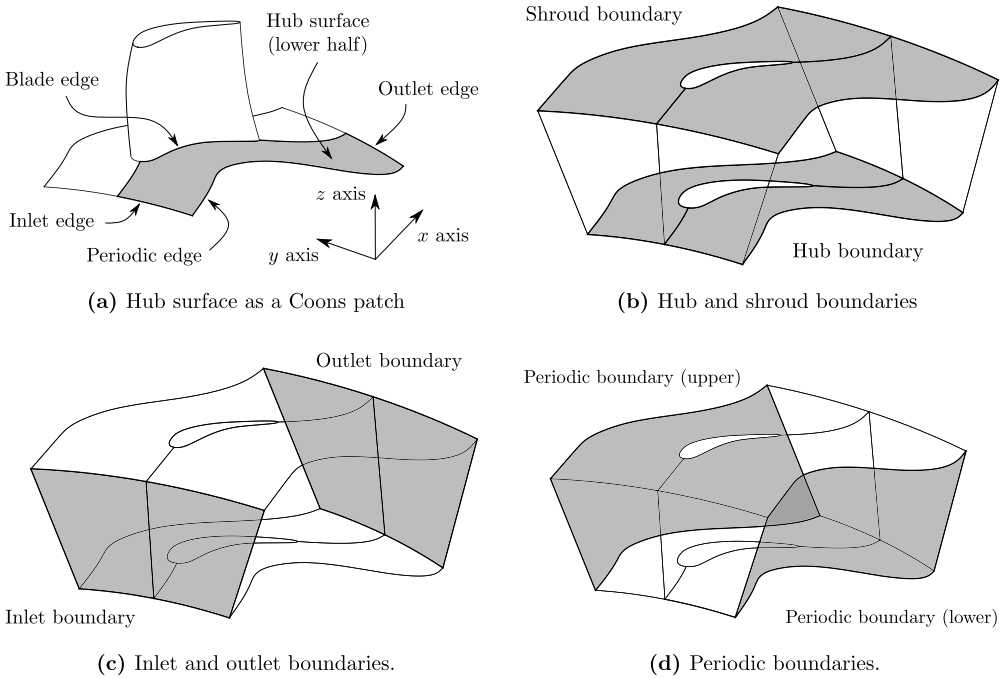

(a) Hub surface as a Coons patch

(b) Hub and shroud boundaries

(c) Inlet and outlet boundaries.

(d) Periodic boundaries.

Fig. 10. Construction of the blade flow domain in three dimensions.

the leading and trailing edges, respectively. The periodic edge is formed by extending the camber line in a similar way and rotating the resulting B-spline about the x-axis through an angle $\theta_b/2$, where $\theta_b = 2\pi/N_b$. Finally, the inlet and outlet edges are defined as NURBS circular arcs that connect the periodic edge with the blade edge. The shroud surface, see Fig. 10(b), is defined in an analogous way and, for the case of rotor blades, it is possible specify a clearance between the tip of the blade and the shroud. Once that the hub and shroud surfaces are defined, it is straightforward to construct the inlet, outlet and periodic surfaces as ruled surfaces [43, pp. 337–340] that connect the limits of the hub and shroud surfaces as illustrated in Figs. 10(c) and 10(d). Note that the parametrization of the blade and flow domain is watertight by construction and it does not rely on intersection and trimming operations. This contrasts with other blade parametrization methods [34,35,37–41] that rely on intersection operations between the blade surface and the hub/shroud surfaces and produce trimmed NURBS patches that have to be specially treated during a shape optimization workflow [45,46].

Application

The flexibility of the proposed three-dimensional blade parametrization method is demonstrated by reconstructing the four blade geometries shown in Fig. 11. The first example, the AACHEN case, is a prismatic axial turbine stator blade [60]. The meridional plane is defined by 4 control points and the design variables are constant in the spanwise direction (1 control point), resulting in a total of 26 design variables. The second case, NASA R67, is an axial compressor rotor blade [61,62]. The blade is highly twisted due to the change in blade speed from root to tip and it was necessary to use 4 control points to describe the spanwise variation of the design variables, resulting in a total of 111 design variables. Similarly the XPROP case illustrates the geometry of an aircraft propeller blade [63]. In this case it was necessary to use 5 control points to describe the twist of the blades, resulting in 113 design variables. Finally, the APU blade is the rotor of a mixed-flow turbine (radial-inflow, axial-outflow) [64,65]. The complex shape of the blade in the meridional plane was described using 14 control points and the spanwise variation of the blade sections was described using 3 control points per design variable, giving rise to 86 design variables. The numerical values of the design variables used to produce the blades were computed from a set of scattered point coordinates using the method described in Section 6.

5. Sensitivity computation and verification

One simple way to approximate partial derivatives of a function is by using a finite difference approximation such as forward finite differences given as

$$\frac{\partial F}{\partial \alpha} = \frac{F(\alpha + h) - F(\alpha)}{h} + \mathcal{O}(h), \tag{29}$$

or central finite differences given as

$$\frac{\partial F}{\partial \alpha} = \frac{F(\alpha + h) - F(\alpha - h)}{2h} + \mathcal{O}(h^2), \tag{30}$$

where $F(\alpha)$ can be identified with $\mathbf{C}^b(u, \alpha)$ in two dimensions or $\mathbf{S}^b(u, v, \alpha)$ in three dimensions and h is the step size used for finite difference computation. Finite difference approximations are susceptible to cancellation error when the step size is small because of the subtraction of very similar numbers in the numerator [66, pp 229–232]. As a result, one is faced with the dilemma of selecting a small step size that minimizes the truncation error but does not lead to a large cancellation error.

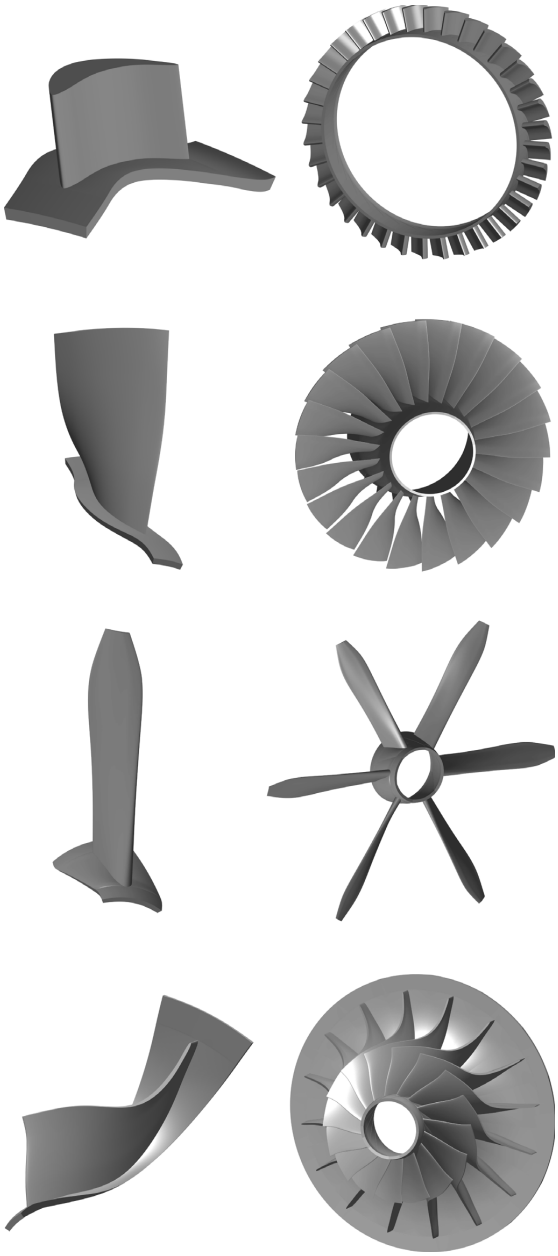

Fig. 11. Geometry of the three-dimensional test cases. From top to bottom: AACHEN stator [60], NASA R67 [61,62], XPROP propeller [63], APU rotor [64,65].

An alternative method that avoids the occurrence of cancellation error is the complex-step method [47–49]. This method uses a complex argument to compute the first derivative of a real-valued function. Indeed, the Taylor series expansion of $F(\alpha)$ in the imaginary axis gives

$$F(\alpha + ih) = F(\alpha) + ih\,\frac{\partial F}{\partial \alpha} - \frac{h^2}{2!}\,\frac{\partial^2 F}{\partial \alpha^2} + \mathcal{O}(ih^3). \tag{31}$$

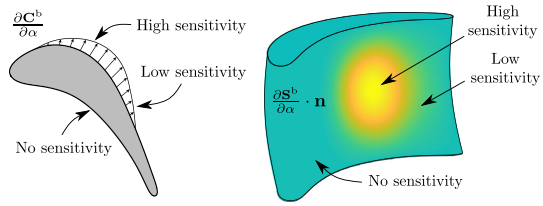

Fig. 12. Sensitivity of the blade geometry with respect to a thickness distribution control point. The sensitivity of the 2D case (left) is represented as a quiver plot. The sensitivity of the 3D case (right) is represented as a colormap of the scalar field given by the dot product of the sensitivity and the unitary vector normal to the blade surface.

Re-arranging the imaginary part of the equation leads to

$$\frac{\partial F}{\partial \alpha} = \frac{\mathrm{Im}\,(F(\alpha + i\,h))}{h} + \mathcal{O}(h^2), \tag{32}$$

which is the complex-step method formula. In contrast to finite difference approximations, this method *is not* susceptible to subtraction error, allowing one to compute first derivatives accurate to the round-off precision of floating point arithmetic by using an arbitrarily small step size.

Algorithmic Differentiation (AD) provides yet another alternative to compute the derivatives of a function with machine precision [67]. AD is a set of techniques to numerically evaluate the derivatives of a function specified as a computer program by applying the chain rule of differentiation to each arithmetic operation of the program. This method offers more functionality and computational efficiency (first and higher order derivatives, forward and reverse modes) than the complex-step method (first derivatives and forward mode only), but it is also more difficult to implement [49].

In this work, the complex-step method was adopted to compute the sensitivity of the surface coordinates with respect to the design variables due to its accuracy, simplicity, and ease of implementation. Fig. 12 illustrates the sensitivity of the blade surface with respect to one thickness distribution control point in two and three dimensions. It can be observed that the sensitivity of the blade changes from point to point and that there may be regions where the sensitivity is zero as a result of the compact-support property of NURBS basis functions [43, p.118].

To verify the correctness of the sensitivity computation the authors performed a convergence study comparing the sensitivities computed using forward finite differences, central finite differences, and the complex-step method for the NASA R67 test case [61,62]. The geometry of the NASA R67 rotor, see Fig. 11, was sampled with 10000 uniformly spaced points within the box $(u, v) \in [0, 1] \times [0, 1]$ and the sensitivity was computed with respect to one design variable (the stagger angle at the hub) for different step sizes in the interval $h \in [10^{-1}, 10^{-15}]$. The error of the sensitivity computation was defined as the mean-square-root deviation between the exact and the estimated sensitivities. The exact sensitivity was assumed to be that computed with the complex-step method using an step size $h = 2.22 \cdot 10^{-16}$, which corresponds to the machine epsilon of double-precision arithmetic [66, pp 8–11].

The results of the convergence study are shown in Fig. 13. For the case of the complex-step method (CS), reducing the step size decreases the error until the trend flattens to a value close to the machine precision. In contrast, the forward finite difference (F-FD) and central finite difference (C-FD) errors decrease as the step size decreases down to a minimum value and then increase because the cancellation error becomes more prominent than the

Table 4
Summary of the test cases and matching results.

Name and reference		Description	Dim.	DVs	Error abs.[a] (mm)	Error rel.[b] (%)
LS89	[53,54]	High-stagger reaction turbine profile	2D	22	0.047	0.067
T106A	[55]	High-deflection reaction turbine profile	2D	22	0.057	0.046
SITR	[56]	Supersonic impulse turbine profile	2D	22	0.067	0.087
STD10	[57]	Slender compressor profile	2D	22	0.020	0.020
AACHEN	[60]	Axial flow turbine stator blade	3D	26	0.060	0.084
NASA R67	[61,62]	High-twist turbo fan blade	3D	99	0.107	0.107
XPROP	[63]	High-twist propeller blade	3D	113	0.127	0.377
APU	[64,65]	Mixed-flow turbine rotor blade	3D	86	0.057	0.080

[a]Defined as the arithmetic mean deviation between the prescribed and the matched blades.
[b]Defined as the quotient of the mean error and the arc length of blade camber line (three-dimensional cases use the camber line at the hub).

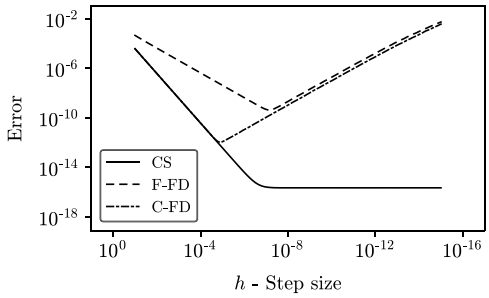

Fig. 13. Sensitivity error at different step sizes for the complex-step method (CS), forward finite differences (F-FD), and central finite differences (C-FD).

truncation error. In addition, it can be observed that the complex-step method and the central finite differences agree in interval when the truncation error dominates ($h \lesssim 10^{-6}$). This verifies that the implementation of the complex-step method is correct. Although not shown here for brevity, the authors performed similar convergence studies for all the design variables of each of the test cases summarized in Table 4 and obtained similar results.

6. Blade matching methodology

In order to optimize the performance of an existing turbomachinery blade, it is essential to find a parametric representation of its geometry, which is usually available as a set of scattered points coordinates $\mathbf{Q}_i$, with $i = 1, 2, \ldots, N_Q$ obtained from a mesh, from sampling a CAD model, or from laser scan measurements. This section proposes a systematic method to find the set of design variables that best approximates the shape of a prescribed blade geometry. The method can be divided in two phases: (1) the point projection phase and (2) the geometry update phase. It is assumed that the designer starts from an initial guess for the design variables that roughly approximates the existing geometry, see Fig. 14(a).

In the point projection phase, the goal is to find the parametric values u_i, in two dimensions, or $(u_i,\ v_i)$ in three dimensions, that minimize the distance with respect to each prescribed point $\mathbf{Q}_i$. The two-dimensional point projection problem can be formulated as

$$\underset{u\in\mathbb{R}}{\text{minimize}} \quad J(u) = \frac{1}{2}\left\|\mathbf{C}^{\mathrm{b}}(u) - \mathbf{Q}_i\right\|^2, \tag{33}$$
$$\text{subject to} \quad 0 \le u \le 1,$$

where J is the distance between the prescribed and the parametrized point. The gradient of the objective function J can be computed analytically as

$$\nabla J = \frac{\partial J}{\partial u} = \left(\mathbf{C}^{\mathrm{b}}(u) - \mathbf{Q}_i\right) \cdot \frac{\partial \mathbf{C}^{\mathrm{b}}}{\partial u}. \tag{34}$$

Similarly, in three dimensions, the point projection problem is given by

$$\underset{(u,v)\in\mathbb{R}^2}{\text{minimize}} \quad J(u,v) = \frac{1}{2}\left\|\mathbf{S}^{\mathrm{b}}(u,v) - \mathbf{Q}_i\right\|^2, \tag{35}$$
$$\text{subject to} \quad 0 \le u, v \le 1$$

and the gradient of the objective function can be computed according to

$$\nabla J = \begin{bmatrix} \dfrac{\partial J}{\partial u} \\ \dfrac{\partial J}{\partial v} \end{bmatrix} = \begin{bmatrix} \left(\mathbf{S}^{\mathrm{b}}(u,v) - \mathbf{Q}_i\right) \cdot \dfrac{\partial \mathbf{S}^{\mathrm{b}}}{\partial u} \\ \left(\mathbf{S}^{\mathrm{b}}(u,v) - \mathbf{Q}_i\right) \cdot \dfrac{\partial \mathbf{S}^{\mathrm{b}}}{\partial v} \end{bmatrix}. \tag{36}$$

Note that the geometry of the parametrized blade *does not change* during the point projection phase. One common pitfall when solving the point projection problem is that the optimization may converge to a local minimum as illustrated in Fig. 14(b). This limitation can be addressed by solving the point projection problem from different starting points and then selecting the global minimum among the various solutions or by sampling the parametrized blade at several locations and then starting the optimization from the test point that is closest to $\mathbf{Q}_i$ [43, pp. 229–234].

In the geometry update phase, the goal is to find the set of design variables α that minimizes the deviation between the parametrized and the prescribed blades. This can be formulated as an unconstrained minimization problem where the objective function is the sum of the distances between each projected point and the corresponding prescribed point. This optimization problem is given by

$$\underset{\alpha\in\mathbb{R}^{\alpha}}{\text{minimize}} \quad J(\alpha) = \sum_{i=1}^{N_Q} \left\|\mathbf{C}^{\mathrm{b}}(u_i,\ \alpha) - \mathbf{Q}_i\right\|^2 \tag{37}$$

in two dimensions and by

$$\underset{\alpha\in\mathbb{R}^{\alpha}}{\text{minimize}} \quad J(\alpha) = \sum_{i=1}^{N_Q} \left\|\mathbf{S}^{\mathrm{b}}(u_i,\ v_i,\ \alpha) - \mathbf{Q}_i\right\|^2 \tag{38}$$

in three dimensions, where α are the design variables listed in Tables 2 and 3, respectively. The gradient of these objective functions is computed using the complex-step method as described in Section 5. In contrast to the point projection phase, the geometry of the parametrized blade is updated until the deviation with respect to the prescribed geometry is minimized, see Fig. 14(c). In order to improve the matching of $(u,\ v)$ and α, the point projection and geometry update problems are solved alternatively until the relative deviation between the prescribed and the parametrized blades does not change more than a small tolerance, e.g. 10^{-8}.

To demonstrate its flexibility and accuracy, the blade matching method was applied to replicate the geometry of eight exemplary blades. The set of test cases is summarized in Table 4 and it

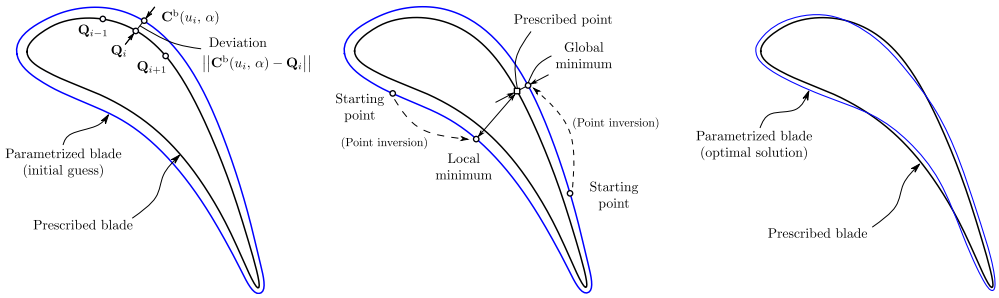

(a) Initial guess. (b) Point projection phase. (c) Geometry update phase.

Fig. 14. Illustration of the blade matching problem in two dimensions. The deviation between the prescribed and parametrized blades after the geometry update phase was exaggerated to improve visibility.

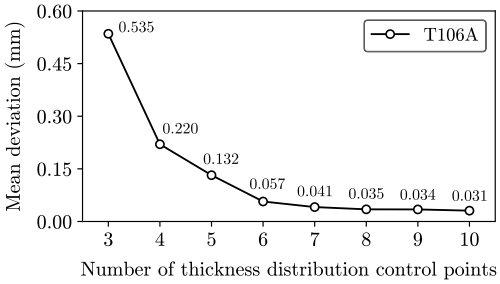

Fig. 15. Matching error as a function of the number of thickness distribution control points for the T106A test case.

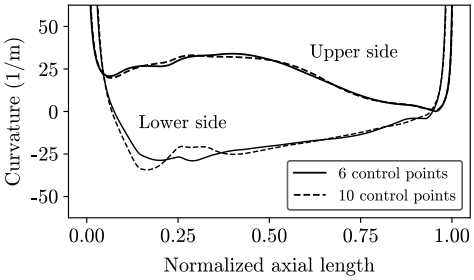

Fig. 16. Curvature distribution of the T106A profile when the matching is performed using 6 and 10 control points.

was conceived to cover a wide range of turbomachinery blade geometries in two (Fig. 4) and three dimensions (Fig. 11). The results of the blade matching in terms of absolute and relative error are summarized in Table 4.

The relative matching error is below 0.38% for all cases and the highest absolute error is 0.127 mm for the XPROP test case, which is of the same order of magnitude as the tolerances used to manufacture axial gas turbine blades ($\approx$ 0.05 mm) [68]. In addition, the deviation could be further reduced by increasing the number of control points used to parametrize the blade. This is illustrated in the convergence study shown in Fig. 15, where the number of control points used to describe the thickness distribution of the T106A case is increased from 3 to 10 points. Specifically, the mean deviation is reduced from 0.057 mm to 0.031 mm when the number of control points is increased from 6 to 10. In addition, Fig. 16 shows the curvature distribution for the T106A blade described using 6 and 10 thickness distribution control points. It can be observed that the curvature variation is smooth for both cases and that increasing the number of control points does not introduce high-frequency undulations that would deteriorate the fluid dynamic performance of the blade. These results indicate that the parametrization and matching methodologies proposed in this work enable the replication of a wide range of geometries with an accuracy comparable to the typical tolerances of modern manufacturing techniques and that the re-parametrization accuracy can be increased by refining the design space.

7. Software structure

The blade parametrization method proposed in this work was implemented in the Python programming language [69] and released under a permissive open source license as the ParaBlade software package [70]. The code was written using object-oriented programming principles and the structure of the package is subdivided in the classes shown in Fig. 17. The implementation integrates the in-house NurbsPy package [71] to define and manipulate NURBS curves and surfaces. In addition, ParaBlade relies on the NumPy library [72] for array operations and on the Pagmo/Pygmo optimization library [73] to solve the blade matching optimization problems by means of the limited-memory BFGS algorithm [74,75].

8. Conclusions

This paper presented a general constructive parametrization method for turbomachinery blades. The method uses typical turbomachinery design variables and NURBS curves and surfaces to produce blade geometries with continuous curvature and rate of change of curvature. In contrast with existing methods, the flow domain parametrization was formulated in an explicit way that avoids intersection and trimming operations and the sensitivity of the geometry is computed by means of the complex-step method, allowing the integration of the parametrization into automated, gradient-based shape optimization workflows.

In addition, the method enables the re-parametrization of a baseline blade geometry defined by a set of scattered point coordinates in a systematic way by solving a two-step optimization

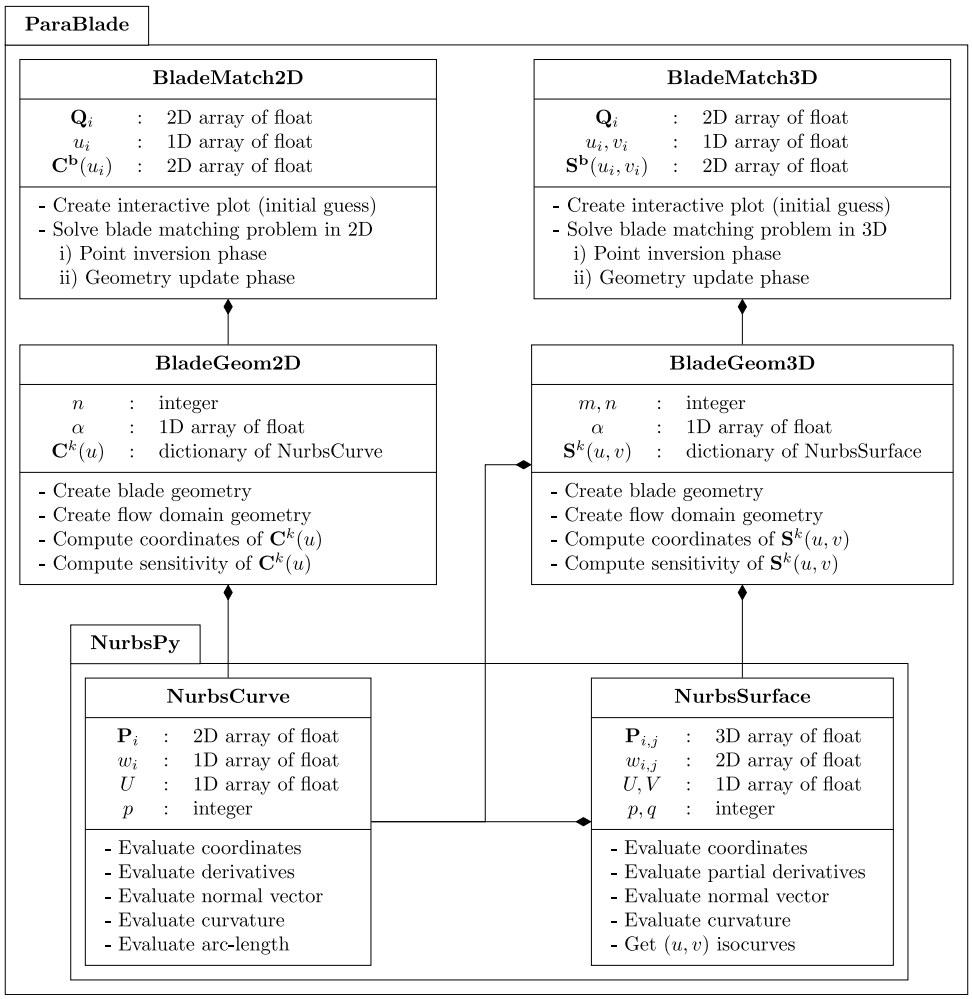

Fig. 17. Class diagram of the ParaBlade and NurbsPy packages. Each class is represented by a box with three compartments containing its name and main attributes/methods. The diamond-ended arrows (♦) represent a composition relation between two classes. This means that the class next to the diamond symbol contains one or more instances of the class at the other end of the line. For instance, the `BladeMatch3D` contains one instance of the `BladeGeom3D` class, which in turn contains several `NurbsCurve` and `NurbsSurface` objects.

problem. To demonstrate its capabilities, the re-parametrization method was applied to replicate the geometry of eight exemplary blades, showing that the proposed parametrization can replicate the geometry of a wide range of turbomachinery blades with an accuracy comparable to the tolerances of current manufacturing techniques for axial gas turbine profiles.

Declaration of competing interest

The authors declare that they have no known competing financial interests or personal relationships that could have appeared to influence the work reported in this paper.

Acknowledgments

The authors gratefully acknowledge the financial support from the Research Council of Norway (EnergiX grant number 255016) for the COPRO project, the Netherlands Organization for Scientific Research (grant project number 14711) and the user partners Equinor, Hydro, Alcoa, GE Power Norway and FrioNordica.

Appendix. Derivation of the endpoint curvature formulas

This appendix contains the derivation of the functions $f(r_{\text{in}})$ and $g(r_{\text{out}})$ that are used to impose the radii of curvature r_{in} and r_{out} at the leading and trailing edges. According to Goldman [76], the curvature of a parametric curve $\mathbf{C}(u)$ is given by

$$\kappa(u) = \frac{\left\|\ddot{\mathbf{C}}(u) \times \dot{\mathbf{C}}(u)\right\|}{\left\|\dot{\mathbf{C}}(u)\right\|^3}. \tag{A.1}$$

In addition, it can be shown [43, pp. 125–127], that the first and second derivatives of a NURBS curve at its *start point* are given by

$$\dot{\mathbf{C}}(u=0) = \left(\frac{p}{u_{p+1}}\right)\left(\frac{w_1}{w_0}\right)(\mathbf{P}_1 - \mathbf{P}_0) \tag{A.2}$$

and

$$\begin{aligned}\ddot{\mathbf{C}}(u=0) = &+\frac{p(p-1)}{u_{p+1}}\left(\frac{1}{u_{p+2}}\right)\left(\frac{w_2}{w_0}\right)(\mathbf{P}_2-\mathbf{P}_0)+\\ &-\frac{p(p-1)}{u_{p+1}}\left(\frac{1}{u_{p+1}}+\frac{1}{u_{p+2}}\right)\left(\frac{w_1}{w_0}\right)(\mathbf{P}_1-\mathbf{P}_0)+\\ &+\frac{2p^2}{u_{p+1}^2}\left(\frac{w_1}{w_0}\right)\left(1-\frac{w_1}{w_0}\right)(\mathbf{P}_1-\mathbf{P}_0),\end{aligned} \tag{A.3}$$

respectively, where p is the degree of the curve, u_k are the knot values, $\mathbf{P}_k$ are the control point coordinates, and w_k are the control point weights. Inserting these expressions into the curvature definition and using the fact that the vector cross product of two parallel vectors is zero we find

$$\begin{aligned}\kappa(u=0) = &\left(\frac{p-1}{p}\right)\left(\frac{u_{p+1}}{u_{p+2}}\right)\left(\frac{w_0\,w_2}{w_1^2}\right)\\ &\times\ \frac{\|(\mathbf{P}_2-\mathbf{P}_0)\times(\mathbf{P}_1-\mathbf{P}_0)\|}{\|\mathbf{P}_1-\mathbf{P}_0\|^3}.\end{aligned} \tag{A.4}$$

Noting that unitary vector perpendicular to the camber line at the leading edge ($\mathbf{n}$) points from $\mathbf{P}_0$ to $\mathbf{P}_1$, see Fig. 2(d), the previous equation simplifies to

$$\kappa_{\text{in}} = \frac{1}{r_{\text{in}}} = \left(\frac{p-1}{p}\right)\left(\frac{u_{p+1}}{u_{p+2}}\right)\left(\frac{w_0\,w_2}{w_1^2}\right)\frac{\|(\mathbf{P}_2-\mathbf{P}_0)\times\mathbf{n}\|}{\|\mathbf{P}_1-\mathbf{P}_0\|^2}. \tag{A.5}$$

Solving for $\|\mathbf{P}_1-\mathbf{P}_0\|$, the location of the control point $\mathbf{P}_1$ that guarantees that the radius of curvature at the leading edge is r_{in} is given by

$$\mathbf{P}_1 = \mathbf{P}_0 \pm \|\mathbf{P}_1-\mathbf{P}_0\|\cdot\mathbf{n} = \mathbf{P}_0 \pm f(r_{\text{in}})\cdot\mathbf{n}, \tag{A.6}$$

where the plus and minus signs correspond to the upper and lower sides of the blade, respectively, and the function $f(r_{\text{in}})$ is given by

$$f(r_{\text{in}})^2 = r_{\text{in}}\left(\frac{p-1}{p}\right)\left(\frac{u_{p+1}}{u_{p+2}}\right)\left(\frac{w_0\,w_2}{w_1^2}\right)\|(\mathbf{P}_2-\mathbf{P}_0)\times\mathbf{n}\|. \tag{A.7}$$

The derivation for the trailing edge is analogous. The first and second derivatives of a NURBS curve at its *end point* are given by

$$\dot{\mathbf{C}}(u=1) = \left(\frac{p}{1-u_n}\right)\left(\frac{w_{n-1}}{w_n}\right)(\mathbf{P}_n-\mathbf{P}_{n-1}) \tag{A.8}$$

and

$$\begin{aligned}&\ddot{\mathbf{C}}(u=1)\\ &= +\frac{p(p-1)}{1-u_n}\left(\frac{1}{1-u_{n-1}}\right)\left(\frac{w_{n-2}}{w_n}\right)(\mathbf{P}_{n-2}-\mathbf{P}_n)+\\ &\quad -\frac{p(p-1)}{1-u_n}\left(\frac{1}{1-u_n}+\frac{1}{1-u_{n-1}}\right)\left(\frac{w_{n-1}}{w_n}\right)(\mathbf{P}_{n-1}-\mathbf{P}_n)+\\ &\quad +\frac{2p^2}{(1-u_n)^2}\left(\frac{w_{n-1}}{w_n}\right)\left(1-\frac{w_{n-1}}{w_n}\right)(\mathbf{P}_{n-1}-\mathbf{P}_n),\end{aligned} \tag{A.9}$$

respectively. Inserting these expressions into the curvature definition we find

$$\begin{aligned}\kappa(u=1) = &\left(\frac{p-1}{p}\right)\left(\frac{1-u_n}{1-u_{n-1}}\right)\left(\frac{w_n\,w_{n-2}}{w_{n-1}^2}\right)\\ &\times\ \frac{\|(\mathbf{P}_{n-2}-\mathbf{P}_n)\times(\mathbf{P}_{n-1}-\mathbf{P}_n)\|}{\|\mathbf{P}_{n-1}-\mathbf{P}_n\|^3}.\end{aligned} \tag{A.10}$$

Noting that unitary vector perpendicular to the camber line at the trailing edge ($\mathbf{n}$) points from $\mathbf{P}_n$ to $\mathbf{P}_{n-1}$, the previous equation simplifies to

$$\begin{aligned}\kappa_{\text{out}} &= \frac{1}{r_{\text{out}}}\\ &= \left(\frac{p-1}{p}\right)\left(\frac{1-u_n}{1-u_{n-1}}\right)\left(\frac{w_n\,w_{n-2}}{w_{n-1}^2}\right)\frac{\|(\mathbf{P}_{n-2}-\mathbf{P}_n)\times\mathbf{n}\|}{\|\mathbf{P}_{n-1}-\mathbf{P}_n\|^2}.\end{aligned} \tag{A.11}$$

Solving for $\|\mathbf{P}_{n-1}-\mathbf{P}_n\|$, the location of the control point $\mathbf{P}_{n-1}$ that guarantees that the radius of curvature at the trailing edge is r_{out} is given by

$$\mathbf{P}_{n-1} = \mathbf{P}_n \pm \|\mathbf{P}_{n-1}-\mathbf{P}_n\|\cdot\mathbf{n} = \mathbf{P}_n \pm g(r_{\text{out}})\cdot\mathbf{n}, \tag{A.12}$$

where the plus and minus signs correspond to the upper and lower sides of the blade, respectively, and the function $g(r_{\text{out}})$ is given by

$$\begin{aligned}&g(r_{\text{out}})^2\\ &= r_{\text{out}}\left(\frac{p-1}{p}\right)\left(\frac{1-u_n}{1-u_{n-1}}\right)\left(\frac{w_n\,w_{n-2}}{w_{n-1}^2}\right)\|(\mathbf{P}_{n-2}-\mathbf{P}_n)\times\mathbf{n}\|.\end{aligned} \tag{A.13}$$

Note that this construction guarantees that the blade is G^2 continuous at the leading and trailing edges since the radius of curvature is the same at the points connecting the upper and lower sides of the blade.

References

[1] Verstraete T. Toward gradient-based optimization of full gas turbines. Mech Eng 2019;141(03):54–5. http://dx.doi.org/10.1115/1.2019-MAR-7.

[2] Samareh JA. Survey of shape parameterization techniques for high-fidelity multidisciplinary shape optimization. AIAA J 2001;39(5):877–84. http://dx.doi.org/10.2514/2.1391.

[3] Banović M, Mykhaskiv O, Auriemma S, Walther A, Legrand H, Müller J-D. Algorithmic differentiation of the open CASCADE technology CAD kernel and its coupling with an adjoint CFD solver. Optim Methods Softw 2018;33(4–6):813–28. http://dx.doi.org/10.1080/10556788.2018.1431235.

[4] Korakianitis T, Papagiannidis P. Surface-curvature-distribution effects on turbine-cascade performance. Trans ASME, J Turbomach 1993;115(2):334–41. http://dx.doi.org/10.1115/1.2929239.

[5] Wu H-Y, Liu F, Tsai H-M. Aerodynamic design of turbine blades using an adjoint equation method. In: 43rd AIAA aerospace sciences meeting and exhibit. 2005, p. 1–13. http://dx.doi.org/10.2514/6.2005-1006.

[6] Walther B, Nadarajah S. Constrained adjoint-based aerodynamic shape optimization of a single-stage transonic compressor. Trans ASME, J Turbomach 2012;135(2):1–10. http://dx.doi.org/10.1115/1.4007502.

[7] Pini M, Persico G, Pasquale D, Rebay S. Adjoint method for shape optimization in real-gas flow applications. Trans ASME, J Eng Gas Turbines Power 2014;137(3):1–13. http://dx.doi.org/10.1115/1.4028495.

[8] Xu S, Radford D, Meyer M, Müller J-D. CAD-based adjoint shape optimisation of a one-stage turbine with geometric constraints. In: ASME turbo expo: Power for land, sea, and air. 2015, p. 1–14. http://dx.doi.org/10.1115/GT2015-42237.

[9] Luo J, Zhou C, Liu F. Multipoint design optimization of a transonic compressor blade by using an adjoint method. Trans ASME, J Turbomach 2013;136(5):1–10. http://dx.doi.org/10.1115/1.4025164.

[10] Walther B, Nadarajah S. Optimum shape design for multirow turbomachinery configurations using a discrete adjoint approach and an efficient radial basis function deformation scheme for complex multiblock grids. Trans ASME, J Turbomach 2015;137(8):1–20. http://dx.doi.org/10.1115/1.4029550.

[11] Vitale S, Albring TA, Pini M, Gauger NR, Colonna P. Fully turbulent discrete adjoint solver for non-ideal compressible flow applications. J Glob Power Propuls Soc 2017;1:252–70. http://dx.doi.org/10.22261/JGPPS.Z1FVOI.

[12] John A, Shahpar S, Qin N. Novel compressor blade shaping through a free-form method. Trans ASME, J Turbomach 2017;139(8):1–11. http://dx.doi.org/10.1115/1.4035833.

[13] Tang X, Luo J, Liu F. Adjoint aerodynamic optimization of a transonic fan rotor blade with a localized two-level mesh deformation method. Aerosp Sci Technol 2018;72:267–77. http://dx.doi.org/10.1016/j.ast.2017.11.015.

[14] Gagliardi F, Giannakoglou KC. RBF-based morphing of B-Rep models for use in aerodynamic shape optimization. Adv Eng Softw 2019;138:1–17. http://dx.doi.org/10.1016/j.advengsoft.2019.102724.

[15] Bahamonde S, Pini M, De Servi C, Rubino A, Colonna P. Method for the preliminary fluid dynamic design of high-temperature mini-organic Rankine cycle turbines. Trans ASME, J Eng Gas Turbines Power 2017;139(8):1–14. http://dx.doi.org/10.1115/1.4035841.

[16] Agromayor R, Nord LO. Preliminary design and optimization of axial turbines accounting for diffuser performance. Int J Turbomach Propuls Power 2019;4(3):1–32. http://dx.doi.org/10.3390/ijtpp4030032.

[17] Damle SV, Dang TQ, Reddy DR. Throughflow method for turbomachines applicable for all flow regimes. Trans ASME, J Turbomach 1997;119(2):256–62. http://dx.doi.org/10.1115/1.2841108.

[18] Persico G, Rebay S. A penalty formulation for the throughflow modeling of turbomachinery. Comput & Fluids 2012;60:86–98. http://dx.doi.org/10.1016/j.compfluid.2012.03.001.

[19] Dunham J. A parametric method of turbine blade profile design. In: ASME turbo expo: Power for land, sea, and air. 1974, p. 1–9. http://dx.doi.org/10.1115/74-GT-119.

[20] Crouse JE, Gorrell WT. Computer program for aerodynamic and blading design of multistage axial-flow compressors. Tech. Rep. TP 1946, NASA Lewis Research Center; Cleveland, OH, United States; 1981, p. 1–110.

[21] Ye ZQ. A systematic computational design system for turbine cascades, airfoil geometry and blade-to-blade analysis. Trans ASME, J Eng Gas Turbines Power 1984;106(3):598–605. http://dx.doi.org/10.1115/1.3239612.

[22] Pritchard LJ. An eleven parameter axial turbine airfoil geometry model. In: ASME turbo expo: Power for land, sea, and air. 1985, p. 1–12. http://dx.doi.org/10.1115/85-GT-219.

[23] Korakianitis T. Hierarchical development of three direct-design methods for two-dimensional axial-turbomachinery cascades. Trans ASME, J Turbomach 1993;115(2):314–24. http://dx.doi.org/10.1115/1.2929237.

[24] Aungier RH. Turbine aerodynamics: Axial-flow and radial-flow turbine design and analysis. 1st ed.. ASME Press; 2006, p. 166–83. http://dx.doi.org/10.1115/1.802418.

[25] Engeli M, Zollinger HJ, Allemann JC. A computer program for the design of turbomachinery blades. In: ASME turbo expo: Power for land, sea, and air. 1974, p. 1–10. http://dx.doi.org/10.1115/78-GT-36.

[26] Casey MV. A computational geometry for the blades and internal flow channels of centrifugal compressors. Trans ASME, J Eng Power 1983;105(2):288–95. http://dx.doi.org/10.1115/1.3227414.

[27] Goel S, Cofer I, Singh H. Turbine airfoil design optimization. In: ASME turbo expo: Power for land, sea, and air. 1996, p. 1–10. http://dx.doi.org/10.1115/96-GT-158.

[28] Giannakoglou KC. Designing turbomachinery blades using evolutionary methods. In: ASME turbo expo: Power for land, sea, and air. 1999, p. 1–9. http://dx.doi.org/10.1115/99-GT-181.

[29] Trigg MA, Tubby GR, Sheard AG. Automatic genetic optimization approach to two-dimensional blade profile design for steam turbines. Trans ASME, J Turbomach 1999;121(1):11–7. http://dx.doi.org/10.1115/1.2841220.

[30] Pierret S, Van den Braembussche RA. Turbomachinery blade design using a Navier-Stokes solver and artificial neural network. Trans ASME, J Turbomach 1999;121(2):326–32. http://dx.doi.org/10.1115/1.2841318.

[31] Pierret S, Demeulenaere A, Gouverneur B, Van den Braembussche R. Designing turbomachinery blades with the function approximation concept and the Navier-Stokes equations. In: 8th symposium on multidisciplinary analysis and optimization. 2000, p. 1–11. http://dx.doi.org/10.2514/6.2000-4879.

[32] Oyama A, Liou M-S, Obayashi S. Transonic axial-flow blade optimization: Evolutionary algorithms/three-dimensional Navier-Stokes solver. J Propul Power 2004;20(4):612–9. http://dx.doi.org/10.2514/1.2290.

[33] Huppertz A, Flassig PM, Flassig RJ, Swoboda M. Knowledge based 2D blade design using multi-objective aerodynamic optimization and a neural network. In: ASME turbo expo: Power for land, sea, and air. 2007, p. 413–23. http://dx.doi.org/10.1115/GT2007-28204.

[34] Verstraete T. CADO: A computer aided design and optimization tool for turbomachinery applications. In: Proceedings of the 2nd International Conference on Engineering Optimization. Lisbon, Portugal:. 2010. p. 1–10.

[35] Siddappaji K, Turner MG, Merchant A. General capability of parametric 3D blade design tool for turbomachinery. In: ASME turbo expo: Power for land, sea, and air. 2012, p. 1–14. http://dx.doi.org/10.1115/GT2012-69756.

[36] Sanchez-Torreguitart I, Verstraete T, Müller L. Optimization of the LS89 axial turbine profile using a CAD and adjoint based approach. International Trans ASME, J Turbomach, Propulsion and Power 2018;3(3):1–20. http://dx.doi.org/10.3390/ijtpp3030020.

[37] Mykhaskiv O, Banović M, Auriemma S, Mohanamuraly P, Walther A, Legrand H, et al. NURBS-Based and parametric-based shape optimization with differentiated CAD kernel. Comput-Aided Des Appl 2018;15(6):916–26. http://dx.doi.org/10.1080/16864360.2018.1462881.

[38] Miller IV PL, Oliver JH, Miller DP, Tweedt DL. BladeCAD: An interactive geometric design tool for turbomachinery blades. In: ASME turbo expo: Power for land, sea, and air. 1996, p. 1–8. http://dx.doi.org/10.1115/96-GT-058.

[39] Gräsel J, Keskin A, Swoboda M, Przewozny H, Saxer A. A full parametric model for turbomachinery blade design and optimisation. In: ASME international design engineering technical conferences and computers and information in engineering conference. 2004, p. 907–14. http://dx.doi.org/10.1115/DETC2004-57467.

[40] Koini GN, Sarakinos SS, Nikolos IK. A software tool for parametric design of turbomachinery blades. Adv Eng Softw 2009;40(1):41–51. http://dx.doi.org/10.1016/j.advengsoft.2008.03.008.

[41] Müller L, Verstraete T. CAD Integrated multipoint adjoint-based optimization of a turbocharger radial turbine. Int J Turbomach Propuls Power 2017;2(3):1–14. http://dx.doi.org/10.3390/ijtpp2030014.

[42] Anand N, Vitale S, Pini M, Colonna P. Assessment of FFD and CAD-based shape parametrization methods for adjoint-based turbomachinery shape optimization. In: Proceedings of the Montreal 2018 global power and propulsion forum. 2018. p. 1–8.

[43] Piegl L, Tiller W. The NURBS book. 2nd ed.. Springer Science & Business Media; 2012, http://dx.doi.org/10.1007/978-3-642-97385-7.

[44] Farin GE. Curves and surfaces for CAGD: A practical guide. 5th ed.. Morgan Kaufmann; 2001.

[45] Taylor NJ. Industrial perspectives on geometry handling for aerodynamics. In: 22nd AIAA computational fluid dynamics conference. 2015, p. 1–12. http://dx.doi.org/10.2514/6.2015-3408.

[46] Xu S, Timme S, Mykhaskiv O, Müller J-D. Wing-body junction optimisation with CAD-based parametrisation including a moving intersection. Aerosp Sci Technol 2017;68:543–51. http://dx.doi.org/10.1016/j.ast.2017.06.014.

[47] Lyness JN, Moler CB. Numerical differentiation of analytic functions. SIAM J Numer Anal 1967;4(2):202–10. http://dx.doi.org/10.1137/0704019.

[48] Squire W, Trapp G. Using complex variables to estimate derivatives of real functions. SIAM Rev 1998;40(1):110–2. http://dx.doi.org/10.1137/S003614459631241X.

[49] Martins JRRA, Sturdza P, Alonso JJ. The complex-step derivative approximation. ACM Trans Math Softw 2003;29(3):245–62. http://dx.doi.org/10.1145/838250.838251.

[50] Piegl L. On NURBS: A survey. IEEE Comput Graph Appl 1991;11(1):55–71. http://dx.doi.org/10.1109/38.67702.

[51] Korakianitis T. Prescribed-curvature-distribution airfoils for the preliminary geometric design of axial-turbomachinery cascades. Trans ASME, J Turbomach 1993;115(2):325–33. http://dx.doi.org/10.1115/1.2929238.

[52] Korakianitis T, Papagiannidis P. Improved turbine-blade design techniques using 4th-order parametric-spline segments. Comput-Aided Des 1993;25(5):289–99. http://dx.doi.org/10.1016/0010-4485(93)90086-4.

[53] Arts T, Lambert de Rouvroit M, Rutherford AW. Aero-Thermal investigation of a highly loaded transonic linear turbine guide vane cascade: A test case for inviscid and viscous flow computations. Tech. rep. 174, VKI Training Center for Experimental Aerodynamics; 1990, p. 1–97.

[54] Arts T, Lambert de Rouvroit M. Aero-thermal performance of a two-dimensional highly loaded transonic turbine nozzle guide vane: A test case for inviscid and viscous flow computations. Trans ASME, J Turbomach 1992;114(1):147–54. http://dx.doi.org/10.1115/1.2927978.

[55] Stadtmüller P, Fottner L. A test case for the numerical investigation of wake passing effects on a highly loaded LP turbine cascade blade. In: ASME turbo expo: Power for land, sea, and air. American Society of Mechanical Engineers Digital Collection; 2001, p. 1–8. http://dx.doi.org/10.1115/2001-GT-0311.

[56] Anand N, Rubino A, Colonna P, Pini M. Adjoint-based aeroelastic design optimization using a harmonic balance method. In: ASME turbo expo: Turbomachinery technical conference and exposition. American Society of Mechanical Engineers Digital Collection; 2020, p. 1–12.

[57] Fransson TH, Verdon JM. Panel discussion on standard configurations for unsteady flow through vibrating axial-flow turbomachine-cascades. In: Unsteady aerodynamics, aeroacoustics, and aeroelasticity of turbomachines and propellers. Springer; 1993, p. 859–89. http://dx.doi.org/10.1007/978-1-4613-9341-2.

[58] Gordon WJ, Hall CA. Construction of curvilinear coordinate systems and applications to mesh generation. Internat J Numer Methods Engrg 1973;7(4):461–77. http://dx.doi.org/10.1002/nme.1620070405.

[59] Golub GH, Welsch JH. Calculation of Gauss quadrature rules. Math Comp 1969;23(106):221–30. http://dx.doi.org/10.2307/2004418.

[60] Stephan B, Gallus HE, Niehuis R. Experimental investigations of tip clearance flow and its influence on secondary flows in a 1-1/2 stage axial turbine. In: ASME turbo expo: Power for land, sea, and air. American Society of Mechanical Engineers Digital Collection; 2001, p. 1–12. http://dx.doi.org/10.1115/2000-GT-0613.

[61] Pierzga MJ, Wood JR. Investigation of the three-dimensional flow field within a transonic fan rotor: Experiment and analysis. Trans ASME, J Eng Gas Turbines Power 1985;107(2):436–48. http://dx.doi.org/10.1115/1.3239744.
[62] Pierzga MJ, Wood JR. Laser anemometer measurements in a transonic axial-flow fan rotor. Tech. rep. TP 2879, NASA Lewis Research Center; Cleveland, OH, United States; 1989, p. 1–216.
[63] van Arnhem N, de Vries R, Sinnige T, Vos R, Eitelberg G, Veldhuis L. Engineering method to estimate the blade loading of propellers in nonuniform flow. AIAA J 2020;58(12):5332–46. http://dx.doi.org/10.2514/1.J059485.
[64] Jones AC. Design and test of a small, high pressure ratio radial turbine. Trans ASME, J Turbomach 1996;118(2):362–70. http://dx.doi.org/10.1115/1.2836651.
[65] Keep JA, Vitale S, Pini M, Burigana M. Preliminary verification of the open-source CFD solver SU2 for radial-inflow turbine applications. Energy Procedia 2017;129:1071–7. http://dx.doi.org/10.1016/j.egypro.2017.09.130.
[66] Press WH, Teukolsky SA, Vetterling WT, Flannery BP. Numerical recipes: The art of scientific computing. 3rd ed.. Cambridge University Press; 2007.
[67] Griewank A, Walther A. Evaluating derivatives: Principles and techniques of algorithmic differentiation. 1st ed.. SIAM; 2008.
[68] Bunker RS. The effects of manufacturing tolerances on gas turbine cooling. Trans ASME, J Turbomach 2009;131(4):1–11. http://dx.doi.org/10.1115/1.3072494.
[69] Python v3.7. 2020, https://www.python.org/.
[70] Parablade v1.0. 2020, http://dx.doi.org/10.5281/zenodo.3894778.
[71] Nurbspy v1.1. 2020, http://dx.doi.org/10.5281/zenodo.3894755.
[72] NumPy v1.18. 2020, https://numpy.org/.
[73] Pagmo/Pygmo v2.15. 2020, http://dx.doi.org/10.5281/zenodo.3738182.
[74] Nocedal J. Updating quasi-Newton matrices with limited storage. Math Comp 1980;35(151):773–82. http://dx.doi.org/10.2307/2006193.
[75] Liu DC, Nocedal J. On the limited memory BFGS method for large scale optimization. Math Program 1989;45(1–3):503–28. http://dx.doi.org/10.1007/BF01589116.
[76] Goldman R. Curvature formulas for implicit curves and surfaces. Comput Aided Geom Design 2005;22(7):632–58. http://dx.doi.org/10.1016/j.cagd.2005.06.005.

Multi-row Adjoint-based Optimization of NICFD Turbomachinery Using a CAD-based Parametrization

Roberto Agromayor*[a], Nitish Anand[b], Matteo Pini[b], and Lars O. Nord[a]

* Corresponding author: roberto.agromayor@ntnu.no

[a] Department of Energy and Process Engineering, NTNU – The Norwegian University of Science and Technology, Kolbj. Hejes v. 1B, NO-7491, Trondheim, Norway

[b] Propulsion & Power, Aerospace Engineering Faculty, Delft University of Technology, Kluyverweg 1, 2629 HS, Delft, The Netherlands

Abstract

The aerodynamic design of turbomachinery components is increasingly carried out by means of automated workflows that integrate high-fidelity physical models with numerical optimization techniques. Currently, most of the adjoint-based design systems documented in the open literature assume that the fluid behaves as an ideal gas, are restricted to the optimization of a single row of blades, or are not suited to impose geometric constraints. In response to these limitations, this paper presents a gradient-based shape optimization framework for the aerodynamic design of turbomachinery blades operating under non-ideal thermodynamic conditions. The proposed design system supports the optimization of multiple blade rows and it integrates a CAD-based parametrization with a RANS flow solver and its discrete adjoint counterpart. The capabilities of the method were demonstrated by performing the design optimization of a single-stage axial turbine that employs isobutane (R600a) as working fluid. Notably, the aerodynamic optimization respected the minimum thickness constraint at the trailing edge of the stator and rotor blades and reduced the entropy generation within the turbine by 36%, relative to the baseline, which corresponds to a total-to-total isentropic efficiency increase of about 4 percentage points. The analysis of the flow field revealed that the performance improvement was achieved due to the reduction of the wake intensity downstream of the blades and the elimination of a shock-induced separation bubble at the suction side of the stator cascade.

Keywords: turbine, compressor, gradient, discrete adjoint, CFD, SU2, open-source, ORC, organic Rankine cycle, real gas, non-ideal compressible fluid dynamics.

This article is awaiting submission and is therefore not included.